DEFORMATION AND DAMAGE MECHANISMS IN SELECTED 2000 SERIES ALUMINUM ALLOYS UNDER BOTH QUASI-STATIC AND DYNAMIC IMPACT LOADING CONDITIONS

A Thesis Submitted to the College of
Graduate Studies and Research
In Partial Fulfillment of the Requirements
For the Degree of Master of Science
In the Department of Mechanical Engineering
University of Saskatchewan
Saskatoon

By
Ahmed Alade Tiamiyu

PERMISSION TO USE

In presenting this thesis in partial fulfillment of the requirements for a Postgraduate degree from the University of Saskatchewan, I agree that the Libraries of this University may make it freely available for inspection. I further agree that permission for copying of this thesis in any manner, in whole or in part, for scholarly purposes may be granted by Prof. Akindele Odeshi, the professor who supervised my thesis work or in his absence, by the Head of the Department or the Dean of the College in which my thesis work was done. It is understood that any copying or publication or use of this thesis or parts thereof for financial gain shall not be allowed without my written permission. It is also understood that due recognition shall be given to me and to the University of Saskatchewan in any scholarly use which may be made of any material in my thesis.

Requests for permission to copy or to make other uses of materials in this thesis in whole or part should be addressed to:

Head of the Department of Mechanical Engineering
University of Saskatchewan
57 Campus Drive
Saskatoon, Saskatchewan S7N 5A9
Canada.

ABSTRACT

In recent times, application of aluminum alloys is favored in the transportation sectors such as the aerospace and automobile industries where reduced fuel consumption and greenhouse gas emission are major priorities. In these applications, these alloys can be exposed to dynamic shock loading conditions as in the case of car crash and birds' collision during aircraft's take-off or landing. This study therefore focused on the deformation and damage mechanisms in AA 2017, AA 2024 and AA 2624 aluminum alloys under both quasi-static and dynamic impact loading conditions.

Cylindrical specimens of the selected aluminum alloys were investigated under both quasi-static loading at 3.2 $x10^{-3}$ s^{-1} using an Instron R5500 mechanical testing machine and dynamic impact loading using the split Hopkinson pressure bar at strain rates ranging between 2000 and 8000 s^{-1}. The effects of strain rate and temper condition on the microstructural evolution in the alloys during mechanical loading were studied. The electron backscatter diffraction (EBSD) technique was used to investigate the texture of the naturally-aged AA 2017 and AA 2624 alloys before and after dynamic shock loading. The contributions of the major alloying elements such as copper, magnesium and silicon to the microstructural evolution and deformation behavior of the alloys under the dynamic shock loading condition were also studied using the energy dispersive spectroscopy (EDS) technique.

Results showed that the morphology and atomic distribution of particles in the investigated alloys are functions of the temper condition. The hardness of all the three alloys was higher in the age-hardened conditions than the annealed ones. Although deformation of the alloy under quasi-static compressive loading was dominated by strain hardening, flow softening leading to strain localization and formation of shear bands occurred once certain critical strain values were reached. Under both quasi-static and dynamic loading, the alloys with low Cu:Mg ratio (AA 2024 and AA 2624) showed higher mechanical strength in age-hardened condition than that with high Cu:Mg ratio (AA 2017). All the alloys in the annealed condition exhibited an enhanced plasticity and formability. Intense strain localization leading to formation of adiabatic shear bands (ASBs) was the principal contributor to failure in the alloys under dynamic impact loading. Both deformed and transformed bands were observed, with cracking occurring mainly along the transformed shear bands. The tendency for formation of adiabatic shear bands is observed to be a function of the

alloy composition, temper condition, strain, strain rate and strain hardening rate. In the natural aging condition, AA 2024 showed the highest susceptibility to formation of ASBs followed by AA 2624 and AA 2017 in that order. On the other hand, AA 2024 has the least susceptibility in the artificially-aged condition. Occurrence of bifurcation of transformed bands in dynamic impacted specimens is dependent on temper condition, strain and strain rate. The mechanism of fracture of the precipitation hardened samples is typical of ductile fracture occurring sequentially by nucleation, growth, and coalescence of micro-voids processes within transformed band. Elongated grains were observed to arrest propagating shear band depending on the angle the band makes with elongated grains. The higher the angle of inclination of a shear band to the grain on its path, the higher the tendency of the grain to stop its propagation.

Texture analysis of the impacted specimens of AA 2017-T451 and AA 2624-T351 shows that the former has a higher tendency for the evolution of ultra-fine DRX grains within the transformed shear band. High strain rate led to the development of CD//<111> orientations at the expense of CD//<110> orientations. Schmid factor calculations performed on few different orientations in the starting microstructure shows that CD//<110> is less susceptible to slip deformation and consequently underwent rotation to CD//<111>.

ACKNOWLEDGMENT

I would like to express my sincere gratitude to my supervisor, Prof. Akindele Odeshi for the opportunity to carry out my M.Sc. study under his guidance. His kindness, time, professional and scientific contributions to the success of my study are deeply appreciated. The contributions of Prof. Ike Oguocha and Prof. Jerzy Szpunar, my advisory committee members are greatly appreciated. I thank Prof. Oguocha for his time, advice, insightful and valuable comments which have remarkably contributed to the success of this study. I am very grateful for Prof. Szpunar's insightful comments especially as it relates to the texture analysis in this study and for granting me the permission to use his EBSD facility.

My appreciations also go to Mr. Rob Peace for his time, advice and patience in training me on most of the equipment used in the course of my MSc program. To Kelley Neale, your constant advice and support at all times are deeply valued. The support of Mr. Nan Fang Zhao in my experimental investigations is also appreciated. To Aderopo Adesola, thanks for your advice and support at all times.

Dr. Ritwik Basu of the department of Mechanical engineering, ITM University, India is greatly appreciated for the time spent in ensuring my sound knowledge of texture of materials. To members of my research group, colleagues and friends; your contribution and moral supports towards the completion of this thesis were indeed needful and helpful. Thank you.

My parents' (Mr & Mrs Tiamiyu) labour in prayers just to see me succeed cannot be forgotten. I would like to use this medium to say thank you for your patience thus far. To my siblings, Saheed, Latifat, Yusuf and Idris; you guys are wonderful and your understanding of matters at such a time as this are really appreciated.

My gratitude also goes to my wife, Raliat Abiodun Tiamiyu, whose patience at every needful time cannot be down played. I had earlier thought that while writing this section of the thesis, you would be referred to as my fiancée, but it pleases the Lord to exceed our imaginations and expectations. Thanks for being an awesome wife.

DEDICATION

"Now unto him that is able to do exceeding abundantly above all that we ask or think, according to the power that worketh in us"

TABLE OF CONTENTS

Permission to use…….....i

Abstract……..ii

Acknowledgment……...iv

Dedication…….....v

Table of Contents..……....vi

List of Tables…….ix

List of Figures…….....x

List Abbreviations and Symbols...…….…xix

Chapter 1: Introduction……1

1.1 Overview……...……...1

1.2 Motivation……..……..2

1.3 Research objectives……...……...3

1.4 Thesis arrangement……..3

Chapter 2: Literature Review…….....4

2.1 Precipitation in 2000 series aluminum alloy……...……....4

2.1.1 Al-Cu based alloys……...……....5

2.1.2 Al-Cu-Mg based alloys ….……..7

2.2 Tensile/Compressive deformation behaviour of metallic materials ……11

2.3 Hardening curve in metallic materials under dynamic shock loading ……..……14

2.4 Shear band in metallic materials under dynamic or ballistic impact ……....15

2.4.1 Aluminum alloys……16

2.4.2 Steels……..……17

2.4.3 Magnesium alloys……..……18

2.4.4 Other metals/alloys……..……..……19

2.5 Shear band in other mechanical processes…….……20

2.6 Initiation and propagation mechanisms of adiabatic shear band……21

2.7 Microstructural evolution in ASB……..22

2.7.1 Dynamic Recovery (DRV)……23
2.7.2 Recrystallization…… 24
2.7.2.1 Rotational Dynamic Recrystallization (RDRX)……25
2.7.2.2 Progressive Subgrain Misorientation (PriSM) Recrystallization……28
2.8 Mechanism of Adiabatic Shear Fracture in Compressed Metallic Materials……..29
2.9 Factors influencing adiabatic shear band formation……...30
2.10 Texture evolution in metallic alloys under shock loading condition……..……32

Chapter 3: Materials and Methodology……....34

3.1 Materials……34
3.2 Heat treatment procedure…..……35
3.3 Mechanical test……..……36
3.3.1 Hardness test……..……36
3.3.2 Dynamic impact test……..……36
3.3.3 Quasi-static Compression test……..……..……38
3.4 Microstructural evaluation……38
3.4.1 Optical and Scanning Electron Microscopy……..39
3.4.2 Electron Backscattered Diffractometry (EBSD) and Energy Dispersive Spectroscopy (EDS)……...39

Chapter 4: Results and Discussion…….……....41

4.1 Microstructure of the as-received AA 2017, AA 2024 and AA 2624 Aluminum Alloys before Mechanical Loading……41
4.1.1 Morphology of second phase particles in AA 2017……42
4.1.2 Morphology of second phase particles in AA 2024……46
4.1.3 Morphology of second phase particles in AA 2624……49
4.2 Quasi-static Mechanical Test……54
4.2.1 Hardness test……..54
4.2.2 Quasi-static compression test……....56
4.3 Dynamic impact test……...……62

4.4 Microstructural Evolution in AA 2017, AA 2024 and AA 2624 aluminum alloys during mechanical Loading ……..……..71
4.4.1 Quasi-static compression…….…..71
4.4.2 Dynamic Impact Loading……..…….82
4.4.2.1 Shear band geometry in dynamic impacted specimen……84
4.4.2.2 Deformed band in AA 2017, AA 2024 and AA 2624 aluminum alloys….91
4.4.2.3 Transformed bands in AA 2017, AA 2024 and AA 2624 aluminum alloys……..…….……..96
4.4.3 Effect of grain morphology on ASB propagation……108
4.4.4 Specimens' fragmentation under dynamic impact loading.……..……....110
4.5 Electron Backscattered Diffraction (EBSD) Analysis……116

Chapter 5: Summary, Conclusions and Recommendations...……...125

5.1 Summary……..125
5.2 Conclusions…….…….125
5.3 Recommendations for future work…….……...……..126

REFERENCES……...……127

APPENDIX A (Standard Operating Procedure for SHPB)…….……...141
APPENDIX B (Analysis of elastic wave data obtained from impact test to generate stress, strain and strain rate data)..……...……...…...…145
APPENDIX C (Copy Right Permissions)……..151

LIST OF TABLES

Table 3.1	Chemical composition of the investigated AA 2000 aluminum alloys (wt. %).	34
Table 3.2	ICP-MS result of the investigated aluminum alloys (wt. %).	34
Table 3.3	Temper designation of the selected aluminum alloys.	35
Table 3.4	Etching time used for the investigated aluminum alloys.	39
Table 4.1	Summary of particle morphology.	53
Table 4.2	Chemical analysis of second phase particles identified by EDS analysis in the selected aluminum alloys.	54
Table 4.3	Mechanical properties and microstructural observations of the investigated alloys under quasi-static loading.	57
Table 4.4	Mechanical properties of selected aluminum alloys under dynamic shock loading.	64
Table 4.5	Experimental data sheet showing the critical values at which ASBs are formed in the dynamic impact specimen of the selected aluminum alloys.	82

LIST OF FIGURES

Fig. 2.1 Aluminum-rich corner of the Al-Cu-Mg phase diagram indicating the phase fields as a function of composition, after long term aging at 190 ^{o}C. While the thick solid line signifies the (α + S) phase boundary at 500 ^{o}C, the dotted lines indicates phase boundaries at 190 ^{o}C. 5

Fig. 2.2 Al-rich corner of the Al–Cu phase diagram showing the metastable solvus boundaries for GP zones, θ'' and θ', together with the equilibrium solvus line for the θ phase. 6

Fig. 2.3 Schematic unit cells of the existing controversial structure models for S-phase, projected along the $[100]_S$ direction. **a**, **b** and **c** are the lattice vectors, and *x* is the fractional coordinates of atoms in the **a** or $[100]_S$ direction. 9

Fig. 2.4 Shear stress versus nominal shear strain for a typical work-hardening material. 12

Fig. 2.5 Typical strain hardening rate-strain curve in (a) twinning-controlled deformation and (b) slip-controlled deformation. 15

Fig. 2.6 Possible shear-band initiation mechanisms in single-phase homogeneous materials. (a) grain-size inhomogeneity, (b) geometrical softening, (c) Peirce–Asaro–Needleman textural localization and (d) dislocation pile-up release. 22

Fig. 2.7 Schematic softening kinetics at three temperature range. 23

Fig. 2.8 Schematic of successive dislocation annihilation mechanisms. 24

Fig. 2.9 Microstructural evolution in high-strain-rate deformation of tantalum: (a) uniform dislocation distribution; (b) elongated dislocation cells; (c) elongated subgrains; (d) subgrain break-up; (e) dynamically recrystallized grains. 26

Fig. 2.10 DRX mechanism for development of ultrafine elongated grains inside ASB observed in copper. 26

Fig. 2.11 SR mechanism in a Ti-Fe alloy (a) Illustration of the eutectic colony denoting the available dislocation motions. [(b) and (c)] Schematic evolution of shear bands: (b) rotation of neighboring subgrains leading orientations close to each-

other and (c) elimination of subgrain boundaries forming larger paths for dislocation motion. 27

Fig. 2.12 Schematic diagram of PriSM recrystallization inside an ASB from the starting single crystal (*a*), to formation of elongated subgrains (*b*), to rotation of equiaxed subgrains (*c*), to high angle misorientations between some subgrains (*d*), The final stage is boundary refinement during cooling (*e*). 28

Fig. 2.13 Schematic illustration of evolution of void and cracking in ASBs, sequence a, b, c corresponds to increasing density of void nucleation sites. 30

Fig. 3.1 Schematic of cylindrical test specimens showing (a) dimension and (b & c) cutting direction. 35

Fig. 3.2 Schematic of split Hopkinson pressure bar (SHPB). 38

Fig. 4.1 Optical micrographs of as received (a) AA 2017-T451, (b) AA 2024-T351 & (c) AA 2624-T351 showing grain and particle morphology. 42

Fig. 4.2 Optical micrographs showing the distribution of second phase particles in the (a) AA 2017-T451, (b) AA 2017-T651 and (c) AA 2017-O alloy before mechanical loading. 43

Fig. 4.3 SEM micrographs showing the distribution of second phase particles in the (a) AA 2017-T451, (b) AA 2017-T651 and (c) AA 2017-O alloy before mechanical loading. 43

Fig. 4.4 EDS maps of the major alloying elements in the second phase particles of AA 2017 aluminum alloy in naturally-aged, artificially-aged and annealed conditions. 45

Fig. 4.5 Optical micrographs showing the distribution of second phase particles in the (a) AA 2024-T351, (b) AA 2024-T651 and (c) AA 2024-O alloy before mechanical loading. 47

Fig. 4.6 SEM micrographs showing the distribution of second phase particles in the (a) AA 2024-T351, (b) AA 2024-T651 and (c) AA 2024-O alloy before mechanical loading. 47

Fig. 4.7 EDS maps of the major alloying elements in the second phase particles of AA 2024 aluminum alloy in naturally-aged, artificially-aged and annealed conditions. 48

Fig. 4.8 Optical micrographs showing the distribution of second phase particles in the (a) AA 2024-T351, (b) AA 2624-T651 and (c) AA 2624-O alloy before mechanical loading. 50

Fig. 4.9 SEM micrographs showing the distribution of second phase particles in the (a) AA 2624-T351, (b) AA 2624-T651 and (c) AA 2624-O alloy before mechanical loading. 50

Fig. 4.10 EDS maps of the major alloying elements in the second phase particles of AA 2624 aluminum alloy in naturally-aged, artificially-aged and annealed conditions. 51

Fig. 4.11 (a) Optical and (b, c & d) scanning electron micrographs showing sub-grain structure in the test specimens before mechanical loading in AA 2624-T351 and AA 2624-T651 aluminum alloy. The GB web is absent in AA 2624-O aluminum alloy sample 53

Fig. 4.12 Vickers hardness values of the AA 2017, AA 2024 and AA 2624 aluminum alloy specimens in naturally-aged, artificially-aged and annealed condition. 56

Fig. 4.13 (a) Engineering stress-strain curves and (b) strain hardening rate-strain curve of AA 2017-T451, AA 2017-T651 and AA 2017-O aluminum alloy under quasi-static compressive loading. 58

Fig. 4.14 (a) Engineering stress-strain curves and (b) strain hardening rate-strain curve of AA 2024-T351, AA 2024-T651 and AA 2024-O aluminum alloy under quasi-static compressive loading. 59

Fig. 4.15 (a) Engineering stress-strain curves and (b) strain hardening rate-strain curve of AA 2624-T351, AA 2624-T651 and AA 2624-O aluminum alloy under quasi-static compressive loading. 60

Fig. 4.16 Engineering stress-strain curves of (a) naturally-aged, (b) artificially-aged and (c) annealed AA 2017, AA 2024 and AA 2624 aluminum alloy under quasi-static compressive loading. 62

Fig. 4.17 Dynamic stress-strain curve of impacted specimens in (a) naturally-aged, (b) artificially-aged and (c) annealed condition as a function of impact momentum. 63

Fig. 4.18 Dynamic stress-strain curve of impacted AA 2024 specimens in (a) naturally-aged, (b) artificially-aged and (c) annealed condition as a function of impact momentum. 66

Fig. 4.19 Dynamic stress-strain curve of impacted AA 2624 specimens in (a) naturally-aged, (b) artificially-aged and (c) annealed condition as a function of impact momentum. 67

Fig. 4.20 (a) Dynamic stress-strain curve and (b) strain hardening rate-strain curve of AA 2017-T451, AA 2017-T651 and AA 2017-O aluminum alloy subjected to an impact momentum of 40 kg.m/s. 69

Fig. 4.21 (a) Dynamic stress-strain curve and (b) strain hardening rate-strain curve of AA 2024-T351, AA 2024-T651 and AA 2024-O aluminum alloy subjected to an impact momentum of 40 kg.m/s. 69

Fig. 4.22 (a) Dynamic stress-strain curve and (b) strain hardening rate-strain curve of AA 2624-T351, AA 2624-T651 and AA 2624-O aluminum alloy subjected to an impact momentum of 40 kg.m/s. 70

Fig. 4.23 Engineering stress-strain curves of (a) naturally-aged, (b) artificially-aged and (c) annealed AA 2017, AA 2024 and AA 2624 aluminum alloys under dynamic impact loading. 70

Fig. 4.24 (a) Optical micrographs showing shear band geometry and (b) SEM micrographs showing edge crack and distribution of second phase particles inside and outside shear bands on the compression plane of AA 2017-T451 specimen after quasi-static loading. 72

Fig. 4.25 Optical and SEM micrographs showing (a) edge crack and (b) inside and outside deformed band on the compression plane of AA 2017-T651 specimen under quasi-static loading. 73

Fig. 4.26 Optical and SEM micrographs showing (a) deformed and (b) outside deformed band on the compression plane of AA 2017-O specimen under quasi-static compression. 74

Fig. 4.27 Optical and SEM micrographs showing microstructural features inside and outside shear bands in AA 2024-T351 alloy after quasi-static loading in compression (a) overview of shear deformed band (b) transformed band (c) outside shear band. 75

Fig. 4.28 Optical and SEM micrographs showing microstructural features inside and outside shear band in AA 2024-T651 specimen after quasi-static loading in compression (a) overview (b) outside shear band (c) deformed band region. No edge crack was observed. 76

Fig. 4.29 SEM micrographs showing microstructural features inside and outside shear band in AA 2024-O specimen after quasi-static loading in compression (a) overview (b) outside shear (c) deformed band region (d) edge crack. 77

Fig. 4.30 Optical and SEM micrographs showing microstructural features on the compression plane of AA 2624-T351 specimen after quasi-static loading (a) overview (b) outside crack region (c) edge crack. 79

Fig. 4.31 Optical and SEM micrographs showing microstructural features on the compression plane of AA 2624-T651 specimen after quasi-static loading (a) overview (b) outside shear band region (c) edge crack. 80

Fig. 4.32 SEM micrographs showing microstructure of AA 2624-O specimen after quasi-static compressive loading (a) overview, (b) outside deformed band (c) inside deformed band 81

Fig. 4.33 Circular Geometry of ASB on the compression plane of (a) AA 2017-T451 alloy with no bifurcation and (b) AA2017-T651 alloy with bifurcation. 85

Fig. 4.34 Circular geometry of ASB on the compression plane (transverse plane) of (a) AA 2024-T351 alloy with no bifurcation and (b) AA 2024-T651 alloy with bifurcation and dual banding. 86

Fig. 4.35 Arc-type geometry of ASB on the compression (transverse) plane of (a) AA 2624-T351 alloy and (b) AA 2624-T651 alloy. Both temper conditions shows branching at the band tip without bifurcation. 87

Fig. 4.36 (a) Optical micrograph showing a parabolic ASB geometry on the longitudinal section of impacted specimen in all three selected aluminum alloys; both natural and artificial aging conditions. (b) Schematic of formation of parabolic ASB geometry with compressive shear angle. 89

Fig. 4.37 (a) Optical micrograph of fully formed transformed band on the longitudinal section of impacted aluminum alloy specimen (b) proposed relationship between ASB geometry and shear angle profile on the longitudinal section of shock loaded precipitation hardened aluminum alloys. 90

Fig. 4.38 Geometry of shear band formation in impacted (a) AA 2017 and AA 2024 (b) AA 2624. 91

Fig. 4.39 Optical micrographs of impacted (a) AA 2017 (b) AA 2024 and (c) AA 2624 specimens showing deformed band morphology. 92

Fig. 4.40 Optical and SEM micrographs of AA 2017-O showing particles within grain boundaries (b) outside and (c) inside deformed band. 93

Fig. 4.41 Optical and SEM micrographs of AA 2024-O showing particles within grain boundaries (a) inside and (b) outside deformed band. 94

Fig. 4.42 Optical and SEM micrographs of AA 2624-O showing particles within grain boundaries (b) inside and (c) outside deformed band. 95

Fig. 4.43 SEM micrographs showing the (a) inside and (b) outside ASB of impacted AA 2017-T451 specimen at an impact momentum of 42.6 kg m/s. 97

Fig. 4.44 SEM showing the (a) inside and (b) outside ASB of impacted AA 2017-T651 specimen at an impact momentum of 43.6 kg m/s. 98

Fig. 4.45 EDS line scan of impacted AA 2017-T451 and AA 2017-T651 specimen across ASB. 99

Fig. 4.46 SEM micrographs of impacted AA 2024-T351 specimen showing the (a) inside and (b) outside ASB. 101

Fig. 4.47 SEM micrographs of impacted AA 2024-T651 specimen showing the (a) inside and (b) outside ASB. 102

Fig. 4.48 EDS line scan of impacted AA 2024-T351 and AA 2024-T651 specimen across ASB. 103

Fig. 4.49 SEM micrographs of impacted AA 2624-T351 specimen showing the (a) inside and (b) outside ASB. 105

Fig. 4.50 SEM micrographs of impacted AA 2624-T651 specimen showing the (a) inside and (b) outside ASB. 106

Fig. 4.51 EDS line scans of impacted AA 2624-T351 and AA 2624-T651 specimen across ASB. 107

Fig. 4.52 Schematic of adiabatic shear band formation in an equiaxed grain structure of AA 2017 and AA 2024 specimens. 109

Fig. 4.53 Schematic of adiabatic shear band formation in an elongated grain structure of AA 2624 specimen. 110

Fig. 4.54 SEM micrographs showing the mode of crack nucleation and propagation along a transformed band in AA 2017-T451 aluminum alloy. 111

Fig. 4.55 SEM micrographs showing the mode of crack nucleation and propagation along a transformed band in AA 2017-T651 aluminum alloy. 112

Fig. 4.56 SEM micrographs showing the mode of crack nucleation and propagation along a transformed band in AA 2024-T651 aluminum alloy. 113

Fig. 4.57 Optical micrographs showing the mode of crack nucleation and propagation along a transformed band in AA 2624-T351 aluminum alloy. 114

Fig. 4.58 Images of typical fractured specimen of the investigated aluminum alloys. 1 and 2 are the fracture surfaces along (cone) and outside adiabatic shear band region respectively. 115

Fig. 4.59 SEM fractographs of AA 2017 alloy specimens in (a-c) T451 and (d-f) T651 temper. 115

Fig. 4.60 SEM fractographs of AA 2024 alloy specimens in (a-c) T351 and (d-f) T651 temper. 116

Fig. 4.61 SEM fractographs of AA 2624 alloy specimens in (a-c) T351 and (d-f) T651 temper. 116

Fig. 4.62 EBSD IPF maps of the as-received (a) AA 2017-T451 and (b) AA 2624-T351 aluminum alloys. 117

Fig. 4.63 IPF maps of deformed AA2017-T451 and AA2624-T351 at (a-b) center and (c-d) near-the-edge of the compression plane. The arrow indicates two of the grains with significant banded structure. Sketches of shear bands' morphologies on compression plane showing location of EBSD measurements, i.e. center and near-the-edge, are presented in (e). 118

Fig. 4.64 (a) The orientations of the selected grains in AA 2017-T451 near the edge converge to a point; a signature of strain free (DRX) grain and (b) grains far away from the band carries the footprint of deformation indicated as a wide orientation spread. 119

Fig. 4.65 Grain boundary fraction plot for the as-received (a) AA 2017-T451 and (b) AA 2624-T351 alloy. 120

Fig. 4.66 Local average misorientation (Kernel) distribution in (a) AA 2017-T451 and (b) AA 2624-T351 alloy. 121

Fig. 4.67 A point-to-origin misorientation profile plots for few different CD//<001> grains taken from both edge (a-c) and center (d-f) of deformed AA2624-T351 sample. 123

Fig. 4.68 (a) LAGB and (b) HAGB fraction plot for deformed AA2017-T451 and AA2624-T351 aluminum alloys. 123

Fig. 4.69 Area fraction of selected fibre (CDs) in impacted (a) AA2017-T451 and (b) AA2624-T351 aluminum alloys. 124

Fig. 4.70 Schmid factor (SF) map and corresponding SF distribution of as-received samples of (a) AA2017-T351 and (b) AA2624-T351: “x” and “y” denotes CD//<110> and CD//<111> orientations respectively. 124

LIST OF ABBREVIATIONS AND SYMBOLS

ABBREVIATIONS

AA	Aluminum association
ASB	Adiabatic shear band
DB	Deformed band
TB	Transformed band
GB	Grain boundary
OM	Optical microscopy
SHPB	Split Hopkinson pressure bar
TWC	Thick wall cylinder
SEM	Scanning electron microscope/microscopy
TEM	Transmission electron microscope/microscopy
ECAP	Equal-channel angular processing
HREM	High resolution electron microscope
EDS	Energy dispersive X-ray spectroscopy
EBSD	Electron backscattered diffraction
XRD	X-ray diffraction (XRD)
ICP-MS	Inductively coupled plasma-mass spectrometry
AISI	American iron and steel institute
SFE	Stacking fault energy
LAGB	Low angle grain boundary
HAGB	High angle grain boundaries
DRX	Dynamic recrystallization
SRX	Static recrystallization
RDRX	Rotational dynamic recrystallization
PriSM	Progressive subgrain misorientation
ALCOA	Aluminum company of America
HV	Vickers hardness
GP Zones	Guinier-Preston zones
GPB Zones	Guinier-Preston-Bagaryatsky zones
SP	Second phase

SPFZ	Second phase particle free zone
PFS	Peak flow stress
IPF	Inverse pole figure
CD	Compression direction

SYMBOLS

C_v	Heat capacity, J/kg K
W_p	Specific work of deformation, J/m^3
σ	Applied Stress, MPa
ε	Applied strain
ρ	Density, kg/m^3
γ	Shear angle, ^{o}

CHAPTER ONE

INTRODUCTION

1.1 Overview

The need to reduce fuel consumption and greenhouse gas emissions in the transportation sector is a major driving force for the development of new lightweight materials or the improvement of the mechanical performance of the existing ones. Research efforts are geared towards reducing the weight of automobile and aerospace materials used without compromising their strength. Aluminum alloys are very attractive for such applications due to their high specific strength [1,2]. Over the years, different grades of aluminum alloys (1000, 2000, 3000, 4000, 5000, 6000, 7000 and 8000 series) emerged as a result of the need for modification by small additions of alloying elements in different proportions in a bid to improve the mechanical, physical and other properties of aluminum [3]. Of all the aluminum grades, only the 2000, 6000, 7000 and some of the 8000 series are heat treatable [4]. One of the most widely used mechanisms for further strengthening the heat treatable aluminum alloys is precipitation hardening, where the alloys are subjected to heat treatment procedures that lead to generation of fine precipitates [1,5]. These precipitates strengthen the alloys by becoming effective barriers to motion of dislocations, thereby making them more resistance to plastic deformation [5]. Depending on the coherency of the interface between the precipitates and the aluminum matrix, dislocations can either cut through or loop around the precipitates, but at stress levels that are higher than that required to move through the aluminum matrix. The non-heat treatable aluminum alloys are commonly strengthened by strain hardening (cold work).

Heat treatable 2000 series aluminum alloys have been widely used in the aerospace and automobile industries due to their high strength-to-weight ratio, excellent fatigue properties, good fracture toughness [6-8] and high resistance to stress corrosion cracking [9]. Although the 2000 series aluminum alloys are Al-Cu or Al-Cu-Mg based, the precipitated phases could span up to five (5) phase fields depending on the concentrations of Cu, Mg and Si [7]. The addition of Cu improves the mechanical strength of the aluminum alloy while Mg and Mn are introduced to further improve the mechanical strength after solution heat treatment [10]. The selected alloys in this study are the AA 2017, AA 2024 and AA 2624 aluminum alloys which are choice materials for aerospace and automotive applications.

AA 2017 aluminum alloy was the first high strength (about 276 MPa yield strength) heat treatable aluminum alloy initially designed for the frame work of rigid airships by the Germans during World War I [11]. They are now extensively employed in aerospace and automobile industries due to their excellent high strength-to-weight ratio [12-14]. Some authors refer to AA 2017 as Al-Cu based alloy [12-16] due to their low magnesium content while other researchers preferred to refer to it as Al-Cu-Mg based alloy because of the magnesium addition [11]. AA 2017 aluminum alloy has large solidification range with the attendant problem of hot tearing which is linked to the level of strains and stresses induced by thermal gradients, shrinkage-related brittleness, hindered feeding of the liquid phase, eutectic and inclusion segregation at the grain boundaries etc. [17]. Also, due to their heterogeneous microstructure, AA 2017 exhibit localised corrosion problems especially in chloride-containing media [12].

The AA 2024 aluminum alloy is the most widely used of the 2000 series aluminum alloys with moderate (about 324 MPa) yield strength [8]. It has good damage tolerance [8,18,19] and good fatigue resistance [9]. It also offers good corrosion resistance due to high tendencies to form inherent protective oxide film on the surface [20]. AA 2024 aluminum alloy is used in lightweight transportation vehicles in the form of sheets and in plates for aircraft fuselage skin, fuselage bulkhead, lower wing skins [20,21], rivets and truck wheel [19]. Despite the extensive use of AA 2024, there are still limitations in industrial applications due to their highly anisotropic grain structures and properties [9]. The AA 2624 is a newly developed AA 2x24 aluminum alloy series intended for application in transportation vehicles such as in aerospace and automobile industries. Extensive research work is yet to be carried out on this alloy.

1.2 Motivation

Aluminum alloys used in automotive and aerospace applications can be exposed to static or dynamic loading conditions. Hence, there is a need to understand their mechanisms of deformation and failure under these conditions. For example, damage to aircrafts due to collision with birds during take-off or landing has been reported [8,22]. Although most commercial aluminum alloys are investigated extensively under quasi-static loading, little is known about their behavior under such severe dynamic impact loading condition. There is need to generate microstructural and mechanical data which can be used to simulate the dynamic response of aluminum alloys to high strain-rate loading. These data can also be utilized in future aluminum alloy development for

enhanced failure resistance under dynamic shock loading. In this study, the mechanical behavior of AA 2624 (an alloy with stricter limits on impurity level in comparison with other AA 2x24 derivatives), AA 2017 and AA 2024 alloys in different temper conditions was investigated under both quasi-static and dynamic shock loading. What influenced the selection of these alloys is their closeness in terms of the concentration of the major alloying element (Cu) and the difference in their Cu/Mg ratios. The effects of these compositional variations, heat treatment temper and loading condition on the mechanical response of the Al-Cu-Mg alloys were investigated.

1.3 Research objectives

The overall goal of this research is to investigate the deformation and damage mechanisms in the selected AA 2017, AA 2024 and AA 2624 aluminum alloys under quasi-static and dynamic shock loading as influenced by temper conditions. In other to realise this overall goal, the specific objectives were to:

1. Determine the effects of strain rate, temper condition and initial texture on the mechanical response and microstructure of AA 2017, AA 2024 and AA 2624 aluminum alloys under quasi-static and dynamic shock loading conditions;
2. Determine the deformation and failure mechanisms in the selected alloys under both quasi-static and dynamic shock loading;
3. Identify the influence of the concentration of copper, magnesium and silicon on the microstructural evolution, deformation and failure behavior of the alloys under the dynamic shock loading condition.

1.4 Thesis arrangement

The current chapter, Chapter One, contains an overview, the motivations and objectives of this research. A summary of some of the previous work by other researchers in areas related to this study are provided as a literature review in Chapter Two. Detailed information about the investigated alloys and experimental procedures are enumerated in Chapter Three. Chapter Four contains the results and discussion, while Chapter Five contains the summary and conclusions drawn from this study.

CHAPTER TWO

LITERATURE REVIEW

2.1 Precipitation in 2000 series aluminum alloys

The investigated aluminum alloys belong to the AA 2000 series aluminium alloys which are commonly strengthened by precipitation hardening. This process involves homogenizing the aluminum alloy at a temperature between the solvus and solidus temperature, followed by quenching to room temperature where alloying elements are retained in a supersaturated solid solution [23]. Upon further heat treatment (aging) below the solvus temperature, atomic diffusion occurs leading to the formation of a sequence of metastable and stable phases as fine precipitates from the supersaturated solid solution. These precipitates are usually too small to be resolved under an optical microscope (OM) or a scanning electron microscope (SEM) except by high resolution electron microscope (HREM). They strengthen aluminum alloys by serving as effective barriers to the motion of dislocations. They can dissolve during heat treatment, as a result of the high solubility of Cu and Mg in Al [24].

Depending on the major and minor alloying elements addition to aluminum, the morphology, geometry, orientation and properties of the precipitates can vary widely in various aluminum alloys. Since the 2000 series aluminum alloys could be Al-Cu or Al-Cu-Mg based, the precipitation sequence can therefore be expected to differ. These are explained separately in the next two subsections. Figure 2.1 shows the possible phase fields that can exist during aging of 2000 series aluminum alloys at 190 ^{o}C and 500 ^{o}C [25]. The phase field in aged Al-Cu based alloys could be ($\alpha + \theta$) or ($\alpha + \theta$ + S) due to the presence of small amount of Mg, while that of Al-Cu-Mg based alloys falls within the (α + S), (α + S + T) or (α + T) region. Therefore, the Cu/Mg ratio in 2000 series aluminum alloys determine, to a large extent, the identity of the strengthening precipitate phases [24].

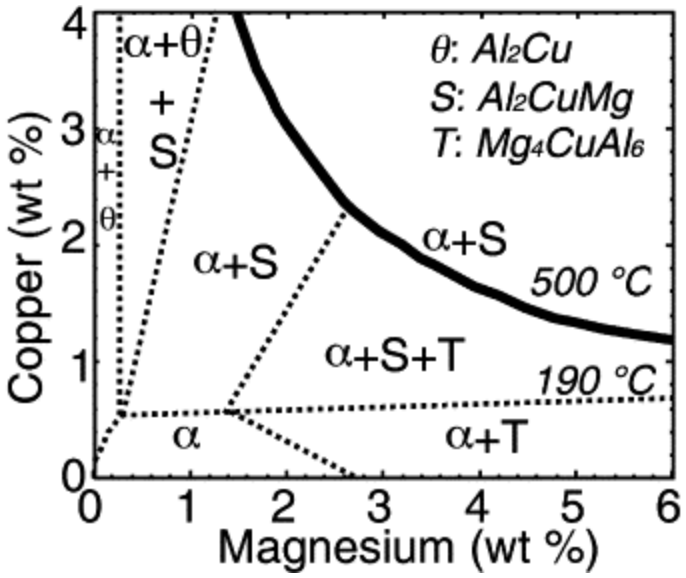

Fig. 2.1. Aluminum-rich corner of the Al-Cu-Mg phase diagram indicating the phase fields as a function of composition, after long term aging at 190 °C. While the thick solid line signifies the (α + S) phase boundary at 500 °C, the dotted lines indicate phase boundaries at 190 °C [25].

2.1.1 Al-Cu based alloys

The Al-Cu based alloys are the basis for the development of many high performance multicomponent aluminum alloys which find widespread applications in the automotive and aerospace industries. One of the major challenges of Al-Cu alloys is encountered during their production; there is high tendency for microcracking to occur during casting [26]. The precipitation sequence of an Al-Cu alloys has been proposed by several authors [24,27,28] to be:

$$Supersaturated\ Solid\ Solution\ (SSS) \rightarrow GP\ zones \rightarrow \theta'' \rightarrow \theta' \rightarrow \theta \qquad \ldots 2.1$$

where GP is Guinier-Preston, $\theta''(Al_3Cu)$ and θ' (Al_2Cu) are metastable phases and θ (Al_2Cu) is a stable phase. The first evidence of the existence of nano-sized GP zones in Al-Cu alloys was independently provided by Guinier and Preston in the late 1930s using different X-ray techniques [29,30]. Another study of GP zones in the early 1990s suggests a three dimensional clusters (GP pre-zones) prior to the formation of GP zones [29]. These GP pre-zones are said to comprise of several Cu rich planes separated by the matrix planes capable of transforming to the GP zone or directly to θ'' phase. Although GP zones and θ'' have plate-like morphology, GP zones are considered to comprise of monolayer of Cu atoms on a {200} lattice plane whereas θ'' consists of multilayer of Cu and Al atoms [23,28]. It was mentioned in another work that the morphologies

of GP zones could be platelet, sphere or needle, depending on the difference in the atomic diameters of solute and solvent elements [29]. In a study on thermodynamic analysis of GP zones, Jing et. al. [28] reported that there exists a critical size of the atomic clustering that corresponds to the nucleation of GP zones. It was observed that the smaller the size of the GP zones, the smaller the driving force for further precipitation.

The evolution of any of the aforementioned phases in an aged Al-Cu alloy is dependent on solute content, the degree of supersaturation and aging temperature [23,27]. Figure 2.2 shows the Al-rich corner of the Al–Cu phase diagram which includes the metastable solvus boundaries for GP zones, θ'' and θ' phases, together with the equilibrium solvus line for the θ phase. Stages in the precipitation sequence (Eq. 2.1) can be suppressed by aging at temperature close to or above the intermediate solvus temperatures [27,28] i.e. if the aging temperature of an Al-Cu based alloy is higher than the GP solvus temperature for a specific mole fraction of Cu, instead of the GP zones, metastable θ'' phase will precipitate as suggested in Fig. 2.2. The evolved precipitates in an age-hardenable aluminum alloy are effective barriers to motion of dislocations in which strengthening is enabled by dislocation-particle interactions which may involve mobile dislocations cutting through the precipitates or forced to loop around depending on the coherency of precipitate-matrix interface [31].

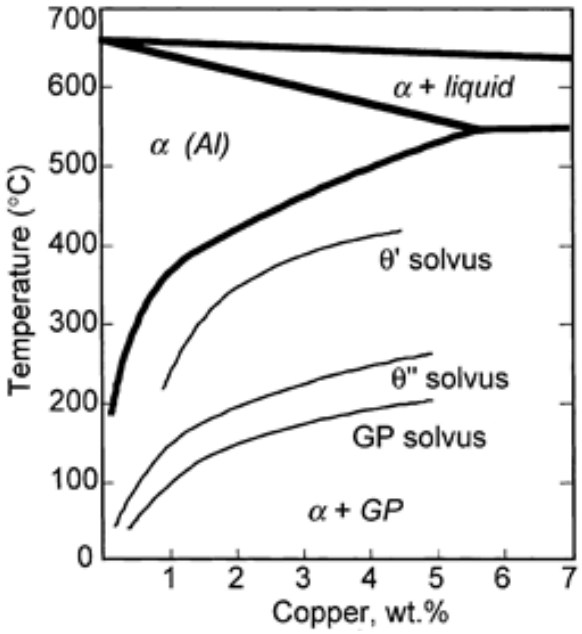

Fig. 2.2. Al-rich corner of the Al–Cu phase diagram showing the metastable solvus boundaries for GP zones, θ'' and θ', together with the equilibrium solvus line for the θ phase [27].

In terms of coherency of the precipitates with the aluminum matrix, coherency is lost as the precipitates changes to the equilibrium phase (θ) i.e. GP zones, θ'', θ' and θ are fully coherent, coherent, semi-coherent and incoherent with the aluminum matrix respectively [16,24]. The loss of coherency from the early phase of precipitation (GP zones) to the equilibrium phase (θ) as aging proceeds is attributed to the continuous growth of existing precipitates till it coarsens by the process referred to as Ostwald ripening [32]. Ostwald ripening is a diffusion-driven process involving the growth of large precipitates at the expense of the small ones so as to reduce the total amount of interfacial area between the two phases. Ostwald ripening are usually not desirable due to the fact that the process leads to deterioration of mechanical properties of age-hardened aluminum alloys [23].

2.1.2 Al-Cu-Mg based alloys

Al-Cu-Mg based alloys are 2000 series aluminum alloys in which precipitates formed are function of the ratio of major alloying elements (mostly Cu/Mg ratio) [33]. Different precipitation stages have been proposed for Al-Cu-Mg alloys. Bagaryatsky was the first to propose four precipitation stages (Eq. 2.2) in the age-hardening of Al-Cu-Mg base alloys. However, the term GPB (Guinier-Preston-Bagaryatsky) zone was first used later by Silcock [34-36].

$$Supersaturated\ Solid\ Solution\ (SSS) \rightarrow GPB\ zones \rightarrow S''/GPB2 \rightarrow S' \rightarrow S \qquad \ldots 2.2$$

where GPB is Guinier-Preston-Bagaryatsky, S'' and S' are metastable phases (distorted version of S phase), S (Al_2CuMg) is a stable phase.

GPB zones are known to be coherent with the aluminum matrix. Coherency is lost as precipitation proceeds to the most stable equilibrium *S* phase. GPB zone was observed to be an ordered structure with cylindrical shape of about 4 nm long and 1-2 nm in diameter along $<110>_{Al}$ directions. Gouma et al. [33] reported the dissolution of GPB after aging treatment of aluminum alloy with Cu/Mg ratio of 0.14 at 180 ^{o}C for 8 h. Sha et al. [7] reported the existence of solute clusters and GPB zones in AA 2024 aluminum alloy, while Bargaryatsky explains that a short ranged ordering consisting of Mg and Cu atoms are considered to be GPB zones [34]. In the recent times, both Cu/Mg clusters and GPB zones have been used interchangeably [33,37,38].

On the orientation, structure and properties of *S''* phase (with suggested structure of $Al_{10}Cu_3Mg_3$ [39]), quite a number of works have been reported using different techniques. Contrary to the report of Ringer et al. [40,41] that the metastable *S''* phase has no link with *S* phase in terms of orientation, structure and composition; the existence of such link was confirmed in a study by Ratchev *et al.*[38]. The *S''* phase has also been reported to have its lattice parameters (a = 0.4 nm, b = 0.925 nm and c = 0.718 nm) to be very close to those of the *S* phase (a = 0.4 nm, b= 0.923 nm and c = 0.714 nm) [33]. In affirmation of the fact that the structure of S" phase is not well understood, various structures such as orthorhombic, tetragonal, cubic and monoclinic has been proposed for this phase [34]. With the use of high-resolution transmission electron microscopy (HRTEM) and Z-contrast imaging on aluminum alloy with low Cu/Mg and small addition of Si, Kovarik et. al. [42] suggests that coherent orientation relationship (OR) exist between *S''* phase and aluminum matrix at the $(021)_{S"}$ // $(014)_{Al}$ and $(011)_{S"}$ // $(021)_{Al}$ interfaces. Using atom probe tomography (APT) and energy dispersive X-ray spectroscopy (EDS), they observed that Si enrichment contributed to the evolution of the *S''* phase when small addition of Si (0.12 wt. %) is present in the aluminum alloy. On the other hand, Wang and Starink [34] reported that high Si content (0.49 wt. %) suppressed the formation of *S''* phase. Wang and Starink [39] also confirmed that *S''* phases are coherent with the aluminum matrix and reported that its coherency is achievable by slightly distorted structure in comparison with *S* phase having coherent orientation relationship of $[100]_{S"}$ // $[100]_{Al}$, $[0\bar{1}1]_{S"}$ // $[053]_{Al,}$ $[013]_{S"}$ // $[011]_{Al}$. Ratchev *et al.* [38] proposed the formation of *S''* phase on dislocation loops and helices whose contribution to early stage hardening cannot be neglected. This phase was also reported to have the potential to transform to *S'* phase.

The orientation, structure and properties of *S'* and *S* phases are, in most cases, discussed together owing to the observation that the former is a precursor to the formation of the later [39]. Some researchers believe that *S'* and *S* phases should be considered same since they have identical structure when observed under high resolution electron microscope (HREM) and the formation enthalpies of both phases were observed to be similar [43]. The equilibrium *S* phase is generally considered to be lath-shaped and non-coherent with the aluminum matrix while *S'* phase is semi-coherent [34].

Several authors [2,39,44] have reported that Perlitz and Westren, using X-ray diffraction (XRD) technique, were the first to propose a structural model for S-phase precipitates called the PW

model. The PW model proposed the structure of the *S* phase as orthorhombic Cmcm (a space group having an inversion point) with 16 atoms per unit cell having lattice parameters; a = 0.4 nm, b = 0.923 nm and c = 0.714 nm (Fig. 2.3). Several years later, other researchers came up with new models for S phase in Al-Cu-Mg alloys. In the late 70s, the Mondolfo model which is a modified PW model with slight differences in lattice parameter (a = 0.4 nm, b = 0.925 nm and c = 0.718 nm) was proposed [2,45]. In this model, there is an atomic position shift and switching of Cu and Mg atoms in comparison to the unit cell of a PW model (Fig. 2.3). That is, one of the $(001)_S$ Cu–Mg atomic layers in the Mondolfo model is shifted along $[010]_S$ with respect to that in the PW model.

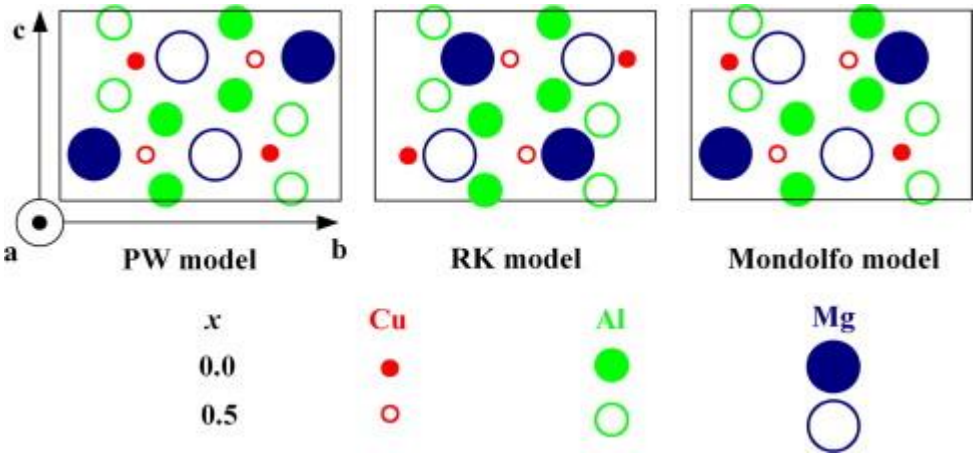

Fig. 2.3. Schematic unit cells of the existing controversial structure models for S-phase, projected along the $[100]_S$ direction. **a**, **b** and **c** are the lattice vectors, and x is the fractional coordinates of atoms in the **a** or $[100]_S$ direction [39].

In the year 2001, Kilaas and Radmilovic [2] proposed a new model (the RK model) with space group (Cmcm) and lattice parameters; $a = 0.403 \pm 0.001$ nm, $b = 0.930 \pm 0.013$ nm and $c = 0.718 \pm 0.01$ nm. This model is similar to the PW model except for the exchange in the position of Cu with Mg atoms (Fig. 2.3). The reasons for the existing controversy in the crystal structure of the *S*-phase are [44]:

a. The results of X-ray diffraction (XRD) measurements on the crystal structure of the S-phase have often been doubted because the weak diffraction of S-phase precipitates with respect to the strong matrix reflections overlap each other.

b. HRTEM images of the *S*-phase are lattice images which can only be interpreted indirectly by image simulation but unfortunately, to include the right aberrations of the objective lens in this simulation is difficult.
c. The interfacial energy and the strain energy have often been neglected in the calculations of the precipitates embedded in the Al-matrix from the first principles.

Although these reasons led to disagreements on the conclusions of the three approaches to the *S*-phase structure, the PW model is still the most acceptable [39]. In recent years, many researchers have suggested different precipitation sequences other than that proposed by Bagaryatsky in Eq. 2.2. The precipitation sequence suggested by Gouma *et al.* [33] for Al-Cu-Mg alloys with Cu/Mg weight ratio of between 0.11 and 0.29 is:

$$SSS \rightarrow Mg/Cu\ clusters\ or\ GPB\ zones\ \rightarrow S'' \rightarrow S' \rightarrow S \qquad \ldots 2.3$$

Ringer *et. al.* [40,41] investigated the precipitation sequence in Al-1.1Cu-1.7Mg (at. %) when aged between 120 and 200^{o}C. They found that age-hardening is first due to the formation of Cu-Mg co-clusters, followed by probable nucleation of GPB zones as the second stage of hardening around co-cluster sites. Proofs linking the orientation, structure and chemistry of S'' to *S* phase was inadequate in their findings such that they considered the inclusion of S'' in the precipitation sequence inappropriate. With these observations, they proposed a new precipitation sequence as follows:

$$SSS \rightarrow Cu/Mg\ co-clusters \rightarrow GPB\ zone \rightarrow S \qquad \ldots 2.4$$

where the Cu–Mg co-clusters are responsible for the initial hardening, *GPB zone* is reported to be the dominant precipitate at peak strengthening and the *S* phase appears in the softening stage.

In another study, Wang and Starink [34] investigated the formation of two possible variants of *S* phase in AA 2024 (0.49 wt.% Si) and AA 2324 (0.08 wt.% Si) Al-Cu-Mg alloys using transmission electron microscopy (TEM) and differential scanning calorimetry (DSC). They established that two distinct *S* phase precipitates (Type I and Type II) are present in these alloys as presented in Eq. 2.5. While increase in silicon content enhanced the evolution of Type I *S* phase, the formation of Type II *S* phase is supressed. Type II *S* phase is said to be a non-coherent precipitate and the more stable of the two.

$$SSS \rightarrow Clusters \rightarrow S''/GPB2 \rightarrow S(Type\ I) \rightarrow S\ (Type\ II) \quad \ldots 2.5$$

In another study on the precipitation sequence of AA 2024 during aging at 170^{o}C, Sha *et al.* [7] observed that solute clustering remained throughout the aging process and it could coexist with GPB zones and *S* phase particles. Therefore, they revised the existing precipitation sequence to:

$$SSS \rightarrow Solute\ clusters \rightarrow Solute\ clusters + GPB\ zone \rightarrow Solute\ clusters + GPB\ zone + S \rightarrow S \quad \ldots 2.6$$

The possible coexistence of phases at different precipitation stages was further established in the work of Charai et. al. [37] on the precipitation phenomena in Al-0.9% Cu-1.4% Mg alloy. At aging temperature around 200 ^{o}C, high resolution electron microscope (HREM) observation coupled to localized Fourier analysis revealed the simultaneous evolution of small pre-precipitates ($clusters\ and\ GPB\ zones$) and larger phases ($S'', S'\ and\ S$).

2.2 Deformation behaviour of metallic materials under mechanical loading

The response of metallic materials to mechanical loading, be it tensile or compressive is microstructure-dependent. On the application of load, metallic material could undergo elastic (brittle material) or elastic and plastic (ductile material) deformation before fracture. Elastic deformation is a non-permanent deformation that results in the stretching of inter-atomic bonds (straining) that tends to hold the atoms that make up the material in position on the account of applied load. The stretched inter-atomic bonds returns to its initial position (deformation recovered) once load is removed. On the other hand, plastic deformation is a permanent deformation that occurs when the elastic limit is exceeded such that existing inter-atomic bonds break, leading to the building of new ones. When the load is removed, deformation is not recoverable. Mechanical properties of deformed metallic specimen are obtained from the stress-strain curves obtained during mechanical loading. The shape and the magnitude of the stress-strain curve depends on several factors which includes the composition of the metallic materials, heat treatment condition, testing temperature and loading conditions (e.g. strain rates, state of stress) [46]. The typical strain rates for a quasi-static loading conditions whose plastic deformation mechanisms are by slip and/or twinning ranged between 10^{-5} and 10^{-1} s^{-1} [47]. Features of plastic

flow during quasi-static loading are necking in tensile loading or buckling in compressive loading [48].

Dynamic shock loading (also called dynamic impact loading) condition involves loading at strain rates usually in excess of 10^3 s^{-1}. Plastic deformation in metallic materials under dynamic impact loading is a complex phenomenon that is characterised by competing strain hardening effect of dislocation multiplication and thermal softening effect resulting from the conversion of impact energy to thermal energy that leads to temperature rise in the impacted samples [49]. It was suggested that 90 % of the kinetic energy of the striking projectile is converted to thermal energy [50]. The description of deformation behavior in metallic materials under different loading condition is illustrated in Fig. 2.4 [51]. The figure shows that a metal under quasi-static loading conditions (where heating is negligible) exhibits continuous hardening to large strain in the stress-strain curve until the material fractures. In the event that plastic working heats up the deformed material as in the case of dynamic impact loading conditions, the material softens resulting in the flow stress reaching a peak value at $\gamma_{max\ stress}$ that is followed by strain softening (the adiabatic curve on Fig. 2.4). A localized thermal softening may become excessive giving rise to a stress collapse that leads to strain localization.

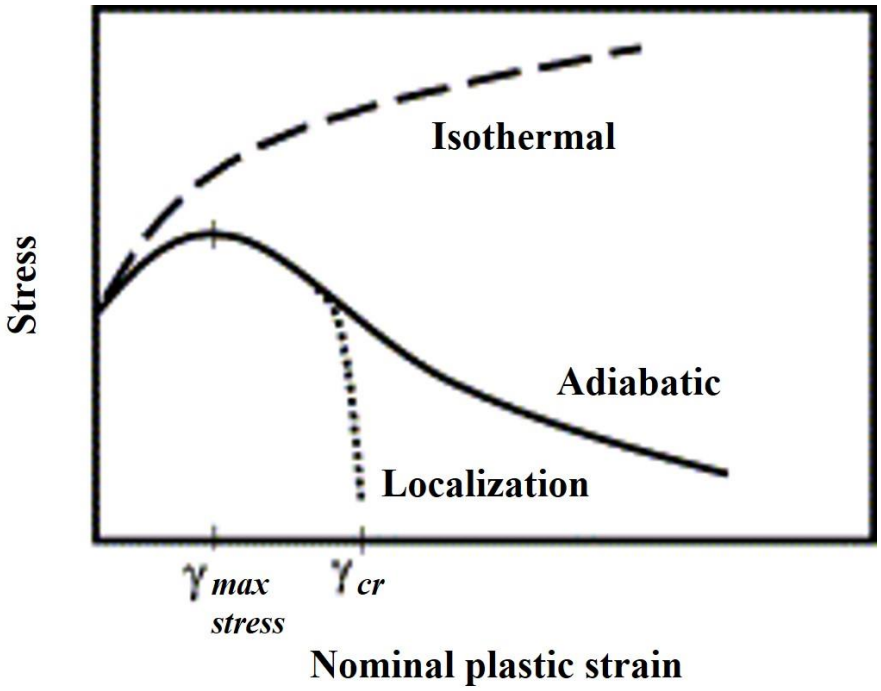

Fig. 2.4. Shear stress versus nominal shear strain for a typical work-hardening material [51].

The reason for thermal softening is not always clear and not necessarily the same for all alloys, yet in agreement with another research work [52], Verlinden *et. al*. [53] gave possible reasons which includes temperature rise of specimen during deformation, coarsening of dynamic precipitates that evolved during the first stage of straining, dynamic recrystallization, subgrain coarsening during straining and texture softening. Verlinden *et. al*. [53] proposed a relative softening equation for the quantitative analysis of thermal or flow softening in deformed metals as follows:

$$\text{Relative Softening, } S_r(\%) = \left(\frac{\sigma_p - \sigma}{\sigma_p} \right) * 100 \qquad \ldots 2.7$$

where σ_p is the peak stress and σ is the stress (MPa) at various strain level beyond the peak stress on the true stress-true strain curves. Other researchers [52,54,55] successfully applied this equation to quantify the amount of relative softening in deformed metals.

Intense thermal softening brought about by adiabatic heating along certain narrow paths during dynamic shock loading of metallic materials is generally believed to cause the generation of adiabatic shear band (ASB) [56]. ASBs are therefore paths of intense shear strain localization due to loss of load carrying capacity from excessive thermal softening in the region of intense adiabatic heating. Generally, shear bands are known to be generated within a short time frame such that they undergo localized instantaneous heating and rapid cooling by the relatively cool matrix around them [57]. Adiabatic shear bands (ASBs) or adiabatic shear localization frequently evolve in metallic materials subjected to various dynamic loading conditions, ballistic or hypervelocity impact, friction stir welding, forging [56], high speed machining/cutting [58], dynamic punch test, explosive loading, shaped charge jet, torsion rolling, explosive welding, etc. [59-61]. Though investigation of shear band evolution was first observed and correctly interpreted by Tresca in the 19th century [62], its mechanistic model was first proposed by Zener and Hollomon who attributed the occurrence of ASB to a competition between strain-rate hardening and thermal softening whereby localized deformation occur when thermal softening dominates strain-hardening [60].

ASBs, which are characteristics of high strain rates deformation, are of two types; deformed band (DB) and transformed band (TB) [57-59][63]. While the deformed band has been reported to contain elongated and distorted grains, the transformed bands are formed from the deformed bands

in many materials as the intensity of strain localization reaches a critical value [57,63]. Transformed bands which mostly exhibit microstructures that are distinctively different from the bulk materials have been reported in most metallic materials to consist of ultra-fine equiaxed grains formed as result of dynamic recovery or dynamic recrystallization [57,61,63]. Transformed bands, also known as white-etching bands present white-etching characteristics under the optical microscope in some alloys such as steels. As a result, some researchers have attributed the etching characteristics of TB to phase transformation [63,64]. Hardness profile across transformed band has shown higher microhardness measurement in the TB (attributed to grain refining) than the matrix/bulk material [64-69]. Formation of ASBs in a shock loaded specimens are often precursors to ductile fracture and they serves as potential sites for crack initiation and propagation [56,70,71]. Though shear band formation is generally accepted to be a deformation mode during high strain rate deformation, it can also occur in specimen under quasi-static loading condition [72-75].

2.3 Hardening curve in metallic materials under dynamic shock loading

Slip and twinning are the two deformation mechanisms that accounts for the plasticity of deformed alloys at room temperature [76]. Therefore, the strain hardening behaviour of these alloys can be influenced by any or both of these mechanisms, depending on which controls the deformation process [77-79]. In the deformation twin-controlled alloy such as Mg alloys, typical strain hardening rate-strain curve is observed with four distinctive stages as shown in Fig. 2.5a [78]. Stage I is the elasto-plastic regime that coincide with the onset of primary extension twinning $\{10\bar{1}2\}$ while stage II is where the formation of primary twin spread and are characterised by increased flow stress but low work hardening rate. In stage III, dense secondary $\{10\bar{1}2\}$ extension twins are formed; they act as barriers to dislocation motions thereby resulting to an increase in strain hardening rate. Stage IV shows a decrease in strain hardening rate up to negative values which are brought about by the saturation of $\{10\bar{1}2\}$ extension twins. Therefore, the transition between stage III and IV results in a hump in the hardening curve. Twinning in other hexagonal closed-packed (HCP) low SFE alloys such as titanium [80] has also been reported to enhance strain hardening rate, thereby exhibiting similar strain hardening rate-strain curve such as Fig. 2.5a.

For alloys such as FCC aluminium alloys, whose plastic deformation occurs mainly by slip mechanism, typical strain hardening rate-strain curve is hump-free as shown in Fig. 2.5b. The

hump-free curve indicates the absence of twinning activity in the deformed alloy i.e. twinning is not the dominant deformation mechanism [81]. This implies that the stage III in deformation slip-controlled alloy (Fig. 2.5b) are void of dense secondary $\{10\bar{1}2\}$ extension twins formation. Stage I is the elasto-plastic regime reported to be region of dynamic recovery in high SFE metals where deformation is substantially accommodated by slip [77]. Stage IV corresponds to the region where strain hardening loss its dominance to flow/thermal softening. In this region, hardening curve could drop below zero. Hump-free hardening curves are therefore the conventional hardening curves in polycrystalline face centered cubic (FCC) materials [82] where slip dominates the deformation process.

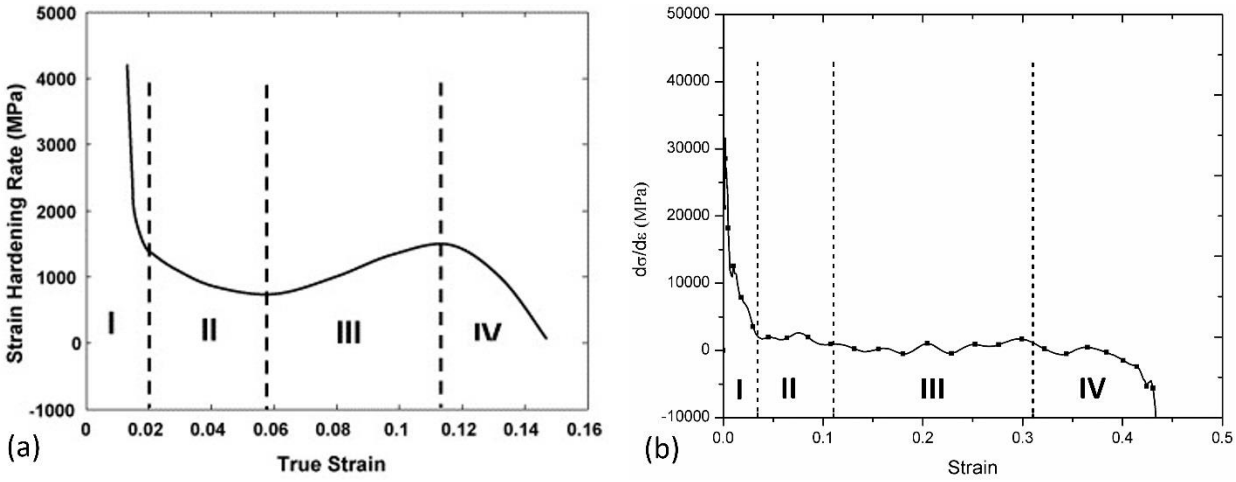

Fig. 2.5. Typical strain hardening rate-strain curve for (a) twinning-controlled deformation [78] and (b) slip-controlled deformation.

2.4 Occurrence of adiabatic Shear bands in metallic materials under dynamic impact loading

The formation of adiabatic shear bands has been reported in most metallic materials. However, the critical condition(s) at which they evolve vary from one alloy to another. This section highlights reports on shear band initiation, propagation and microstructure in major commercial alloys under various kind of high-strain rate loading conditions.

2.4.1 Aluminum alloys

Occurrence of both deformed and transformed bands have been reported in aluminium alloys subjected to dynamic shock loading. For example, Li et al. [57] observed dozens of shear bands in AA 7075 aluminum alloy after explosive loading and attributed the formation of ultrafine equiaxed grains in the transformed bands to dynamic recrystallization. Yang et al. [83] investigated the spatial distribution of shear bands in thick wall cylinders (TWC) of rolled AA 7075 aluminum alloy after explosive loading. The cylinders were machined such that their axis were directed at angles are 0^o, 90^o or 45^o to the rolling direction. Using the Schmid factor theories, they observed self-organization of multiple adiabatic shear band in the specimens machined in different orientation. While the 90^o specimens exhibited the least average nucleation rate of shear band with obvious shielding effect and largest spacing, the 45^o specimen possess the maximum average nucleation rate with spacing larger than the 0^o specimen. Shielding effect occur when grown bands are fraction of total possible initiation sites which are brought about by the restriction of the growth of other smaller bands by the longer ones [83,84].

In another research finding, Yang et al. [85] reported that shear bands initiate at the inner boundary of AA 7075-T651 aluminum alloy tube and their tips propagate along the maximum shear stress at 45^o or 135^o with the tube radius. Their work highlights the importance of stress state for the development of ASBs. This stress states were suggested to make shear bands bifurcates and annihilate. A comparative study on the dynamic behaviour of AA 7075 alloy in T73 and annealed temper conditions using the TWC technique was also conducted [86]. This work revealed that due to the difference in the mechanical and physical properties of the alloy in the two temper conditions, the adiabatic shearing energy barrier for the annealed specimen was nearly 2.5 times higher than that of the T73 specimen; a result that brought about the absence of adiabatic shear bands in annealed sample under same loading condition with the T73 temper that generated multiple ASBs.

Owolabi *et al.* [47] studied the dynamic deformation behaviour of AA 6061-T6 aluminum alloy in compression and torsion using a digital image correlation (DIC) system and the elastic wave technique. Apart from the observation of intense shear localization under both dynamic loading conditions, their results also showed that the strain values obtained in DIC technique were in

agreement with those obtained using the elastic wave method. A comparative study on strain localization and adiabatic shear failure in AA 6061 and AA 2099 aluminum by Odeshi *et al.* [87] indicated that the AA 2099 alloy has higher deformation resistance than AA 6061 alloy under quasi-static loading condition while the reverse holds when both alloys were subjected to dynamic impact loading. Higher crack susceptibility was reported for AA 2099 than AA 6061 during impact loading on the account of the high susceptibility of AA 2099 specimen to occurrence of adiabatic shear bands, especially transformed bands. In another study, Adesola *et al.* [88] observed the influence of aging condition on the damage evolution in AA 6061 alloy under quasi-static and dynamic loading conditions. This alloy in T4 temper condition shows the highest strain hardening capability than in T7 and T8 temper under quasi-static loading, and shows higher susceptibility to shear strain localization and adiabatic shear failure under impact loading. Using the SHPB technique to generate strain rate of approximately 10^3 s^{-1} in AA 8090 Al-Li alloy at ambient temperature and 77 K, Xu et al. [48] observed that specimens impacted at the ambient temperature were less susceptible to cracking along localized shear than specimen impacted at much lower temperatures. They also established that unless a critical value of strain for the occurrence of deformed and transformed is reached, no shear band will form.

Particle reinforcement of an aluminium alloy to increase strength can also affect susceptibility to occurrence of ASBs and failure under dynamic impact loading. For example, Owolabi et al. [89] observed that though the reinforcement of AA 6061-T6 alloy with alumina particles improves its strength and stiffness, susceptibility to strain localization and adiabatic shear failure increases with particulate reinforcement. Microstructural evaluation after impact revealed that particles in the shear band formed in aluminum matrix composite were more closely packed than in the bulk material while shear bands in the unreinforced AA 6061-T6 contain ultrafine grains..

2.4.2 Steels

Ferrous alloys which are commonly used in armor tanks and other applications are exposed to different type of explosives or ballistic impacts leading to failures initiated by occurrence of adiabatic shear bands. Previous research studies on the dynamic impact response of ferrous alloys such as steels have shown that occurrence of transformed adiabatic shear bands triggers fragmentation mode at high strain rates.

Characterization of AISI 304L stainless steel after exposure to dynamic shock loading conditions by Meyers et al. [90] using transmission electron microscope (TEM) revealed two distinct regions within the shear band; the first consist of grains having sizes ranging between 0.1 and 0.2 μm with well-defined grain boundaries while the second showed amorphization (glassy structure) within the shear band. This work also reported that the AISI 304L stainless steel deforms by martensitic transformation, stacking faults and twinning outside the shear band region. Lins et al. [91] investigated the occurrence of ASBs in a hot-rolled interstitial free (IF) steel under high strain rate loading conditions and observed equiaxed grain structure within the shear band irrespective of the test temperature. In a study on the formation of ASBs during high strain-rate deformation of AISI 4340 steel using a torsional split Hopkinson bar system, Bassim [92] reported that ASB tends to initiate at local defects and inhomogenities in the alloy while specimen geometry and dimensions also influence the tendency of the alloy to develop adiabatic shear band. A fractographic examination of quench-hardened and tempered AISI 4340 steel that fragmented under dynamic impact loading indicates knobby fracture modes along the adiabatic shear band region suggesting melting inside the shear bands the impact loading [93]. Tempering martensitic AISI 4340 steel at 620^{o}C for 2 h prior to shock loading resulted in the formation of deformed bands that are less susceptible to cracking [71]. Annealing the impacted AISI 4340 steel specimens containing transformed shear band at 650^{o}C for 20 min eliminated the transformed bands and reduced the cracking tendency if subsequently subjected to mechanical load. During dynamic shear loading of an ultra-fine-grained (UFG) iron with grain size of approximately 500 nm, adiabatic shear bands (ASBs) formed while cracks nucleated and propagated along the shear bands [67]. A two-stage process was reported for the development of ASB in the iron; the nucleation and thickening stages. The thickening stage is a stage where the evolution of ASB is accompanied by increase in both thickness and micro-hardness of the ASB. TEM observations indicated that grains in the shear bands were further refined compared to the grains in the UFG iron.

2.4.3 Magnesium alloys

The hcp crystal structure of Mg alloys with only a few active slip systems makes them to generally exhibit limited ductility at low temperatures. Although they have many potential applications in automotive and aerospace industries due to their low density, the challenges in mechanical forming of Mg alloys to produce them in wrought form hinders their widespread application [94]. The poor

formability of Mg alloys at room temperature is due to limitation of plastic deformation mode to slip on basal planes and twinning [77].

The study of ASB formation in AM60B Mg alloy during ballistic impact at 0.5 kms^{-1} indicated the evolution of the deformation twins, deformed and transformed bands [63,64]. Deformed bands were characterized by severely deformed grains with high density dislocation while transformed bands were composed of the ultrafine and equiaxed grains attributed to the twinning-induced rotational dynamic recrystallization mechanism. Microhardness was observed to be higher in the shear band region than the bulk material, which was attributed to strain hardening, grain refining and elemental composition of the parent metal. In another study, three deformed zones were observed in the microstructure of AM60B Mg alloy subjected to ballistic impact at 4 kms^{-1}; dynamic recrystallization (DRX) zones, high and low densities deformation twin zones [95]. At a ballistic impact velocity of 5 kms^{-1} [96], four deformed zones namely DRX zones, DRX and deformation twin zone, high and low densities deformation twin zones were observed.

Generally, it is important to mention that Mg alloys can easily recrystallize under dynamic shock loading due to three reasons [65]. First, the slip systems of Mg alloys are few and dislocations pile up easily so that dislocation density can meet the requirement for DRX. Secondly, Mg and its alloys are of lower stacking fault energy (SFE) and extended dislocation (combined partial dislocations) is hard to feature so that slip and climb becomes difficult; therefore, dynamic recovery become slow thereby promoting recrystallization. Thirdly, grain boundary diffusion occurs more readily in Mg alloys and the dislocation energy that pile up on the subgrain boundaries can be absorbed by the boundaries which speeds up the rate of DRX. Other Mg alloys in which ASBs were observed after high strain-rate include AM50 [97] and Mg-Gd-Y alloy [65] among others.

2.4.4 Other metals/alloys

Occurrence of ASBs is not peculiar only to aluminum and ferrous alloys, it has been reported in most of other engineering metals and alloys. The adiabatic shear bands has been reported in Ti6441 titanium alloys with equiaxed grains and lamella microstructures [98]. The titanium alloy with lamella microstructure was observed to be less susceptible to formation of ASBs than the equiaxed ones. ASB branching was observed in the alloy with lamella structure hence, requiring additional

energy for further propagation of ASB by consuming plastic deformation work. Shear band initiation and pattern development in commercially pure titanium was observed and investigated by Nesterenko et al. [62] using a TWC technique. Initiated bands were observed to form spiral trajectories with periodic spacing that decreases with the progression of collapse. Yang et al. [61] studied the microstructural evolution in a near beta-Ti alloy under dynamic shock loading. Although TEM observations indicated the microstructure inside ASB to consist of fine equiaxed subgrains, the β to $\omega_{(althermal)}$ phase transformation was also observed inside the ASB. Further analysis suggests that high alloying element content of this alloy and formation of shear band offers thermodynamic and kinetic conditions for the $\omega_{(althermal)}$ phase transformation. In a study on the formation mechanism of shear bands in ultrafine lamella Ti-Fe eutectics under static compression at room temperature, Zhu et al. [99] reported alternating lamella and serrated structures inside the ASBs. They proposed that shear bands in this alloy are due to the geometric evolution and could therefore not be referred to as adiabatic shear band since equiaxed grains which are signature of ASBs were not found. Other titanium alloy such as Ti-1300 [100] and Ti-6Al-4V [101] have also been studied in relation to ASB evolution. Evolution of ultrafine and equiaxed grains by rotational dynamic recrystallization mechanism was observed in transformed bands that develop in shock loaded zirconium alloy [59]. Other alloy where ASB was observed is the tungsten heavy alloy (WHA) [102]. This study confirmed that the geometry of specimen and surface friction have considerable effect on the tendency for ASB formation.

2.5 Shear band in other mechanical processes

Shear band formation which are thought to be predominantly signature of metals subjected to dynamic shock loading has been observed to occur in other mechanical processes such as rolling. Rostova and Zakharov [103] reported the formation of shear bands in cold rolled Al-Li alloy, which they attributed to be a result of concentrated plastic strain. Inagaki and Kohara [104] studied shear band evolution in Al-Mg alloy polycrystals containing between 0.5 and 5 % Mg subjected to cold rolling up to about 95 % reduction. They reported that the tendency for shear banding is strongly influenced by the concentration of Mg. When Mg content was less than 2.5 %, shear bands were formed at rolling reduction of 95 % while lower percentage reduction (50 %) was required for shear band formation in the aluminum alloy containing more than 2.5 % Mg. Lee and Chan [105] analysed the micro plasticity of shear band cracks in rolled AA 2024 aluminum alloy

in annealed and age-hardened temper conditions. No shear band was observed in rolled annealed specimen. On the other hand, shear bands confined within an individual grain (grain-scale shear bands)) at low rolling reductions while shear bands traversing more than one grain (sample-scale SB) at higher rolling strains were observed in rolled age-hardened specimen. Other alloys where shear bands evolve in cold rolling operation are AA 7075 aluminum alloy [106] and commercial titanium [60]. Complex macroscopic shear bands have been reported in ultrafine-grained (UFG) materials processed by severe plastic deformation methods such as the equal-channel angular pressing (ECAP) [107].

2.6 Initiation and propagation mechanisms of adiabatic shear band

Shear bands are initiated as a result of steady exhaustion of crystallographic slip [105] and/or local fluctuations in strain and temperature [62]. Their initiation occurs with a crystallographic slip in a favoured individual grain which tends to propagate into adjacent grains by cooperative slip or cross-slip. This leads to the spread of shear localization over the total cross-section of the deformed specimen which eventually propagate to macroscopic shear band [72]. Figure 2.6 highlights possible grain-scale microstructural initiation mechanisms for shear bands in single-phase homogeneous materials [62]. The first possibility (Fig. 2.6a) suggests that since the distribution of grains in metals are of varying sizes such that larger grain exhibits a lower yield stress (σ_1) and smaller grain possesses higher yield stress (σ_2) in agreement with Hall-Petch equation. In this case, larger grains will deform at the expense of the smaller grains, hence, becoming an initiation site for shear band. The second possibility (Fig. 2.6b) is the tendency for the occurrence of localized softening caused by grain rotation. The increase in Schmid factor of a plastically deformed grain leads to localized softening that can initiate shear band. Pierce et al. [108] and Anand and Kalidindi [109] modelled the mechanism of localization through the cooperative plastic deformation. This mechanism, which is the third possibility states that the localized deformation of one grain can propagate along a band as depicted in Fig. 2.6c. The fourth mechanism (Fig. 2.6d) was proposed by Armstrong and Zerilli [110] and it shows that dislocation pile-up can burst through a grain boundary to generate local temperature rise and plastic deformation that has the capacity to initiate shear band. In all, it is evident that crystallographic peculiarities play a major role in the initiation of shear band. The ductile failure of materials subjected to ballistics impact, armor penetration and explosive loading is initiated mainly by formation of ASBs, yet they are not well understood

owing to its complexities as a physical phenomenon than most other failure mode in engineering materials. Due to these complexities, numerical simulations have therefore been stated to be the most efficient way to study shear band propagation [111]. However, most of the research study on the phenomenon of adiabatic shear banding in metallic alloys has focussed on experimental investigation of the microstructure evolution leading to ASBs formation.

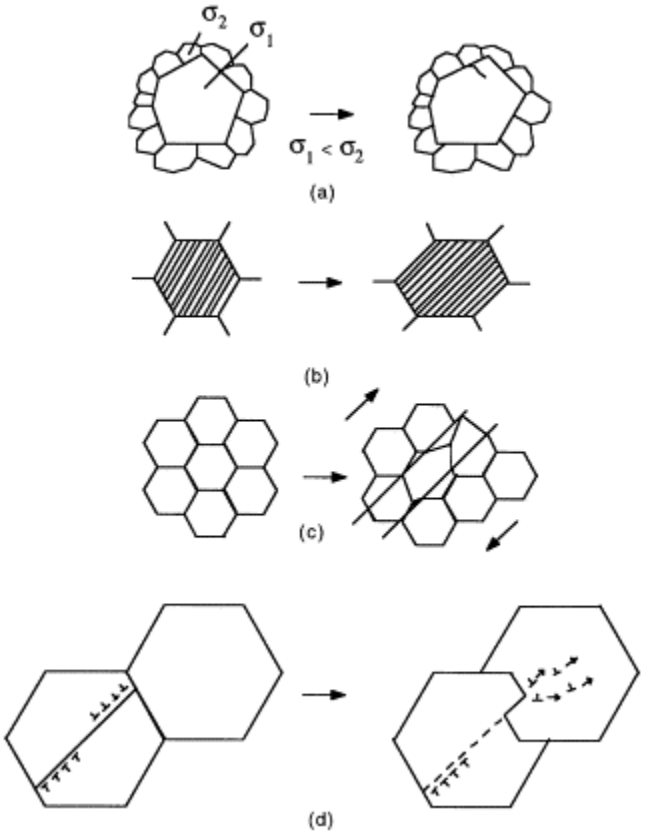

Fig. 2.6. Possible shear-band initiation mechanisms in single-phase homogeneous materials. (a) grain-size inhomogeneity, (b) geometrical softening, (c) Peirce–Asaro–Needleman textural localization and (d) dislocation pile-up release [62].

2.7 Microstructural evolution in ASB

It is generally believed that microstructural changes in metallic materials subjected to thermo-mechanical processes (TMP) including high strain rate loading can be attributed to a combined effect of strain hardening and thermal softening caused by temperature rise in the deformed specimen. This often leads to strain localisation and formation of shear bands. The softening mechanisms are suggested to be dynamic recovery, dynamic recrystallization or phase transformation [57,66,90,99][112-114]. The dominating mechanism in plastically deformed

material is dependent on the amount of temperature rise within the specimen. Recovery, which in most cases, leads to a slow and logarithmic decrease of hardness tends to dominate deformation process at low temperature, typically between 0.4-0.5 T_m, where T_m is the melting temperature. At higher temperatures (above $0.7T_m$), recrystallization occur more rapidly without much prior recovery. Intermediate temperatures suggests that both mechanisms contribute significantly to softening as schematically shown in Fig. 2.7 [114].

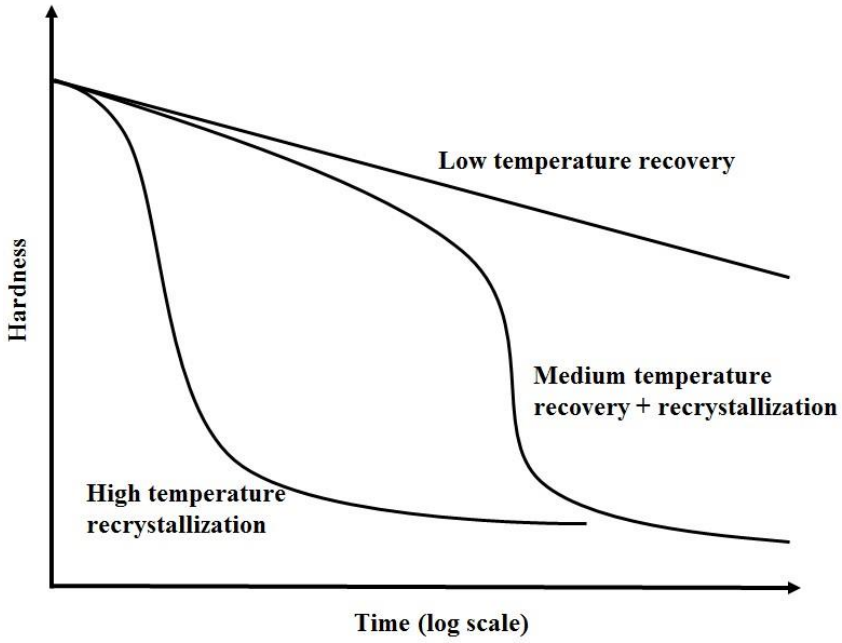

Fig. 2.7. Schematic softening kinetics at three temperature range. (Adapted from Ref. [114]).

2.7.1 Dynamic Recovery (DRV)

This is a process in which dislocations are rearranged into a more energetically favorable configuration. These configuration are usually referred to as subgrain or cell structure which is characterized by heavily dislocated boundaries that tends to have similar orientation as the parent grains. As strain rate increases, cell size in plastically deformed material decreases while the subgrain misorientation increases [115]. Recovery, which occurs during deformation is called dynamic recovery (DRV), while that occurring when a previously deformed alloy is exposed to elevated temperature is called static recovery (SRV). The mechanism of recovery includes; point defects such as vacancies and interstitials annihilate by diffusion to sinks (dislocations). This is then followed by mutual dislocation annihilation by attraction of mobile dislocations of opposite sign lying on the same slip planes. Dislocation climb and cross is promoted by the increase in

temperature during deformation, thereby increasing dislocation mobility. The third stage of the recovery mechanism is polygonization which involves the organization of free, random dislocations into dislocation walls or sub-boundaries. Finally, sub-boundary walls coalesce as subgrain grows. A schematic representation of this recovery mechanism called successive dislocation annihilation mechanism is shown in Fig. 2.8. It is expedient to state that recovery only affects properties such as hardness and microstructural features like, dislocation density, subgrain size and misorientation but the original shape of grains usually remain unchanged [115].

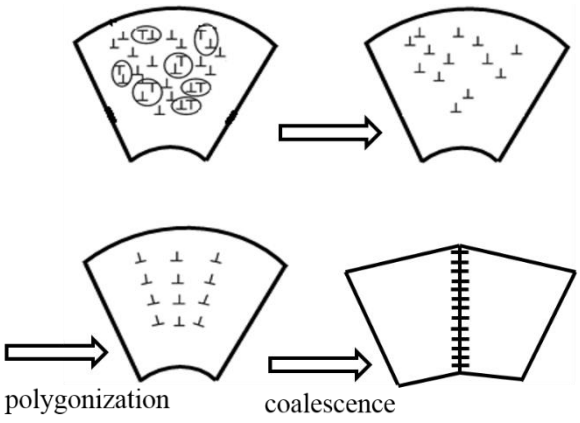

Fig. 2.8. Schematic of successive dislocation annihilation mechanisms. (Adapted from Ref. [114]).

2.7.2 Recrystallization

This is a phase-transformation process that takes place in most metallic materials especially when deformed at high temperatures, high strain rates or heated after cold working [111]. During the process of recrystallization, new grains are formed within the parent matrix. These grains, which usually have a different orientation from the original grains, contains sharp-faceted boundaries characterized by low dislocation density in its interior [112,115,116]. There has been some controversy over the effects of recovery on recrystallization, and it is generally believed that these two processes are competing [115]. Recrystallization can occur during deformation [dynamic recrystallization (DRX)] or during exposure to elevated temperature after cold work [static recrystallization (SRX)] deformation. The SRX occur by a grain migration mechanism while DRX is the result of the gradual rotation of subgrains coupled with dislocation annihilation [117]. The work of McQueen and Bergerson [118] on the hot deformation of tubular specimen suggests that two ways to distinguish DRX from SRX are in their respective grain size and number of annealing twins in the grains. Their observation suggests that recrystallized grains are smaller in DRX than

in SRX while fewer number of annealing twins was found in the grains of the former than the later. It was reported that dynamic recrystallization (DRX) leading to the formation of fine grains in ASBs occurs during high strain-rate deformation of metallic alloys [111]. Both rotational dynamic recrystallization (RDRX) and progressive subgrain misorientation (PriSM) recrystallization have been reported to occur in transformed adiabatic shear bands as they form during high strain-rate deformation of metals and alloys.

2.7.2.1 Rotational Dynamic Recrystallization (RDRX)

Derby [119] classified dynamic recrystallization mechanisms into migrational and rotational. While the former (common in metals) is governed by diffusion and develops by the way of nucleation and growth of recrystallized grains, the latter (common in quartz, marble, salt and other geological materials) is completed through self-rotation of subgrains [58]. Migrational dynamic recrystallization mechanism is ruled out in explaining the fine grain structure observed in ASB because the formation time of ASB is extremely short. The RDRX mechanism (Fig. 2.9) which involves concurrent plastic deformation was suggested by Nesterenko *et al.* [117] and the model became one of the most accepted mechanisms to explain ultrafine grain structure inside transformed ASBs. The first stage of this mechanism (Fig. 2.9a) is the accumulation of random, but yet homogenously distributed dislocations which eventually re-arranges to elongated dislocation cells in the second stage (Fig. 2.9b). The elongated dislocation cells become elongated subgrains in the third stage (Fig. 2.9c) as deformation continues. With further increase in deformation, subgrains break up into equiaxed subgrains due to interfacial energy minimization in the fourth stage (Fig. 2.9d). The fifth and final stage involves rotation of the subgrains resulting in the evolution of dynamically recrystallized grains (Fig. 2.9e). The results of a study on the microstructural evolution in copper during high strain rate deformation by Tang *et al.* [120] indicated elongated ultrafine grains rather than equiaxed ultrafine grains in the ASBs (Fig. 2.10). The mechanism of formation of the elongated ultrafine grains were reported to be similar to the rotational dynamic recystallization mechanism proposed by Nesterenko *et al.* [117]. Tang et al. [120] suggested that in addition to the RDRX mechanism presented in Fig. 2.9, where the evolution of equiaxed micrograins is the final stage of the recrystalization process, equiaxed grains are re-elongated due to effective shear deformation as indicated in Fig. 2.10.

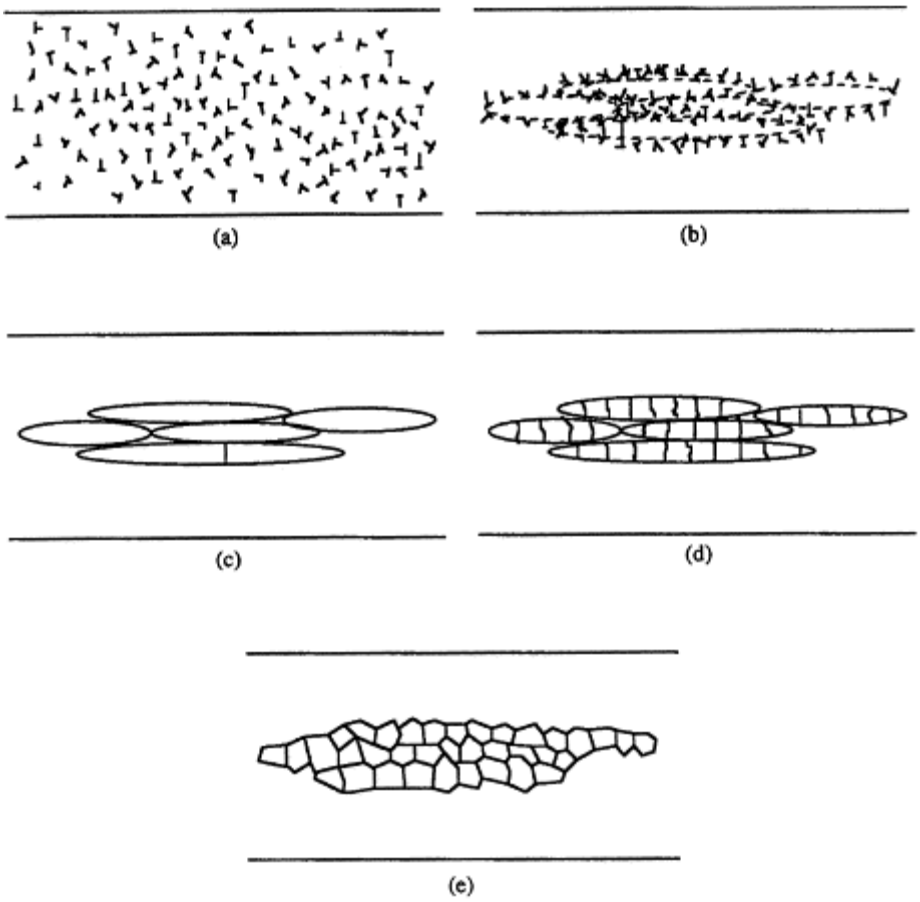

Fig. 2.9. Microstructural evolution in high-strain-rate deformation of tantalum: (a) uniform dislocation distribution; (b) elongated dislocation cells; (c) elongated subgrains; (d) subgrain break-up; (e) dynamically recrystallized grains [117].

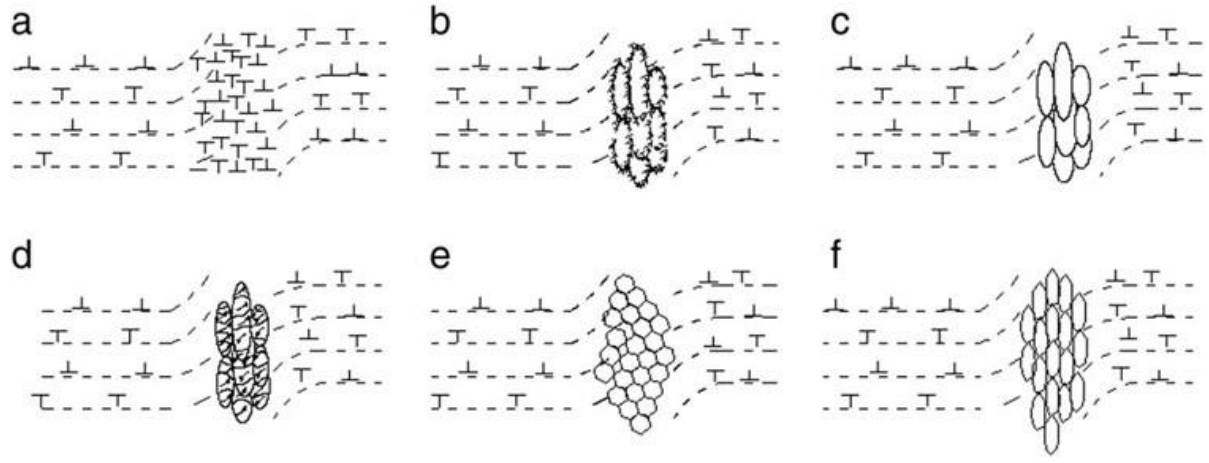

Fig. 2.10. DRX mechanism for development of ultrafine elongated grains inside ASB observed in copper [120].

Formation of ASBs with eutectic lamelar structure in Ti-Fe alloy under quasi-static compressive loading was reported by Zhu *et al.* [99]. The alternating lamellae were reported to be parallel to the shear band propagation path. The mechansm of formation the lamelar structure in the ASBs is called subgrain rotational (SR) mechanism. This is a revised form of the rotational mechanism and it is illustrated in Fig. 2.11. The eutectic colonies in the Ti-Fe ultrafine eutectic sample are depicted in Fig. 2.11a where the β-Ti (dark) and FeTi (white) phases are the solid solution and intermettallic compound respectively. The FeTi phases are taken to be the barriers that hinders the motion of dislocations in the β-Ti matrix. When plastic deformation occurs, adjacent subgrains rotate to make their orientations closer to each other or even identical (Fig. 2.11b). The lamellae between subgrains extend along the same direction as a result of the subgrain rotation such that barriers presented by the boundaries vanish in sequence. The process provides a larger path for motion of dislocation in the β-Ti phase (Fig. 2.11c) leading to formation of ASBs as a result of the localized dislocation motion [99].

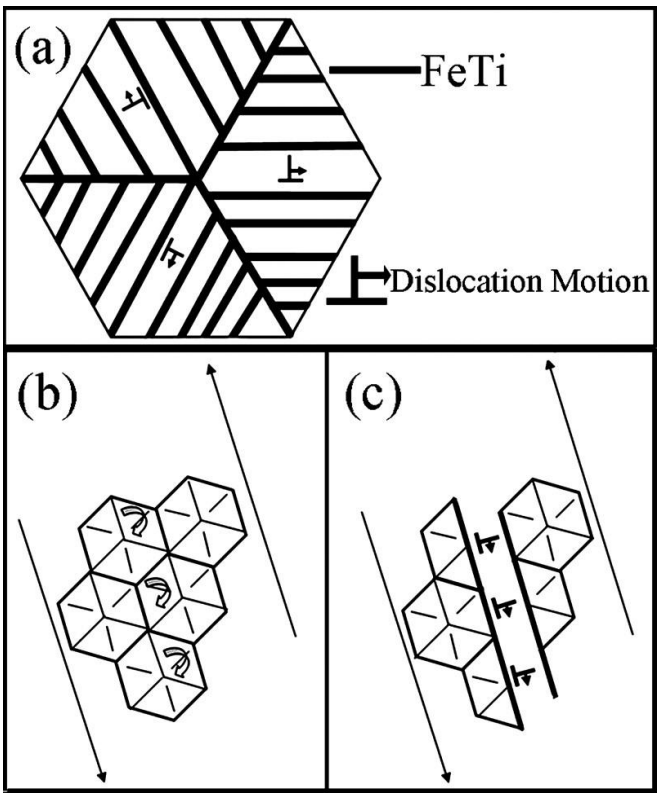

Fig. 2.11. SR mechanism in a Ti-Fe alloys (a) Illustration of the eutectic colony denoting the available dislocation motions. [(b) and (c)] Schematic evolution of shear bands: (b) rotation of neighboring subgrains leading orientations close to each other and (c) elimination of subgrain boundaries forming larger paths for dislocation motion [99].

2.7.2.2 Progressive Subgrain Misorientation (PriSM) Recrystallization

It has been reported that the existing kinetic models for recrystallization cannot account for the formation of recrystallized grains in the time scale and temperature history for ASB formation and subsequent cooling. For this reason, Hines et al. [115] using crystal plasticity theory, presented a feasible model (Fig. 2.12), called progressive subgrain misorientation (PriSM) Recrystallization. It has been reported by these researchers that the subgrain size in a recovered microstructure is inversely proportional to the applied stress. Therefore, further increase in strain rate or strain after the formation of subgrain tends to decrease its size. This subgrain size decrease does become discontinuous on the event that a critical subgrain diameter appears after a given amount of deformation. At this stage, the subgrain size is no longer inversely proportional to the strain. In the event that continued deformation no longer reduce the subgrain size, the subgrain microstructure begins to rotate as a means of accommodating further deformation, resulting in highly misoriented, equiaxed grains inside ASBs. On the completion of deformation where deformed specimen began to cool down, no additional dislocations are added to the boundaries. The boundaries begin to refine by reducing the excess dislocation dipoles through dislocation annihilation by dislocation climb. Once there is enough time during cooling for boundary refinement to occur, faceted, high-angle boundaries will be created, and recrystallized grains will form in the shear band. Hence, the mechanism suggests that the recrystallized grains formed in ASBs is the result of rotation of the recovered microstructure itself [115].

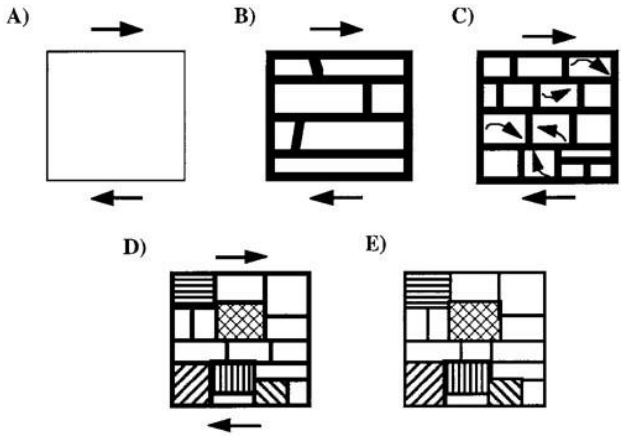

Fig. 2.12. Schematic diagram of PriSM recrystallization inside an ASB from the starting single crystal (*a*), to formation of elongated subgrains (*b*), to rotation of equiaxed subgrains (*c*), to high angle misorientations between some subgrains (*d*), The final stage is boundary refinement during cooling (*e*) [115].

2.8 Mechanism of Adiabatic Shear Fracture in Compressed Metallic Materials

Since the evolution of ASBs serves as a precursor to ductile fracture and catastrophic failure of metallic material under dynamic impact load [83,121], the degree of structural damage in the shear bands leading to eventual fracture along such bands can be assessed to decipher the mechanism of failure [72]. Fracture can be classified as ductile or brittle. While ductile fracture occur almost during adiabatic formation when the band is hot and weak, brittle fracture is common in transformed bands in steel which occur after the termination of deformation and the quenching of the hot band by the adiabatic matrix material to form the hard, brittle, transformed structure.

Shear bands which are reported to be favored initiation sites for failure, occur typically by nucleation, growth and the coalescence of voids inside the thermally softened region. In other words, void formation in ASBs in metallic materials are associated with thermal softening and preferential melting inside the shear band region [72,122]. Voids formation in the shear band as deformation proceeds under the impact loading could be due to the existence of the stress gradient between the lower yield strength in ASB region and the higher yield strength in the surrounding matrix [68,72]. Other suggested mechanisms for micro-voids nucleation in metals include, vacancy accumulation at a high stress region, grain boundary sliding, and void nucleation ahead of dislocation pile-ups [93,123,124]. Odeshi and Bassim [93] reported that the dynamic failure of AISI 4340 steel under impact loading proceeds in five sequential stages: First the formation of micro-voids inside the shear bands occur, followed by the coalescence of these micro-voids forming void-clusters. The third stage involves elongation of the microvoids in direction parallel to the shear bands followed by initiation of two very fine micro-cracks parallel to the shear bands at opposite ends of the void-clusters. The final stage involves lengthwise growth and interconnection of adjacent micro-cracks leading to crack growth and propagation along the shear bands. Timothy and Hutchings [122] illustrated the possible mechanism for the evolution of void and eventual fracture in ASBs as a function of void nucleation sites' density (Fig. 2.13). In a shear band region where nucleation sites are widely separated (Fig. 2.13a), voids will grow without coalescing even under the combined effect of tensile and shear stresses in the shear band. There exists a critical void separation (Fig. 2.13b) below which coalescence occurs with surface forces of the voids as the driving force. In the event that void nuclei are closely spaced (Fig. 2.13c), voids will coalesce almost immediately they form, leaving no trace of intermediate ligaments.

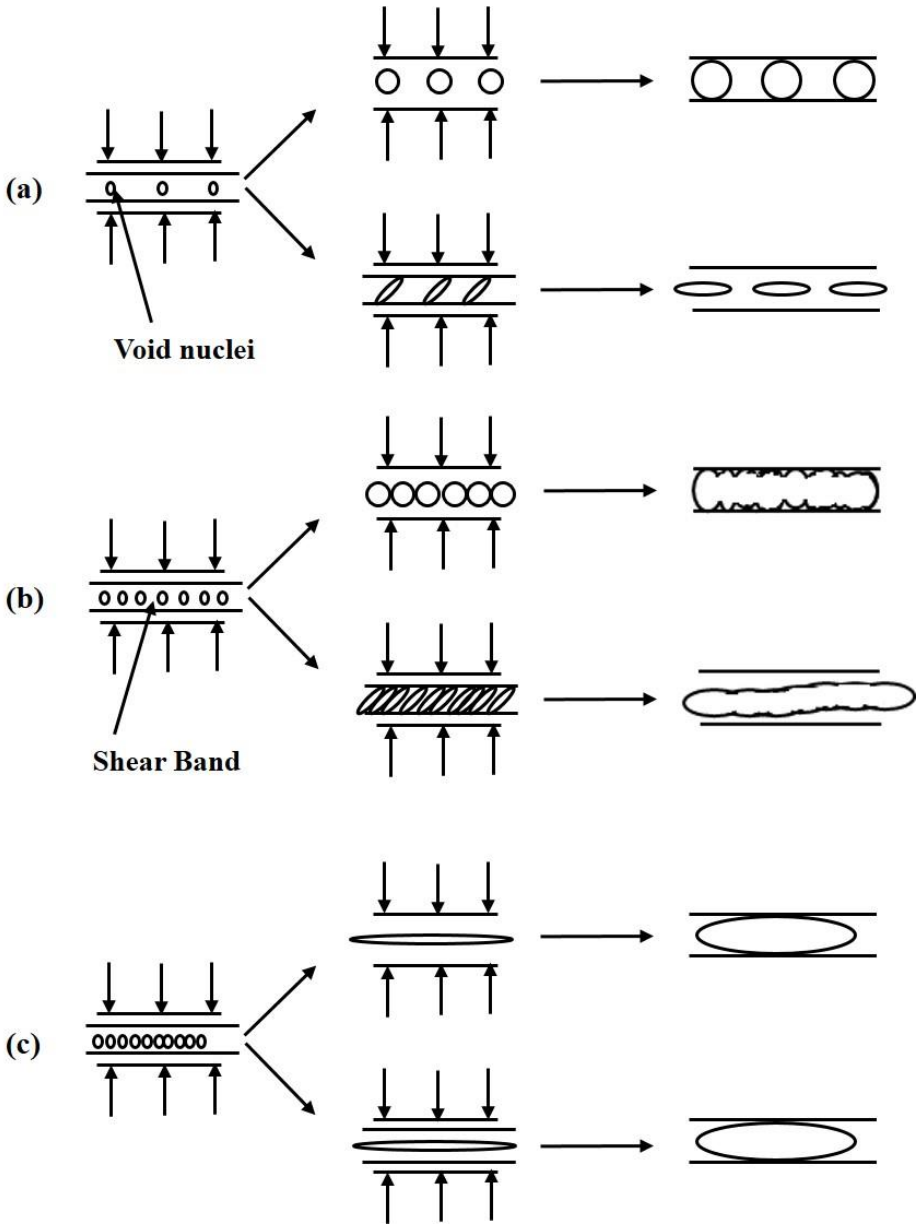

Fig. 2.13. Schematic illustration of evolution of void and cracking in ASBs, sequence a, b, c corresponds to increasing density of void nucleation sites. (Adapted from Ref. [122]).

2.9 Factors influencing adiabatic shear band formation

Owing to the fact that ASBs are potential crack initiation sites where eventual catastrophic failure will most likely occur in metals under dynamic shock loading, it is of outmost importance to study how various microstructural and loading variables affects the formation of adiabatic shear bands. These is being done from the perspective of both material science and solid mechanics [125].

Temperature of samples before impact and the amount of temperature rise within deformed specimen plays a major role in ASB formation. Wang [126] reported that a lower initial sample temperature leads to earlier occurrence of shear strain localization. However, the temperature rise in the shear band that evolve in a shock-loaded specimen can be estimated from the stress-strain data as presented in Eq. 2.8 [72].

$$T = T_o + \frac{0.9\, W_p}{\rho\, .C_v} \qquad \ldots 2.8$$

where T_o is the room temperature (or specimen initial temperature); C_v is the heat capacity, ρ is the density and W_p is the specific work of deformation which can be expressed as:

$$W_p = \int \sigma\, .\, d\varepsilon \qquad \ldots 2.9$$

where σ and ε are stress and strain respectively. Dynamic recovery or DRX will occur in shear band once the temperature inside the ASB rises to about 0.4 - 0.5 T_m, where T_m is the melting point of the metal [72].

It has been suggested that that there exist critical strains and strain rates above which shear strain localization leading to formation of adiabatic shear bands will occur [72]. The stacking fault energy (SFE) of a metallic material is a factor that can make shear band formation easy or difficult [127]. Metals having low SFEs show easy susceptibility to ASB formation while shear band formation in metals with increasing SFEs shows to be increasingly difficult. In a low SFE metals, shear bands in crystals are reported to be accompanied by mechanical twinning while high SFE metals are accompanied by slip [128]. Shear band preferentially nucleate and develop within the lamella of mechanical twins in the former or within the microstructure of layered dislocation wall that is parallel to one of the active slip planes in the latter during deformation. Morii and Nakayama [129], in a study on the effect of θ' precipitates on shear band formation in Al-2%Cu alloy, suggested that the presence of lamella structure composed of deformed θ' platelets and aluminum matrix is an important factor in shear band formation. In a another study, Yang et al. [100] investigated the effects of phase composition on ASB formation in Ti-1300 alloy specimens containing single β phase or different contents of α phase in specimens containing α + β phases. They reported that at earlier stage of deformation, specimen with less α phase is more susceptible to adiabatic shear localization and cracks. At a later deformation stage, shear bands in specimen containing single β

phase propagate faster than specimens consisting of α + β phases. Some other factors that can affect the formation of ASB includes, strain rate sensitivity, microstructure [68], specimen geometry and dimension, local defects [92,102], and notches [130,131] among others.

2.10 Texture evolution in metallic alloys under shock loading condition

Texture describes the crystal distribution and grain orientation in alloys [132]. Due to the strong influence of crystallographic texture on deformation behavior of metallic alloys, texture analysis of plastically deformed polycrystalline materials has continued to attract the attention of researchers [75]. It has been established that metallic materials subjected to high velocity or ballistic impacts exhibits microstructural features including ASBs that depend on the initial texture of the material before mechanical loading [133,134].

Using the electron back scattered diffraction (EBSD) and X-ray diffraction (XRD) technique, Gurao et al. [135] studied the evolution of crystallographic texture in polycrystalline copper and nickel under quasi-static and dynamic loading conditions. They observed an increase in LAGB (a characteristic of heavily deformed metal) and corresponding decrease in HAGB in Cu and Ni under quasi-static loading to a strain of 0.85. Reverse was observed to be the case in Cu and Ni samples under dynamic shock loading; an observation attributed to the formation of new grains by recrystallization. In general, transmission of LAGB formed at early stage of deformation to HAGB has been reported to be controlled by dynamic recovery rate (usually accelerated by higher temperatures). An increase in HAGB at the expense of LAGB is connected to subdivision of grain or development of new grains by recrystallization [135,136].

Although it was initially suggested that the strain rate effect on deformation texture is minimal as the choice of slip systems in FCC crystals is not sensitive to the strain rate [137], however, Bhattacharyya *et al.* [138] observed a strong dependence of strain rate on crystallographic texture of oxygen-free high conductivity (OFHC) copper under both quasi-static and dynamic loading conditions. They reported that increasing the strain rate results in an increase in strain hardening which in turn influences the crystallographic texture of the alloy. Gurao et al. [137] observed that the texture in Cu-10Zn alloy under dynamic impact loading condition become weaker in comparison with its specimens under quasi-static loading. The authors attributed the weak texture to activity of higher number of slip systems in the alloy under dynamic loading conditions. The

results of another study on strain-rate effect on deformation texture in α–Fe under both quasi-static and dynamic loading conditions shows no change in texture of specimen deformed below 1.0 strain at both loading conditions. On the other hand, texture becomes sharper at stain level above 1.0 [132].

Li *et al.* [139] reported on the role of second phase particles on deformation mechanisms and texture of selected Mg-Al-Zn alloys under plane-strain compression at strain rates of 10^{-2} and 10^{-4} s^{-1}. The authors found that high volume fraction of β phase ($Mg_{17}Al_{12}$) in AZ91 alloy reduced activities of twinning and promoted DRX resulting in weak deformation textures at high strain. In another study, Xue *et al.* [75] showed the evolution of misorientation gradients in grains near shear bands in both hot-rolled (as-received) and pre-shocked 304 steels. They concluded that the characteristics of localized deformation was dependent on the initial condition; the as-received (hot rolled) steel exhibits larger misorientation gradient than the pre-shocked steel near the shear band. Texture analysis on the 304 steel after dynamic shock loading conditions revealed that there was reorientation of grains with <110> in path towards the shear direction and {111} plane aligning with the shear plane near the shear band. The work of Paul *et al.* [140] suggested that crystal lattice rotates to the point where {111} slip planes becomes nearly parallel to the maximum shear direction in an FCC metal (Al-0.23%wt.Zr) under low rate of deformation. They observed that the continuity of slip direction is responsible for shear bands occurring across grain boundaries. Gurao *et al*. [141] identified the presence of fine micron-sized grains with <100> texture inside shear band that developed in impacted AA 2099-T8 aluminum alloy.

CHAPTER THREE

MATERIALS AND METHODOLOGY

3.1 Materials

The investigated 2000 series aluminum alloys were rolled AA 2017, 2024 and 2624 alloys. They were received in the naturally-aged condition; AA 2017-T451, AA 2024-T351 and AA 2624-T351. Table 3.1 provides the elemental composition range for the AA 2017 and AA 2024 alloys as obtained from ASM material data book [143] and the composition of AA 2624 as supplied by the manufacturer, Alcoa Canada. Inductively coupled plasma-mass spectrometry (ICP-MS) analysis was conducted to ascertain the chemical composition of the investigated alloys (Table 3.2). As at the time of this analysis which was conducted in room 211, Department of Geological Sciences Building, University of Saskatchewan, there was no standard reference for quantifying Si. The result of ICP-MS in Table 3.2 shows to be in agreement with the published and supplied data for the investigated alloys (Table 3.1). The heat treatment procedure commonly used in generating the as-received T351 and T451 temper conditions in the aluminum alloys are summarized in Table 3.3 [142].

Table 3.1. Chemical composition of the investigated AA 2000 aluminum alloys (wt. %).

	Al	**Cu**	**Mg**	**Mn**	**Fe**	**Si**	**Zn**	**Ti**	**Cr**	**Others**
AA 2017 [143]	Bal	3.5-4.5	0.4-0.8	0.4-1.0	≤0.7	0.2-0.8	≤0.25	≤0.15	≤0.10	≤0.15
AA 2024 [143]	Bal	3.8-4.9	1.2-1.8	0.3-0.9	≤0.5	≤0.5	≤0.25	≤0.15	≤0.10	≤0.15
AA 2624 (Alcoa)	Bal	4.1	1.4	0.6	-	-	-	-	-	-

Table 3.2. ICP-MS result of the investigated aluminum alloys (wt. %).

	Al	**Cu**	**Mg**	**Mn**	**Fe**	**Zn**	**Ti**	**Cr**	**Si + Others**
AA 2017	90.57	3.39	0.57	0.58	0.19	0.14	0.01	0.03	4.50
AA 2024	91.26	3.90	1.34	0.60	0.22	0.01	0.02	0.02	2.62
AA 2624	93.79	3.44	1.24	0.53	0.06	0.00	0.02	0.00	0.92

Table 3.3. Temper designation of the selected aluminum alloys [142].

Temper designation	Heat treatment procedure	Product forms
T351	Solution heat treatment followed by a stress relief by stretching to about 1-3% for rod/bar or 1.5-3% for plate before naturally aged	Plate; rolled or cold finished bar
T451	Solution heat treatment followed by a stress relief by stretching to about 1-3% before naturally aged	Rolled or cold finished rod and bar

It can be observed from Table 3.1 that AA 2017 aluminum alloy is an alloy with Cu:Mg ratio of approximately 6.7 while the ratio for both AA 2024 and AA 2624 alloys is about 2.9. AA 2017 alloy can be regarded as an Al-Cu alloy due to its low Mg content. AA 2024 and AA 2624 alloys contain higher amount of Mg than AA 2017 and are Al-Cu-Mg alloys. The as-received alloys were machined into cylindrical test specimens with diameter of 9.5 mm and length of 10.5 mm. The axes of the cylindrical test specimens are parallel to the rolling direction (RD) as schematically shown in Fig. 3.1.

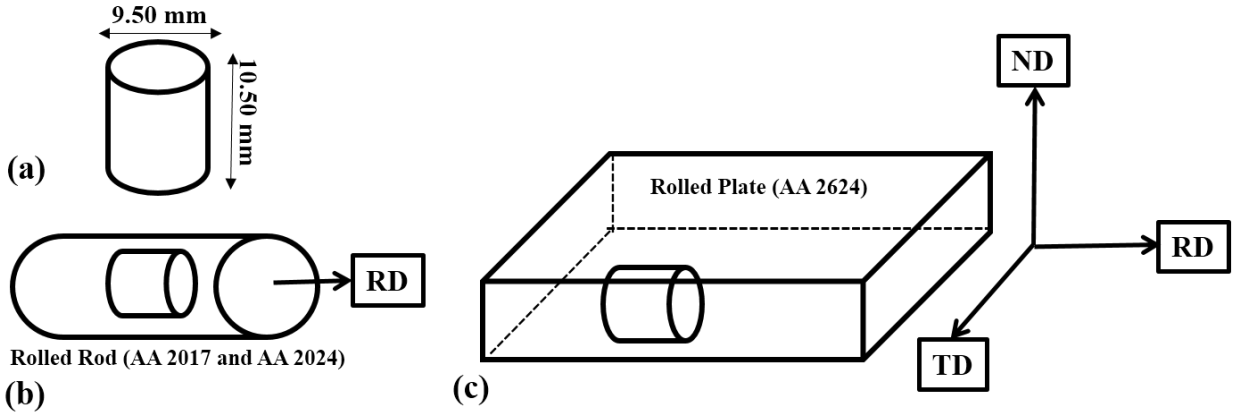

Fig. 3.1. Schematic of cylindrical test specimens showing (a) dimension and (b & c) cutting direction.

3.2 Heat treatment procedure

Some of the machined specimens of the selected aluminum alloys were further heat treated to obtain T651 and O temper. Annealing heat treatment for the three alloys involves the heating of

specimens to 413^{o}C, soaking for 3 hours followed by a two-step cooling process. The first step involves slow cooling at 30^{o}C per hour to 260^{o}C followed by air cooling from this temperature to room temperature. The as-received AA 2017-T451 and AA 2624-T351 were artificially aged at 100°C for 10 hours and air-cooled to obtain T651 temper. The AA 2024-T351 alloy was artificially aged at 191°C for 10 hours and air-cooled to obtain T651 temper. The heat treatment temperature was based on the standard heat treatment procedure for the alloys in the literature. The heat treatment processes were carried out using the Thermo Scientific Lindberg Blue M furnace located in the material science lab, Engineering Building, University of Saskatchewan, Canada.

3.3 Mechanical test

3.3.1 Hardness test

In order to observe the effect of temper condition on the hardness of the three aluminum alloys, microhardness tests were carried out using Mitutoyo Micro Vickers hardness testing machine MVK-H1. The specimens were subjected to a load of 200 gf for 10 seconds. The test was repeated nine more times in a sample. Common errors such as indenting too close to the edge of test samples and/or indenting too close to previous indents were avoided. Therefore, the average values of ten (10) hardness measurements are reported for each specimen in this study.

3.3.2 Dynamic Impact test

The dynamic impact test was conducted on the cylindrical specimens of the alloys using split Hopkinson pressure bar (SHPB). A schematic illustration of the SHPB system is presented in Fig. 3.2. It consists of an incident bar and a transmitter bar. The tests specimens were sandwiched between the two bars while a 2.04 kg blunt projectile was fired by a light gun to impact the incident bar at momentum varying between 30 and 48 kg.m/s to create elastic waves which travelled through the incident bar to rapidly deform the test specimens at strain rates in excess of 2000 s^{-1}. The projectile, incident and transmitted bars are made of maraging steel (Mar 300). The equipment was designed and constructed by the College of Engineering machine shop at the University of Saskatchewan. The standard operating procedure (SOP) of the SHPB, which was developed in the course of this research is presented in Appendix A. Elastic wave data captured by strain gages attached to incident and transmitter bar were used in generating stress, strain and strain rate data (details are provided in Appendix B) using the Eqs. 3.1 to 3.3 [144]. The high strain-rate compression tests were conducted at room temperature although considerable increase in

temperature occurred in the specimens as impacted specimens became so hot after impact that they could not be touched with bare hand. This test was conducted two more times on different samples under same condition to ensure repeatability of test.

$$\sigma = (A_B/A_S)\, E_B \varepsilon_T \quad \ldots 3.1$$

$$\varepsilon = -2 \left(\frac{C_B}{L_S}\right) \int_0^t \varepsilon_R \, dt \quad \ldots 3.2$$

$$\dot{\varepsilon} = -2 \left(\frac{C_B}{L_S}\right) \varepsilon_R \quad \ldots 3.3$$

where A_B and A_S are cross-sectional areas of the bars (incident and transmitter) and specimen respectively; ε_T and ε_R are transmitted and reflected strain pulses respectively; C_B, E_B, L_S and t are respectively the speed of elastic waves in the bar, elastic modulus of the bar material, initial length of specimen and time. The velocity of elastic waves in the bar, C_B can be calculated using Eq. 3.4.

$$C_B = \sqrt{E_B/\rho} \quad \ldots 3.4$$

where elastic modulus (E_B) for maraging steel is given as 180 GPa and density (ρ) is given as 7960 kg m^{-3}. C_B, when calculated, was approximately 4750 m s^{-1}. Alternatively, C_B can be determined experimentally by striking the incident bar in contact with transmitted bar with no specimen in between them using Eq. 3.5 [144].

$$C_B = 2l/\Delta t \quad \ldots 3.5$$

where l is the distance from the strain gage location to the specimen end of the incident bar; and Δt is the time interval between the incident and reflected pulses when subjected to the impact by the striker.

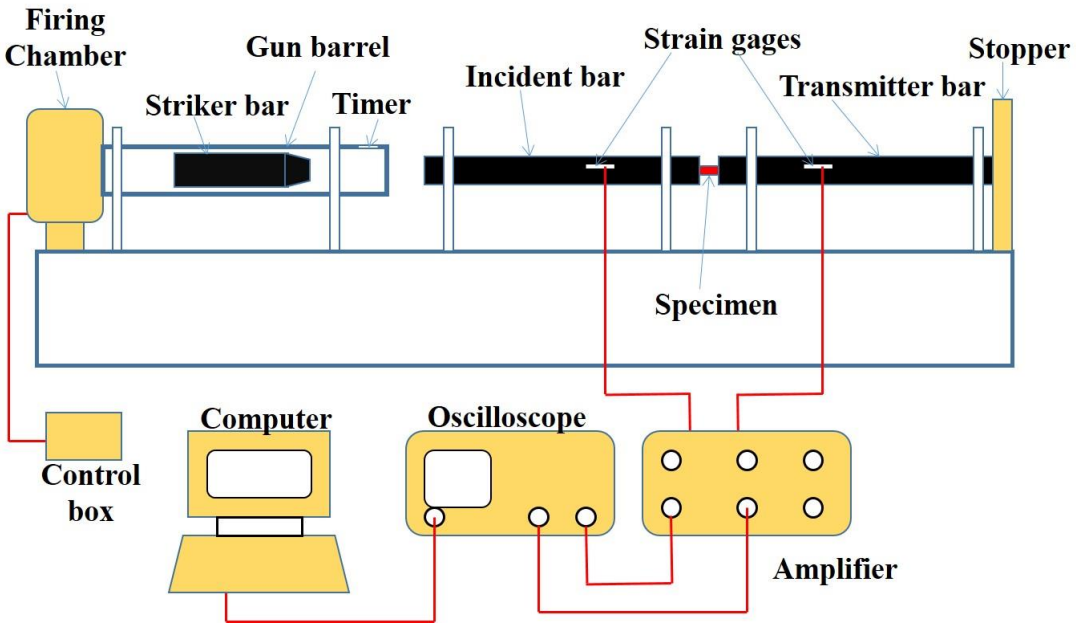

Fig. 3.2. Schematic of split Hopkinson pressure bar (SHPB).

3.3.3 Quasi-static compression test

For a better comparative study of the mechanical behaviour of the aluminum alloys of interest, specimens of the alloys were also tested under quasi-static loading condition using an Instron R5500 mechanical testing machine. The specimens were subjected to compressive loading using a cross speed of 2 mm/min to a maximum load of 100 kN. This cross speed generated a strain rate of 3.2×10^{-3} /s in the specimens. A repeatability test was conducted under same condition. All the compression tests were carried out at room temperature.

3.4 Microstructural evaluation

Microstructural evaluation of the alloy specimens before and after mechanical loading was preceded with metallographic sample preparation, which begins with cold-mounting of specimens using acrylic resin (a mixture of VersoCit-2 powder and liquid in ratio 2:1) in a LECOMAT® pressure vessel. This was followed by pre-grinding, fine grinding and polishing (diamond and oxide) of the compression plane of the specimens to obtain a mirror-like surface finish. The 320 and 800 grade SiC emery papers were used for the pre-grinding stage while 9 µm MD-Largo cloth with 9 µm MD-Largo suspension were used for fine grinding Diamond polishing was done using 3 µm MD-Mol with 3 µm MD-Mol suspension and 1 µm MD-Nap clothes with 1 µm MD-Nap suspension. For active oxide polishing, 0.04 µm OPS cloth with 0.04 µm OPS suspension were

used. For EBSD measurements, all steps mentioned above were followed except that 0.04 µm OPS oxide polishing was replaced with a 24 hour colloidal silica suspension polishing using VibroMet™ 2 Vibratory Polisher in order to create a strain free surface.

3.4.1 Optical and Scanning Electron Microscopy

After obtaining a mirror-like surface finish, etching was done using a solution consisting of 25 ml methanol, 25 ml HNO_3, 25 ml HCl and 1drop of HF. The optimum etching time for each alloy depended of the temper condition as presented in Table 3.4. A longer etching time resulted in chemical burning of the polished surface. Microstructural investigation of the specimens was conducted using Nikon MA100 inverted metallographical microscope with Pax-it! image analysis software and JEOL-JSM-6010LV scanning electron microscope using secondary electron imaging and accelerated voltage ranging between 15 and 20 kV.

Table 3.4. Etching time used for the investigated aluminum alloys.

Alloy	**AA 2017**			**AA 2024**			**AA2624**		
Temper condition	T451	T651	O	T351	T651	O	T351	T651	O
Etching Time (s)	50	50	10-15	50	10-15	5	50	50	5

3.4.2 Electron Backscattered Diffractometry (EBSD) and Energy Dispersive Spectroscopy (EDS)

EBSD measurements were performed on both un-deformed and shock loaded samples of the as received alloys using a SU 6600 Hitachi field emission scanning electron microscope coupled with an Oxford Instruments Nordlys Nano EBSD detector. AZTEC 2.0 data acquisition software was used to acquire the electron diffraction patterns with a binning of 4 × 4 pixels. Six bands for pattern recognition followed by high acquisition rates (20 frames) were used. The data acquisition software indexes the diffraction patterns to assess the crystallographic orientation at each and every point in the selected region of the scan. A typical step size of 2.05 µm was used for obtaining large area (1030 µm x 674 µm) scans for the as-received specimens and 1.63 µm was used for obtaining (844 µm x 539 µm) area scans on the deformed specimens. The conditions of beam and the video were kept identical for the as-received and deformed specimens. The EBSD raw data were further

analyzed using the Oxford Instruments Channel 5 post processing software. This software defines the grains orientation and grain boundaries misorientation. Grain boundaries (GB) were defined as continuous regions of misorientation (misorientation angle >5°). In the present analysis, GBs with a misorientation angle (θ) < 10° are considered as LAGB, 10° < θ < 15° as medium angle grain boundaries (MAGBs) and θ> 15° as high angle grain boundaries (HAGB). Average grain size was measured as the average of the diameter of all the grains in the map.

The grain size diameter was obtained from the grain area assuming the "equivalent circle diameter", which is the diameter of a circle that has the same area. The size of a grain was obtained from the number of data points in the grain multiplied by their pixel size. Average misorientation represented the average misorientation of each measurement point with respect to all eight (as in a square grid) neighbors (kernel); provided that any of these neighbors' misorientation does not exceed 5 deg. In this study, mean angular deviation (MAD) was used as statistical measure of accuracy for the automated indexing. Measurement points below 1.5 degrees are considered as a good fit. EDS measurement was conducted using the same SU 6600 Hitachi field emission scanning electron microscope used for EBSD but with an EDS detector. In terms of test conditions, the accelerating voltage used was 15 keV and dead time required to process x-ray pulses was set to be more than 40 but less than 60 %.

CHAPTER FOUR

RESULTS AND DICUSSION

The results obtained from experimental investigations are presented and discussed in this chapter. It contained five subsections, first of which focussed on the microstructural evolution in the investigated AA 2017, AA 2024 and AA 2624 aluminum alloys before mechanical loading. The second and third subsections contain research findings on the mechanical response of these alloys to quasi-static and dynamic loading conditions respectively. The fourth focusses on the microstructural evolution in the aluminum alloys during quasi-static and dynamic loading. The fourth section dealt with shear bands' characterization in the impacted specimens. The results of texture measurements in rolled AA 2017-T451 rod and rolled AA 2624-T351 plate before and after dynamic shock loading are presented in the fifth subsection.

4.1 Microstructure of the as-received alloys before mechanical loading

Optical micrographs taken from a plane perpendicular to rolling direction of the as-received alloys are presented in Fig 4.1. The grain boundaries of the AA 2017 alloy could not be observed under the optical microscope (Fig. 4.1a). These might be due to the difficulty of the etchant in preferentially attacking the grain boundaries within the optimum etching time. Equiaxed grain structure was observed in the optical micrographs of the AA 2024 alloy (Fig. 4.1b) while AA 2624 alloy consist of elongated grains (Fig. 4.1c). The micrographs revealed the influence of prior mechanical processes (rolling) on the grain structure. The equiaxed grain structures in the AA 2024 alloy is attributed to the fact that it was rolled as a rod with constraint at the circumference during rolling. Two sides of the AA 2624 plate are unconstrained during rolling leading to the observed elongated structure on the plane perpendicular to the rolling direction.

The microstructures consist of aluminum phase and second phase particles of varying geometry and sizes (Fig. 4.1). In this thesis, the second phase particles will be referred to as SP particles or simply 'particles'. The second phase particles in the microstructures presented in Fig. 4.1 can be deleterious to mechanical properties because of the possibility of them acting as sources of micro-crack initiation and growth, more so that their strength contributions to the yield strength of the alloys are not substantial [24]. The morphology (from SEM micrographs) and the compositional analysis using energy dispersive X-ray spectroscopy of the second phase particles observed in the

investigated alloys are highlighted in the next subsections and summarized in Tables 4.1 and 4.2. The ultrafine precipitates that form in the alloys during precipitation heat treatment are highlighted in section 2.1.1 and 2.1.2. They have sizes in the nano range and cannot be resolved under OM and SEM. Only high resolution transmission electron microscope can be used to resolve and investigate these fine precipitates which contribute largely to high strength of precipitation-hardened aluminum alloys.

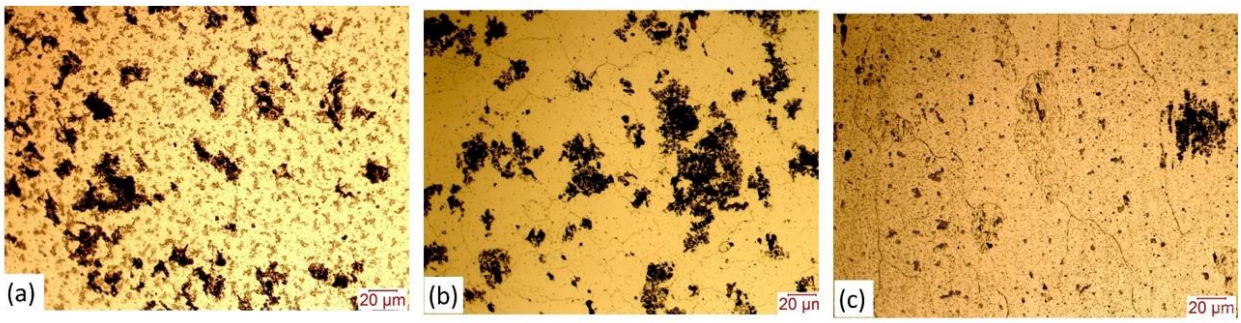

Fig. 4.1. Optical micrographs of as received (a) AA 2017-T451, (b) AA 2024-T351 & (c) AA 2624-T351 showing grain and particle morphology.

4.1.1 Morphology of second phase particles in AA 2017

Optical and SEM micrographs of the AA 2017 samples in T451, T651 and O temper conditions before mechanical loading are presented in Figs. 4.2 and 4.3. The microstructures consist of dispersed second phase particles embedded in a continuous aluminum phase. AA 2017 is an Al-Cu alloy containing lower amount of magnesium addition as shown in Table 3.1. In Al-Cu alloys, aluminum combines with copper to form Al_2Cu precipitates with GP, θ'', θ' and θ as possible phases depending on the temper condition. The presence of Mg, though in small amount, could result in the formation of Al_2CuMg (S) phase which can co-exist with the Al_2Cu (θ). In the present study, the as-received AA 2017-T451 shows clustering of irregularly shaped SP particles in the microstructure (Fig. 4.2a). SEM micrographs at higher magnification (Fig. 4.3a) revealed that these SP particles are made up of clusters of pyramidal-shaped particles. Clustering of SP particles was observed to be less in AA 2017 alloy in both T651 (Fig. 4.2b) and O (Fig. 4.2c) temper condit-

Fig. 4.2. Optical micrographs showing the distribution of second phase particles in the (a) AA 2017-T451, (b) AA 2017-T651 and (c) AA 2017-O alloy before mechanical loading.

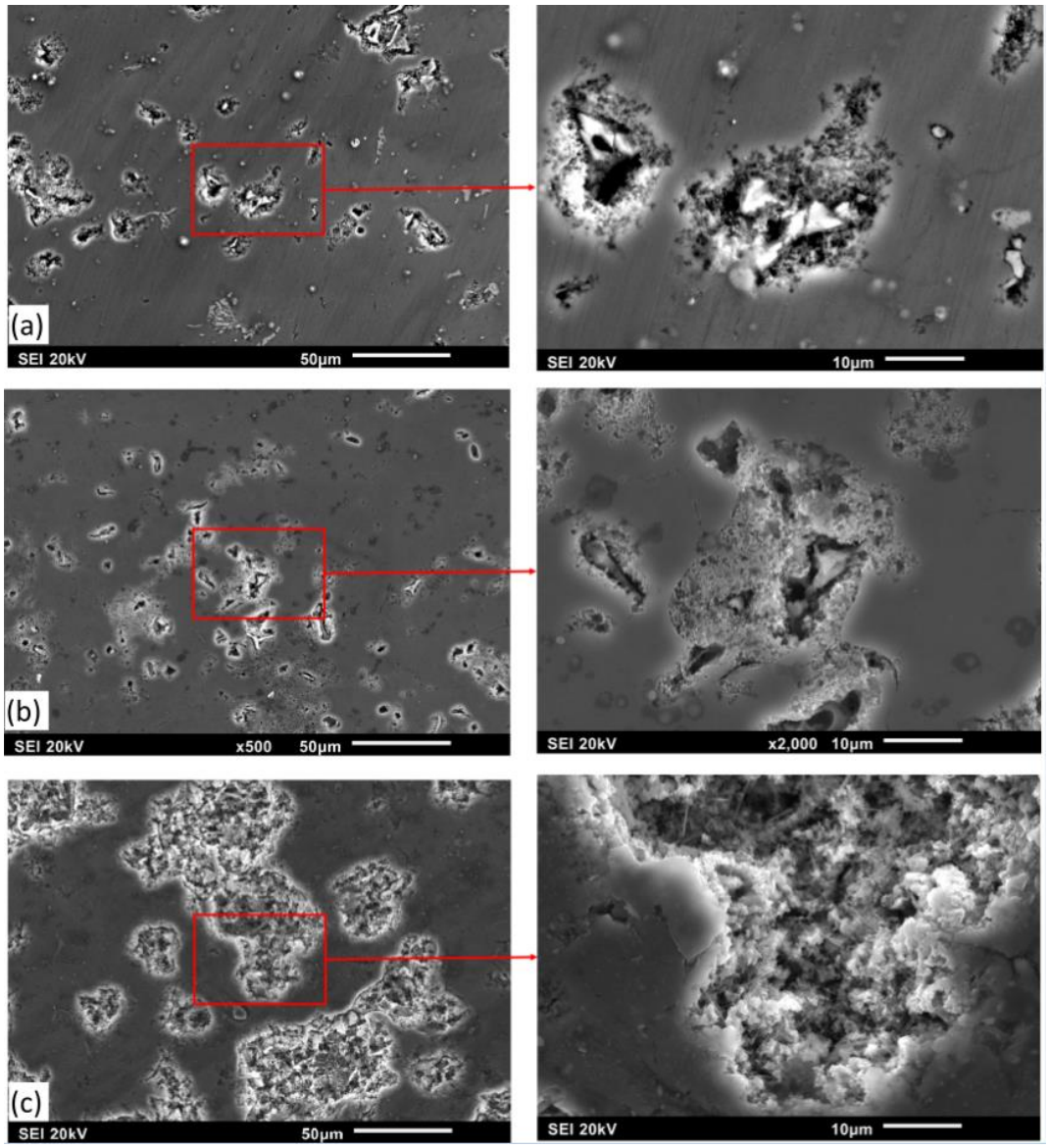

Fig. 4.3. SEM micrographs showing the distribution of second phase particles in the (a) AA 2017-T451, (b) AA 2017-T651 and (c) AA 2017-O alloy before mechanical loading.

ions, though further coalescing and growth of SP particles attributed to higher Si content in AA 2017 [145] was observed in the annealed alloy. SEM micrographs showed that the irregular-shaped SP particles in AA 2017-T651 contains rod like sub-particles (Fig. 4.3b), while needle-shaped particles were observed within the second phase structure of the AA 2017-O alloy (Fig. 4.3c).

The results of chemical analysis of the SP particles in the alloys using EDS are summarized in Table 4.2. Among all temper samples, SP particles in the annealed sample have the highest concentration of aluminum but lower contents of alloying elements than the particles in age-hardened AA 2017 alloy. The decrease in concentration of aluminum in the continuous α-aluminum during annealing of AA 2017-T451 specimens suggests migration of aluminum atoms from the continuous α-aluminum phase to the SP particles. EDS analyses of the second phase particles in an artificially-aged AA 2017 alloy in a previous study also showed the presence of iron rich precipitates such as Al_3Fe or $Al_{12}(Fe,Mn)_3Si$ in addition to Al_2Cu (θ) and Al_2CuMg (S) equilibrium phases [146]. Annealing of the as-received AA 2017-T451 also resulted in a decrease in the Cu content of the SP particles in the current investigation. EDS maps (Fig. 4.4) showing the major alloying elements (indicated by unique color) in the second phase particles of AA 2017 alloy for all investigated temper conditions are presented in Fig. 4.4. Mg content, though expected, is low in the SP particles in all temper conditions while other alloying elements such as Mn, Fe and Si are of brighter color field in the naturally-aged sample and tends to become dimmer in artificially-aged and annealed conditions in this order. Therefore, the higher concentration of strength-improving-element (Cu) and other alloying elements in the SP particles of the T451 and T651 imply that the SP particles of these temper conditions could have higher strength than particles in the annealed specimens. Quantitative analyses of the microstructures of the alloy show that the average volume fraction of SP particles in AA 2017-T451, AA 2017-T651 and AA 2017-O are about 0.11, 0.13 and 0.39 respectively. Higher fraction of SP particles in AA 2017-O specimen is an indication of particle growth at the expense of the continuous α-Al matrix during annealing as confirmed in the micrographs (Fig. 4.3c).

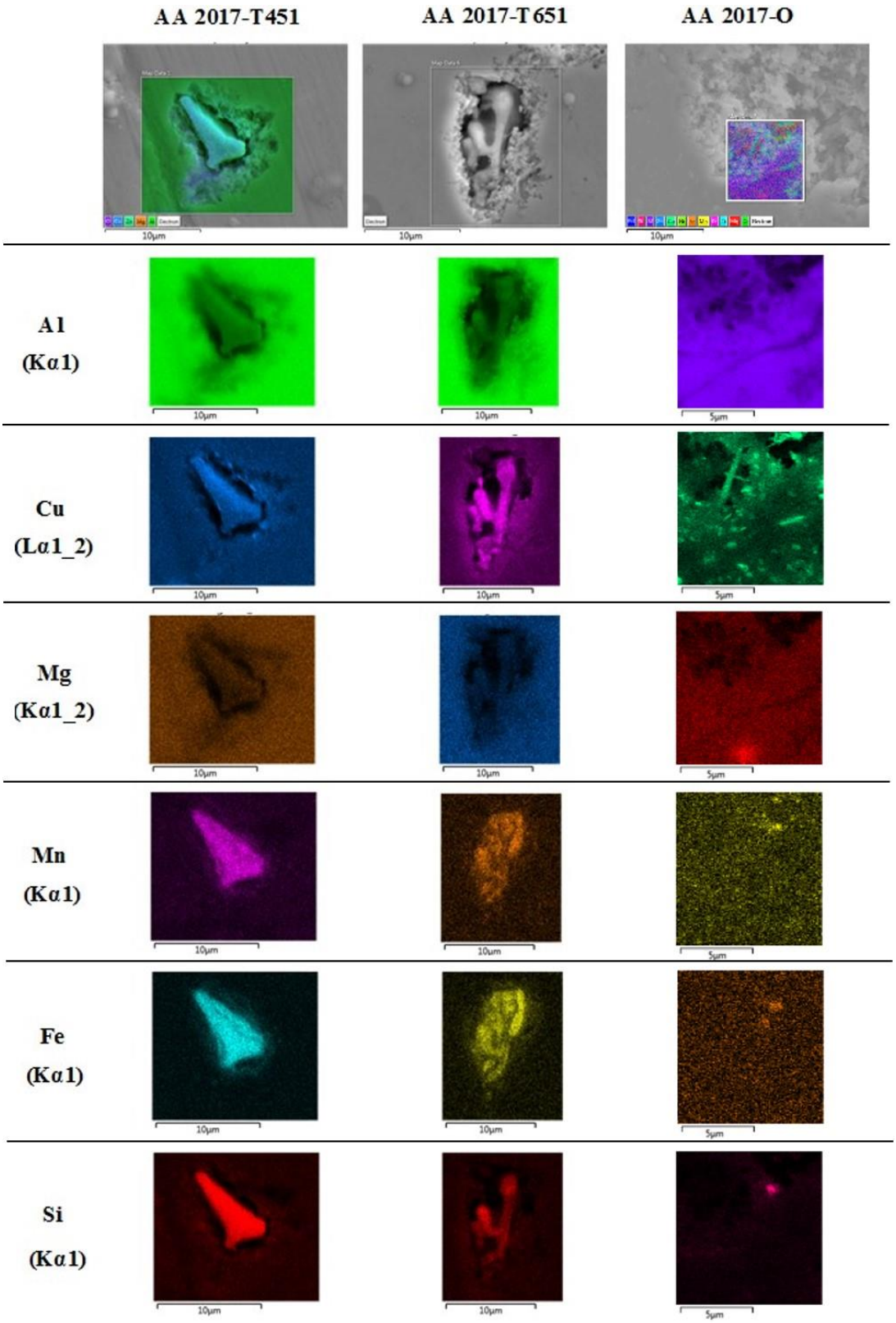

Fig. 4.4. EDS maps of the major alloying elements in the second phase particles of AA 2017 aluminum alloy in naturally-aged, artificially-aged and annealed conditions.

4.1.2 Morphology of second phase particles in AA 2024

Typical microstructures of the AA 2024 alloy in T351, T651 and O temper conditions before mechanical loading are presented in Figs 4.5 and 4.6. AA 2024 is an Al-Cu-Mg alloy containing higher amount of magnesium addition than the AA 2017 alloy (Table 3.1). Similar to what is obtainable in Al-Cu alloys, aluminum combines with major alloying elements (Cu and Mg) in Al-Cu-Mg alloys to form Al_2CuMg phases with GPB, S'', S' and S as possible precipitates depending on the temper condition. The optical micrograph of AA 2024 in the natural aging condition (Fig. 4.5a) composed of irregularly shaped second phase particles without clustering. SEM micrographs at higher magnification (Fig. 4.6a) revealed that the SP particles are made up of irregularly-shaped sub-particles. Clustering of SP particles was also not observed in the microstructure of AA 2024 in both T651 (Fig. 4.5b) and O (Fig. 4.5c) temper conditions. Unlike AA 2017 alloy, in which coalescing and growth of SP particles was observed in the annealed specimens, minimal growth with no coalescing of SP particles was observed in the AA 2024-O specimen. Si content in aluminum alloys accelerate the coarsening of SP particles [145]; its lower content in AA 2024-O could be responsible for the suppressed particle coarsening and coalescence.

While SP particles in AA 2024-T651 are comprised of spherical sub-particles (Fig. 4.6b), AA 2024-O (Fig. 4.6c) are comprised of spherical/needle-like sub-particles. Unlike in the case of the AA 2017 alloy, the EDS maps of AA 2024 alloy (Fig. 4.7) indicates low Mg content (dark color) in the SP particles of T351 temper sample and its content become higher (brighter color) in the T651 and O temper. On the other hand, other alloying elements in the particle such as Mn, Fe and Si are of brighter color in the naturally-aged sample which becomes dimmer in artificially-aged and annealed conditions suggesting that particles in T651 and O temper specimen are Mg-rich.

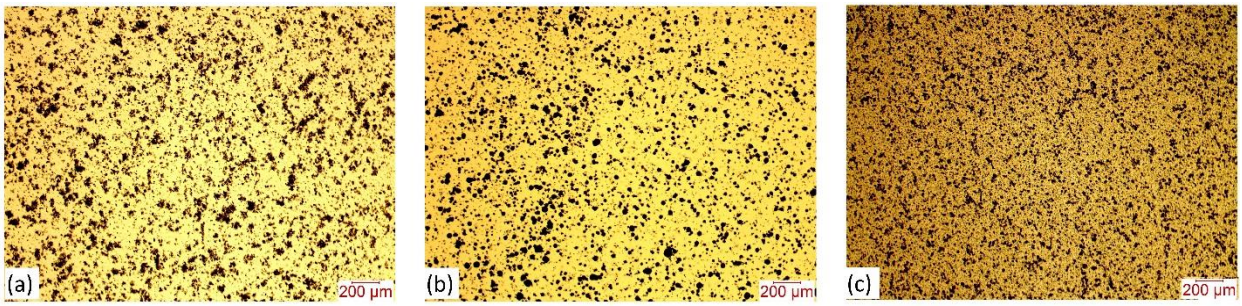

Fig. 4.5. Optical micrographs showing the distribution of second phase particles in the (a) AA 2024-T351, (b) AA 2024-T651 and (c) AA 2024-O alloy before mechanical loading.

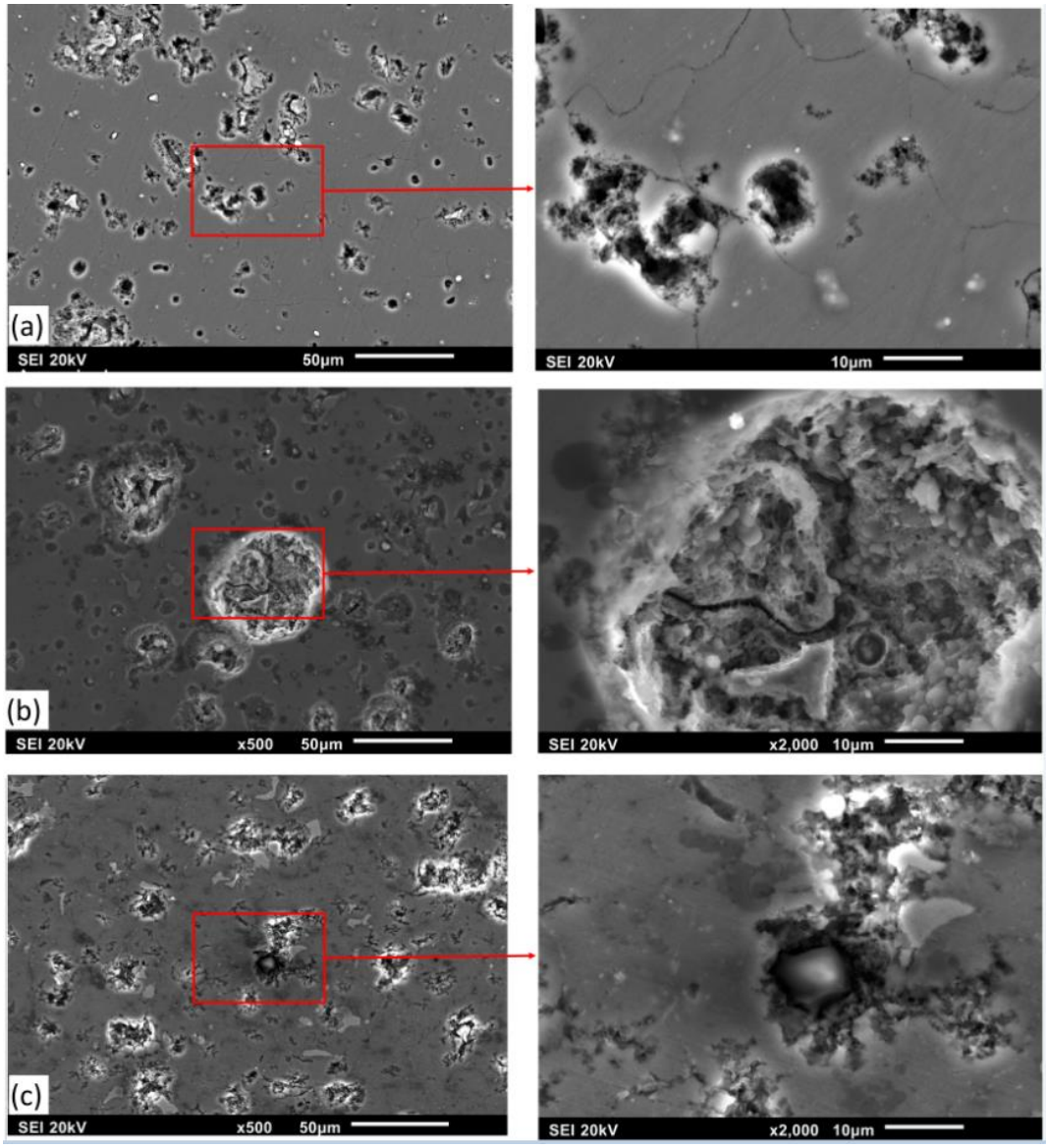

Fig. 4.6. SEM micrographs showing the distribution of second phase particles in the (a) AA 2024-T351, (b) AA 2024-T651 and (c) AA 2024-O alloy before mechanical loading.

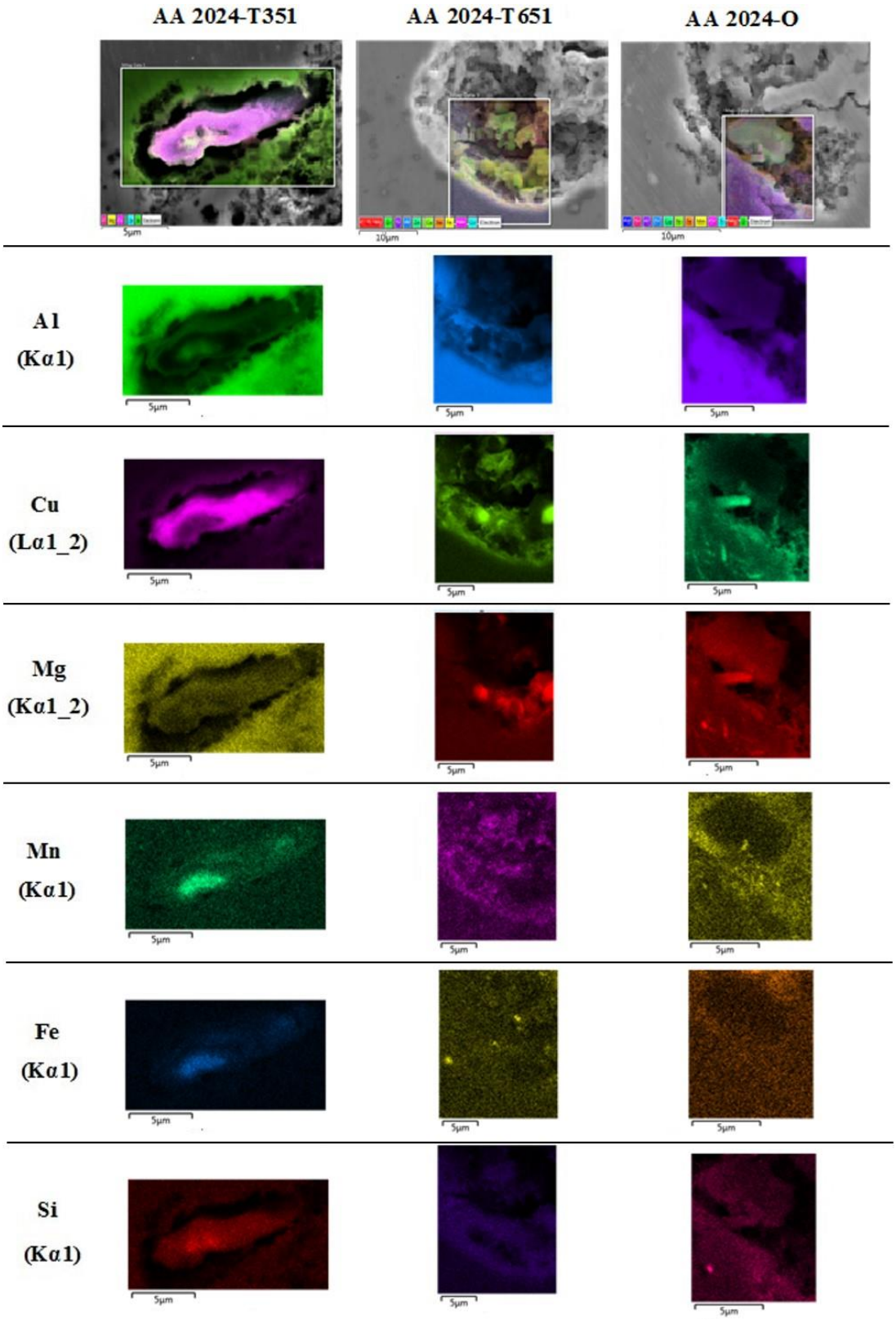

Fig. 4.7. EDS maps of the major alloying elements in the second phase particles of AA 2024 aluminum alloy in naturally-aged, artificially-aged and annealed conditions.

One notable difference between the AA 2017 and AA 2024 alloys is that SP particles in AA 2024 have lower concentration of alloying elements with little or no Mn. EDS analyses indicated a decrease in concentration of Al in the matrix of AA 2024 from T351, T651 and O in that order (Table 4.2). This also suggests diffusion of Al from matrix into the SP particles during annealing and artificial aging of the received AA 2024 alloy. The concentration of Cu in the T351 SP particle is observed to be more than that of Al by 45 % whereas the concentration of Cu dropped by 81, 98 and 90 % in the T651, O (sphere) and O (needle) SP particles respectively. Quantitative analysis of these microstructures shows that the average volume fraction of SP particles in AA 2024-T351, AA 2024-T651 and AA 2024-O are about 0.13, 0.16 and 0.18 respectively. This confirms the minimal coarsening of SP observed in AA 2024-O sample in comparison with the AA 2017 as shown in Fig. 4.6c.

4.1.3 Morphology of second phase particles in AA 2624

The microstructure of the AA 2624 alloy in various temper conditions showing particle morphology are presented in Figs 4.8 and 4.9. Like the AA 2024, AA 2624 alloy is also an Al-Cu-Mg alloy containing substantial Mg content (Table 3.1). The optical micrograph of AA 2624-T351 alloy shows second phase particles which align to form a kind of lamella arrangement (Fig. 4.8a). A combination of SEM analysis (Fig. 4.9a) and EDS maps (Fig. 4.10) reveal that these second phase (SP) particles are made up of dark-small and white spherically-shaped particles with Cu and Mg as the major alloying elements (Table 4.2). In the T651 temper, the SP particles were observed to coalesce (Fig. 4.8b, 4.9b & 4.10) while the AA 2624 alloy in annealed condition shows clustering of needle-like particles which are dispersedly distributed on the compression plane (Fig. 4.8c, 4.9c & 4.10).

The EDS maps (Fig. 4.10) indicates lower Mg content (dark color) in the SP particles of T351 and T651 specimens and its content had become higher (brighter color) in the annealed specimen. The concentration of other alloying elements such as Mn, Fe and Si are low (dark color field) in all temper supporting earlier observation of stricter limit on impurity level in AA 2624 alloy. Generally, SP particles in AA 2624 are composed of same elements (Al, Cu and Mg) in all temper conditions, but variation exists in their atomic ratios. Among the alloys, AA 2624 has the least number of elements that make up their SP with no Mn. The Cu and Mg ratios in the dark-small and white spherically-shaped particles are the same in both naturally and artificially aged AA 2624

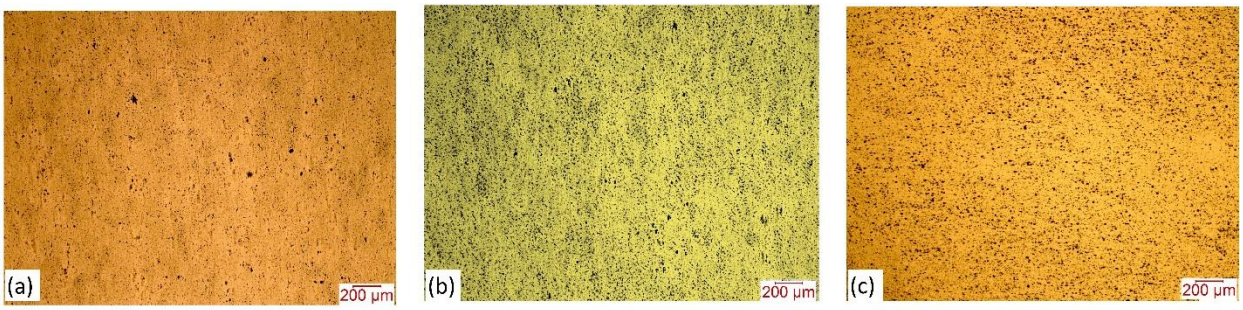

Fig. 4.8. Optical micrographs showing the distribution of second phase particles in the (a) AA 2024-T351, (b) AA 2624-T651 and (c) AA 2624-O alloy before mechanical loading.

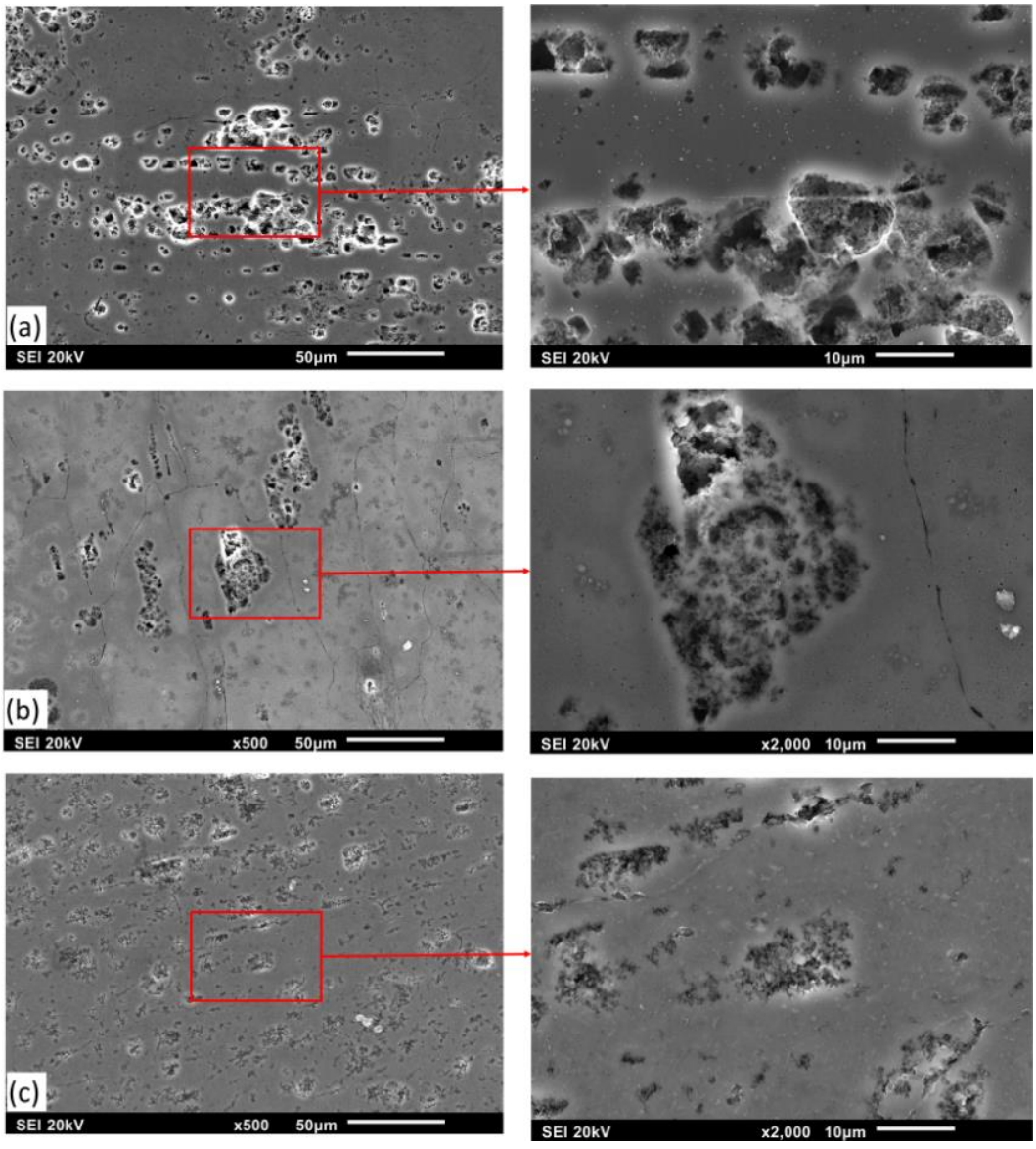

Fig. 4.9. SEM micrographs showing the distribution of second phase particles in the (a) AA 2624-T351, (b) AA 2624-T651 and (c) AA 2624-O alloy before mechanical loading.

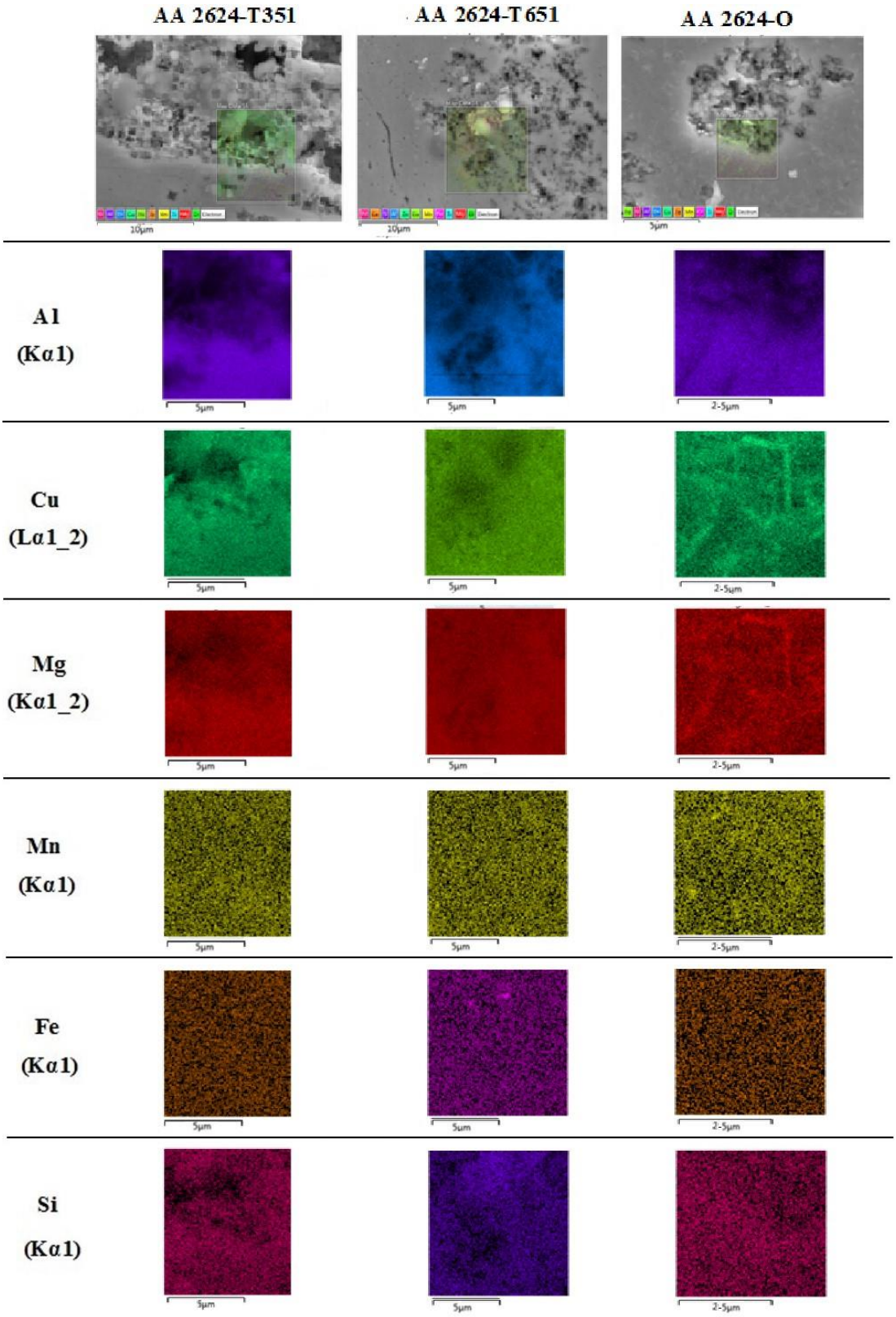

Fig. 4.10. EDS maps of the major alloying elements in the second phase particles of AA 2624 aluminum alloy in naturally-aged, artificially-aged and annealed conditions.

samples while EDS analyses indicate that only Al atoms diffused into the particles during artificial aging of the T351specimens. The concentration of Al in the matrix of AA 2624 in T351, T651 and O temper condition are approximately the same (about 85%). This suggests that the diffusion of Al from the matrix to the SP observed in AA 2017 and AA 2024 during artificial aging and annealing of their as-received naturally-aged samples was suppressed in the AA 2624 alloy. In the three temper conditions, atomic percent of Cu in the particles are more than those observed in the continuous α-aluminum phase. Quantitative analysis of the microstructures shows that the average volume fraction of SP in AA 2624-T351, AA 2624-T651 and AA 2624-O are about 0.10, 0.13 and 0.12 respectively. This indicates minimal growth of SP observed in AA 2624 alloy during artificial aging or annealing processes.

A unique characteristic feature observed in the microstructure of rolled age-hardened (T351 and T651) AA 2624 aluminum alloy is the presence of network of subgrain boundaries which are resolvable under OM and SEM (Fig. 4.11). The network of grain boundaries appear to be confined within an individual grain (grain-scale); resulting into subgrains. Cracking were observed within grain exhibiting this microstructural feature which are widely dispersed in the alloy. It is speculated that the subgrain feature could be a result of concentrated plastic strain in the specific grains during the mechanical processing (rolling) of the as-received alloy. None of the grain-scale feature was observed in the annealed specimens suggesting a possibility of coalescence of the subgrains back to single grain during annealing. Rostova and Zakharov [103] had also observed localized plastic strain in cold rolled Al-Li alloy which they attributed to the operation method (rolling) and large amount of dispersed particles [δ’(Al_3Li) and Al_3Sc] present in the alloy.

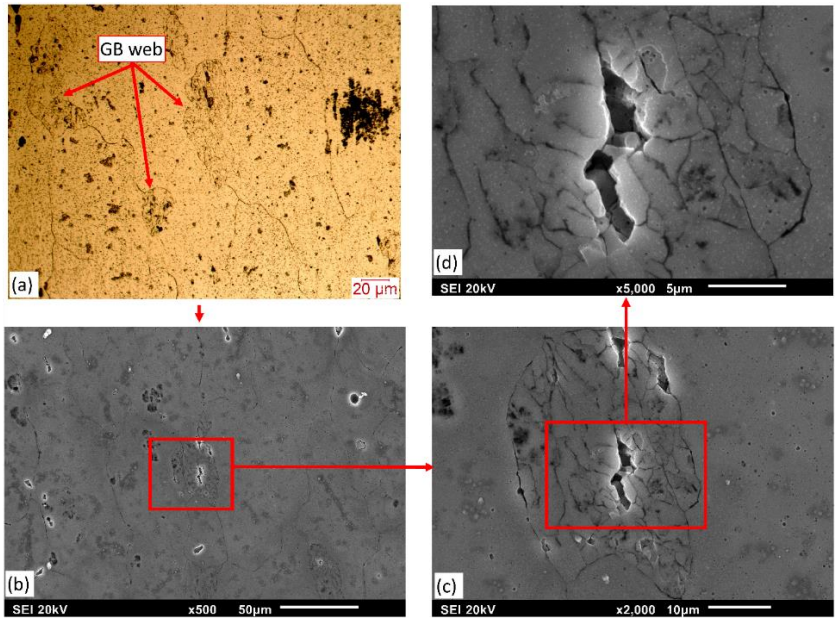

Fig. 4.11. (a) Optical and (b, c & d) scanning electron micrographs showing sub-grain structure in the test specimens before mechanical loading in AA 2624-T351 and AA 2624-T651 aluminum alloy. The GB web is absent in AA 2624-O aluminum alloy sample.

Table 4.1. Summary of particle morphology.

Alloy	**Grain shape**	**Particle shape (Overview)**	**Constituent particle shape**	**Volume fraction of particles**
AA 2017-T451	Equiaxed	Irregularly-shaped cluster	Pyramidal	0.11
AA 2017-T651	Equiaxed	Irregular	Rod-like	0.13
AA 2017-O	Equiaxed	Irregular	Needle-like	0.39
AA 2024-T351	Equiaxed	Irregular	Irregular	0.13
AA 2024-T651	Equiaxed	Circular	Spherical	0.16
AA 2024-O	Equiaxed	Irregular	Spherical/ Needle-like	0.18
AA 2624-T351	Elongated	Lamella	Spherical	0.10
AA 2624-T651	Elongated	Lamella coalesce	Spherical	0.13
AA 2024-O	Elongated	Clustering	Needle/Rod-like	0.12

Table 4.2. Chemical analysis of second phase particles identified by EDS analysis in the selected aluminum alloys.

Alloy	Temper		Atomic percent					
			Al	**Cu**	**Mg**	**Mn**	**Fe**	**Si**
AA 2017	Natural (T451)	Matrix	83.6	1.9	0.6	0.2	0.0	0.1
		Particles	53.7	6.1	0.1	3.3	5.8	5.4
	Artificial (T651)	Matrix	83.6	1.9	0.3	0.3	0.0	0.3
		Particles	37.9	8.9	0.2	1.9	3.0	2.0
	Annealed (O)	Matrix	72.1	1.7	0.4	0.3	0.0	0.2
		Particles	74.7	1.8	0.2	1.3	0.2	0.2
AA 2024	Natural (T351)	Matrix	94.3	2.1	1.6	0.5	0.1	0.1
		Particles	24.9	45.4	0.7	0.5	1.3	0.4
	Artificial (T651)	Matrix	86.0	2.0	1.4	0.3	0.0	0.1
		Particles	36.4	8.7	4.4	0.2	0.1	0.2
	Annealed (O)	Matrix	84.8	0.8	0.5	0.3	0.1	0.0
		Particles (sphere)	34.5	0.7	2.8	0.3	0.1	0.1
		Particles (needle)	37.0	4.7	3.5	0.7	0.1	0.2
AA 2624	Natural (T351)	Matrix	85.3	1.8	1.4	0.2	0.0	0.0
		Particles*	71.5	3.2	1.1	0.1	0.0	0.0
		Particles^{+}	31.7	2.9	0.6	0.3	0.0	0.0
	Artificial (T651)	Matrix	84.4	1.9	1.4	0.3	0.1	0.0
		Particles*	79.2	2.6	1.0	0.1	0.1	0.1
		Particles^{+}	28.1	2.2	0.5	0.1	0.0	0.1
	Annealed (O)	Matrix	85.0	1.6	1.2	0.1	0.1	0.0
		Particles	71.6	4.4	2.9	0.5	0.0	0.0

*Dark-smaller spherical particles $^{+}$White spherical particles

4.2 Quasi-static Mechanical Test

4.2.1 Hardness test

Fig. 4.12 presents a comparison of the hardness of the alloys in the three investigated tempers. For the AA 2017 alloy in T451 (as-received), T651 and O temper, the hardness values are 131, 114 and 54 HV respectively. Artificial aging and annealing of the T451 samples resulted in about 13

% and 59 % decrease in hardness respectively. It is evident from these hardness measurements that the optimum aging condition for the alloy was already attained by natural aging. Similarly, the average values of the AA 2024 alloy in T351 (as-received condition), T651, and O temper conditions are 126, 138 and 59 HV respectively. Unlike the AA 2017 alloy, the hardness value of as received AA 2024-T351 increased by 10 % after the artificial aging while the hardness of AA 2024-T351 samples decreased by 53 % on annealing. Therefore, in contrast to the observation in AA 2017 alloy, it can be concluded that the optimum aging condition for the alloy was not attained by natural aging since the hardness value of artificially-aged sample was higher. Parel et al. [147] had shown an increase in the hardness of AA 2024 alloy when artificially aged below 200^{o}C. At this aging temperature, the authors attributed increased hardness to the non-existence of S phase coarsening and dissolution. For AA 2624 alloys, the hardness of the AA 2624-T351 (135 HV) remain virtually unchanged when artificially aged to T651 temper. Like AA 2017 and AA 2024 alloys, the hardness of the as received naturally aged AA 2624 decreased by 59 % when annealed. On the comparison of the hardness of the three alloys when sort by temper conditions, AA 2624 (135 HV) has the highest hardness value in the naturally-aged condition while both AA 2024 and AA 2624 shows higher hardness values than AA 2017 in the artificially-aged condition. In the annealed condition, though the hardness values of all the alloys were comparable, AA 2024 was highest.

The changes in the hardness value with temper conditions are attributed to the changes in the orientation and morphology of strength contributing precipitates or particles in the microstructure developed in each corresponding temper conditions [148]. Therefore, the higher hardness of the alloys in age-hardened conditions (T351/T451 and T651) is as a result of the presence of coherent/semi-coherent precipitates. In the as-received naturally-aged condition, while AA 2017 alloy can be speculated to be strengthened by coherent GP/GPB zones (due to presence of low amount of Mg) and/or θ''/S'' phases, AA 2024 and AA 2624 are strengthened predominantly by GPB zones and/or S'' phase [7,25,37]. Similarly, in artificially-aged condition, AA 2017 alloy can be speculated to be strengthened by coherent θ''/S'' and/or semi-coherent θ'/S' phases while AA 2024 and AA 2624 are strengthened by coherent S'' and/or semi-coherent S'. The low hardness value in annealed samples could also be attributed to the presence of incoherent equilibrium precipitates (θ and S) with longer mean free path between them [1] and noodle-like particles with

higher atomic percent of Al compared to other particles in natural and artificial aging conditions in all the three alloys. While AA 2017-O alloy can be speculated to comprise of incoherent equilibrium θ / S phases, AA 2024-O and AA 2624-O are comprised of incoherent S phase [27].

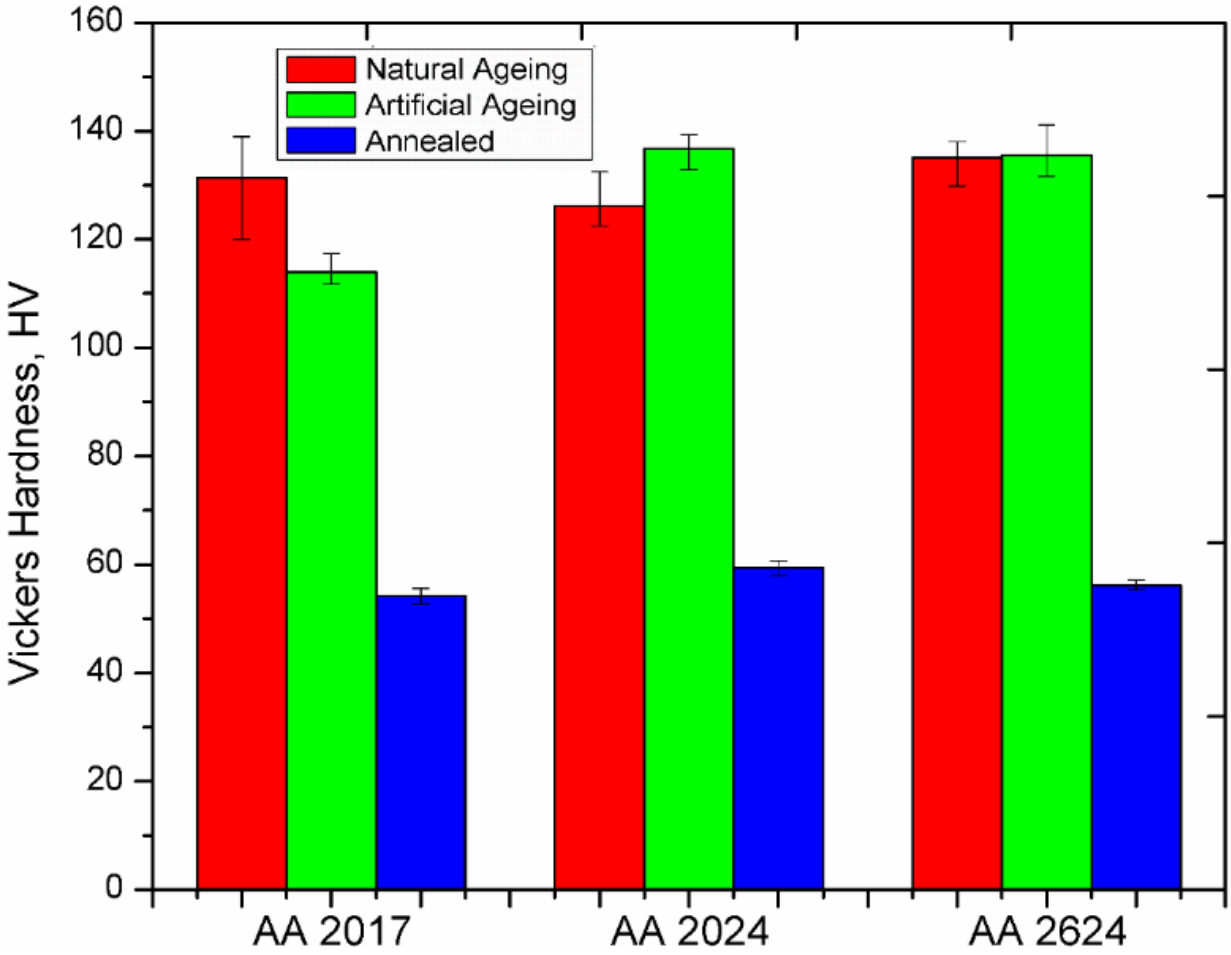

Fig. 4.12. Vickers hardness of the AA 2017, AA 2024 and AA 2624 aluminum alloy specimens in naturally-aged, artificially-aged and annealed condition.

4.2.2 Quasi-static compression test

The typical stress-strain curves obtained from quasi-static compressive loading of the investigated alloys up to the maximum applied load of 100 kN at a strain rate of 3.2 x 10^{-3} /s are presented in Figs. 4.13 to 4.15. The summary of mechanical properties of the alloys under quasi-static loading are presented in Table 4.3, which also include result of microstructural investigation indicating the occurrence of ASB.

Table 4.3. Mechanical properties and microstructural observations of the investigated alloys under quasi-static loading.

Alloy	Temper	Yield stress (0.2%)	Engineering Strain	ASB
AA 2017	T451	360	0.65	DB
	T651	340	0.64	DB
	O	120	0.78	DB
AA 2024	T351	440	0.64	Somewhat TB
	T651	570	0.66	Slight DB
	O	130	0.78	DB
AA 2624	T351	435	0.63	Absent
	T651	440	0.62	DB
	O	125	0.78	DB

AA 2017 alloy

For AA 2017 alloy in T451, T651 and O temper (Fig. 4.13), the yield stresses were determined to be 360, 340 and 120 MPa respectively. The total engineering strains developed were determined to be similar for T451 and T651, but slightly higher for O temper. The decrease in yield stress of AA 2017-T451 after artificial aging suggest that the alloy was already in peak aged condition and artificial aging resulted in over-aging due to loss of coherency of the precipitates. Loss of coherency will normally translate to reduced resistance to slip since the strengthening effect of dislocation looping around incoherent precipitates is less than that of dislocation cutting through coherent precipitates [31]. Coarsening of precipitates by Ostwald ripening can occur, leading to increase in the distance between precipitates. The shear stress required for dislocation to loop around incoherent precipitates is indirectly proportional to the distance between them [31]. The yield strength of the annealed is very low due to dissolution of strengthening precipitates at the annealing temperature and coarsening of equilibrium precipitates, which are less effective barriers to the motion of dislocations (slip). This is in agreement with the particle coarsening observed in the SEM micrographs of AA 2017-O specimen (Fig. 4.3c). The quasi-static stress-strain curve of the T651 specimen, which is slightly below that of the T451 specimen at the on-set of plastic deformation overlap one another when the strain exceeds 0.5. This suggests that strain hardening maybe more pronounced in the artificially aged sample at high strain thereby eliminating of the effect of the lower yield strength of the artificially aged specimens. This explains the reason why there is no difference in the engineering strain of the artificially and naturally-aged specimens despite the noticeable difference in their yield strengths.

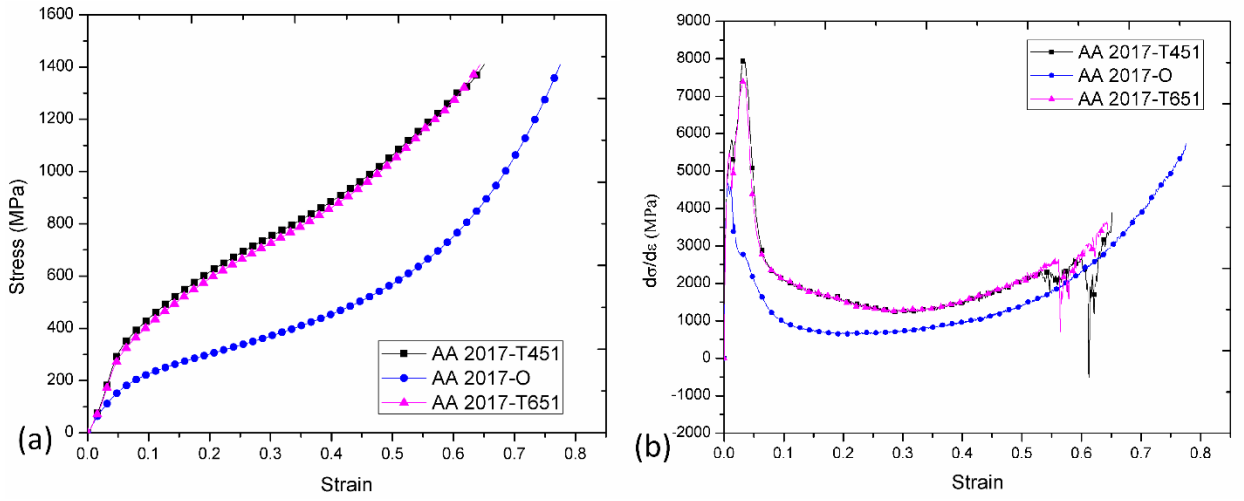

Fig. 4.13. (a) Engineering stress-strain curves and (b) strain hardening rate-strain curve of AA 2017-T451, AA 2017-T651 and AA 2017-O aluminum alloy under quasi-static compressive loading.

The strain hardening curves for the AA 2017 alloy samples are presented in Fig. 4.13b. Strain hardening rate curve for the T451 and T651 specimens overlap except that the former shows more spikes at higher strain than the later. The strain hardening rates for the annealed specimens are consistently lower than those of the other specimens up to a strain of about 0.55 above which spikes are observed in the hardening curves of the age-hardened alloys. The downward spikes observed in the strain hardening curves at higher strain may be due to the effect of recovery whereby dislocation gains sufficient energy to break through barrier. The spikes, which are also signatures of flow softening occurrences in the compressed specimens were observed as sharp discontinuity in the stress strain curves when plotted on an enlarged scale. With this understanding, it could be hypothesized that the tendency to form localized shear strain in compressed specimen is higher in T451 than T651 owing to the more pronounced downward spikes in the former than the later. This will be confirmed from the microstructure of the specimens after quasi-static loading.

AA 2024 alloy

The stress strain curves for the AA 2024 alloy under quasi static loading are presented in Fig. 4.14. The yield strength of the alloy in T351, T651 and O temper are 440, 570 and 130 MPa respectively. Unlike AA 2017 alloy, the yield stress of naturally aged AA 2024-T351 increased substantially upon further artificial aging. These values and trend are in agreement with what was obtained in

hardness test which can be attributed to the fact that the optimum aging condition for this alloy was not attained in the as-received natural aging condition. Therefore, during the artificial aging more coherent precipitates were most likely formed, increasing resistance to slip. As observed in the AA 2017 alloy, there is no significance difference in the total engineering strain developed in AA 2024 alloy in the T351 and T651 temper. The higher deformation in the annealed sample is due low resistance to deformation caused by the absence of strengthening coherent precipitates.

Although the quasi-static stress-strain curves of the AA 2024 (Fig. 4.14a) shows higher yield stress in T651 than T351 specimens, the ability to resist further plastic deformation due to strain hardening becomes higher in T351 than T651 at strain above 0.17. At about 0.43 strain (Fig. 4.14b), the strain hardening of AA 2024-T351 had become lower but increased again at strain above 0.56. Though the strain hardening rates for the annealed specimens are lower than those of the other temper specimens up to a strain of about 0.65, there exists a strain range (about 0.13 to 0.23 strain) where the strain hardening rate of AA 2024-O coincide with the AA 2024-T651 specimen. It could be speculated that the tendency to form localized shear strain in compressed specimen is higher in T351 specimen than T651 and O owing to the absence of downward spike (drop in flow stress) in the curves of T651 and O temper specimens (Fig. 4.14b).

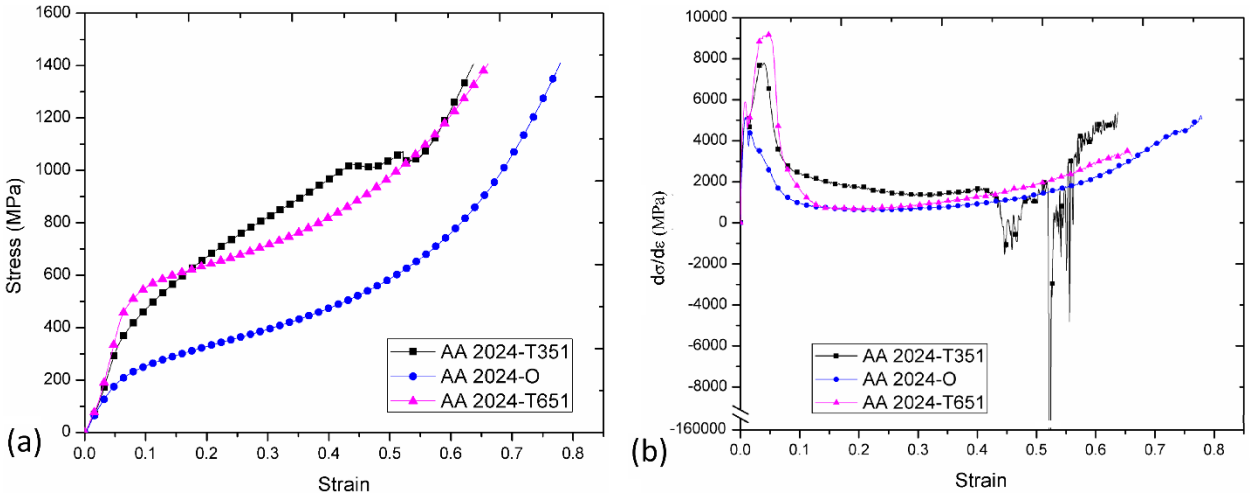

Fig. 4.14. (a) Engineering stress-strain curves and (b) strain hardening rate-strain curve of AA 2024-T351, AA 2024-T651 and AA 2024-O aluminum alloy under quasi-static compressive loading.

AA 2624 alloy

Fig. 4.15a shows the quasi-static stress-strain curve of AA 2624 alloy in T351, T651 and O temper. The yield stress of the AA 2624-T351, AA 2624-T651 and AA 2624-O are 435, 440 and 125 MPa respectively, the trend of which is in agreement with what was obtained in the hardness test. The total engineering strain developed in T351, T651 and O temper were determined to be 0.63 0.62 and 0.78 respectively. This also suggests that the peak stress was not attained by the natural aging and that artificial aging led to formation of more coherent precipitates (Al_2CuMg); leading to higher yield strength of the artificially aged sample. Like AA 2017-O and AA 2024-O, the yield strength of AA 2624-O is lower than AA 2624-T351 and AA 2624-T651 due to the dissolution or coarsening of the fine coherent or semi-coherent precipitates which act as barriers to plastic deformation by slip.

The strain hardening curves for the AA 2624 samples (Fig. 4.15b) indicate that unlike AA 2024 specimens, brief drop in strain hardening rate at higher strain between 0.43 and 0.47 in AA 2624-T351 was not suppressed on the artificial aging. The strain hardening rates for the annealed specimen is lower than those of the other temper specimens except in the strain range 0.43 and 0.47 where spikes are observed in the strain hardening curves of the age hardened alloys. The tendency to form localized shear strain in compressed specimen is higher in both T351 and T651 specimens than O temper owing to the absence of downward spike(s) in the curve of O temper specimens (Fig. 4. 15b).

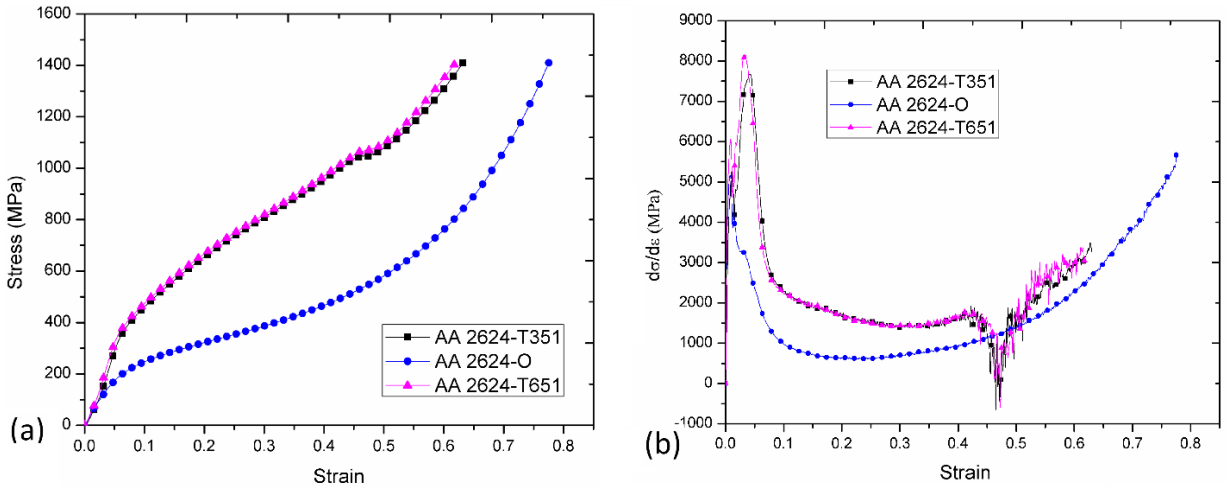

Fig. 4.15. (a) Engineering stress-strain curves and (b) strain hardening rate-strain curve of AA 2624-T351, AA 2624-T651 and AA 2624-O aluminum alloy under quasi-static compressive loading.

Comparison between stress strain curves for the three alloys

Stress strain curves comparing the mechanical behaviour of the three investigated alloys under various temper conditions are presented in Fig. 4.16. The AA 2024 and AA 2624 alloys in naturally-aged condition shows higher yield stresses and strain hardening rate capabilities than the AA 2017 alloy (Fig. 4.16a). The higher Cu and Mg content (and lower Cu to Mg ratio) capable of forming coherent GPB zones and/or S'' precipitates in the naturally-aged condition could be responsible for higher yield strength in AA 2024-T351 and AA 2624-T351 alloys. This is because though both θ and S phases exhibits metallic character, the former is ductile while the latter is brittle [6]. It is therefore, harder for dislocations to move past the S precipitates than the θ precipitates such that alloys comprised of S phases exhibits better mechanical properties than the θ phase ones. Though the strength contribution of second phase particle is minimal, in addition to the presence of Cu, particles in AA 2017-T451 also constitutes higher concentration of Fe, Si and Mn while AA 2024-T351 and AA 2624-T351 constitutes majorly higher concentration of Mg. Therefore, if AA 2024-T351 and AA 2624-T351 shows better mechanical strength than the AA 2017-T451 specimens, it is suggested that the combined strength-contributing effect of Fe, Si and Mn in AA 2017-T451 is lower than the Mg contribution in AA 2024-T351 and AA 2624-T351 specimens.

In the artificial aging condition (Fig. 4.16b), the yield stress of AA 2024 was found to be higher than the yield stresses of AA 2624 and AA 2017. The formation of coherent S'' and/or semi-coherent S' precipitates in the artificially-aged condition could be responsible for higher yield strength in AA 2024-T651 and AA 2624-T651 alloys [37]. Though the AA 2024 has the highest yield strength, the resistance to further plastic deformation became lower at higher strain while the AA 2624 alloy strain hardens the most. Therefore, artificial aging best improve the yield strength and suppress the occurrence of flow softening (localized shear strain) in AA 2024 alloys. The annealing of all as-received naturally-aged AA 2017, AA 2024 and AA 2624 alloys (Fig. 4.16b) shows their yield stresses to be approximately the same and stress-strain curves nearly overlap for all the three alloys. This could be as a result of the formation of stable equilibrium precipitates in all annealed alloys. This confirm that the difference in the strength of the age-hardened alloys is due only to the fine precipitates formed during age-hardening and not to variation in the type of second phase particles formed during solidification. It has also been suggested by other researchers that second phase particles play no major role in the strength of precipitation hardened alloy, but

could be detrimental to mechanical properties by acting as cracking initiation sites [24]. Annealing was observed to best suppress flow softening and the tendency for shear strain localization in the three alloys, but strength becomes compromised.

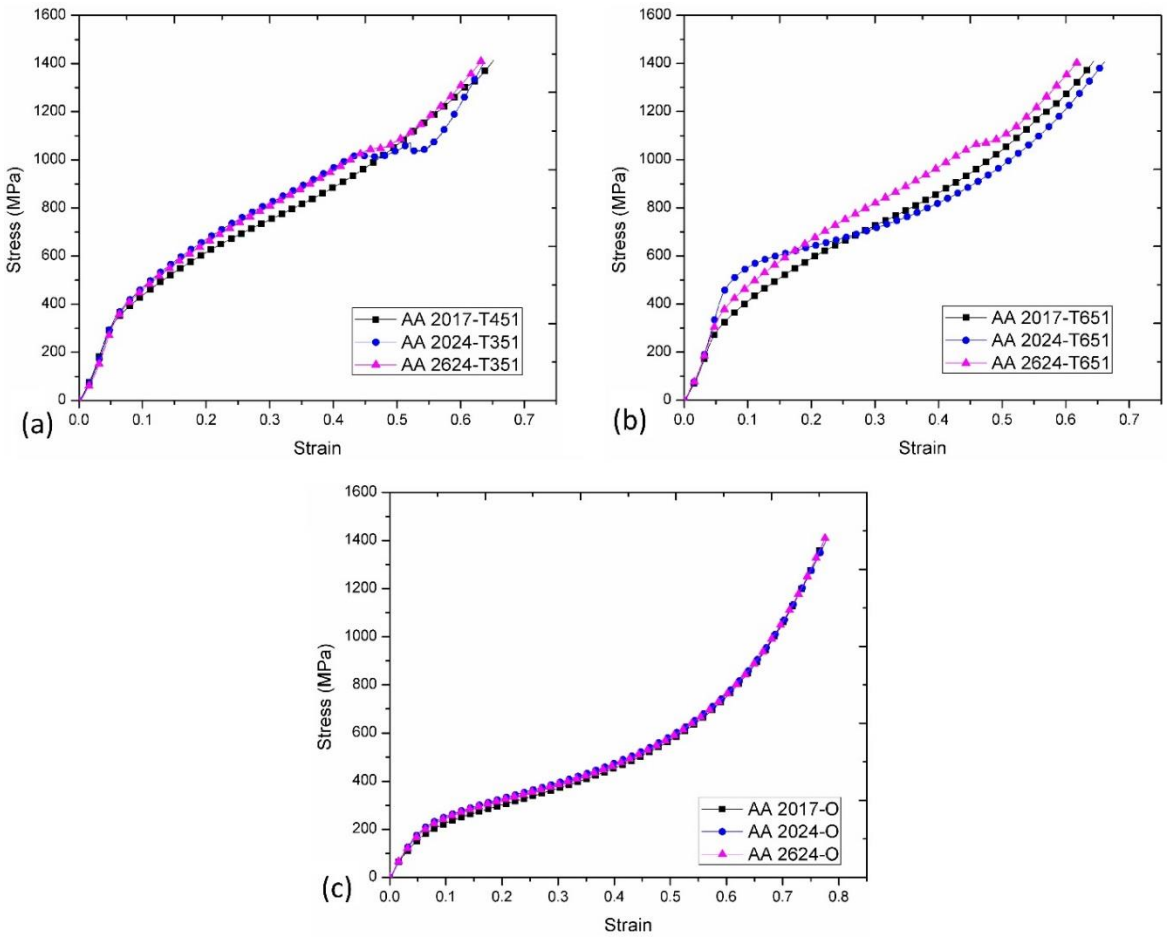

Fig. 4.16. Engineering stress-strain curves of (a) naturally-aged, (b) artificially-aged and (c) annealed AA 2017, AA 2024 and AA 2624 aluminum alloy under quasi-static compressive loading

4.3 Dynamic impact test

The results of the dynamic impact test on the alloys are summarized in Table 4.4 while the obtained dynamic stress-strain curves are presented in Figs. 4.17- 4.19. As the impact momentum increases, the strain rates and the total engineering strain increased in all investigated alloys, though they are function of the temper conditions. As a result of their low mechanical strength, higher strains and strain rates were generated in the annealed specimens than the age-hardened specimens. The flow stresses of annealed specimens under dynamic impact loading are also lower than those of the age hardened alloys. Thermal softening and strain hardening compete during the plastic deformation

process and they determine the maximum peak stress [49]. The dynamic stress-strain curves of the alloys show an initial elastic deformation that is quickly followed by a plastic deformation regime. Two major peaks are observed on the curves. The first peak occurs not long after the yield point and the drop in stress after this peak could be attributed to dislocation gaining sufficient force to break through barriers and gain mobility. This could be as a result of the initial increase in temperature as the impact energy is converted to thermal energy. Eventually strain hardening as a result of increase deformation resulting in dislocation multiplication begins to dominate again leading to an increase in stress to the second peak flow stress. For the purpose of this study, the first and second peak flow stress (PFS) will be referred to as PFS I and PFS II respectively. Occurrence of strain softening immediately after yielding has also been reported in the stress-strain curves of several aluminum alloys during hot deformation [52,54] The post PFS I softening is more pronounced in the annealed specimens than in those that were age hardened.

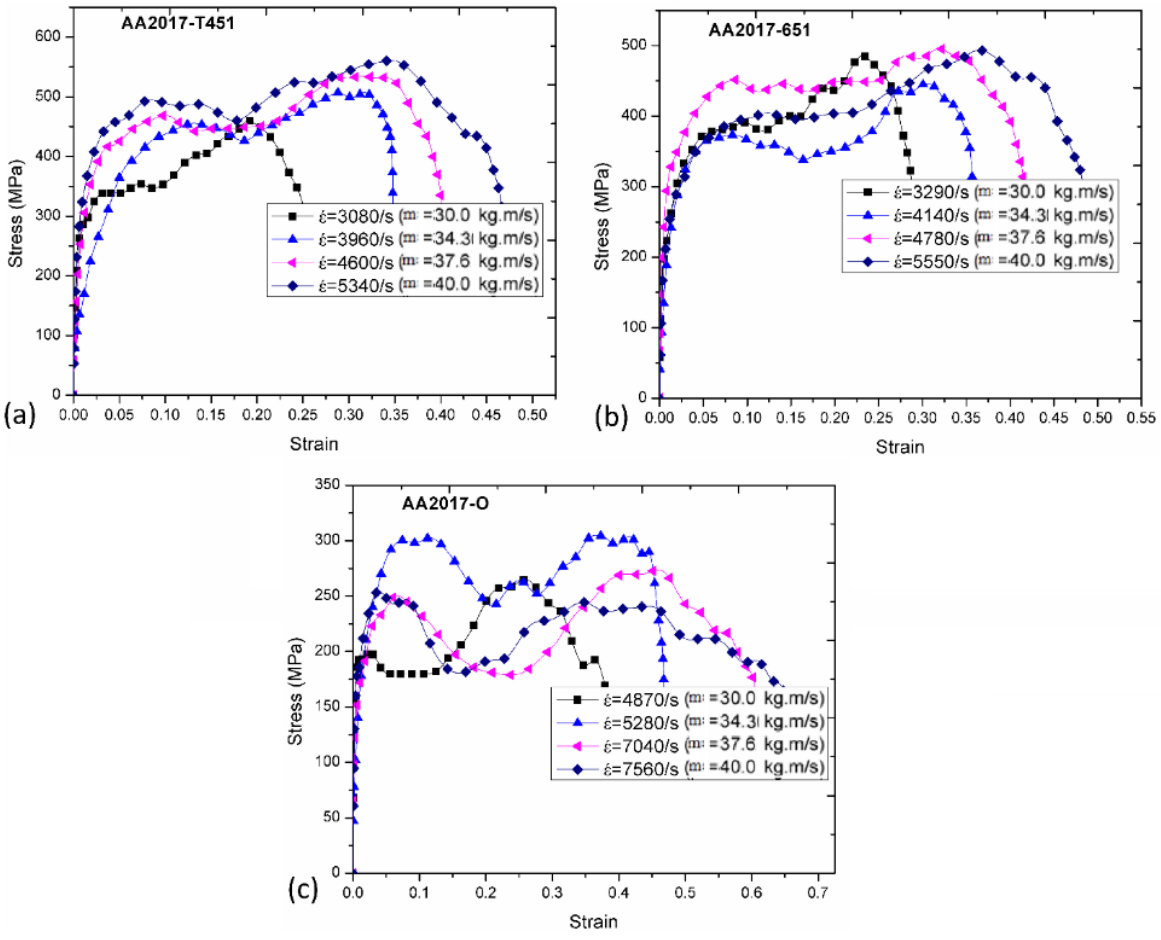

Fig. 4.17. Dynamic stress-strain curves of the AA 2017 alloys in (a) naturally-aged, (b) artificially-aged and (c) annealed condition as a function of impact momentum.

Table 4.4. Mechanical properties of selected aluminum alloys under dynamic shock loading.

Alloy	Temper	IM, kg.m/s	SR, s^{-1}	PFS I, MPa	PFS II, MPa	Eng. Strain
AA 2017	T451	30.0	3080	344	460	0.26
		34.3	3960	456	507	0.34
		37.6	4600	469	532	0.40
		40.0	5340	495	561	0.47
	T651	30.0	3290	391	486	0.28
		34.3	4140	373	446	0.35
		37.6	4780	452	496	0.41
		40.0	5550	404	494	0.48
	O	30.0	4870	198	265	0.43
		34.3	5280	303	305	0.47
		37.6	7040	251	274	0.61
		40.0	7560	254	232	0.68
AA 2024	T351	30.0	2820	430	554	0.23
		34.3	3580	514	587	0.30
		37.6	4230	521	618	0.37
		40.0	5080	536	620	0.43
	T651	30.0	2780	488	527	0.24
		34.3	3690	536	508	0.32
		37.6	4610	537	506	0.40
		40.0	5230	537	504	0.46
	O	30.0	4610	201	245	0.40
		34.3	5640	300	297	0.50
		37.6	6730	257	241	0.59
		40.0	7230	244	263	0.65
AA 2624	T351	30.0	2920	438	551	0.24
		34.3	3600	502	562	0.31
		37.6	4250	516	581	0.37
		40.0	4890	511	601	0.43
	T651	30.0	2810	447	560	0.24
		34.3	3630	483	542	0.31
		37.6	4360	516	589	0.37
		40.0	4970	555	677	0.43
	O	30.0	4750	170	233	0.42
		34.3	6130	275	275	0.53
		37.6	6790	194	245	0.60
		40.0	7570	224	247	0.68

Significant increase in temperature occur in specimens subjected to dynamic shock loading at room temperature, making high deformation rate somewhat similar to hot deformation. About 90% of the impact energy is suggested to convert to thermal energy during dynamic impact loading [50]. The major difference is in the fact that stress-strain curves for hot deformation decreases continuously after yielding until failure; on the other hand, the stress strain curves obtained in this impact study shows a subsequent domination of strain hardening due to dislocation multiplication as deformation proceeds leading to the second peak stress (PFS II). The softening occurring immediately after PFS I can be attributed to dynamic recovery occurring by dislocation annihilation and arrangement by gliding, climbing and cross-slipping after an early dislocation multiplication. Beyond the PFS II, thermal softening dominated the plastic deformation process leading to continuous drop in flow stress as a result of loss of load-carrying capability caused by excessive temperature increase in the specimens. A point of instability is eventually reached, where excessive thermal softening leads to a very sharp drop in flow stress. These sharp drop in flow stress has been attributed to adiabatic heating leading to shear strain localization along the narrow bands called adiabatic shear bands [51,56]. It is evident that the mechanical response of the investigated alloys is largely influenced by the thermal softening occurring as result of temperature increase in the specimens during impact.

The maximum flow stress appear to increase with strain rates for the age-hardened alloys, however the dependency of the deformation process on the complex competition between strain hardening and thermal softening makes a linear relation between maximum flow stress and strain rates unobtainable. Whereas, only AA 2024-T651 specimens show PFS I corresponding to the maximum flow stress with post yield strain hardening not sufficient to raise the flow stress to the level of PFS I before the occurrence of intense localized thermal softening leading to stress collapse. PFS II is the maximum flow stress for all other specimens. All alloys in annealed condition (AA 2017-O, 2024-O and AA 2624-O specimens) exhibits an enhanced plasticity and formability which are characterized by lower strength and higher impact strain.

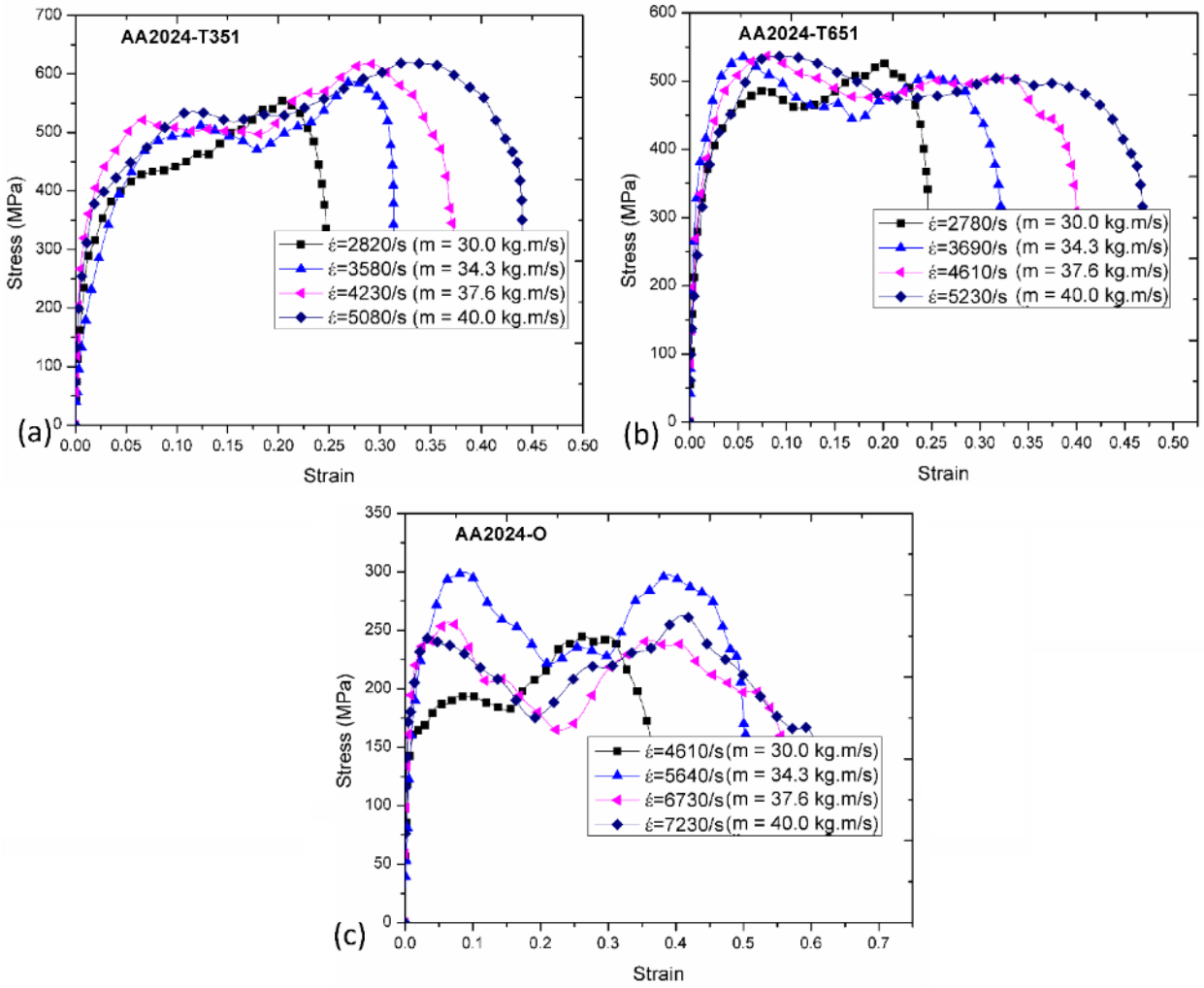

Fig. 4.18. Dynamic stress-strain curve of impacted AA 2024 specimens in (a) naturally-aged, (b) artificially-aged and (c) annealed condition as a function of impact momentum.

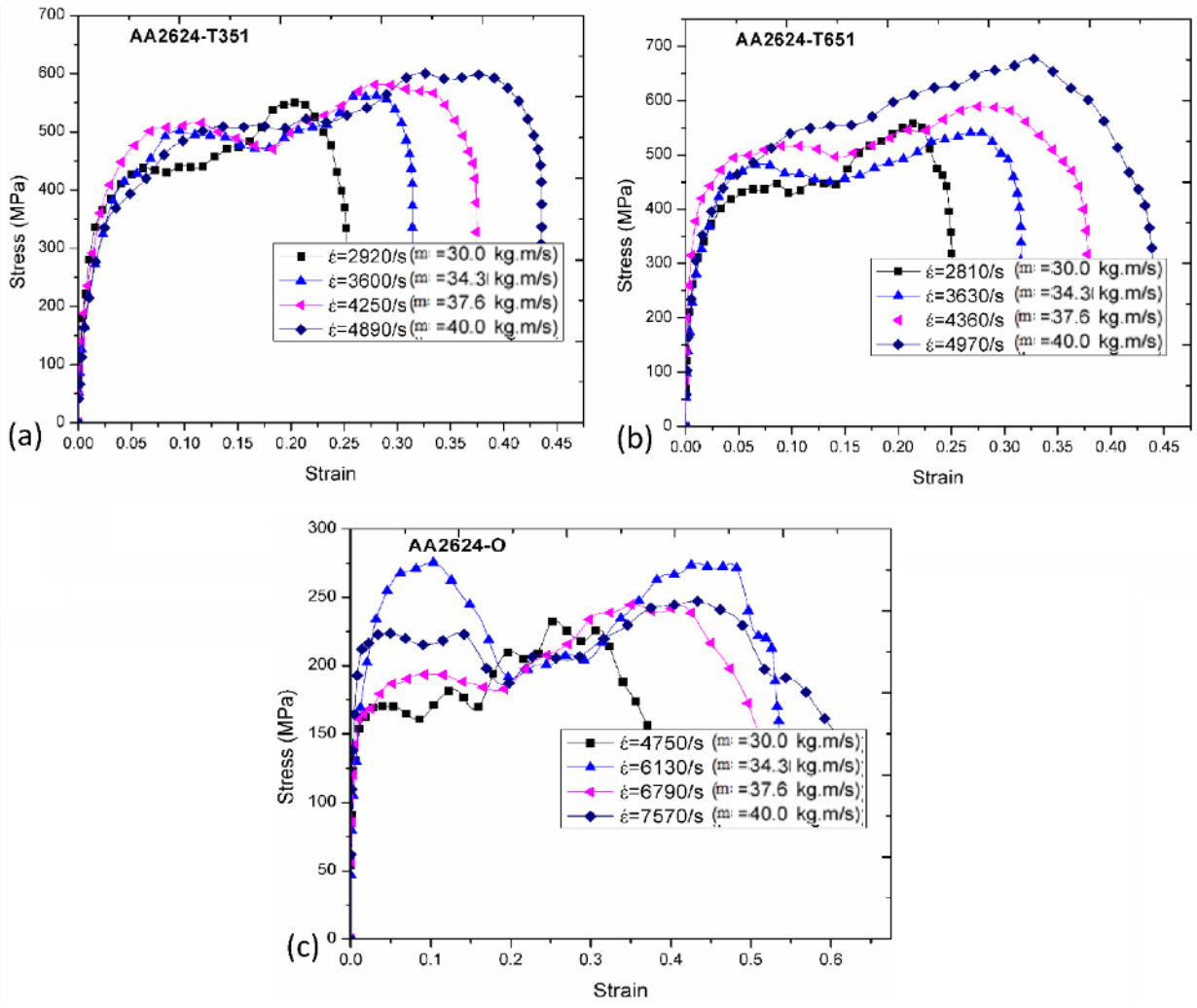

Fig. 4.19. Dynamic stress-strain curve of impacted AA 2624 specimens in (a) naturally-aged, (b) artificially-aged and (c) annealed condition as a function of impact momentum.

Comparison of the mechanical behaviour of the alloys under the same impact load

The mechanical strength of precipitation hardened alloys such as the investigated AA 2000 series aluminum alloys is a function of the nature of the precipitates, especially the coherency of the precipitates with the continuous α-aluminum phase. A change in the nature of the precipitates from coherent or semi-coherent (shearable) to incoherent (non-shearable) affects the resistance of these alloys to deformation [149]. The dynamic stress-strain and hardening curves of the investigated alloys are compared when subjected to the same impact momentum of 40 kg.m/s (Fig. 4.20-4.22). While 2017-T451 and 2624-T651 specimens exhibits superior mechanical strength (both PFS I & II) among the three temper of AA 2017 and AA 2624 respectively, AA 2024 shows better yield strength in T651 specimen and improve maximum peak flow stress in T351 specimen. The

annealed specimens, which have the lowest flow stress, have the highest total strain and deformed at higher strain rates than those of the age-hardened specimens. The reason for better mechanical properties in age-hardened samples could be attributed to the presence of coherent or semi-coherent (shearable) precipitates that have the ability to hinder dislocation motions thereby increasing strength while lower strength in annealed samples are attributed to the dissolution and coarsening of incoherent (non-shearable) S precipitates [147,150].

The strain hardening curves in Figs. 4.20b-4.22b shows that strain hardening rate drops below zero in all alloys and temper conditions, though at different strain. While the strain hardening rate drops below zero earliest in annealed (lower strength) samples at low strain, the strain hardening rate of age-hardened specimens with the highest PFS II tend to drop below zero (thermo-mechanical instabilities) first at higher strain. It could be therefore concluded based on the aforementioned observation that the higher the PFS II of dynamic impacted samples (irrespective of the alloy), the earlier the tendency of thermomechanical instabilities (thermal softening). The absence of hump in the stage III (see Fig. 2.5 for stages) in hardening curve is an indication that twinning activities are absent and deformation are rather controlled by slip in the alloy during impact [82]. Khan et. al [81] reported the absence of peak (i.e. hump-free) in the hardening curve of compressed AZ31 sheet alloy which they attributed to the non-dominant of twinning as the mechanism of deformation. The drop in the hardening curve below zero on majorly two occasions (at low and high strain levels) confirms that the investigated alloys are alloys which possess dual-peaks in their respective dynamic stress-strain plots.

To better understand the influence of major alloying elements or Cu:Mg content on the dynamic response of the AA 2017, AA 2024 and AA 2624 alloys, the stress-strain curves of the alloys in the three temper are co-plotted for specimens impacted at 40.0 kg m/s (Fig. 4.23). The mechanical strength of the alloys with low Cu:Mg (AA 2024 and AA 2624) are higher than those with high Cu:Mg alloys (AA 2017) in both age-hardened samples. While θ phase is an important strengthening phase in the AA 2017 alloy with high Cu:Mg, *S* phase is the strengthening phase in the AA 2024 and AA 2624 alloys with low Cu:Mg [151]. Furthermore, it was earlier mentioned that *S* phases are better strength-contributing precipitates than θ phase due to the brittleness of the former than the later [6]. It is therefore suggested that the higher mechanical strength in age-hardened AA 2024 and AA 2624 alloys are attributed to the formation of coherent GPB zones and/or S'' precipitates (Al_2CuMg) and perhaps the Mg-rich second phase particles (Table 4.2).

This confirms the strength-contributing prowess of Mg in 2000 series aluminum alloys. In Fig. 4.23b, the ability to resist further plastic deformation is lowered in AA 2024-T651 alloy thereby having an approximately equal PFS II with the AA 2017-T651. Annealed samples (Fig. 4.23c) which exhibits comparable mechanical response in all alloys show relatively deeper inflection point on the stress-strain curve before strain hardening up to the PFS II.

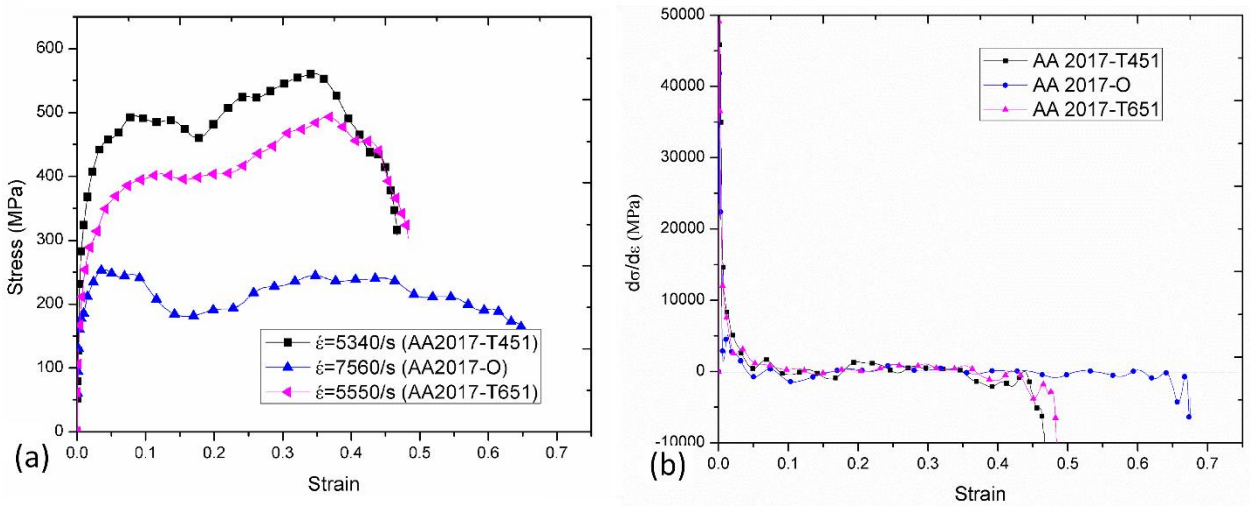

Fig. 4.20. (a) Dynamic stress-strain curve and (b) strain hardening rate-strain curve of AA 2017-T451, AA 2017-T651 and AA 2017-O aluminum alloy subjected to an impact momentum of 40 kg.m/s.

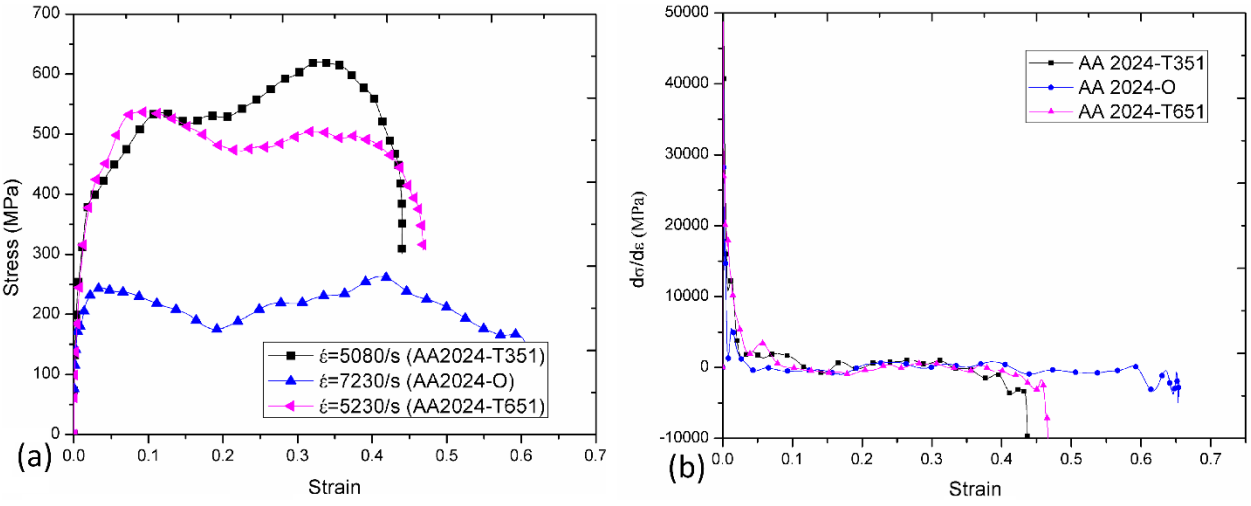

Fig. 4.21. (a) Dynamic stress-strain curve and (b) strain hardening rate-strain curve of AA 2024-T351, AA 2024-T651 and AA 2024-O aluminum alloy subjected to an impact momentum of 40 kg.m/s.

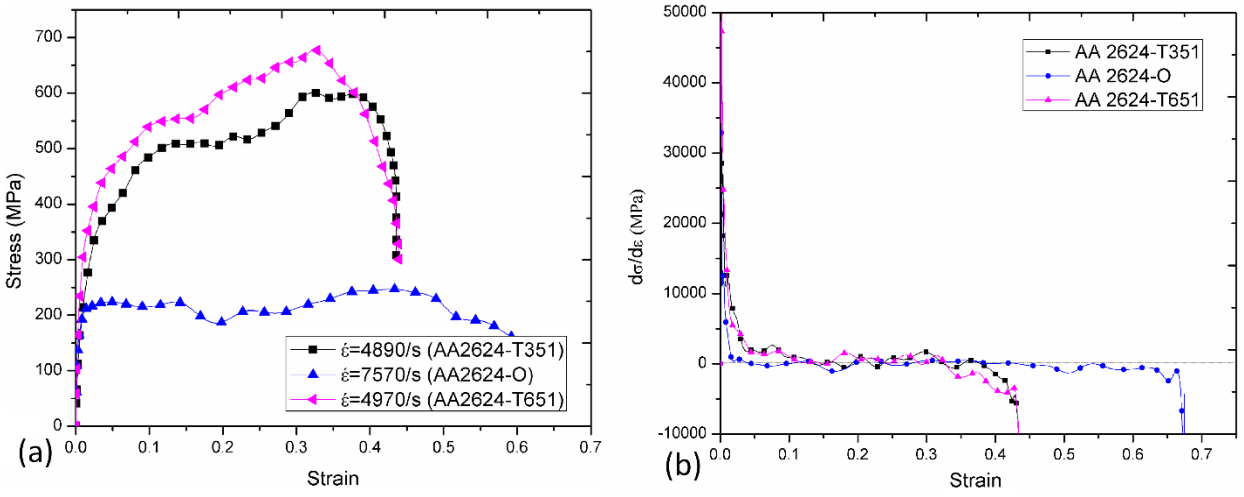

Fig. 4.22. (a) Dynamic stress-strain curve and (b) strain hardening rate-strain curve of AA 2624-T351, AA 2624-T651 and AA 2624-O aluminum alloy subjected to an impact momentum of 40 kg.m/s.

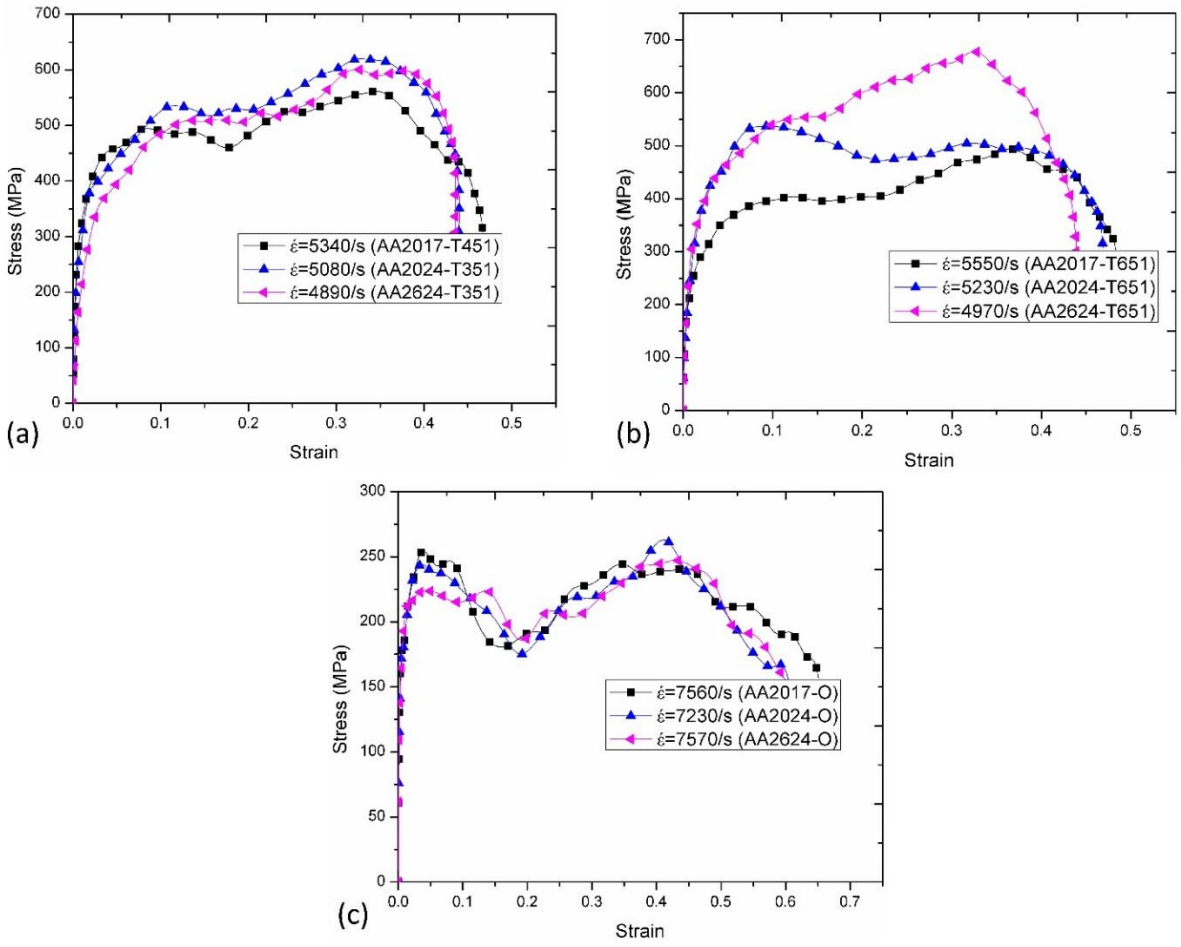

Fig. 4.23. Engineering stress-strain curves of (a) naturally-aged, (b) artificially-aged and (c) annealed AA 2017, AA 2024 and AA 2624 aluminum alloys under dynamic impact loading.

In conclusion to this section, a prior study on hot deformation of AA 6082 aluminum alloy where a single yield peak was obtained in the stress strain curve, Zhang and Baker [55] observed the amount of post-yield softening to be higher in T4 temper than in annealed (O temper) condition. The authors attributed higher post yield softening in the AA 6082-T4 to higher tendency of the T4 specimen to experience dynamic recrystallization in comparison to the annealed specimen whose level of supersaturation is low. This is contrary to what was observed in post-yield softening of all the three aluminum alloys under dynamic impact loading in this study. From the experimental data, yielding was observed to occur within the first 80 microseconds after the start of deformation in the three temper conditions. The temperature reached at this stage and the time ruled out the possibility of dynamic recrystallization and particle coarsening during the dynamic shock loading of the selected aluminum alloys. Rather, the temperature and time reached in the post-PFS II softening in this study, postulates dynamic recrystallization possibilities. Unlike hot deformation where temperature of the specimen is assumed to be relatively uniform throughout the deformation period (ignoring any temperature increase due to deformation), temperature of the impacted aluminum alloy specimens in this study increases from ambient temperature to the peak temperature beyond the maximum flow stress (PFS II). The lower relative softening of the annealed alloy specimens beyond the second peak (PFS II) can be attributed to their lower tendency to experience intense adiabatic heating leading to stress collapse and adiabatic shear banding as will be discussed in the next section.

4.4 Microstructural evolution in AA 2017, AA 2024 and AA 2624 aluminum alloys during mechanical loading

4.4.1 Quasi-static compression

Fig. 4.24 shows the microstructural features of an AA 2017-T451 specimen after quasi-static compressive loading. Circular region of localized deformation (deformed band) is observed close towards the edge of the circular cross-section of the specimen. The arrangement of the second phase particles inside and outside deformed band region on the compression plane (Fig. 4.24a) suggests that deformation was inhomogeneous. While the particles in the core (outside shear band region) of the specimen are like the morphology of particles in the microstructure of an un-deformed sample (Fig. 4.2a), evolved shear band shows elongated particles structure arranged in layers in a circular fashion near the edge. The deformed band

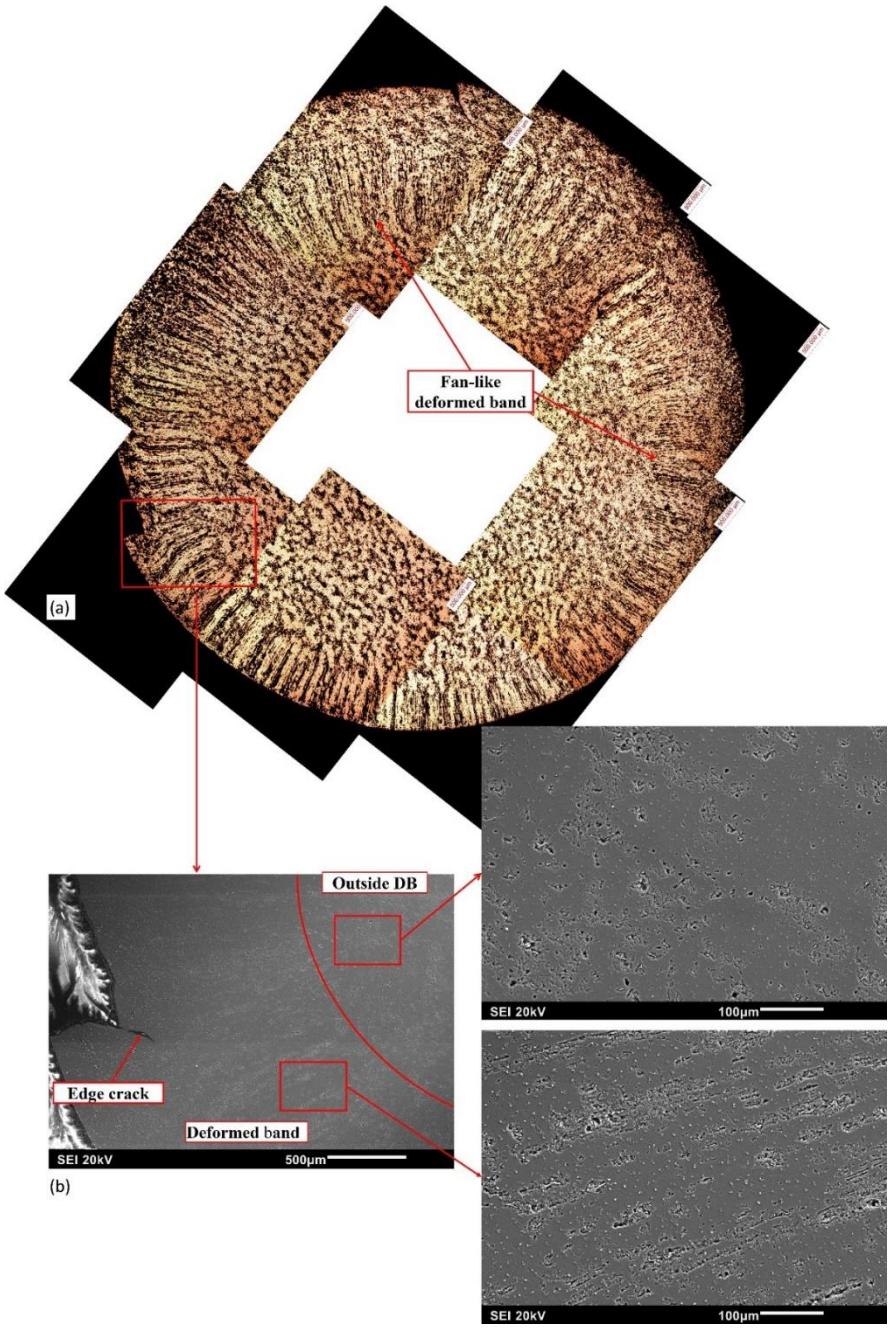

Fig. 4.24. (a) Optical micrographs showing shear band geometry and (b) SEM micrographs showing edge crack and distribution of second phase particles inside and outside shear bands on the compression plane of AA 2017-T451 specimen after quasi-static loading.

(Fig. 4.24b) shows more closely packed elongated particles in such a manner that makes the entire compression plane appear fan-like (Fig. 4.24a). Cracks were observed to initiate from the edge, propagate first into the specimen, and detour in the direction of the deformed band when they reach the shear band region. Equiaxed grain structure outside deformed band region, elongated grains

and particles inside deformed band and the initiation of edge cracks were observed in the artificial aged AA 2017-T651 specimen (Fig. 4.25). Partly dissolved particles self-organizes themselves at the crack front (Fig. 4.25a), therefore suggesting the key role particles play in crack propagation within a deformed specimen. Although deformed bands with elongated and aligned second phase particles were also observed in the AA 2017-O specimen (Fig. 4.26), no evidence of edge cracking in the annealed specimens was observed.

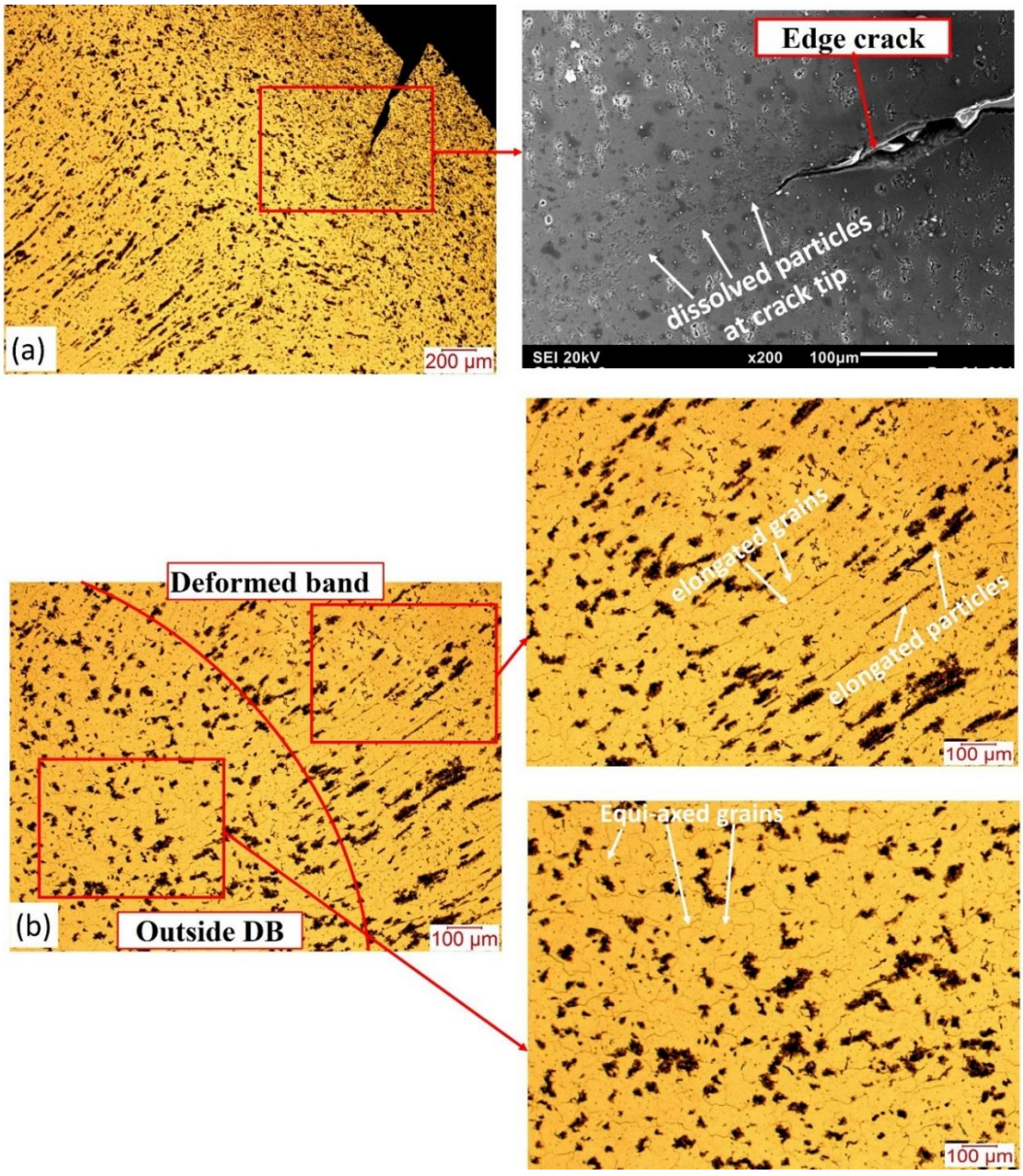

Fig. 4.25. Optical and SEM micrographs showing (a) edge crack and (b) inside and outside deformed band on the compression plane of AA 2017-T651 specimen under quasi-static loading.

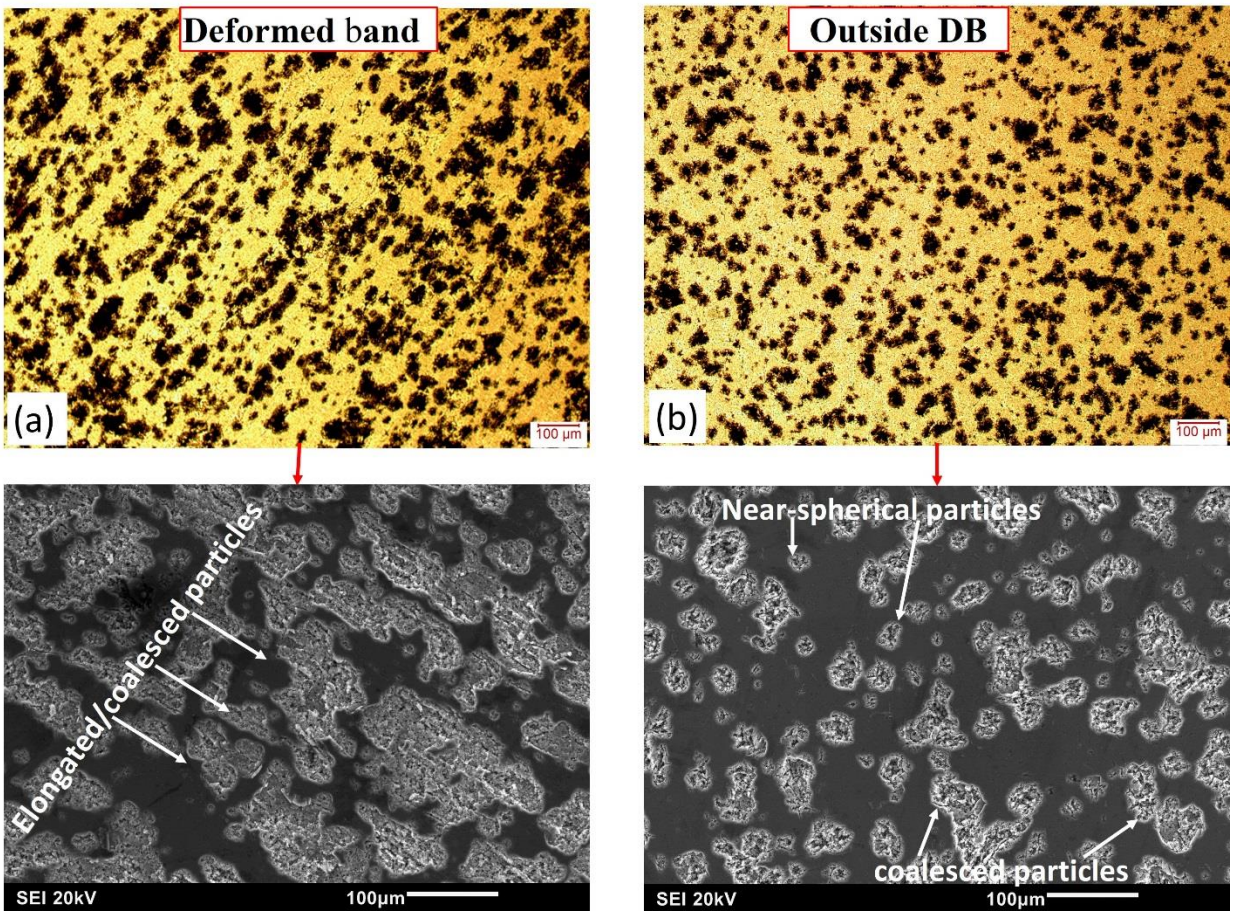

Fig. 4.26. Optical and SEM micrographs showing (a) deformed and (b) outside deformed band on the compression plane of AA 2017-O specimen under quasi-static compression.

Deformed bands with similar morphologies as observed in the age-hardened AA 2017 alloy were also observed in the compression plane of AA 2024-T351 alloys after quasi-static compressive loading (Fig. 4.27). Strain localization leading to formation of shear band is observed to be more severe in the A 2024-T351 specimens with regions of the band having features similar to the transformed shear bands commonly observed in alloys exposed to dynamic impact loading (Fig. 4.27b). The dissolution of second phase particles observed within this region suggests an appreciable temperature rise in the specimen. Like dynamic impact test where about 90 % of impact energy are converted to heat in the deformed specimen, heat generated in this sample under quasi-static compression (though far lower than that obtained in a dynamic test condition) may also be due to higher flow stress and hardening rate of AA 2024-T351 sample. Equation 2.9 had shown that higher flow stress results in higher plastic work of deformation which in turn increases specimen's temperature (Eq. 2.8). The hardening curve of AA 2024-T351 in Fig. 4.14 had earlier

shown severe softening occurring between 0.43 and 0.56 strain. It is therefore suggested that shear strain localization in compressed AA 2024-T351 (Fig. 4.27) began at about 0.43 strain. Zhu et al [99] had earlier observed localized shear strain region in Ti-Fe ultrafine eutectic under quasi-static compression. They attributed the formation of lamella structure in the shear band to subgrain rotational mechanism; a revised form of rotational mechanism illustrated and explained in sub-section 2.7.2.1. Artificial aging (T651) of the AA 2024-T351 alloy reduced the severity of strain localization and cracking susceptibility (Fig. 4.28). The deformed band observed in AA 2024-T651 is not well developed and with no edge crack. The absence of edge crack can be attributed to the low hardening rate in this specimen as observed in its stress strain curves in which unlike AA 2024-T351, hardening curve of AA 2024-T651 in Fig. 4.14 shows no form of mechanical instability (softening) at higher strain.

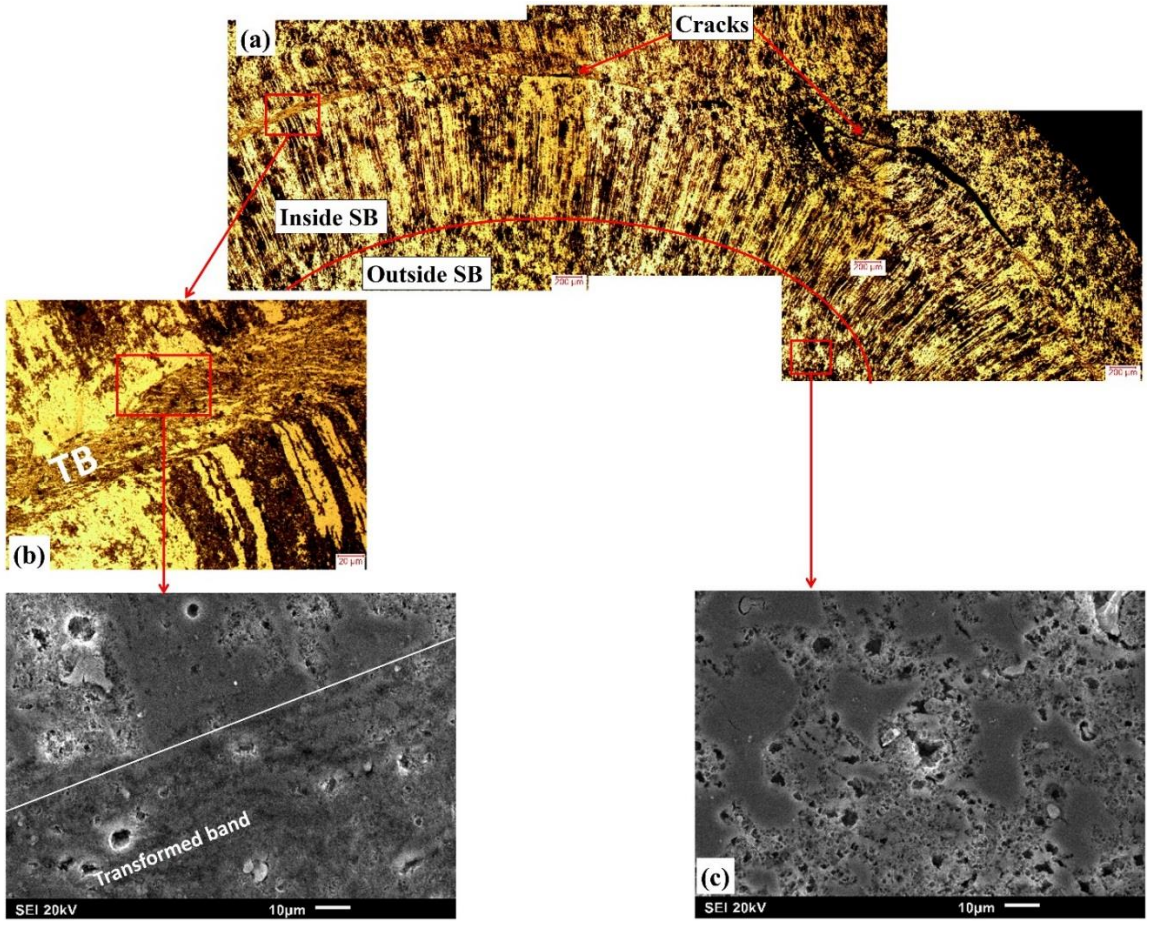

Fig. 4.27. Optical and SEM micrographs showing microstructural features inside and outside shear bands in AA 2024-T351 alloy after quasi-static loading in compression (a) overview of shear deformed band (b) transformed band (c) outside shear band.

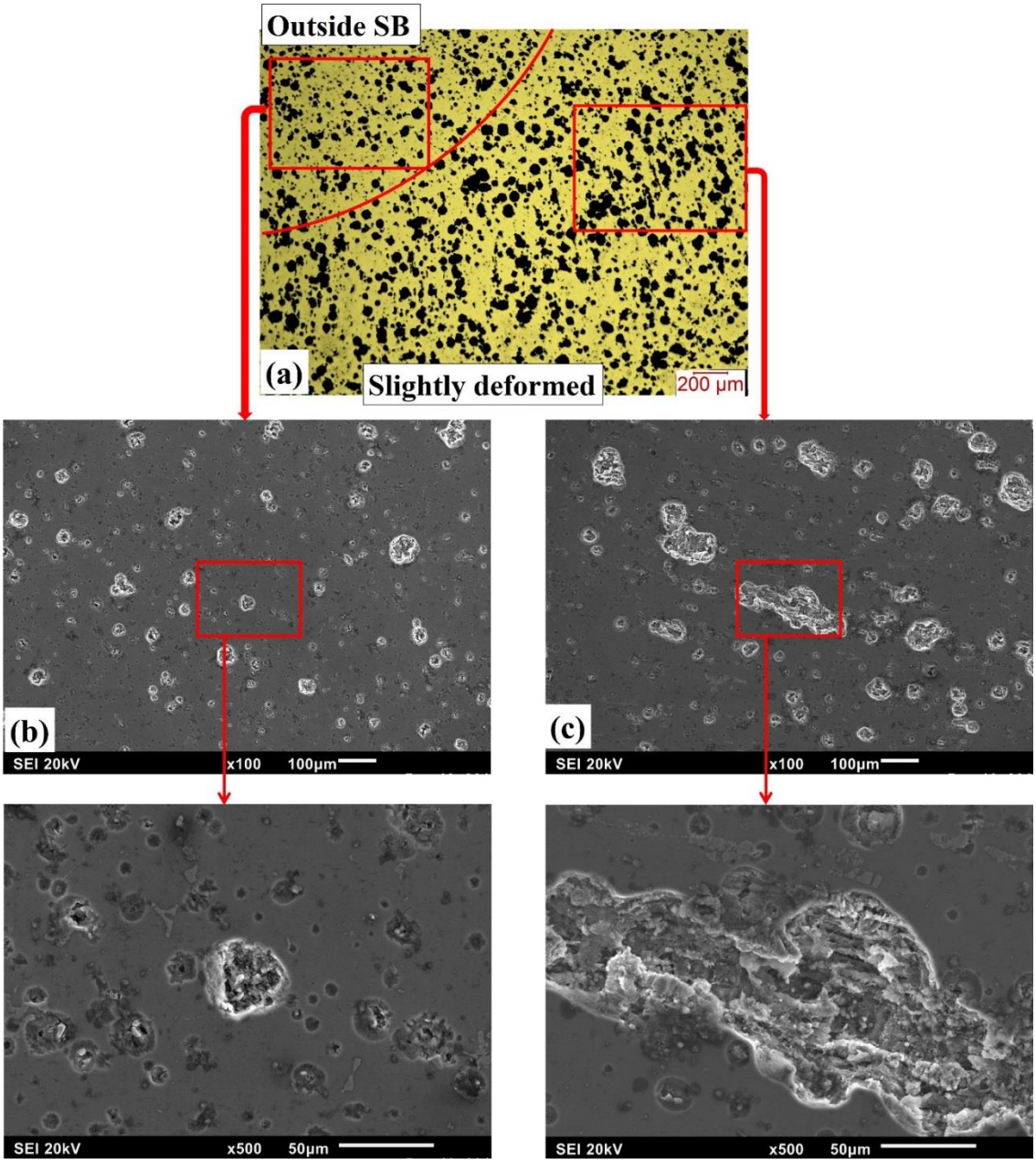

Fig. 4.28. Optical and SEM micrographs showing microstructural features inside and outside shear band in AA 2024-T651 specimen after quasi-static loading in compression (a) overview (b) outside shear band (c) deformed band region. No edge crack was observed.

Beside the equiaxed and elongated grain structure observed on the outside and inside deformed band respectively (Fig. 4.29), edge cracking was observed in the AA 2024-O specimen after quasi-static compressive loading. The edge cracks were unexpected owing to the fact that the annealed specimen is characterized by low hardness (Fig. 4.12), low yield strength and high plasticity (Fig. 4.14). A major explanation for this 'strange' behavior may be due to high strain hardening

observed in the annealed alloy at strain levels above 0.7 on its stress-strain and hardening curves (Fig. 4.14). The high hardening rate at high strain would have improved the mechanical strength.

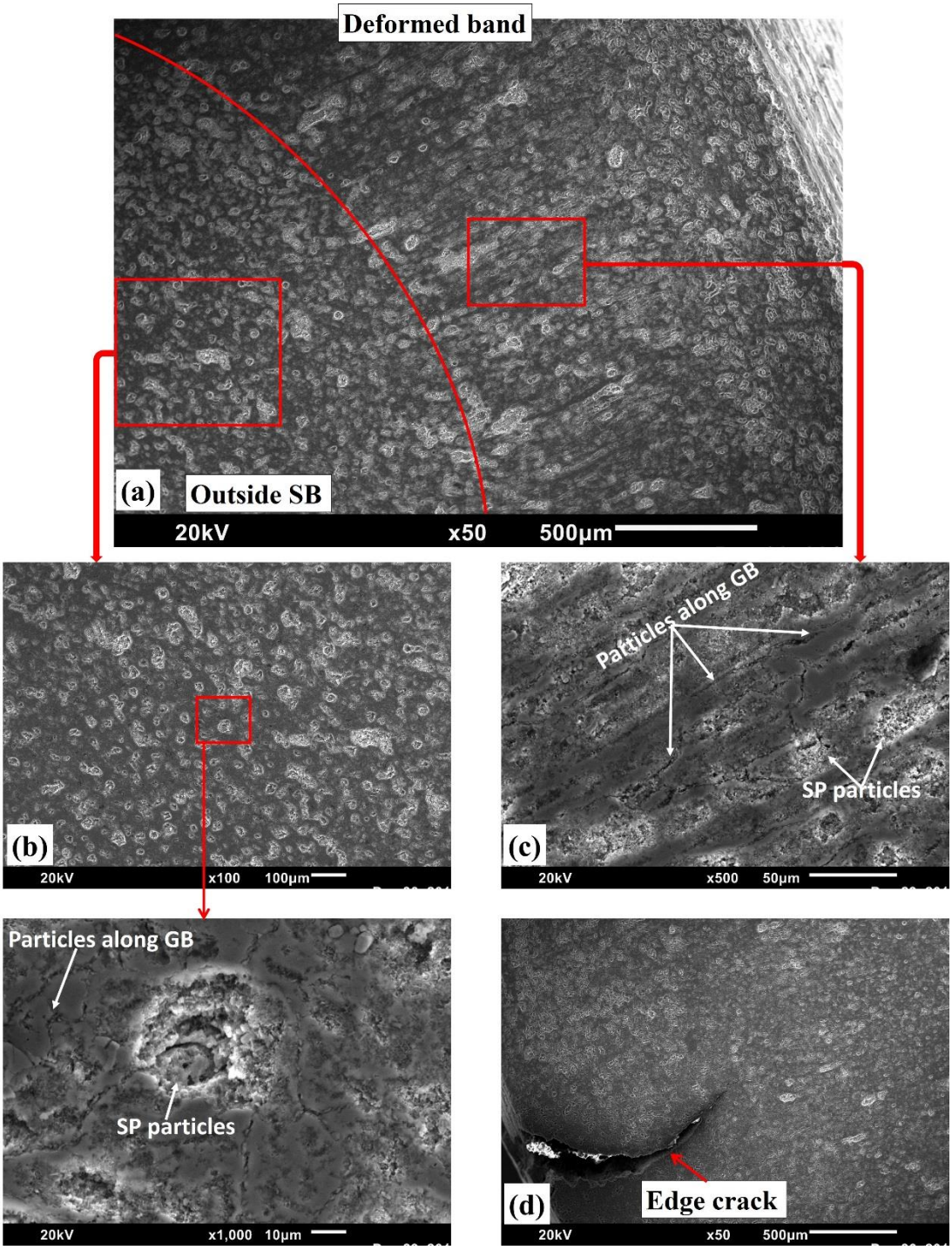

Fig. 4.29. SEM micrographs showing microstructural features inside and outside shear band in AA 2024-O specimen after quasi-static loading in compression (a) overview (b) outside shear band (c) deformed band region (d) edge crack.

of the annealed specimen thereby enhancing its susceptibility to cracking. The strain hardening rate of annealed sample had slightly exceeded that of AA 2024-T651 specimen above the 0.7 strain. At about 0.73 strain, a slight drop in the hardening curve of AA 2024-O was observed. This suggests that hardening rate of the alloy can play a role in determining its susceptibility to crack initiation during quasi-static compressive loading.

The microstructural evolution in AA 2624-T351 specimen under quasi-static compressive loading is documented in Fig. 4.30. Unlike AA 2017 and AA 2024 alloys in which deformation was observed to be inhomogeneous due to presence shear band irrespective of temper conditions, optical micrograph (Fig. 4.30a) of AA 2624-T351 shows that deformation is relatively homogenous since there was no evidence of shear band formation in the deformed specimens. The specimens were however observed to crack from the edge during the quasi-static compressive loading. Higher magnification micrographs (Fig. 4.30b) on the compression plane shows that the lamella structure of particles had become distorted outside crack region (Fig. 4.30a) while tree-like edge crack was observed to have propagated along nearby particles (Fig. 4.30c). It is evident from the microstructure of the AA 2624-T651 after quasi-static loading in compression that artificial aging of the alloy to T651 temper increases the susceptibility to shear band formation and edge cracking that eventually detour along the band (Fig. 4.31). Although AA 2624-T351 specimen shows only edge crack evolution on compression and AA 2624-T651 shows both shear band and edge crack evolution, AA 2624-O (Fig. 4.32) shows high viscous flow shear band with no evidence of edge crack. With an appreciable reduction in inter-particle spacing in AA 2624-O specimen, Fig. 4.32a revealed elongated particles outside shear band region (Fig. 4.32b) and distorted or wavy particles along the shear flow direction (Fig. 4.32c). It is therefore also suggested that age-hardened AA 2624 alloy (T351 and T651) with higher hardness value (Fig. 4.12), higher yield strength and strain hardening rate (Fig. 4.15) are more prone to edge crack than AA 2624-O specimen. It could therefore be speculated that the formation of shear band in the three alloys (AA 2017, AA 2024 and AA 2624) under quasi-static compression can be attributed to concentrated plastic strain since the temperature rise in compressed specimens is far lower compared to that required for ASB formation in specimens under dynamic shock loading conditions.

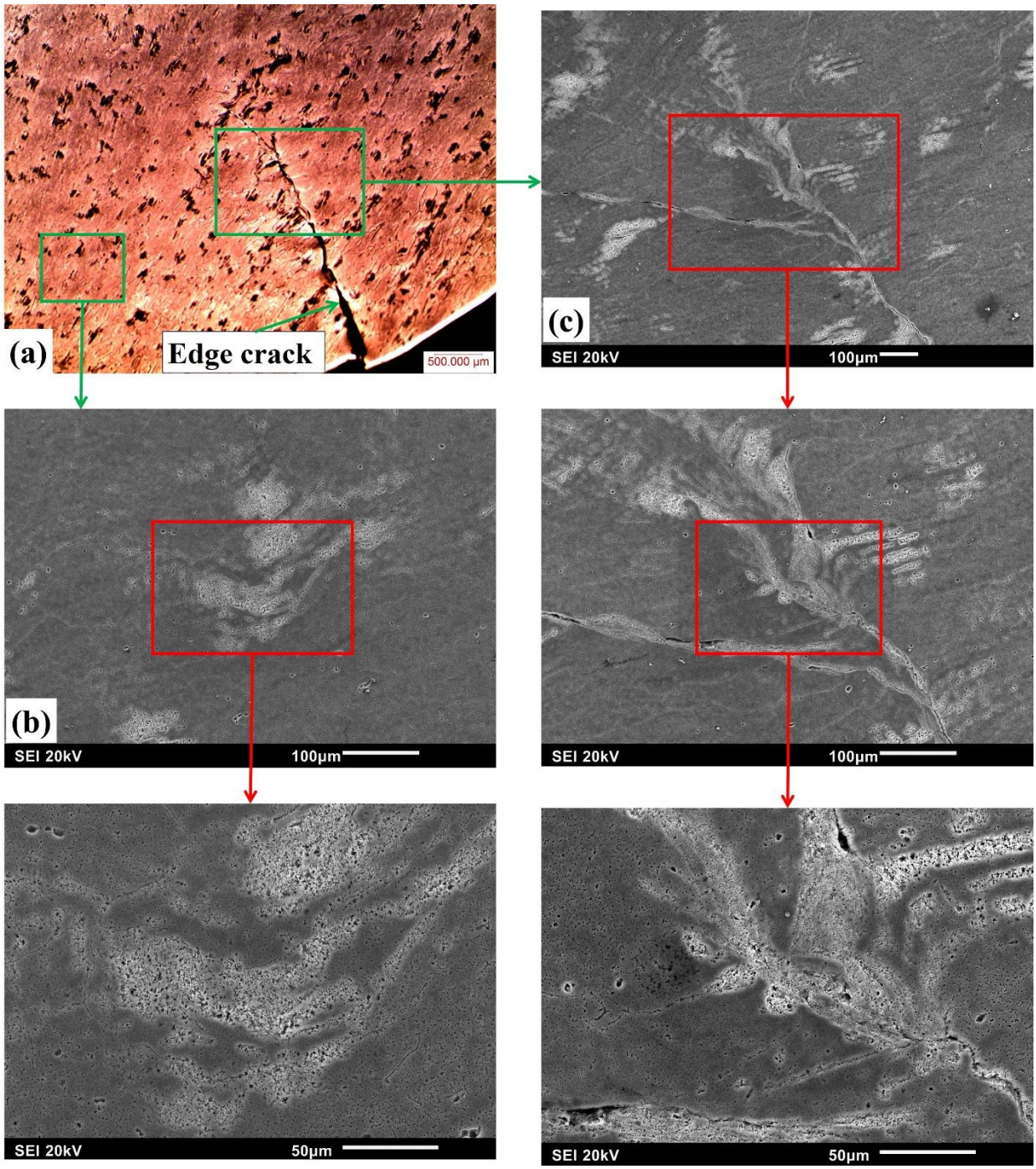

Fig. 4.30. Optical and SEM micrographs showing microstructural features on the compression plane of AA 2624-T351 specimen after quasi-static loading (a) overview (b) outside crack region (c) edge crack.

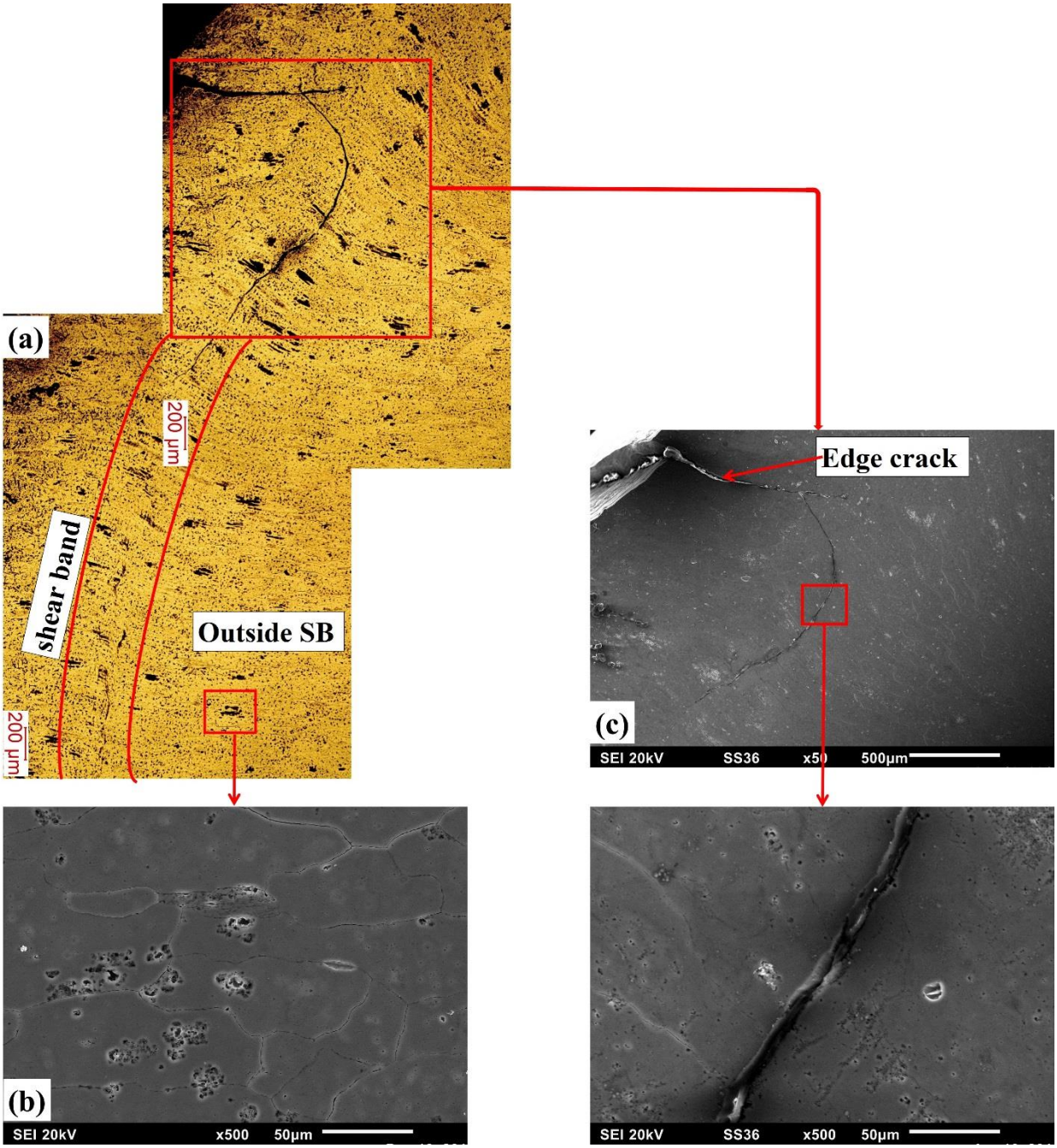

Fig. 4.31. Optical and SEM micrographs showing microstructural features on the compression plane of AA 2624-T651 specimen after quasi-static loading (a) overview (b) outside shear band region (c) edge crack.

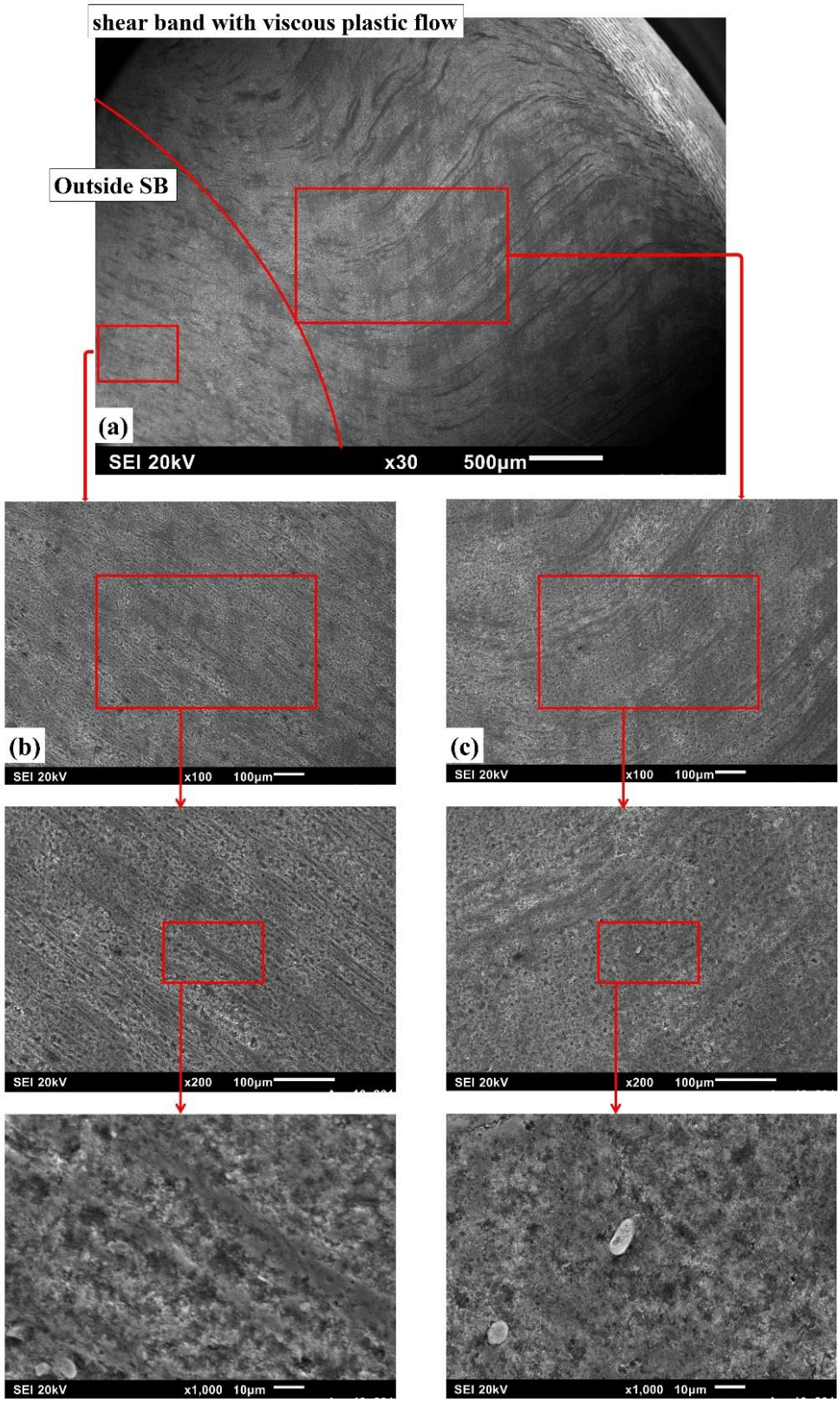

Fig. 4.32. SEM micrographs showing microstructure of AA 2624-O specimen after quasi-static compressive loading (a) overview, (b) outside deformed band (c) inside deformed band.

4.4.2 Dynamic Impact Loading

Experimental data sheet for the dynamic impact test of the investigated alloy specimens showing critical values at which shear bands are formed are presented in Table 4.5. Deformation were relatively homogeneous (no band formation) for all the specimens at lower applied impact momentums of 30 and 34.3 kg.m/s. At higher momentums, deformed and/or transformed bands were observed in some specimens. It has been suggested that transformed bands develop from deformed bands which first form as the severity of strain localization increased in materials under dynamic impact loading [48].

Table 4.5. Experimental data sheet showing the critical values at which ASBs are formed in the dynamic impacted specimen of the selected aluminum alloys.

	AA 2017			***AA 2024***			**AA 2624**		
	T451	**T651**	**O**	***T351***	***T651***	***O***	**T351**	**T651**	**O**
IM, kg.m/s at the onset of DB	40.0	37.6	40.0	*37.6*	*37.6*	*40.0*	40.0	37.6	41.5
Critical strain for DB	0.47	0.41	0.68	*0.37*	*0.40*	*0.65*	0.43	0.37	0.72
Critical SR, s^{-1} for DB	5340	4780	7560	*4230*	*4610*	*7230*	4890	4360	8010
IM, kg.m/s at the onset of TB	41.5	41.5	No TB	*40.0*	*44.4*	*No TB*	41.5	40.0	No TB
Critical strain for TB	0.53	0.54	No TB	*0.43*	*0.60*	*No TB*	0.47	0.43	No TB
IM, kg.m/s at fracture	42.6	43.6	No fracture	*42.0*	*47.9*	*No fracture*	42.0	42.0	No fracture

The conditions (impact momentum, strain and strain rates) at which deformed or transformed bands were first observed in the deformed specimens, as the impact momentum was raised, varied depending on the alloy composition and the temper condition. These dynamic loading conditions give an indication of the propensity of the alloys to develop adiabatic shear bands and eventually fail. Other researchers have suggested the existence of critical strain and strain rates required for occurrence of adiabatic shear bands in other metallic alloys [72]. In all the three alloys the annealed

specimens showed the least tendency for formation of adiabatic shear bands. Previous study by Xue et al. [121] showed that there is higher sensitivity to ASB initiation in austenitic stainless steel (AISI 304L) than the annealed steels. The authors attributed the lower tendency for ASB formation in the annealed specimen to softening and low dislocation density in constituent grains. Similarly, In another separate findings, multiple ASBs was reported in AA 7075-T73 aluminum alloy [86]. The authors observed that no ASB was formed in the annealed specimen (AA 7075-O) despite been subjected to same loading condition with the AA 7075-T73 specimen; a behavior they attributed to low mechanical strength and higher adiabatic shearing energy barrier in the annealed specimen. While no transformed bands was formed in any of the annealed specimens in this study, deformed band was not observed until the impact momentum was increased to 40.0 kg.m/s (7560 /s), 40 kg.m/s (7230 /s) and 41.5 kg.m/s (8010 /s) for AA 2017, AA 2024 and AA 2624 alloy respectively. This suggests that the AA 2624 has the least tendency to form shear bands in the annealed temper condition. Both deformed and transformed bands were observed in the impacted age-hardened alloys depending on the strain rates. In the naturally-aged temper, the AA 2017 and AA 2624 alloys showed the least tendency to develop both deformed bands and transformed bands. Artificial aging of the alloys make the AA 2624 more susceptible to formation of deformed bands than AA 2017 and AA 2024. The tendency for the deformed band to develop to transformed bands is higher in the artificially aged AA 2624 alloy which could be attributed to its improved mechanical strength at this temper.

The formation of shear band in impacted specimen often occur in a very short time and therefore imposes great difficulties on observing the damage evolution during deformation without a high speed camera. Therefore, a viable alternative to revealing damage evolution in the material during such rapid deformation is to investigate the microstructure of the materials after deformation. This will be quite helpful in understanding the deformation process since deformed structures are closely related to deformation process [57,61,63]. The microstructures of the impacted alloy showing deformed and transformed bands are presented in Figs. 4.33-4.35. Whereas the deformed bands consist of elongated grains and alignment of second phase particles in shear flow direction, the transformed bands consist of unique microstructures that suggest particle dissolution inside the transformed bands during formation. Detailed discussion on the geometry and microstructural features of the both bands will be discussed in the subsequent subsections.

4.4.2.1 Shear band geometry in dynamic impacted specimen

To better comprehend the full geometry, shear band geometry on the compression plane (transverse section) and the longitudinal planes were examined. The combination of shear band overview on the compression and longitudinal plane will therefore give the shear band geometry in the entire impacted sample.

Shear bands' geometry on the compression (transverse section) plane

The ASB formed in both the alloys rolled into cylindrical rods during processing (AA 2017 and AA 2024) are circular on the compression plane of the impacted specimen. Specimens from the two alloys maintain their cylindrical shape after impact. Fig. 4.33 shows the geometry of transformed band on the compression plane of AA 2017 alloy in T451 and T651 temper. No bifurcation of shear bands was found along the circular band on the compression plane of AA 2017-T451 sample (Fig. 4.33a). Similar observation was made on the compression plane of other aluminum alloys such AA as 6061-T6 [88] and AA 7075 [57] subjected to dynamic impact loading. The same circular geometry of adiabatic shear bands were observed on the compression plane of the impacted AA 2017-T651, but unlike the AA 2017-T451 sample, bifurcation of ASBs was observed as shown in Fig. 4.33b. Cracks were observed to propagate along the transformed bands in the AA 2017 alloy.

In the AA 2024 alloy, circular transformed band without bifurcation was also observed in the T351 temper (Fig. 4.34a). As in the case of AA 2017, the dynamic impact of artificially-aged AA 2024 alloy results in bifurcation of shear band (Fig. 4.34b). Yang *et al.* [85] speculated that bifurcations in AA 7075 aluminum alloy, which was deformed using thick-walled cylinder explosion technique, were formed when the propagation of a shear band is hindered by the presence of some active barriers such as impurities, precipitate phase particles and other possible defects that increased the resistance and made it almost impossible for the propagated band to develop along the original direction. In the current study, none of such active barrier was observed in the region where the ASB split in the AA 2017-T651 and AA 2024-T651 alloy specimens. The region ahead of the bifurcation point is relatively free of second phase particles (Figs 4.33b & 4.34b). It is however possible that the barrier is pushed into the shear band region by plastic flow of the soft matrix under pressure leaving a second phase particles free zone (SPFZ) at the point of bifurcation.

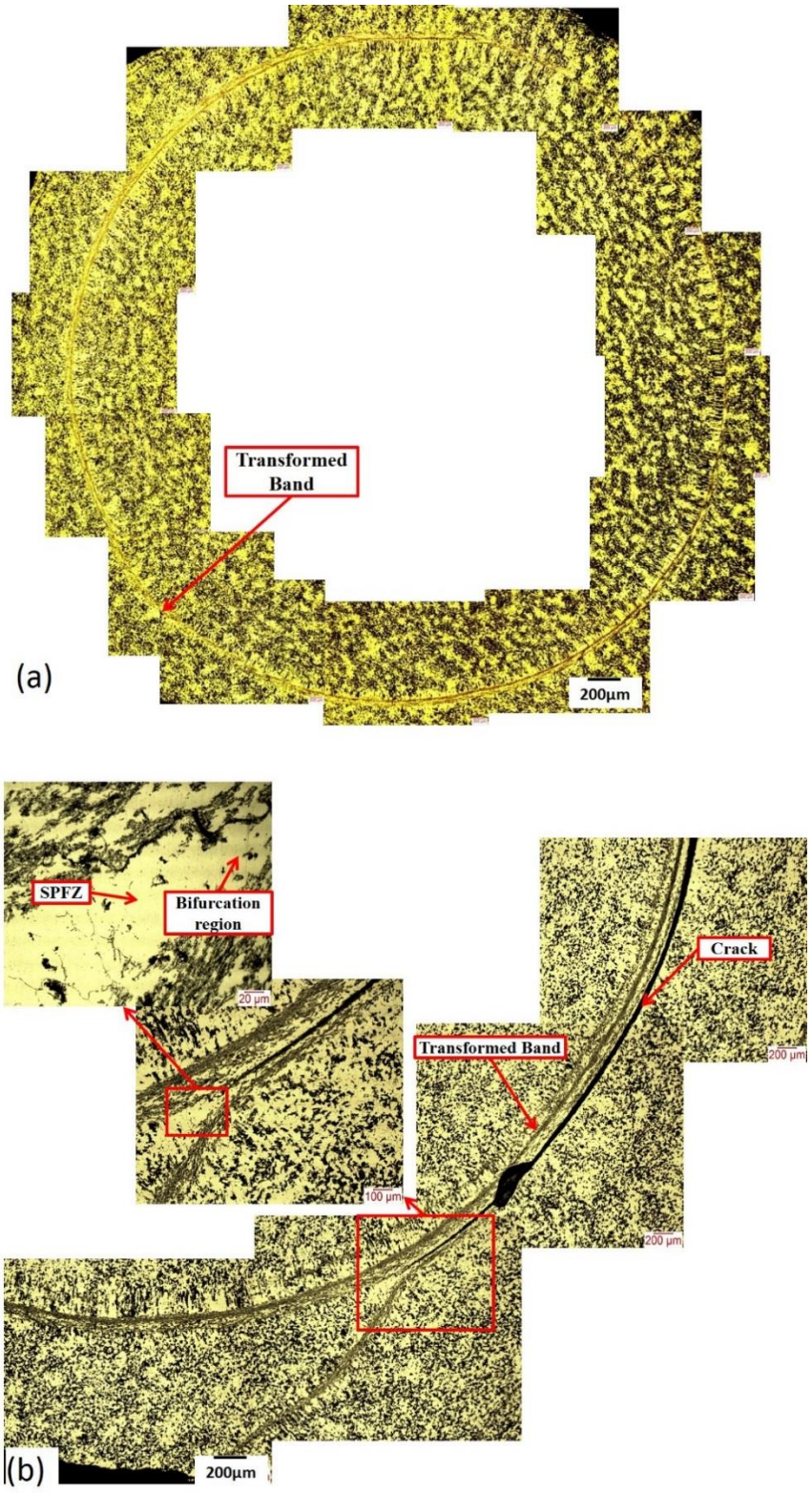

Fig. 4.33. Circular Geometry of ASB on the compression plane of (a) AA 2017-T451 alloy with no bifurcation and (b) AA2017-T651 alloy with bifurcation.

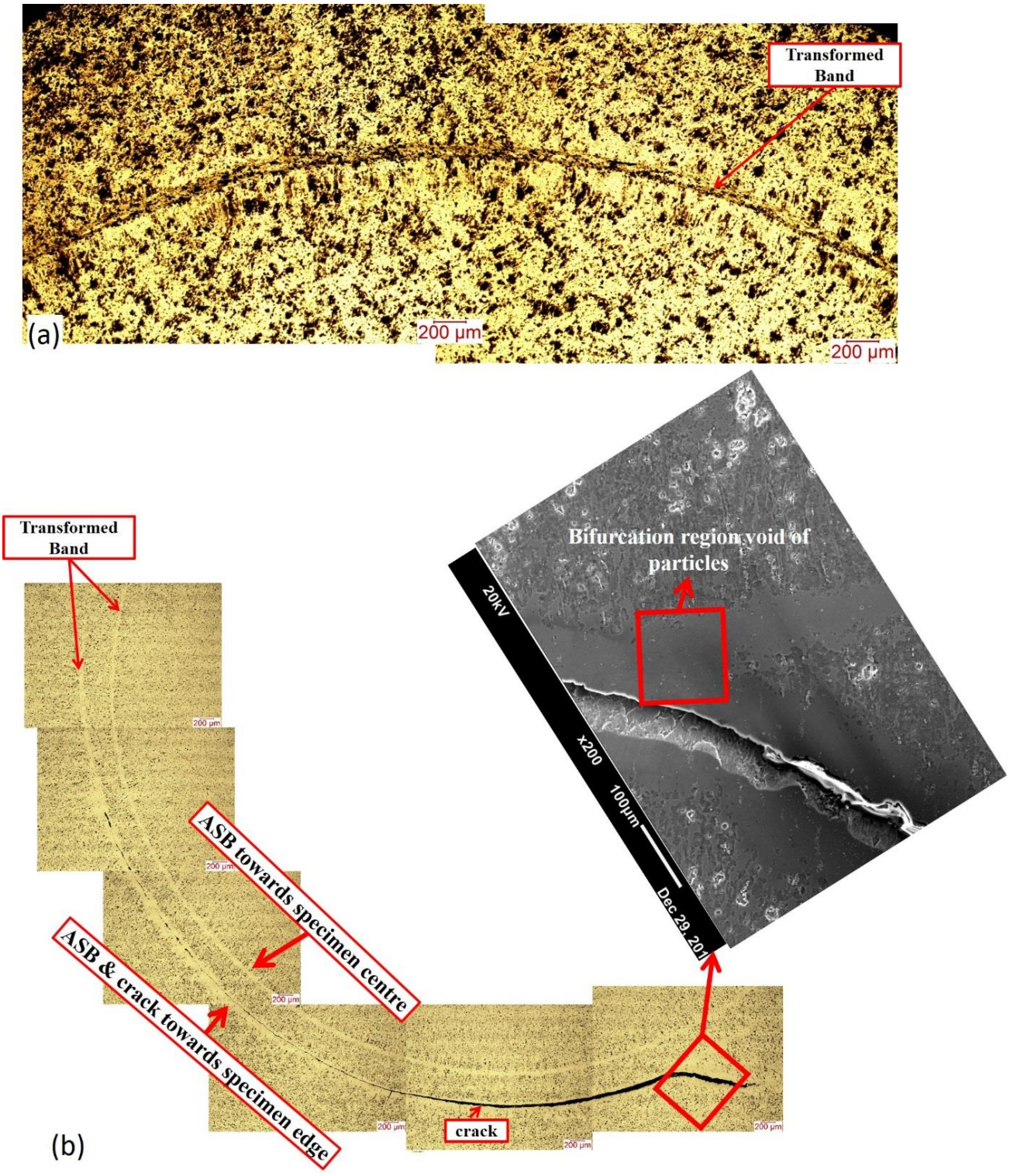

Fig. 4.34. Circular **g**eometry of ASB on the compression plane (transverse plane) of (a) AA 2024-T351 alloy with no bifurcation and (b) AA 2024-T651 alloy with bifurcation and dual banding.

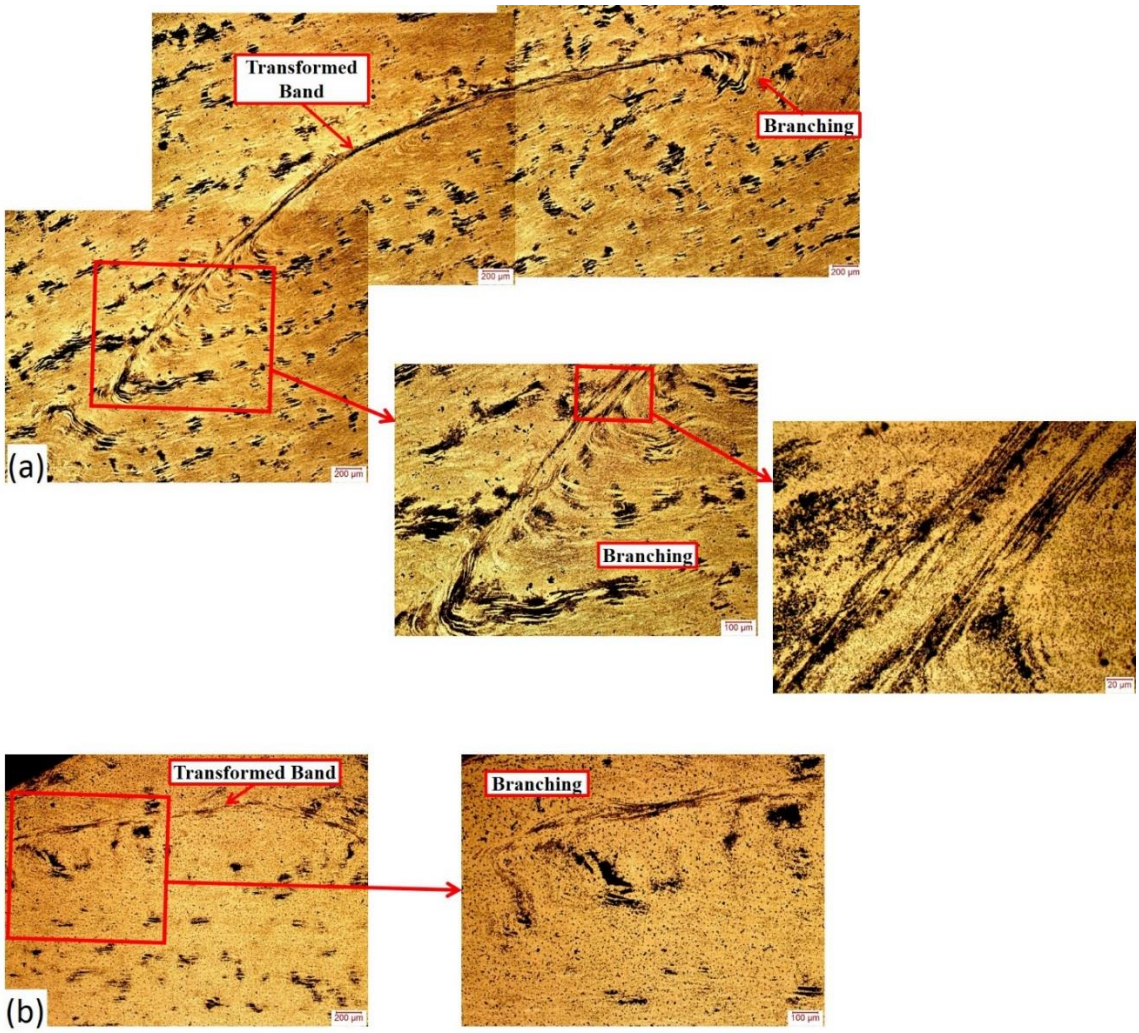

Fig. 4.35. Arc-type **g**eometry of ASB on the compression (transverse) plane of (a) AA 2624-T351 alloy and (b) AA 2624-T651 alloy. Both temper conditions shows branching at the band tip without bifurcation.

These results show that the occurrence of bifurcation during ASB propagation can be influenced by the temper condition. In addition to bifurcation, multiple bands were observed in the impacted AA 2024-T651 specimen (Fig. 4.34b). The mechanism behind the evolution of double ASBs is not completely understood. On the compression plane (Fig. 4.34), the presence of crack and bifurcation in the transformed band towards sample edge and their (crack and bifurcation) absence in shear band closer to specimen center confirmed that deformation is non-uniform.

The rolled plate AA 2624 samples show a different shear band geometry than the rolled rods (AA 2017 and AA 2024). AA 2624 samples in T351 and T651 temper loss their cylindrical shape to

been elliptical after impact. While arc-type geometry of shear band was observed at the two but opposite vertices of the elliptically-shaped specimen, the two co-vertices were void of shear band formation. No shear band bifurcation was observed in AA 2624 impacted specimens; rather, severe branching at band tip in both T351 and T651 specimens (Fig. 4.35).

Shear bands' geometry on the longitudinal section

Figure 4.36 represent the typical geometry of the adiabatic shear bands as observed on the longitudinal sections of the alloys after impact loading. On the longitudinal plane, the ASB formed in all age-hardened alloys appeared to have parabolic shape (Fig. 4.36a). The parabolic shear band regions are also regions of intense shearing of elongated grains and second phase particles. The intensity of shearing as shown in Fig. 4.36a was observed to decrease from one base surface of cylindrical tests specimens (near the output bar of the SHPB) to the other surface (input bar). This is schematically illustrated in Fig. 4.36b. Continuous solid lines A-E and A'-E' represents direction of alignment of elongated grains and second phase particles in rolling direction of the specimen before impact, while the continuous dash line represents the center line of the test specimen. Microstructural examination of the impacted samples shows that the alignment of the elongated grains and second phase particles become discontinuous at specific regions as shown on the discontinuous solid lines A_1-E_5 and A_1'-E_5'. These regions of discontinuity correspond to the parabolic ASBs on the longitudinal section of the impacted sample.

In order to quantify and characterize the intensity of SB along the parabolic region, compressive shear angle, γ is used. This is the angle between the lines of direction of elongated grains before and after impact. It appears that deformed band (say lines E_5 and E_5') are characterized by low compressive shear angle ($\gamma < 90^o$) and transformed band (say lines A_1 and A_1') are characterized by high compressive shear angle ($\gamma \geq 135^o$). There exists a region of transition from TB to DB or vice-versa (say lines C_3 and C_3'). At this region, compressive shear angle was found to be in a range i.e. $90^o \leq \gamma \leq 135^o$. Shear band in Fig. 4.36a is largely deformed with few transformed band at the compression plane near output bar of the SHPB. As the impact momentum increases (Fig. 4.37a), TB first propagated throughout the parabolic SB at about 45^o to the compression plane, followed by the initiation and propagation of crack along the TB. This confirmed the widely accepted proposition that crack initiate within TB and not DB [57]. Put differently, no crack will initiate in an ASB until transformed band is fully formed. Therefore, the relationship between ASB

and shear angle on the longitudinal section of shock loaded aluminum alloys in the naturally and artificially aged conditions can be proposed as in Fig. 4.37b. From the samples' compression plane near the edge, shear angle and intensity of shear band formed decreases until a region near the center of the sample beyond which shear angle and intensity of shear band increase again towards the compression plane.

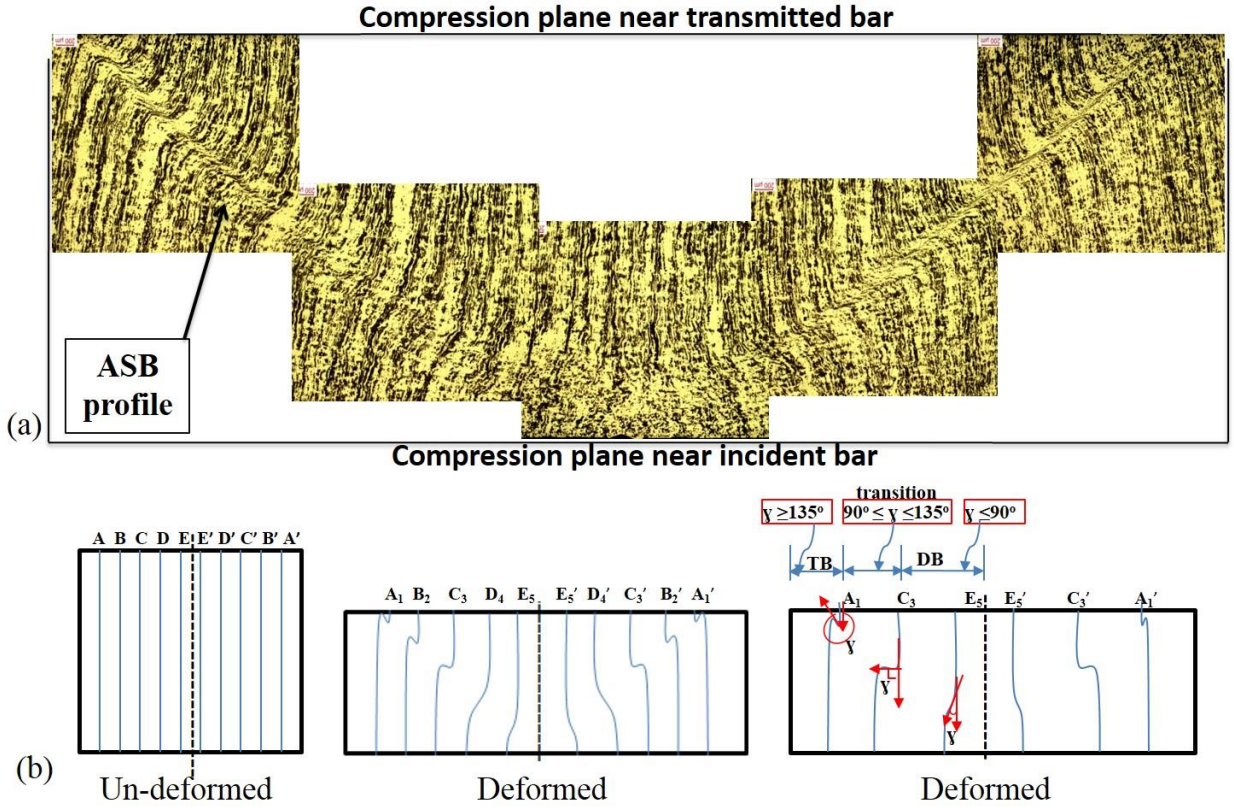

Fig. 4.36. (a) Optical micrograph showing a parabolic ASB geometry on the longitudinal section of impacted specimen in all three selected aluminum alloys; both natural and artificial aging conditions. (b) Schematic of formation of parabolic ASB geometry with compressive shear angle.

It can be concluded from the geometry of ASBs on the transverse and longitudinal sections of AA 2017 and AA 2024 (rolled rod) that shear bands form a single thin-walled cone in the entirety of the specimen as schematically presented in Fig. 4.38a. On the other hand, the shear bands appear as split cone in AA 2624 (rolled plate) as schematically shown in in Fig. 4.38b. The difference could be attributed to the prior mechanical processing of the as-received alloys (rolled rod or rolled plate) before the dynamic impact test. Therefore, it could be suggested that the mechanical history of an alloy could influence the geometry of shear band when loaded under dynamic condition.

Conical shaped ASBs have also been reported in AISI 4340 steel subjected to dynamic impact loading, except that two inverted cones were observed in the steel instead of one as observed in aluminum alloy in the current study [93]. The difference in the number of cones could be as a result of the difference in the crystallographic slip systems of the two alloys (aluminum alloy and AISI 4340 steel) as it is speculated that shear band tends to propagate along slip systems such that shear plane become parallel to the slip plane while the shear direction also become aligned with the slip direction [59].

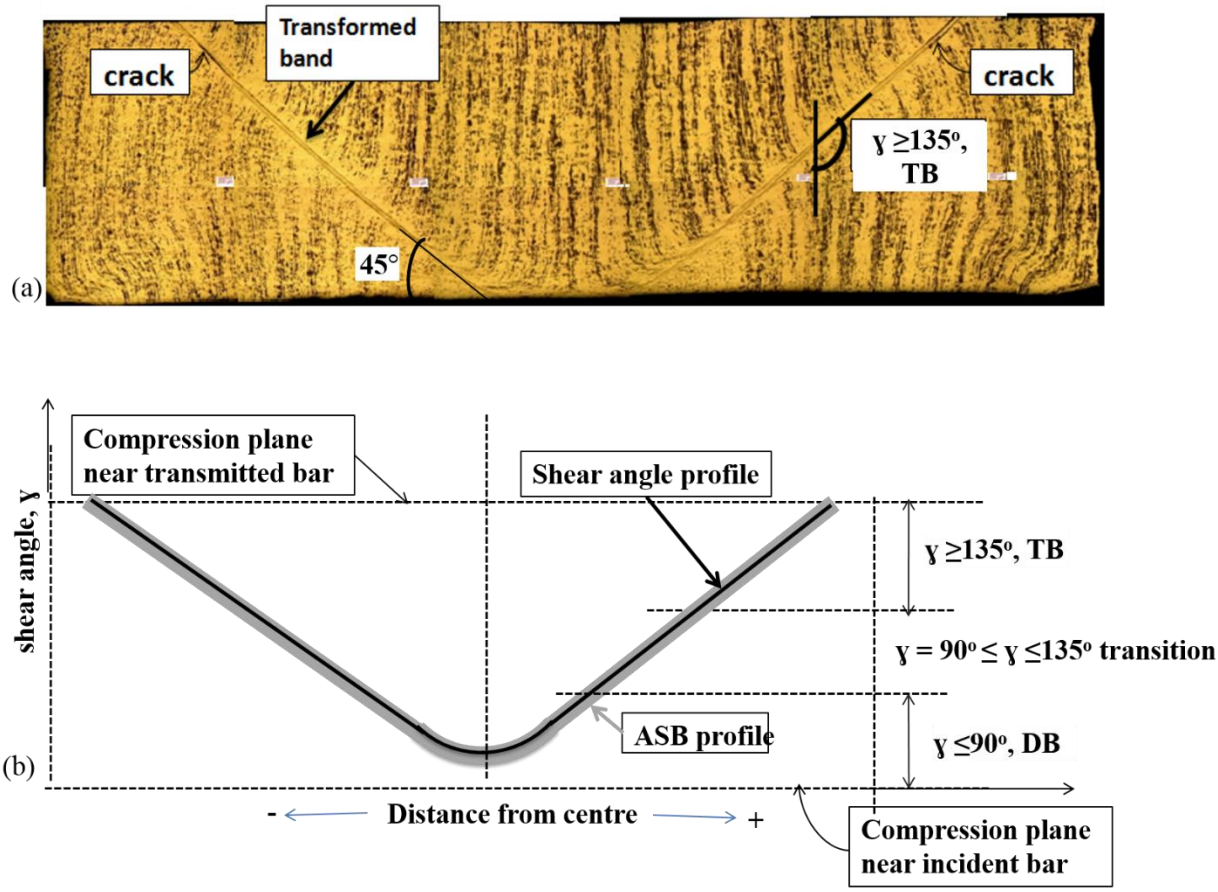

Fig. 4.37. (a) Optical micrograph showing fully formed transformed band on the longitudinal section of an impacted aluminum alloy specimen (b) proposed relationship between ASB geometry and shear angle profile on the longitudinal section of shock loaded precipitation hardened aluminum alloys.

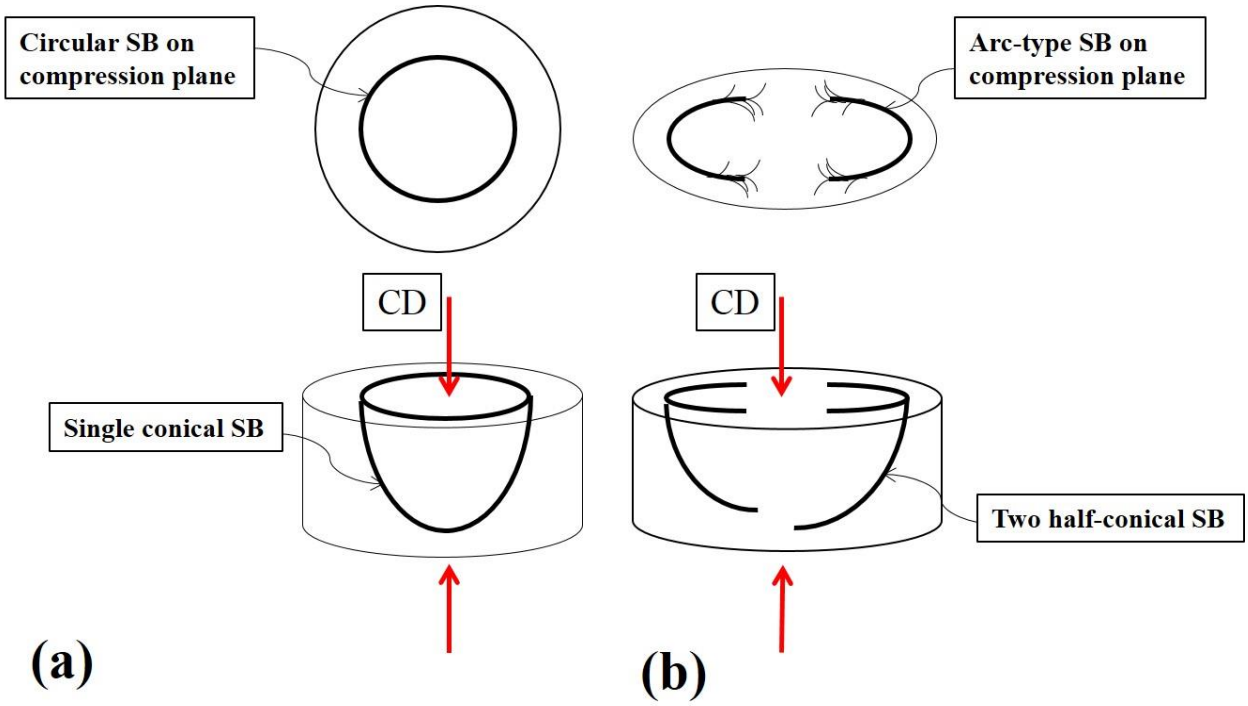

Fig. 4.38. Geometry of shear band formation in impacted (a) AA 2017 and AA 2024 (b) AA 2624.

4.4.2.2 Deformed band in AA 2017, AA 2024 and AA 2624 aluminum alloys

The deformed bands observed in the AA 2017 and AA 2024 alloys are of similar morphology for the three investigated temper conditions (Fig. 4.39 a & b). They consist of self-organized elongated particles in the shear direction. In other words, second phase particles align themselves along the plastic flow direction in the deformed bands. Fig. 4.39c shows that deformed band in AA 2624 are composed of distorted grains and second particles alignment forming a kind of distorted lamella structure that results from pronounced viscous plastic flow not far away from the specimens' edge. The current study observed that the critical strain and strain rate at which DB evolve is affected by alloys' temper condition as summarized on Table 4.5. Higher critical strain and strain rate values for DB evolution in annealed samples than the precipitation hardened ones imply that improved plasticity by annealing helps delay the evolution of DB.

At higher impact momentum where transformed band is formed in age-hardened specimens, the evolution of DB in annealed specimens remained persistent in all the three alloys. While both AA 2017-O (Fig. 4.40) and AA 2024-O (Fig. 4.41) specimens shows deformed region characterized by elongated grains and grain boundary (GB) precipitates than outside DB, impacted AA 2624-O

specimen in Fig. 4.42 shows deformed band with high viscous flow characterized by elongated grains and particles in the shear flow direction. Since the annealed specimens did not form transformed bands but deformed band, no fracture was expected, neither were they found after the impact loading.

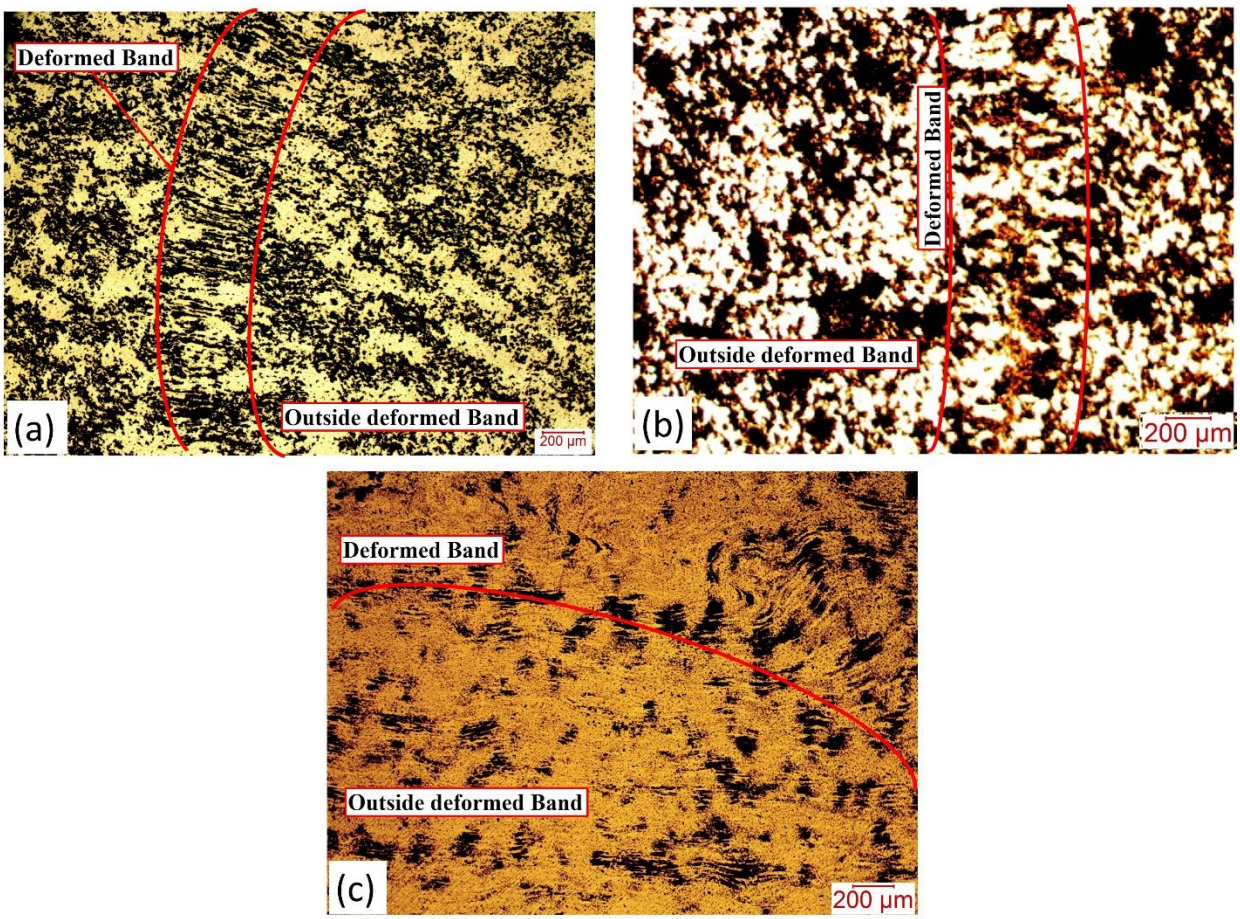

Fig. 4.39. Optical micrographs of impacted (a) AA 2017 (b) AA 2024 and (c) AA 2624 specimens showing deformed band morphology.

However, the precipitation along grain boundaries substantially increased in the impacted annealed specimen for all investigated alloys compared to the un-deformed samples. The intensity of precipitation was also observed to be more in the deformed band regions than outside DB. The grain boundary precipitation is suggested to be aided by the temperature rise in the alloy during the deformation process. Such grain boundary precipitations which have been suggested to be detrimental to formability of alloys were not observed in the specimens in age-hardened condition

[152]. Therefore, a possible reason for the lower strength in the annealed samples under the impact loading could be that the grain boundary precipitation causes the weakening of the sample [153].

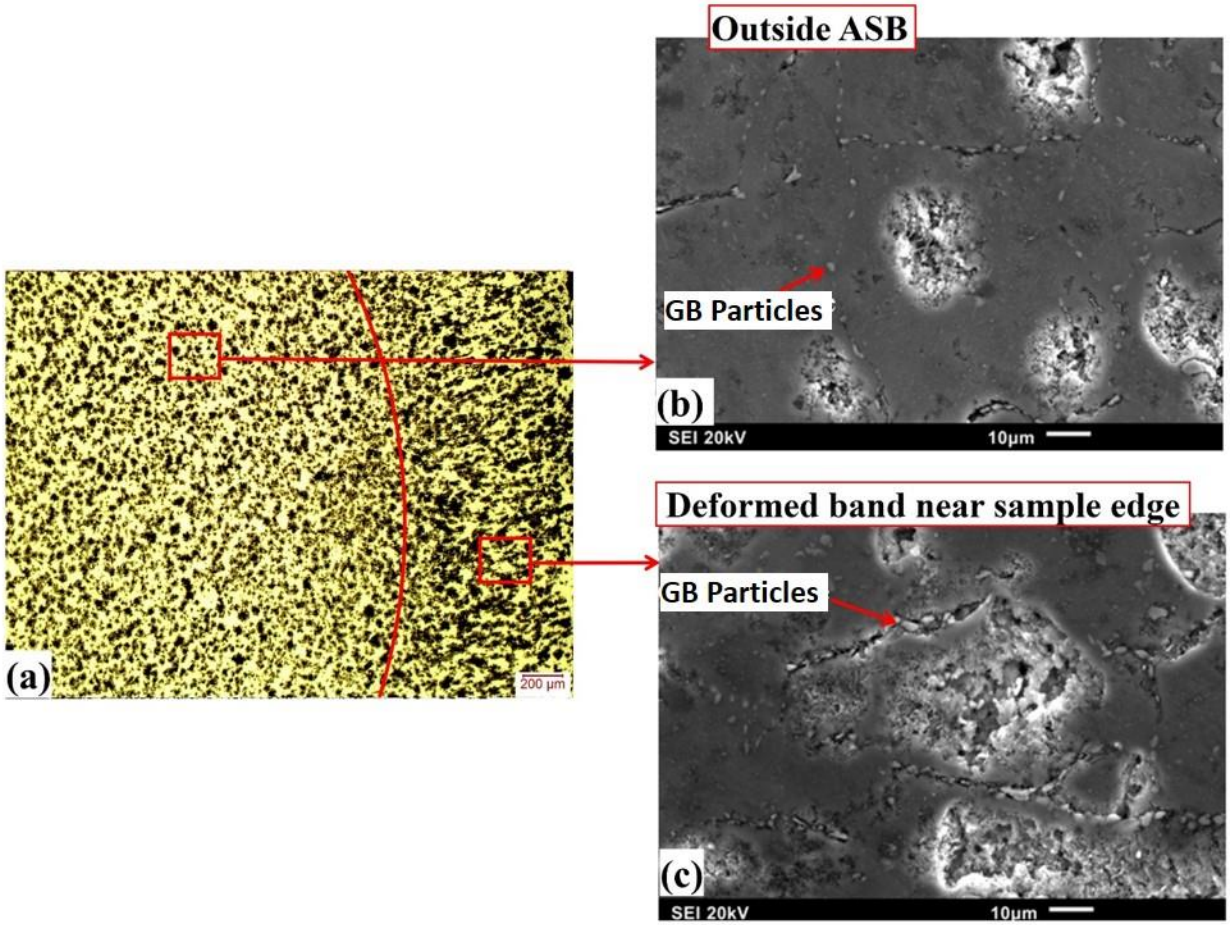

Fig. 4.40. Optical and SEM micrographs of AA 2017-O showing particles within grain boundaries outside (b) and inside (c) deformed band.

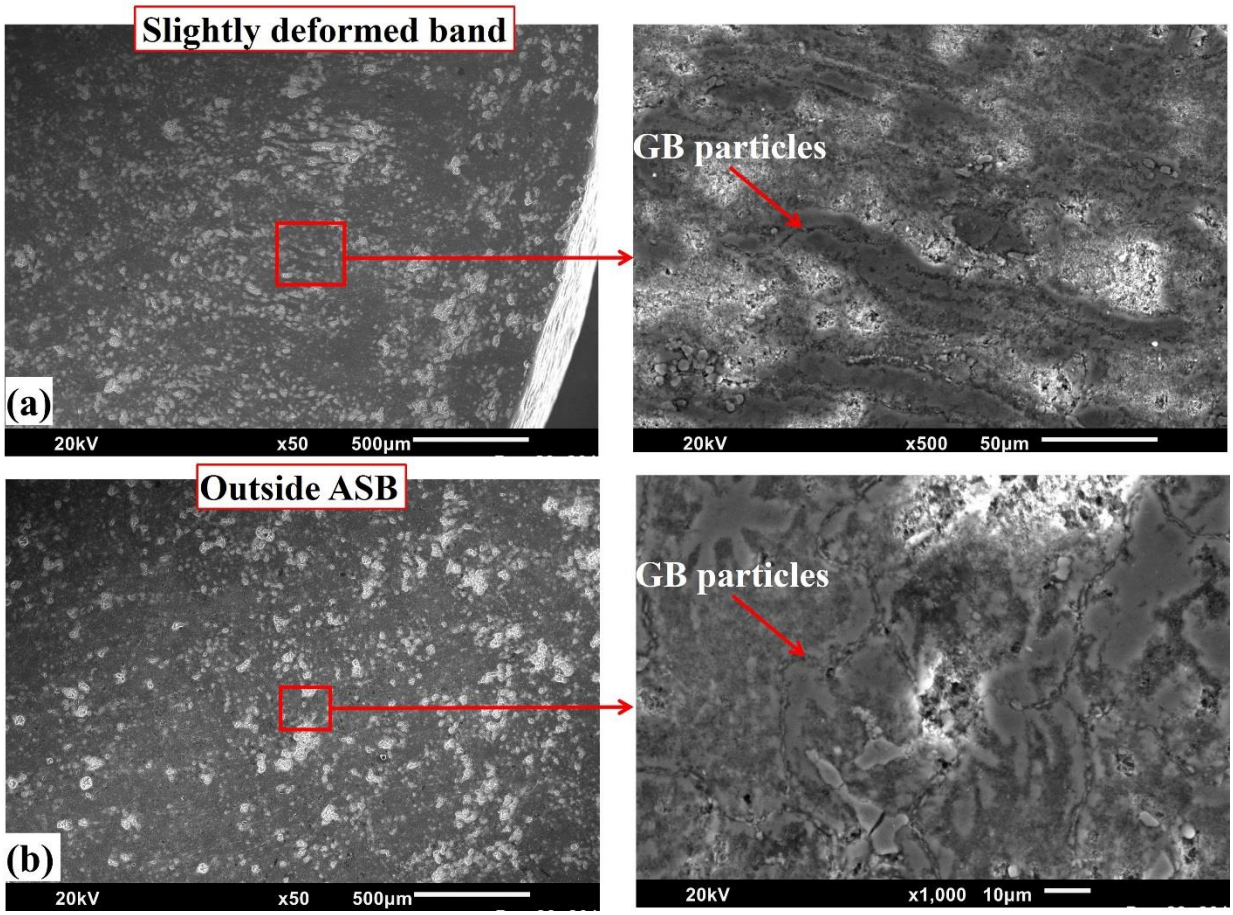

Fig. 4.41. Optical and SEM micrographs of AA 2024-O showing particles within grain boundaries (a) inside and (b) outside deformed band.

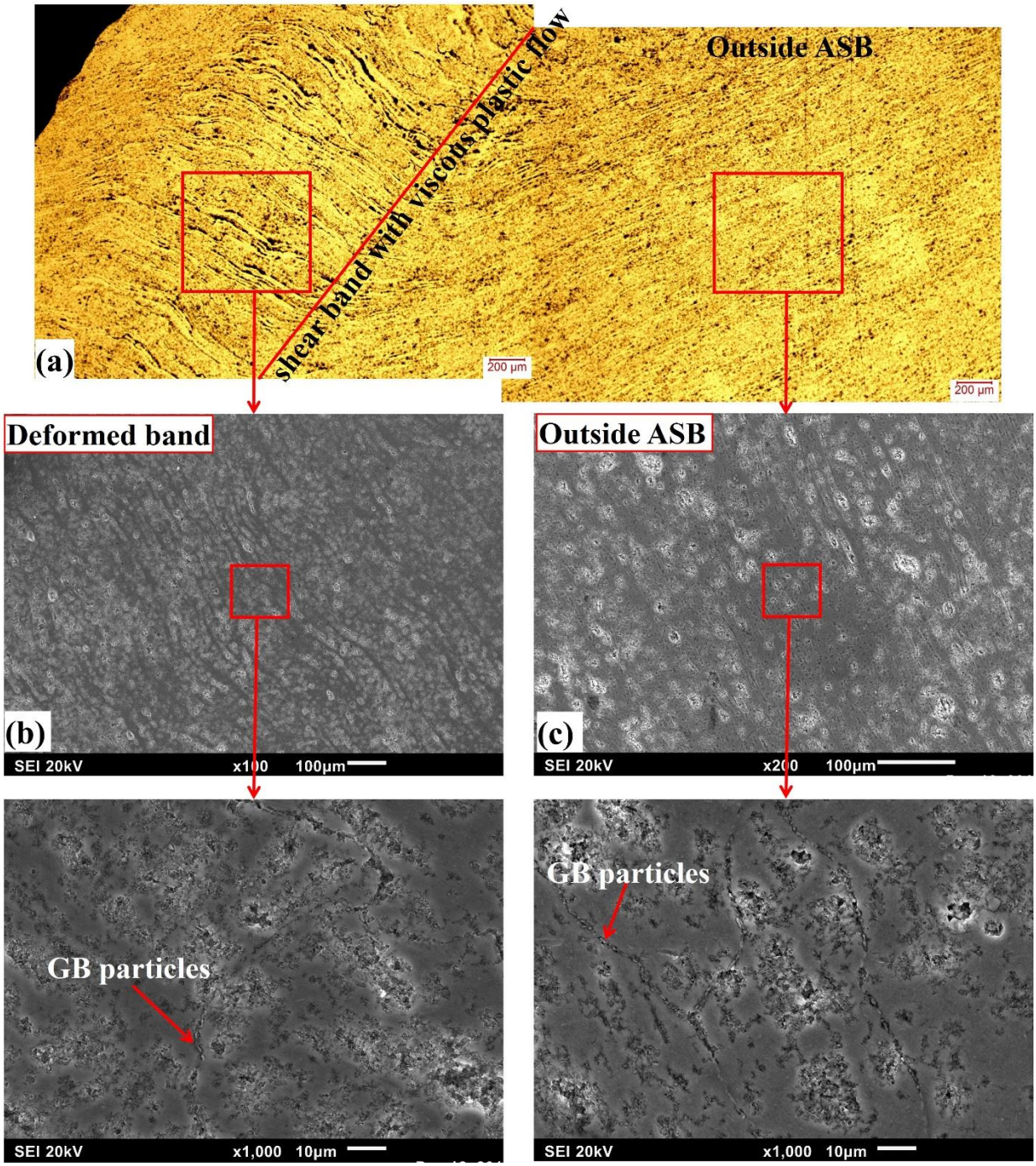

Fig. 4.42. Optical and SEM micrographs of AA 2624-O showing particles within grain boundaries outside (b) and inside (c) deformed band.

4.4.2.3 Transformed bands in AA 2017, AA 2024 and AA 2624 aluminum alloys

AA 2017 aluminum alloys

The onset of transformed bands observed in the age-hardened samples occurred at an impact momentum of 41.5 kg.m/s for both temper (AA 2017-T451 and AA 2017-T651); thereby suggesting a comparable susceptibility of the alloy to the occurrence of transformed bands in both temper conditions. SEM micrographs showing the morphology of transformed bands in the AA 2017-T451 and AA 2017-T651 temper are presented in Figs. 4.43 & 4.44. Transformed band in both temper were observed to evolve with deformed band on both sides of the TB. Li et al. [57] had similarly observed microstructural changes from the core (equiaxed grains) of TB to DB at the edge consisting of elongated grains. The grain morphology within the TB in both T451 and T651 specimens could not be effectively resolved with the SEM. It appears that TB consists of dissolved second phase particles with islands of second particles free zones (SPFZ) in both temper. While the SPFZs are observed to be dispersedly found on the compression plane outside shear band (Figs. 4.43b & 4.44b) as in the case of a non-deformed sample, they were observed to be 'swept' towards the center of the TB.

EDS line scan (Fig. 4.45) across the shear band was conducted for AA 2017 alloy at T451 and T651 temper. Lower concentration of Al, Mg, Mn and Fe atoms were observed in the shear band where dissolution of particles occur than the region outside the shear band in both temper specimens. Only Cu and Si atoms were observed to be of higher concentration inside the shear band region than its outside. It has been reported in a separate paper that Si-contained phases are crack initiation sites or crack growth enhancer [39]. Therefore, the presence of more Si atoms in shear band regions of AA 2017-T451 and AA 2017-T651 as observed in Fig. 4.45 may raise the cracking susceptibility in the shear band.

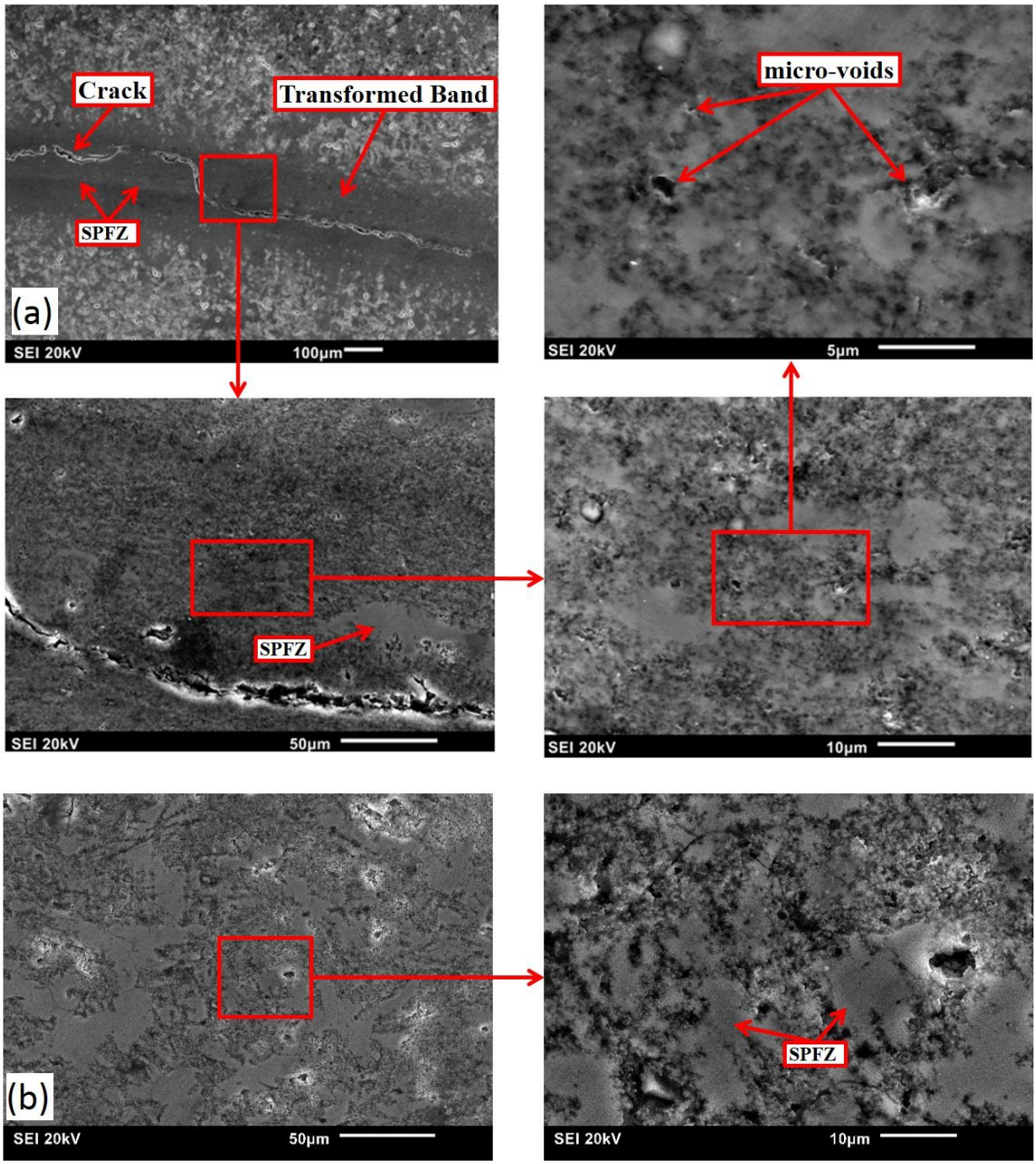

Fig. 4.43. SEM micrographs showing the (a) inside and (b) outside ASB of impacted AA 2017-T451 specimen at an impact momentum of 42.6 kg m/s.

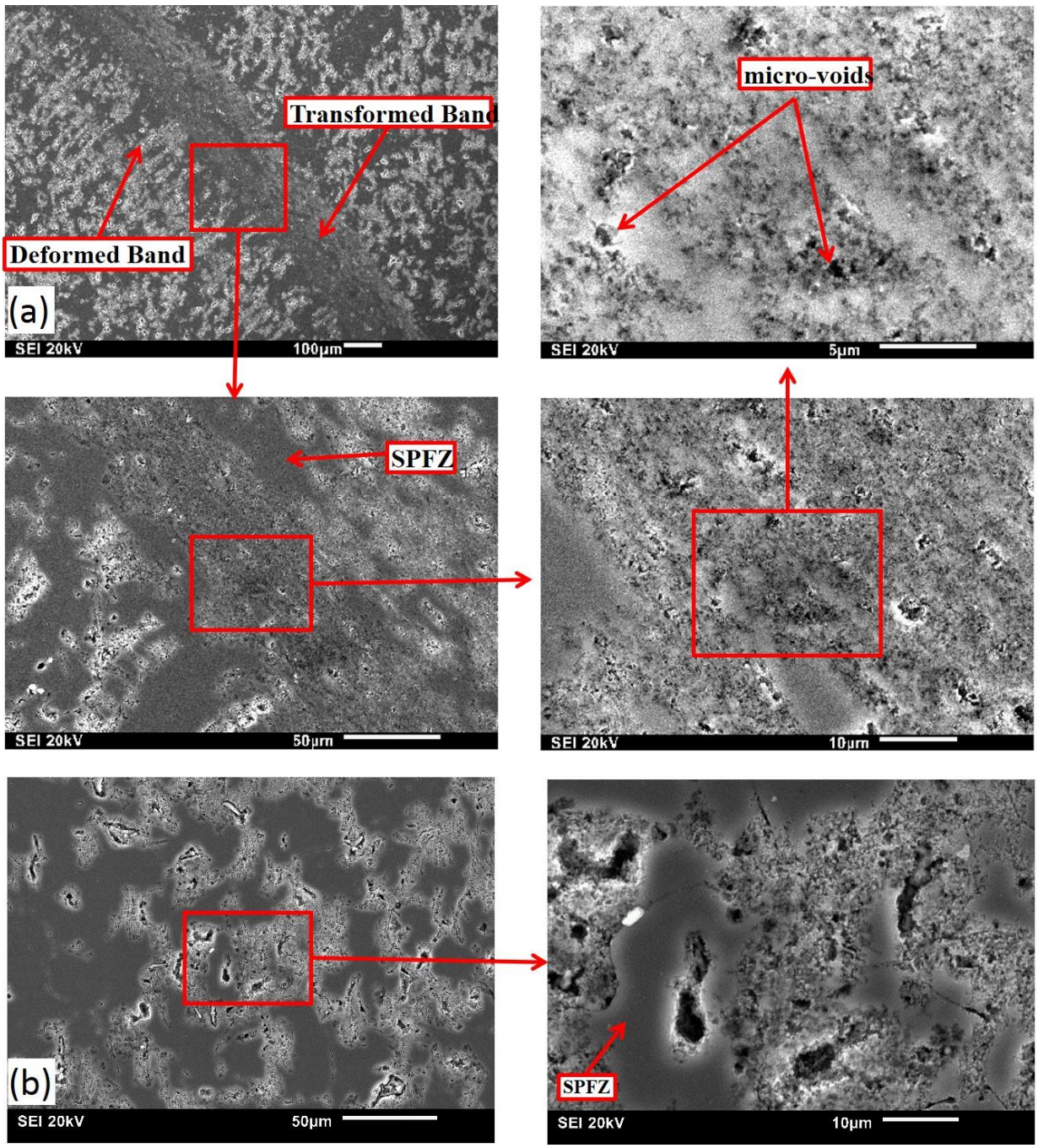

Fig. 4.44. SEM showing the (a) inside and (b) outside ASB of impacted AA 2017-T651 specimen at an impact momentum of 43.6 kg m/s.

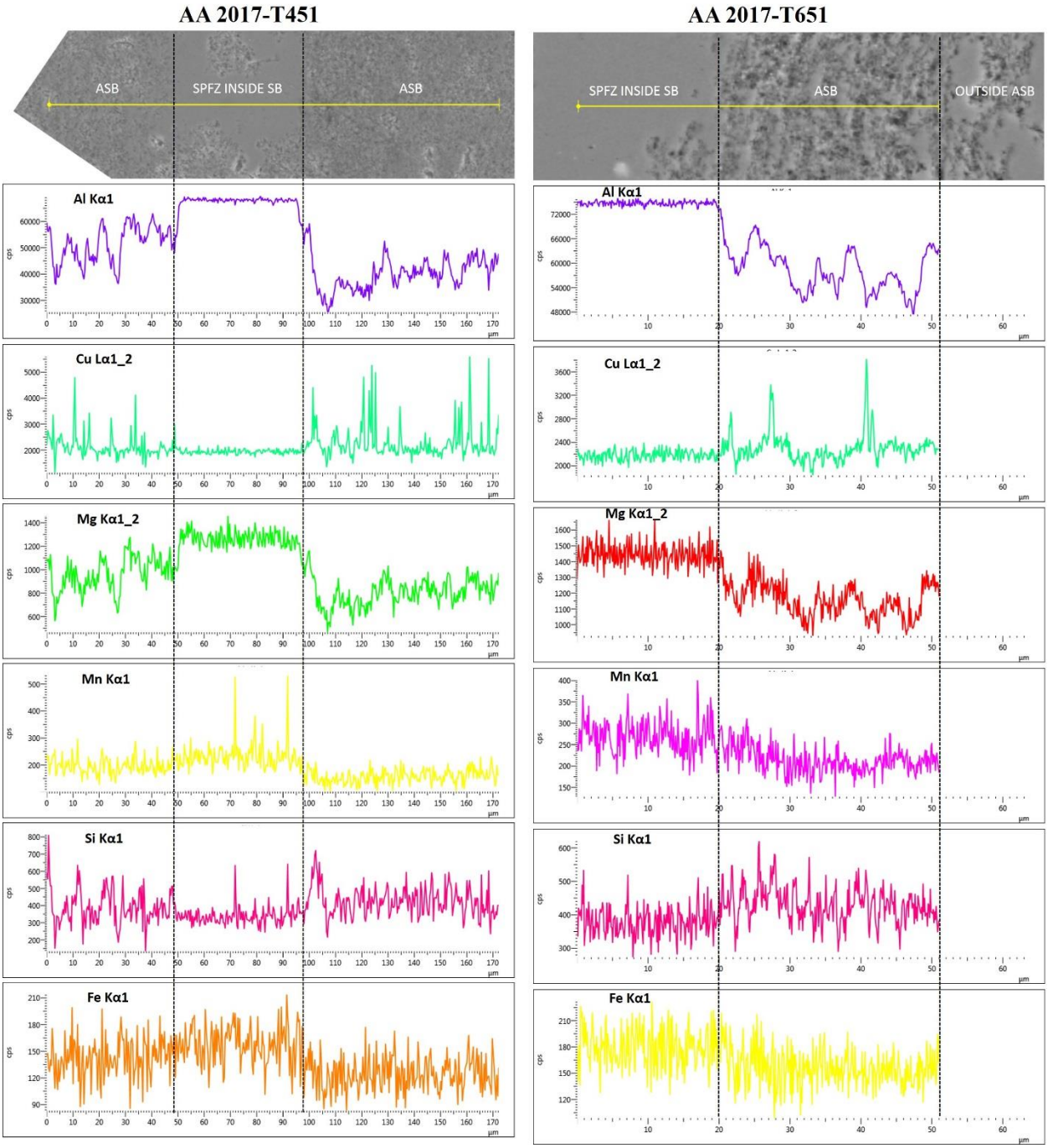

Fig. 4.45. EDS line scan of impacted AA 2017-T451 and AA 2017-T651 specimen across ASB.

AA 2024 aluminum alloys

Transformed bands were first observed to evolve in the age-hardened AA 2024-T351 and AA 2024-T651 specimen at an impact momentum of 40.0 kg.m/s and 44.4 kg.m/s (Table 4.5). In addition to the lower impact momentum required for the onset of TB in AA 2024-T351, lower

critical strain value was reached in AA 2024-T351 (0.43 strain) than in AA 2024-T651 (0.60 strain). Unlike AA 2017 alloy, appreciable difference in impact momentum (IM) and critical strain required for the onset of TB in T351 and T651 temper suggests different susceptibility of the alloy to the occurrence of transformed bands in both temper conditions. It is therefore clear that the artificial aging of AA 2024-T351 suppressed the susceptibility of the alloy to transformed band formation. The reason for the earlier TB evolution in AA 2024-T351 specimen could be due to higher PFS II (Fig. 4.18) and strain hardening rate (Fig. 4.21b) than the artificially-aged samples. In a previous study, it was observed that higher strength alloy under compression at room temperature are more susceptible to shear localization with highest degree of microstructural break down [154]. Unlike AA 2017 alloy where the earlier susceptibility of T651 temper to deformed band does not guarantee earlier susceptibility of same temper to transformed band or eventual fracture, AA 2024-T351 shows to be more susceptible to DB, TB and eventual fracture than AA 2024-T651 specimen (Table 4.5).

Micrographs showing the features of transformed bands formed in the AA 2024 alloy at T351 and T651 temper are presented in Figs. 4.46 and 4.47 respectively. The characteristics of the transformed band in both temper are quite dissimilar unlike what was obtained in the AA 2017 specimens. In AA 2024-T351 specimen (Fig. 4.46), transformed band were observed to develop with deformed bands on both sides of the TB. The elongated particles (DB) on both sides of the TB aligned in the perpendicular direction to the TB propagation path. It also appear as in the case of age-hardened AA 2017 alloy that TB consists of dissolved second phase particles with islands of second particles free zones (SPFZ). Microvoids were observed in region containing dissolved particles inside the transformed bands. The microvoids appeared in a circular particle clustering with less band contrast (darker) in Fig. 4.46a can serve as crack initiation sites. On the other hand, transformed bands in AA 2024-T651 specimen (Fig. 4.47a) are devoid of second phase particles. It is suggested that the temperature rise within the band resulted in a complete dissolution of second phase particles such that elements making up the dissolved particles could have migrated towards the adjacent side of the shear band. The aforementioned features were not observed outside the shear band (Fig 4.47b), rather SEM micrographs revealed the distortion of relatively circular second phase particle when the sample was not deformed (Fig. 4.6b). The microstructure of the TB in AA 2024 specimens could not be effectively resolved with the SEM.

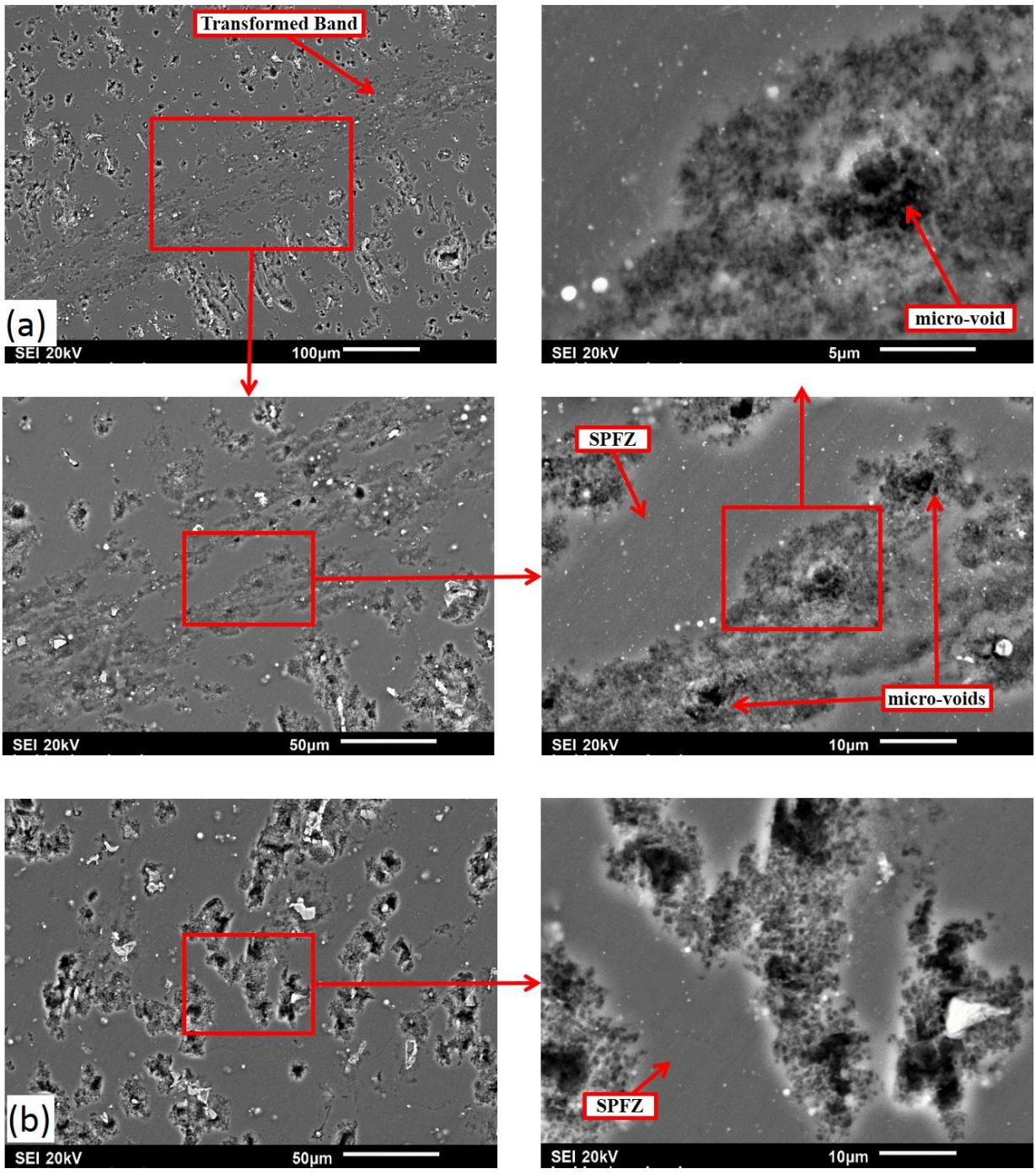

Fig. 4.46. SEM micrographs of impacted AA 2024-T351 specimen showing the (a) inside and (b) outside ASB.

EDS line scan (Fig. 4.48) across the shear band was conducted for AA 2024 alloy at T351 and T651 temper. The result confirms the influence of thermal treatment on shear band formation. While Cu is the only element with more atoms in the microvoids found in the shear band of AA

2024-T351 alloys than its outside shear band, atomic percent of Al, Mg, Mn and Si are lesser in the circular particle clusters (microvoids) than the SPFZs/matrix. In impacted AA 2024-T651 specimen, EDS line scan shows that the atomic percent of only Al and Mg are more in the shear band than its surroundings (outside ASB). Though the atomic percent of Cu seems to be more outside the shear band than inside, the Cu atoms are more than Mg atoms in the band. Therefore, the ASB developed in AA 2024-T651 has composition similar to that of a matrix.

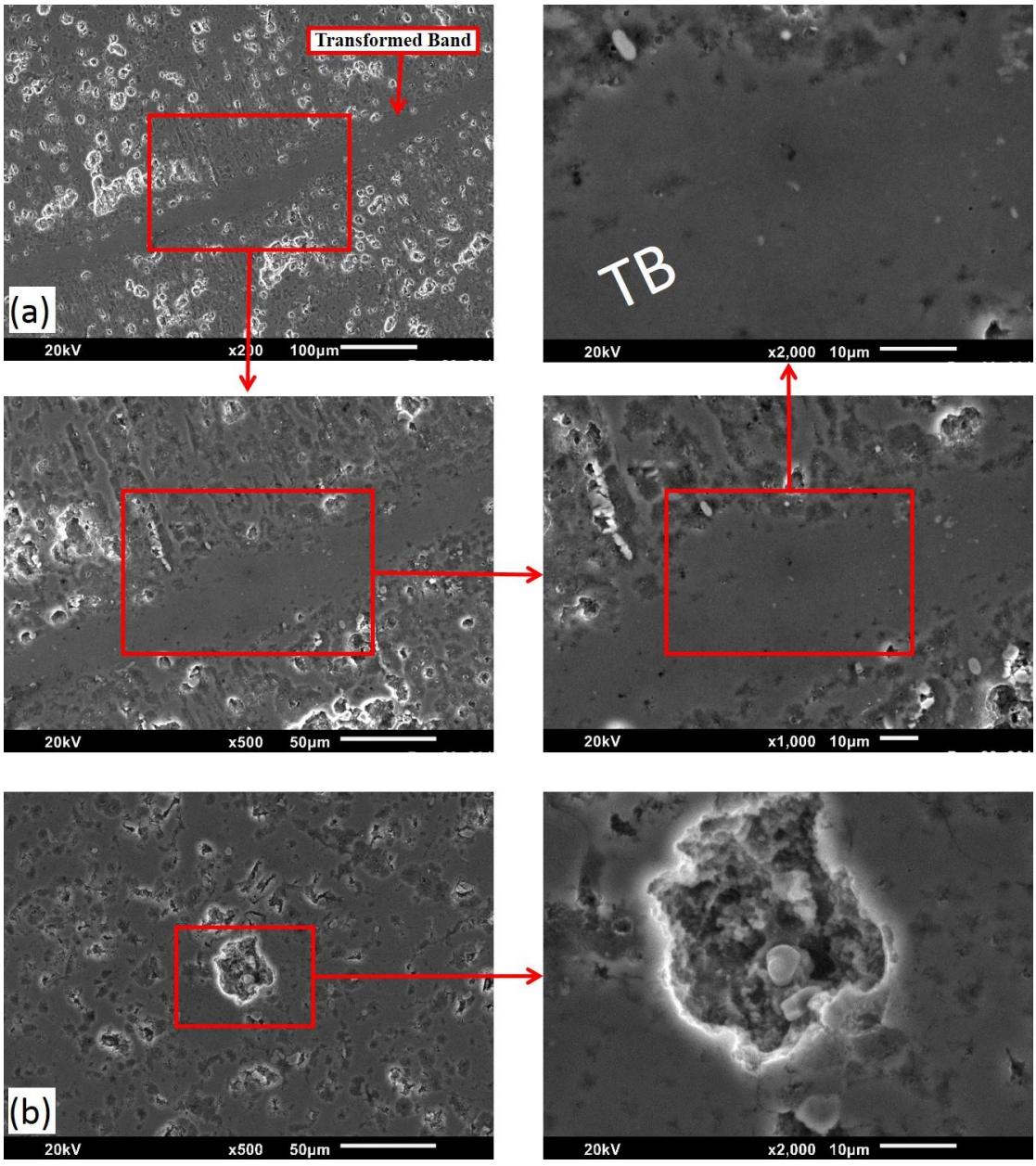

Fig. 4.47. SEM micrographs of impacted AA 2024-T651 specimen showing the (a) inside and (b) outside ASB.

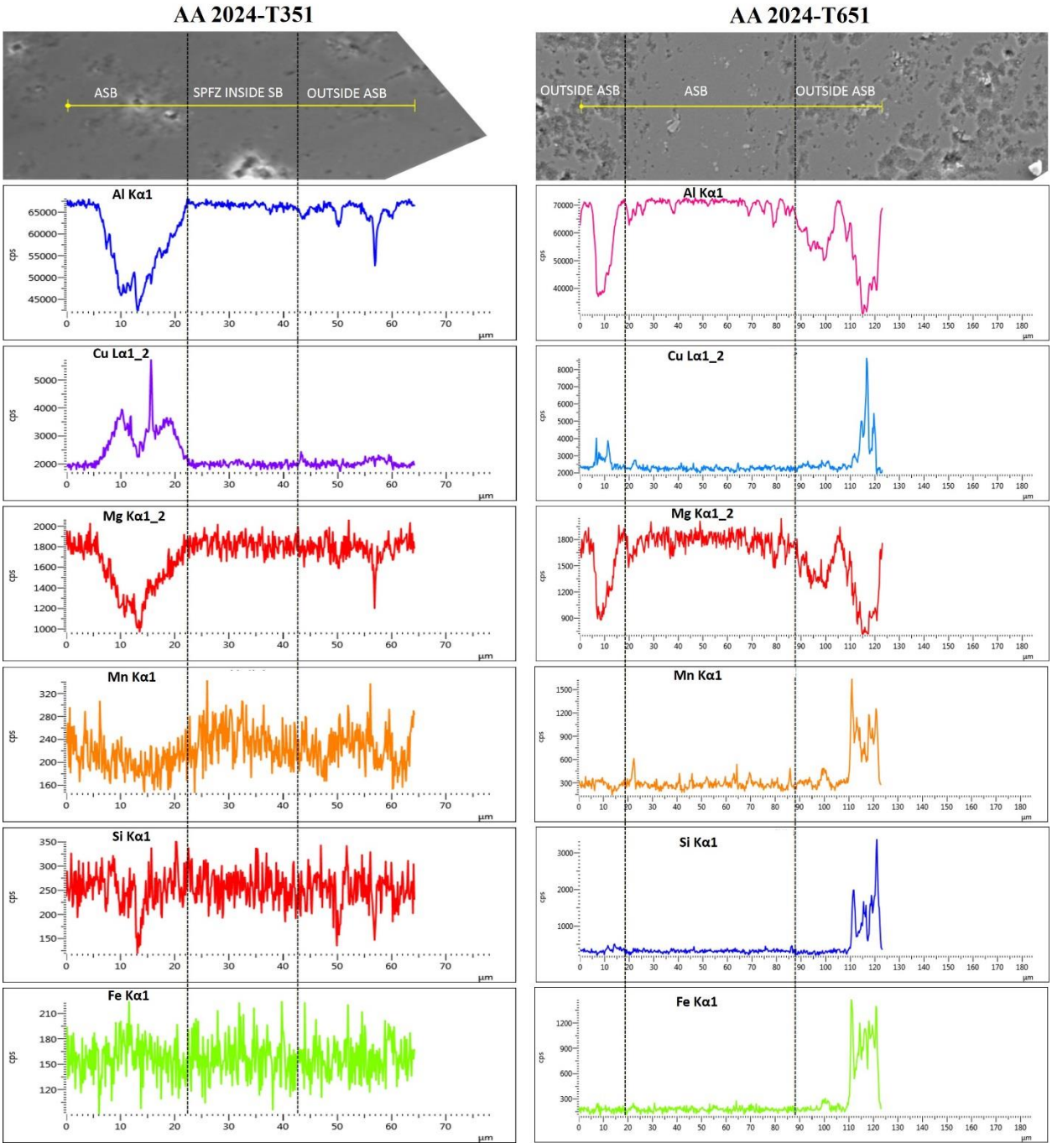

Fig. 4.48. EDS line scan of impacted AA 2024-T351 and AA 2024-T651 specimen across ASB.

AA 2624 aluminum alloys

Formation of transformed bands in age-hardened alloys was first observed in the age-hardened AA 2624 (T351 and T651) specimens both at impact momenta of 41.5 kg.m/s and 40.0 kg.m/s respectively (Table 4.5). The lower impact momentum required for the onset of TB in AA 2624-

T651 indicates that further artificial aging of the as received alloys as done in this study increases the strength of specimen; but make it more susceptible to formation of transformed band. Though the alloy fracture at the same impact momentum (42.0 kg.m/s) in both temper conditions, it can be concluded that AA 2624-T651 proved to be more susceptible to DB and TB formation than AA 2624-T351 specimens (Table 4.5). SEM micrographs showing the characteristics of the transformed bands that developed in the AA 2624 alloy at T351 and T651 temper are presented in Figs. 4.49 & 4.50. As mentioned in the previous section, deformed band in AA 2624 are composed of distorted grains and particle alignment forming a distorted lamella structure. Transformed bands in AA 2624-T351 (Fig. 4.49) were observed to evolve and propagate along the deformed bands at higher strain rates and strains. Second phase particles containing small dark spherical particles were observed to crush within the TB. Unlike AA 2017 and AA 2024 alloys, no microvoids were observed to form inside the transformed bands. Similarly, transformed band in AA 2624-T651 specimen (Fig. 4.50a) contains grains whose morphology was not resolvable under the SEM. The difference between the TB formed on AA 2624-T351 (Fig. 4.49a) and AA 2624-T651 (Fig. 4.50a) specimen is in the more viscous plastic flow adjacent to both sides of the TB in the former than the later.

EDS line scan (Fig. 4.51) across the shear band on AA 2624 alloy in T351 and T651 temper shows that Cu is the only element with more concentration in atomic percent in the shear band of AA 2624-T351 alloys than outside shear band while atomic percent of Al, Mg, Mn and Si are more in the matrix than shear band region. The elemental distribution across shear band in AA 2624-T351 was similar to what was obtained in the AA 2024-T351. In impacted AA 2624-T651 specimen, EDS line scan shows that in addition to Cu, the atomic percent of Si has tremendously increased more in the shear band than its surroundings (outside SB). It will be recalled that AA 2624 alloy is a newly developed alloy with stricter limit on impurity level (Table 3.1), yet the identification of Si atom in the sample imply that the presence of trace elements such as Si cannot be neglected. It is supposed that Si migrated into the ASB region from the region adjacent to it.

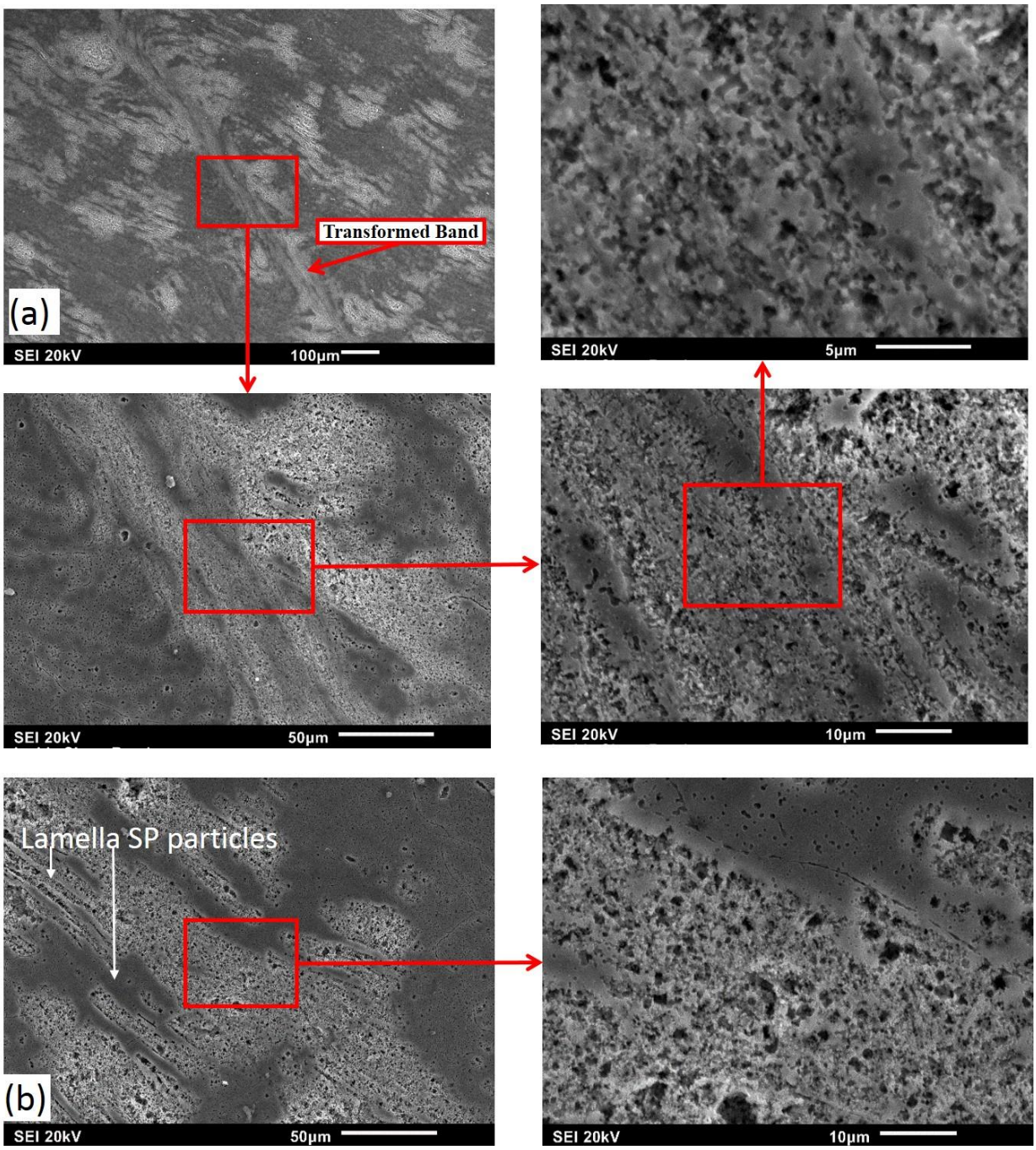

Fig. 4.49. SEM micrographs of impacted AA 2624-T351 specimen showing the (a) inside and (b) outside ASB.

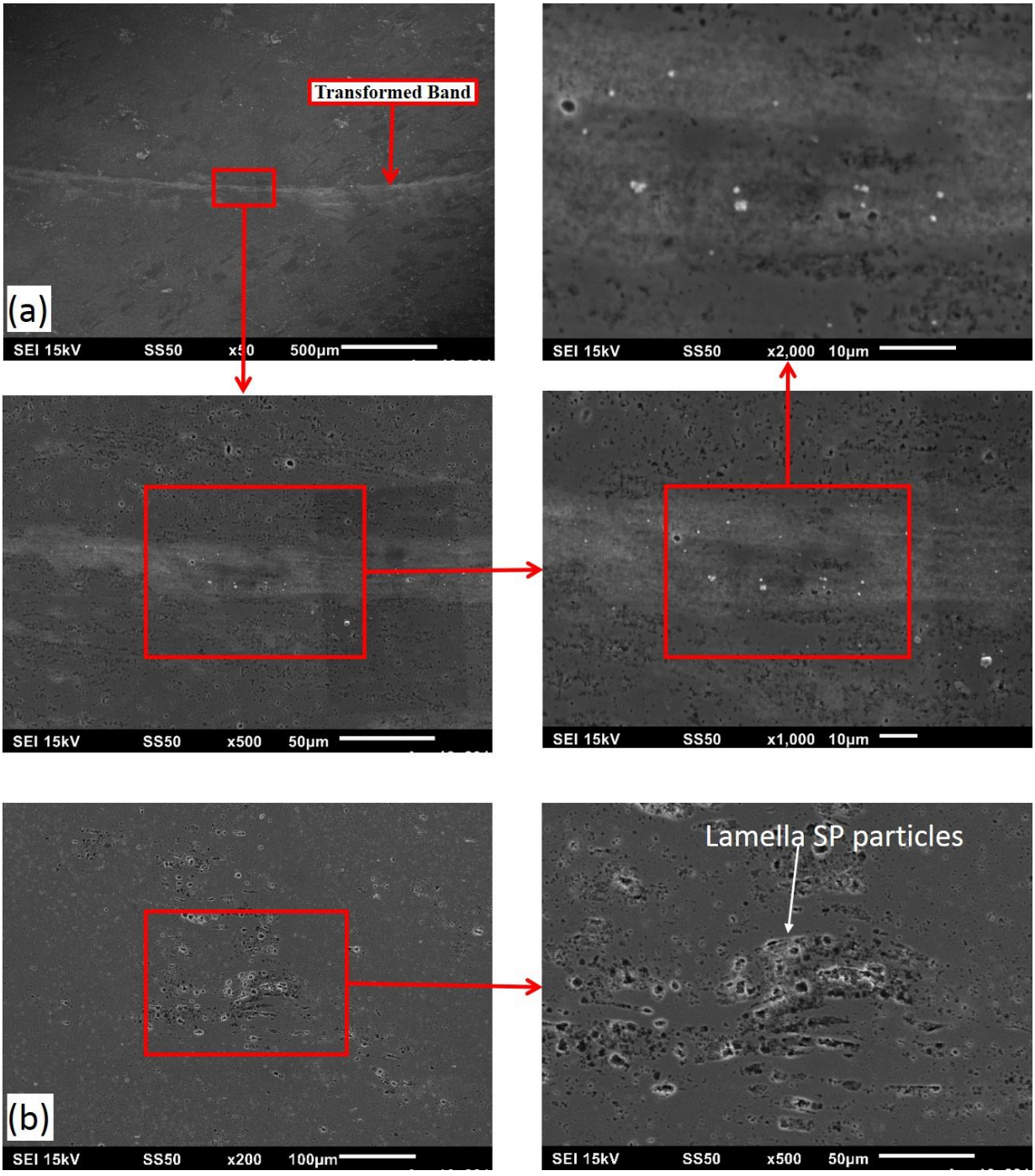

Fig. 4.50. SEM micrographs of impacted AA 2624-T651 specimen showing the (a) inside and (b) outside ASB.

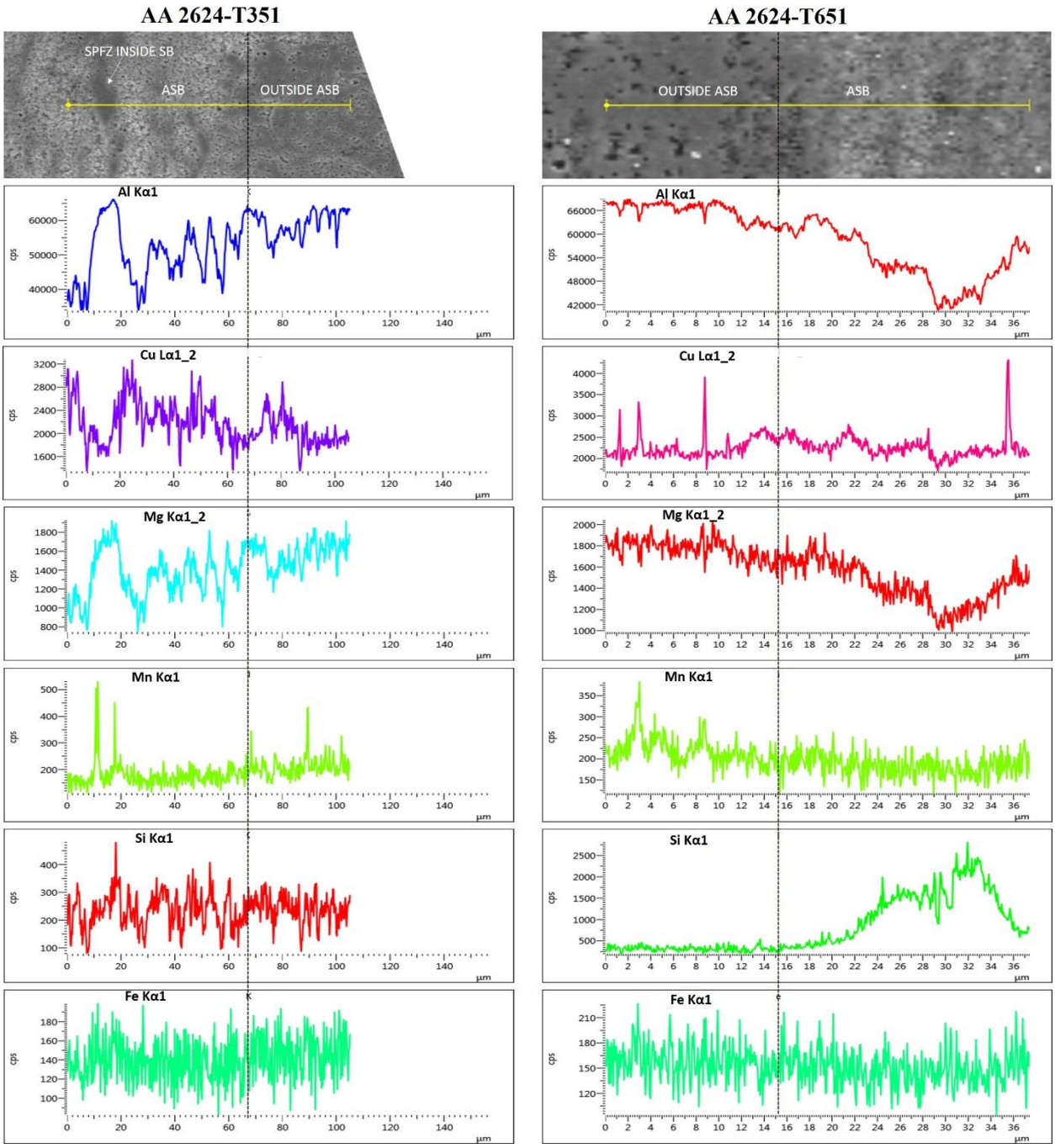

Fig. 4.51. EDS line scans of impacted AA 2624-T351 and AA 2624-T651 specimen across ASB.

In summary, the higher the strength of the investigated aluminum alloys, the higher the strain hardening rate and the higher is its susceptibility to form adiabatic shear band and eventual fracture. Though the aforementioned inference is true for specimens in both loading conditions (quasi-static and dynamic), the mechanism of formation of shear band in quasi-static samples are

quite different from those of dynamic impact samples [75]. In this present study, the fact that samples were not observed to be hot immediately after compression (unlike dynamic shock loaded samples) and ultrafine equiaxed grains were not observed in the microstructure of shear band region but rather elongated in a fan-like fashion nullifies the use of the adjective 'adiabatic' to qualify shear band formed under quasi-static compression. The mechanism of shear band formation under quasi-static loading are then suggested to be a result of subgrain rotational mechanism rather than adiabatic softening [99]. Strain localization leading to shear band is therefore a function of condition of loading i.e. either quasi-static isothermal or dynamic conditions [74] as well as the temper condition as reported in this study.

4.4.3 Effect of grain morphology on ASB propagation

Observations reported in section 4.4.2.1 provide a hint on how adiabatic shear band propagation could be influenced by grain shape. It was earlier observed that alloys received in rolled rod condition (AA 2017 and AA 2024) have an equiaxed grain structure on compression plane as schematically shown in Fig. 4.52a. In both alloys, deformed and transformed band were observed to self-organize; taking the shape of the cylindrical specimen (Fig. 4.52b). On the other hand, alloy received in rolled plate (AA 2624) is composed of elongated grain structure on compression plane (rolling direction) as schematically shown in Fig. 4.53a. After impact, transformed band is speculated to have initiated first at point A (grain 1) as depicted in Fig. 4.53b. According to Hall-Petch equation (Eq. 4.1) in terms of flow stress, it is expected that flow stress required to deform an elongated grain will vary depending on the orientation of the grain with respect loading direction.

$$\sigma(\varepsilon) = \sigma_o(\varepsilon) + K_1(\varepsilon) D_{GB}^{-1/2} \quad \ldots 4.1$$

where σ is the flow stress, $\sigma_o(\varepsilon)$ and $K_1(\varepsilon)$ are constants at a given strain, D_{GB} is the grain diameter (distance between grain boundaries) [155]. From Eq. 4.1, flow stress is in two parts; the first ($\sigma_o(\varepsilon)$) is the flow stress of grain interior which is independent of grain size and the other ($K_1(\varepsilon) D_{GB}^{-1/2}$) which is grain size dependent, is considered a strength contribution as a result of additional resistance to dislocation motion caused by the presence of grain boundaries. Therefore, the larger the distance travelled (D_{GB}) by dislocation on slip plane before encountering a grain boundary (barrier), the lower the flow stress required to plastically deform the material. Applying

the Hall-Petch relation, the larger the distance travelled by a propagating shear band (symbolized as ⊥) within a grain before encountering a grain boundary, the lower the driving force required to make TB propagate. It then appears that D_{GB} decreases as TB propagates from A to B from grain 1 to grain 4 (Fig. 4.53e). Therefore, as transformed band propagates from A (grain 1) to B (grain 4) as shown in Fig. 4.53c & d, the intensity of ASB decreases as the angle between propagating shear band and intersected grains increases from θ_1 (0^o) to θ_4 (approx. 90^o). Grain 4, has the capacity to arrest transformed band because at the tip of the transformed band, the driving force (large strain) required for its formation is not enough; propagation therefore becomes hindered [57]. This could explain the concept of shear band arrest (branching) at B which depends on the angle the propagating shear band makes with the elongated grain. In agreement with this finding, previous study on the formation of adiabatic shear bands in Ti6441 titanium alloys with equiaxed grains and lamella microstructures had also shown that the titanium alloy with the latter microstructure is less susceptible to the formation of ASBs than the former [98]. In conclusion, geometry of the neighbouring grains relative to the shear band propagation direction plays an important role in shear band propagation.

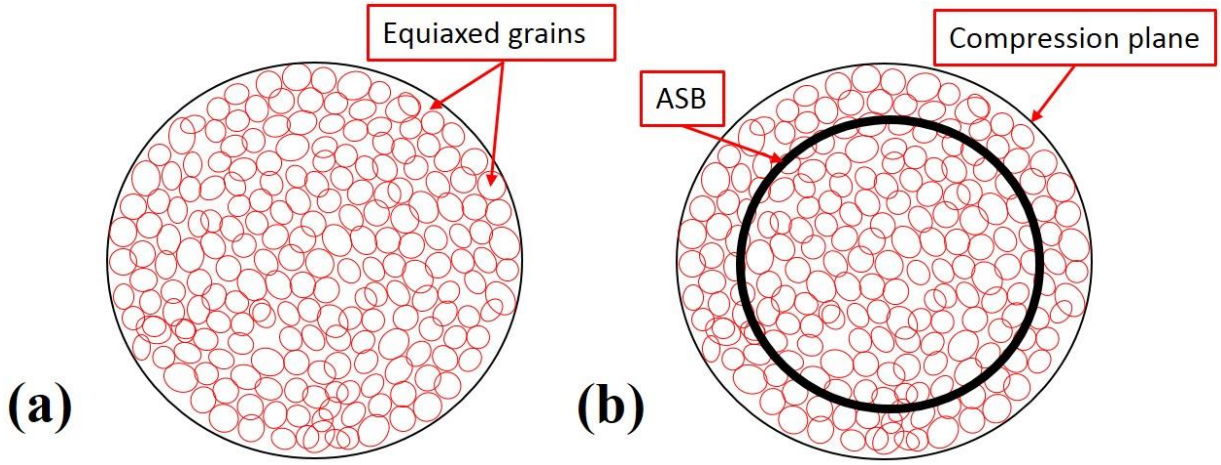

Fig. 4.52. Schematic of adiabatic shear band propagation path in an equiaxed grain structure of AA 2017 and AA 2024 specimens.

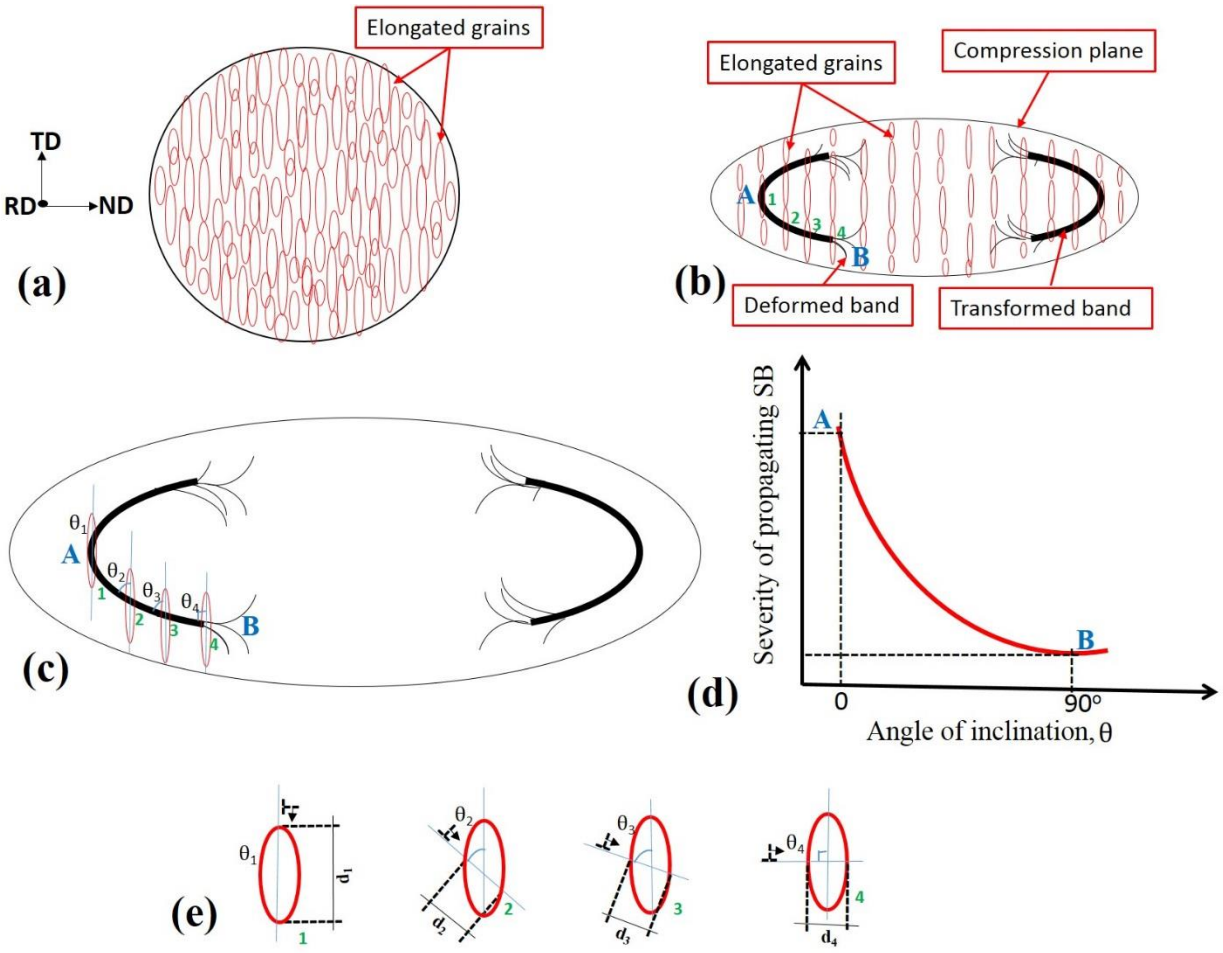

Fig. 4.53. Schematic of adiabatic shear band formation on the compression plane consisting of elongated grain in AA 2624specimens.

4.4.4 Specimens' fragmentation under dynamic impact loading.

In this section, the mode of crack nucleation and propagation leading to specimens fracture in those that fragmented will be discussed. Generally in all age-hardened specimen that formed TB, fracture was initiated by cracks which originated in the transformed bands and propagated inside them. As observed in previous sections, there is no evidence of cracking in the regions outside the transformed bands, not even inside deformed bands. This confirms that fragmentation of the alloys under dynamic impact loading will be triggered by formation and cracking of transformed bands. Transformed bands in steel for instance have been reported to be much harder than the parent material and therefore become more susceptible to cracking [71]. The same hardness profile was observed in aluminum alloy, in which higher hardness in TB was attributed to the strengthening

effects of ultra-fine equiaxed grains and residual deformation structure inside the transformed bands [57].

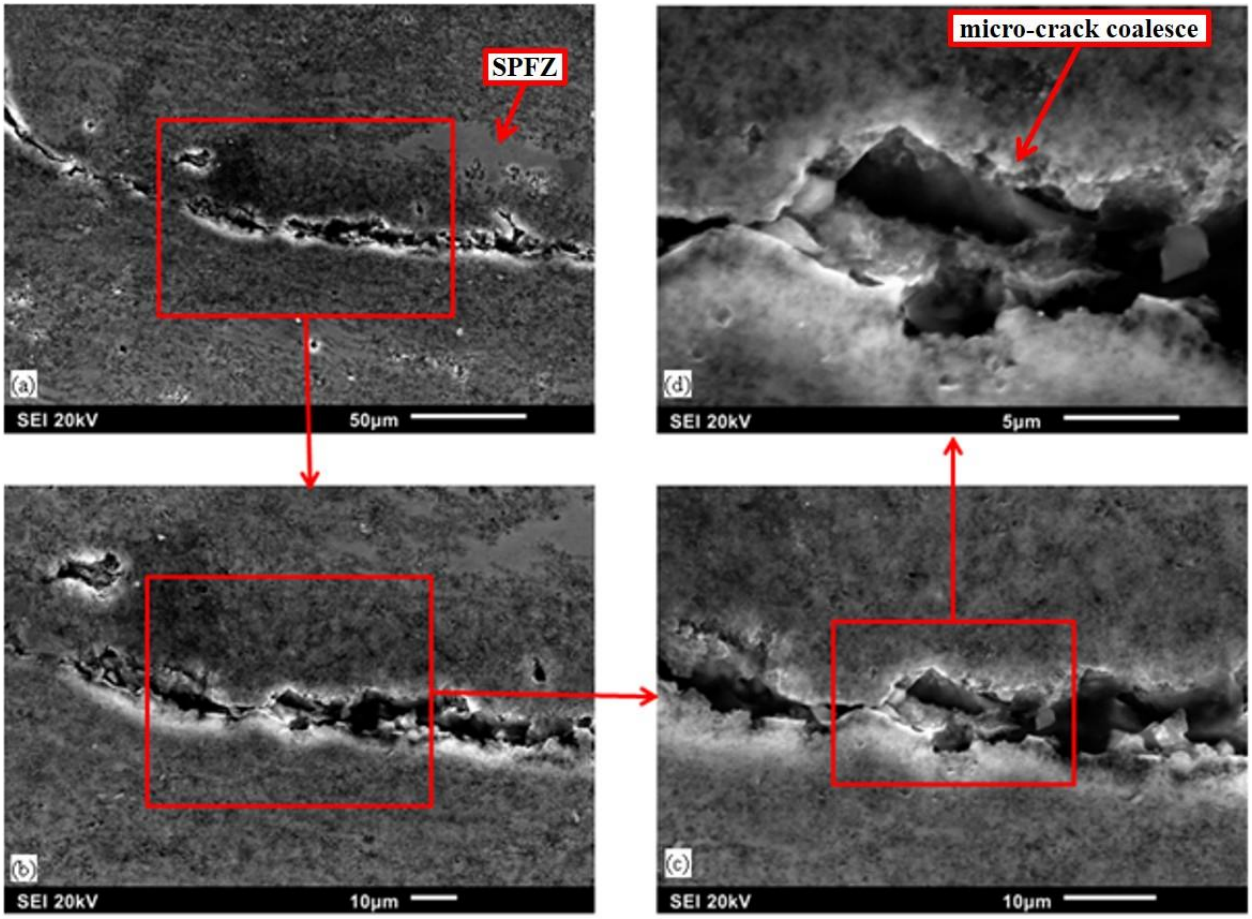

Fig. 4.54. SEM micrographs showing the mode of crack nucleation and propagation along a transformed band in AA 2017-T451 aluminum alloy.

The micrographs shown in Figs. 4.54 and 4.55 illustrate the facture mode along the transformed bands in AA 2017 alloy, which are similar in both precipitation hardened samples. Elliptically shaped micro-voids appear to first form within the transformed band. No micro-voids were observed to nucleate in regions of second phase particles free zone (SPFZ). Ma *et. al* [156] had earlier reported that the SEM fractographs of deformed 5A02-O specimens under quasi-static and dynamic tensile tests shows the presence of the Fe-rich and Mn-rich intermetallics at the bottom of the dimpled fracture surface indicating that the onset of damage comes from the second-phase particles. Aside that nucleation of micro-voids could be influenced by second phase particles in a transformed band; micro-voids could also evolve due to the existence of stress gradients in ASBs.

The existence of the stress gradient in itself has the capacity to generate tensile stress which open voids in the shear band as deformation proceeds under the impact loading [68,72].

Other suggested mechanisms for micro-voids nucleation in metals include, vacancy accumulation at a high stress region, grain boundary sliding, and void nucleation at the head of dislocation pile-ups [93]. As deformation proceeds, micro-voids coalesce and grow into micro-cracks that propagate along the transformed bands (Fig. 4.54). There exist also regions of potential micro-voids nucleation sites that are observed in a low band contrast (darker) at both ends of already formed micro-cracks within the dissolved particles (Fig. 4.55). These potential sites could grow into crack voids that could propagate rapidly along the transformed bands leading to catastrophic fracture. Therefore, the mechanism of failure of the precipitation hardened AA 2017 samples is typical of ductile fracture, occurring sequentially by nucleation, growth and coalescence of micro-voids within the transformed band.

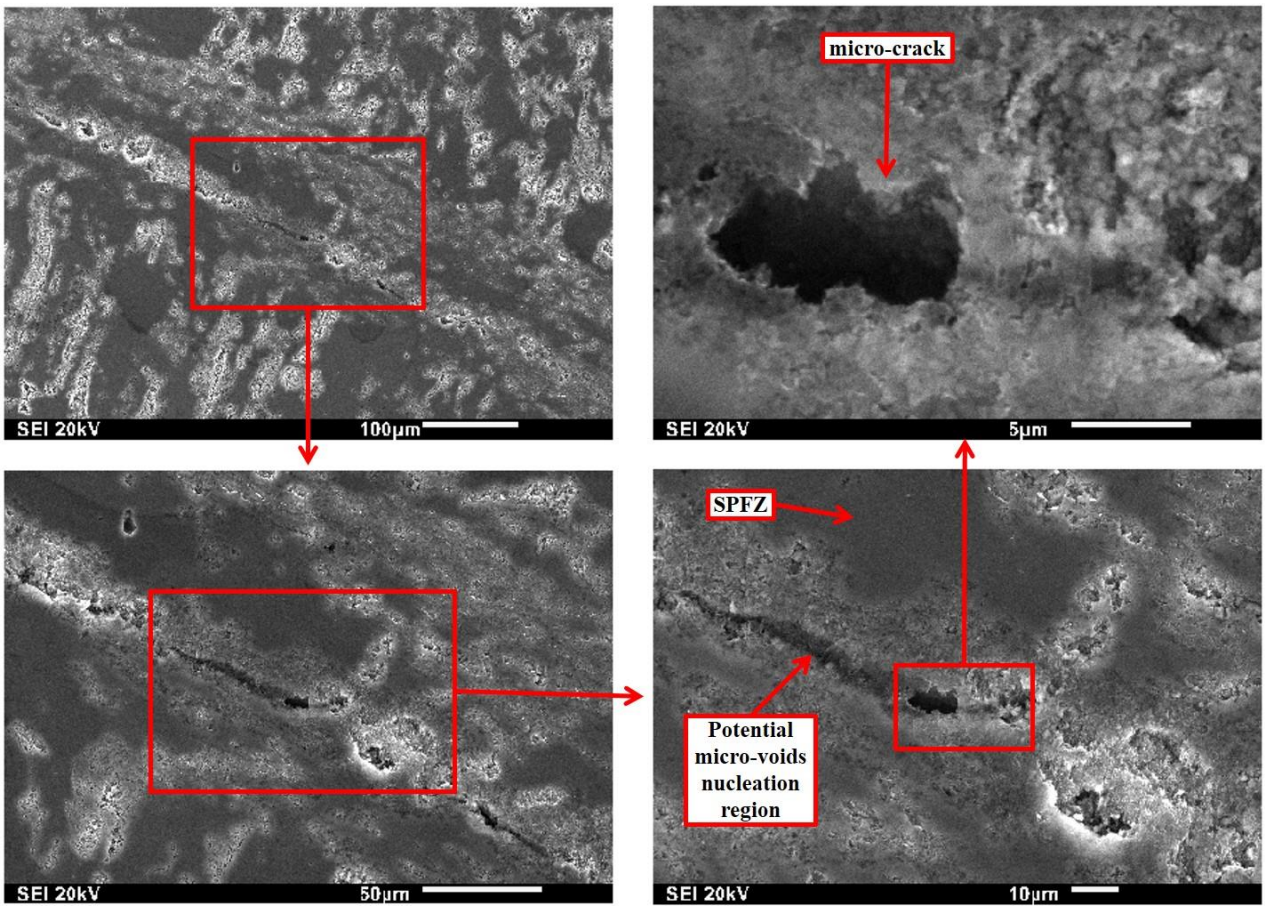

Fig. 4.55. SEM micrographs showing the mode of crack nucleation and propagation along a transformed band in AA 2017-T651 aluminum alloy.

In AA 2024 alloys, the failure mechanisms of the T351 temper specimen are quite different from the T651 temper. The failure mechanisms in 2024-T351 is similar to that explained for AA 2017-T451 specimen. This is because like AA 2017-451 sample, AA 2024-T351 consists of dissolved second phase particles, islands of second particles free zones (SPFZ) and microvoids which appeared in circular clustering of particles as clearly shown in Fig. 4.46a. For AA 2024-T651 specimens, the near-absence of particles inside its transformed shear band makes fracture initiation and propagation more difficult than the AA 2024-T351 sample. This is confirmed by the higher impact momentum and strain rate required to fracture AA 2024-T651 than AA 2024-T351 samples (Table 4.5). The failure mechanism in AA 2624 alloy (T351 and T651 temper) could not be completely deciphered in this study owing to the difficulty in obtaining fractured specimen that could suggest the failure mode on the compression plane. Figure 4.57 indicate the influence of second phase particles to shear band formation and propagation in age-hardened AA 2624 like in the case of AA 2017 (T451 and T651 temper) and AA 2024 (T351) alloys. Hence, sequential nucleation, growth and coalescence of micro-voids within the transformed band could therefore be concluded to be the mode of fracture in the AA 2624 alloy.

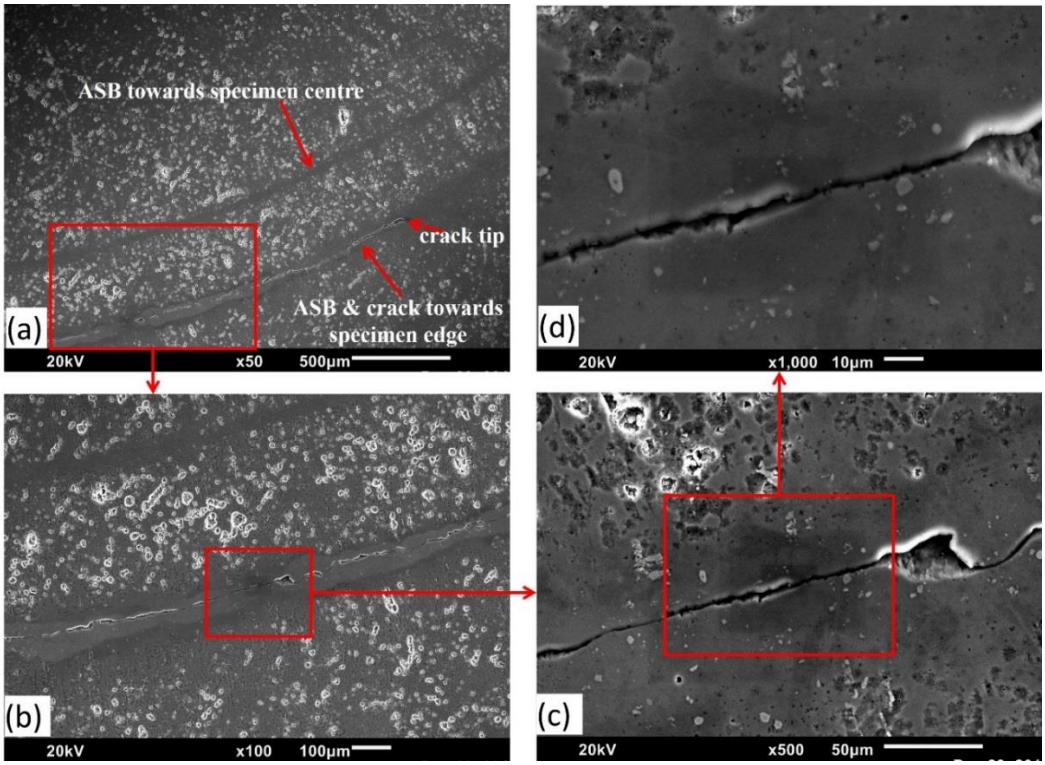

Fig. 4.56. SEM micrographs showing the mode of crack nucleation and propagation along a transformed band in AA 2024-T651 aluminum alloy.

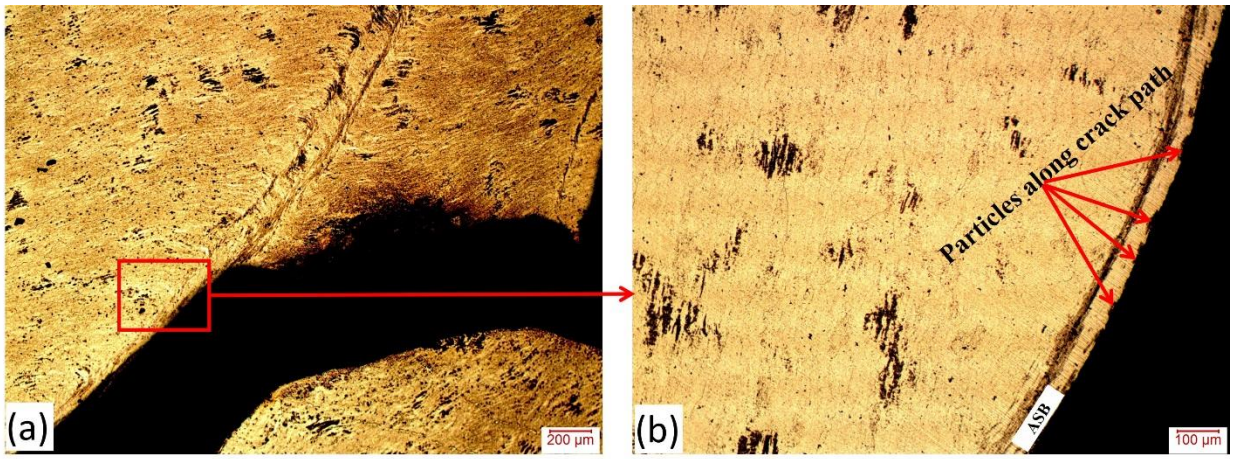

Fig. 4.57. Optical micrographs showing the mode of crack nucleation and propagation along a transformed band in AA 2624-T351 aluminum alloy.

Figure 4.58 shows typical specimens that fragmented under dynamic impact loading at high strain rates. Fracture surface showed two distinct regions; the first (1) is the fracture surface along the conical geometry of ASB while the second (2) is the fracture surface outside the conical geometry of ASB indicating fracture propagation through the bulk material outside the shear band to complete the fragmentation process. SEM fractographic analysis (Figs. 4.59 - 4.61) shows the difference between the fracture mode of 1 and 2. The absence of grain boundaries in the SEM fractographs of both regions suggests that transgranular fracture is the dominant fracture mechanism rather than intergranular [10]. This is anticipated since the shear bands along which cracks initiate and grow do not propagate along grain boundaries. Fracture surface feature on region 1 (ASB region) are mostly elongated coarse dimples which are indication of ductile shear fracture [156] while fine dimples were observed in the region outside ASB. The size of dimple has been reported to have a direct relationship with strength and ductility of an alloy. Fine dimples are characteristics of fractured region with high strength, whereas the reverse holds for fracture surface characterized by coarse dimples [157]. Dimples were also observed by Odeshi and Bassim [93] in the ASB fractured region when the dynamic fracture of a high strength low alloy steel was studied. The results of fractographic study also suggest that fracture mode in these alloys can be influenced by temper condition. For instance, in the AA 2017, AA 2024 and AA 2624 specimens, the artificial aging of the naturally-aged specimens result in the narrowing of elongated dimples in ASB region.

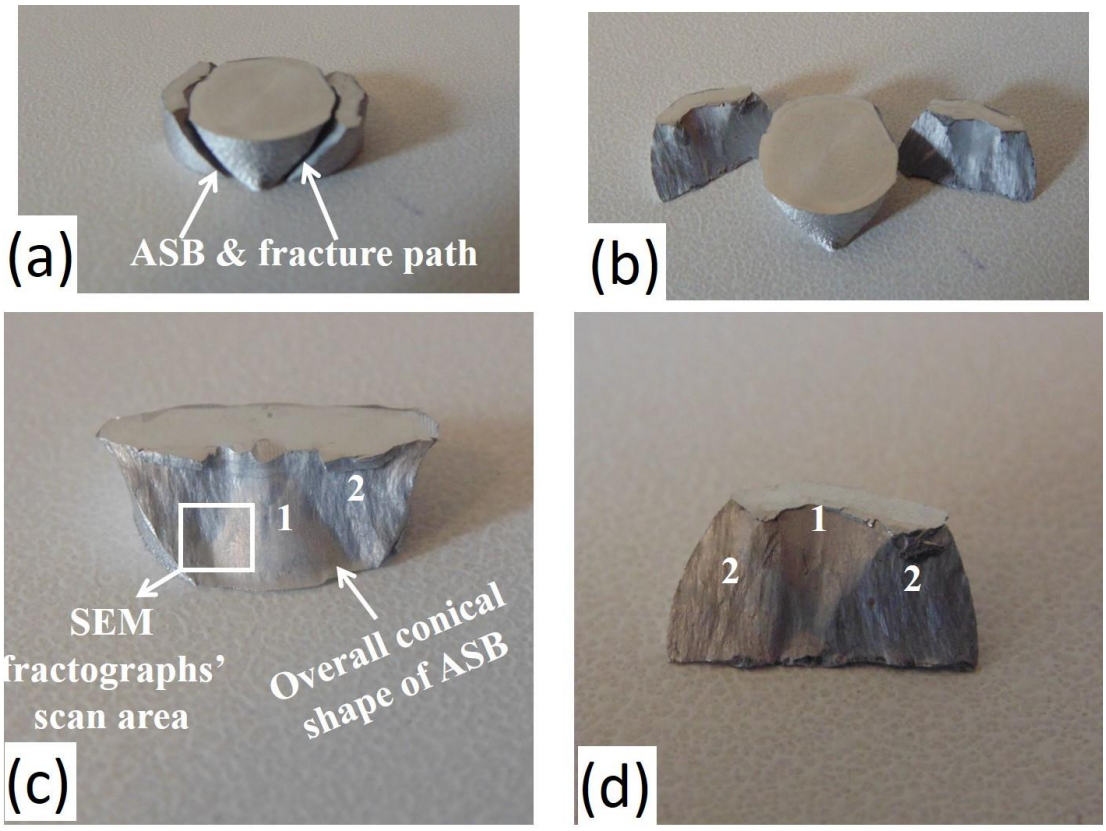

Fig. 4.58. Images of typical fractured specimen of the investigated aluminum alloys. 1 and 2 are the fracture surfaces along (cone) and outside adiabatic shear band region respectively.

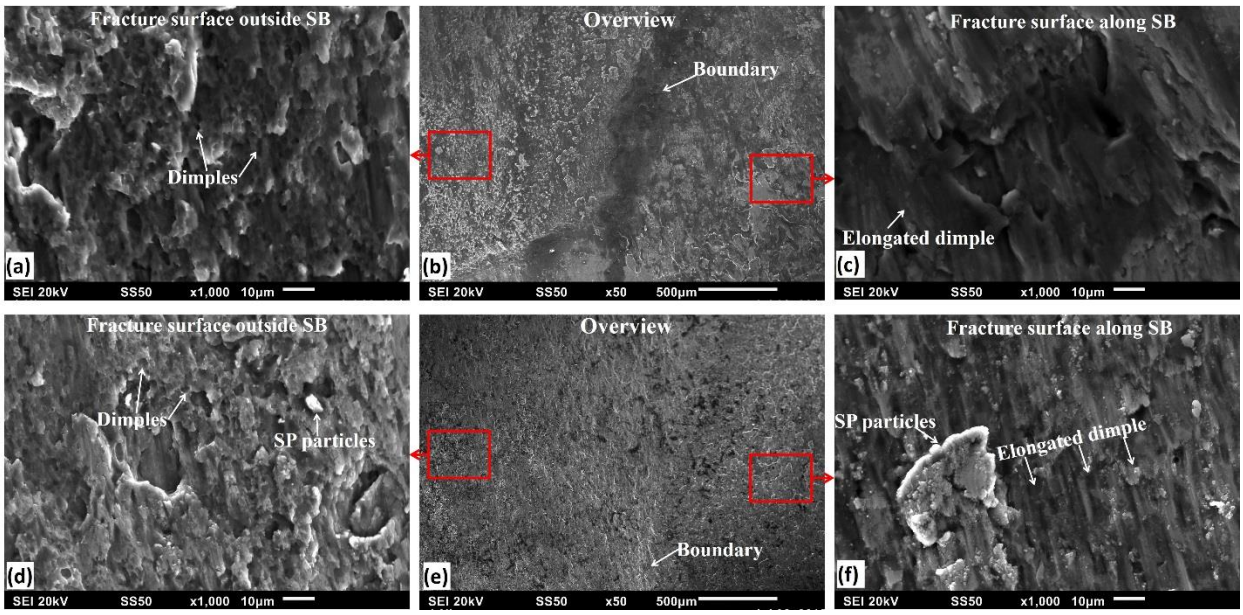

Fig. 4.59. SEM fractographs of AA 2017 alloy specimens in (a-c) T451 and (d-f) T651 temper.

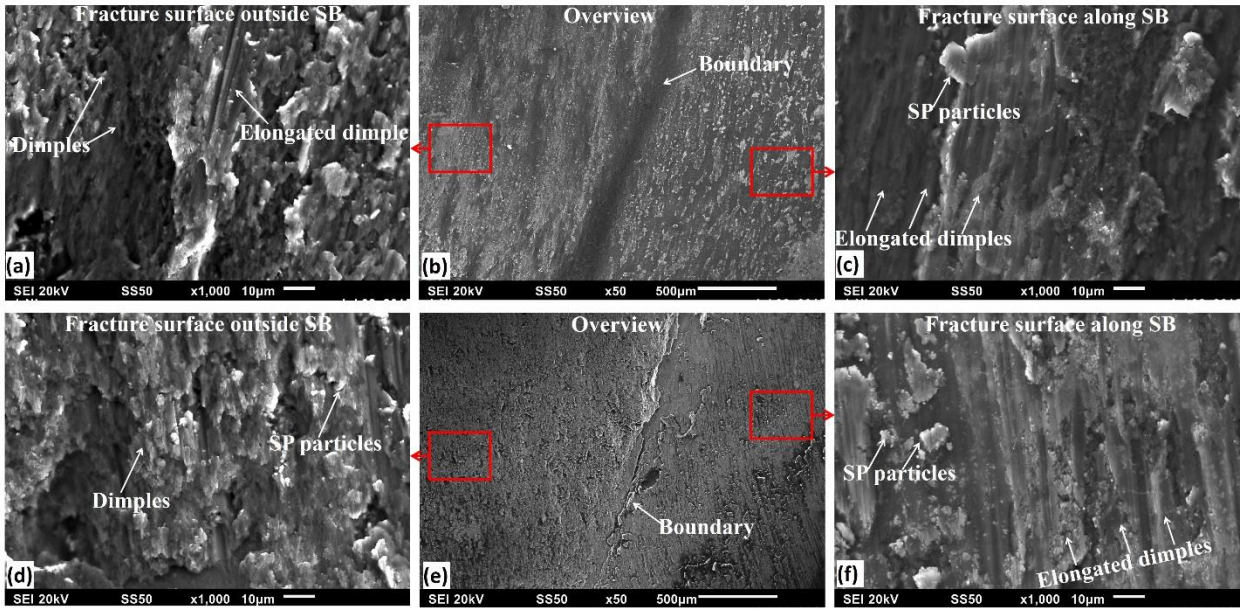

Fig. 4.60. SEM fractographs of AA 2024 alloy specimens in (a-c) T351 and (d-f) T651 temper.

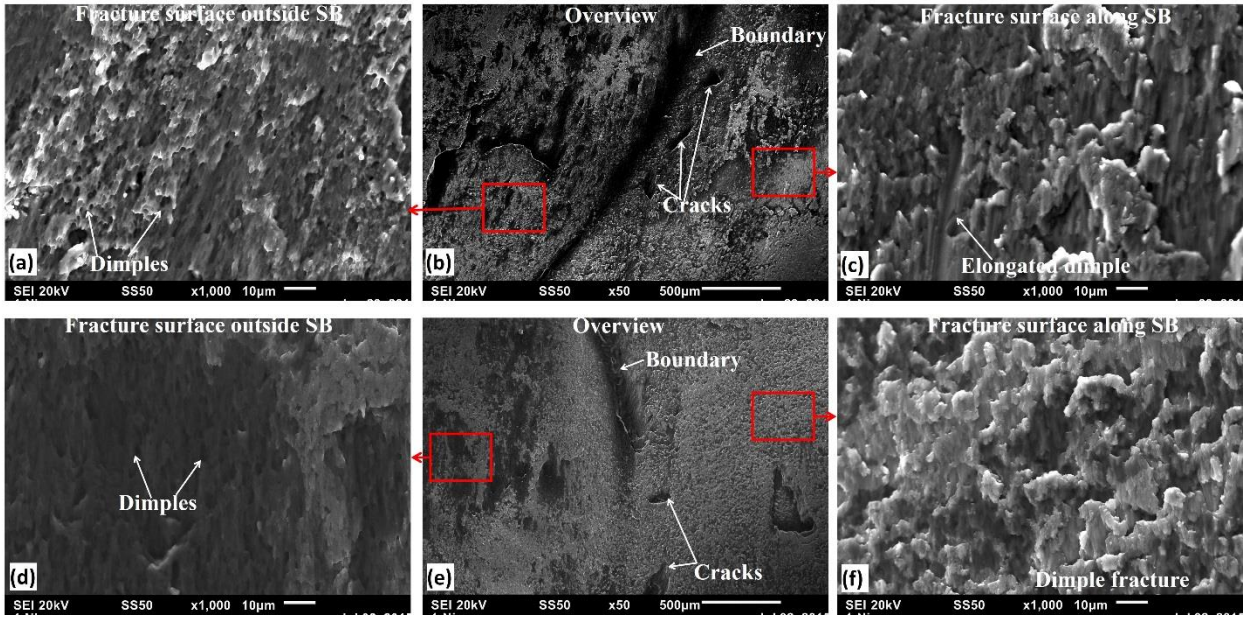

Fig. 4.61. SEM fractographs of AA 2624 alloy specimens in (a-c) T351 and (d-f) T651 temper.

4.5 Electron Backscattered Diffraction (EBSD) Analysis - Texture

Texture analyses of the as-received of only AA 2017-T451 and AA 2624-T351 alloys before and after impact loading were carried out in this study. Texture measurements on AA 2024 alloy could not be done due to equipment break down and shortage of time as at the time of thesis writing.

EBSD inverse pole figure (IPF) maps showing the microstructure of the as-received alloys before dynamic shock loading are presented in Fig. 4.62. These images were taken on a plane perpendicular to axis of the AA 2017-T451 rod and to the rolling direction of the AA 2624-T351 plate. Although the grain morphology could not be clearly characterized using an optical microscopy, however, IPF maps show orientation and morphology of grains in each alloy. On the plane perpendicular to the rolling direction which was the compression plane during impact, the rolled AA 2017 rod showed equiaxed grains while the grains in the AA 2624 are elongated. It will be recalled that schematic presentation of grain morphologies on the compression planes of the alloys (Figs. 4.52 and 4.53) indicate equiaxed for AA 2017 and elongated grains for AA 2624. EBSD measurements were made on the compression plane in the regions where shear bands propagated and at the center of the specimen where no shear band was observed. The IPF maps for the two as-received AA 2017-T451 and AA 2624-T351 alloys are presented in Fig. 4.63. Sketches of the morphologies of ASB as observed on the compression planes of the impacted specimens are reproduced in Fig. 4.63e to show the location of the EBSD measurements (near-the-edge and center). Although optical micrographs shows clear shear bands in both alloys (Figs 4.33 and 4.35), shear bands in the AA 2624 alloy is not clearly visible in the EBSD measurements

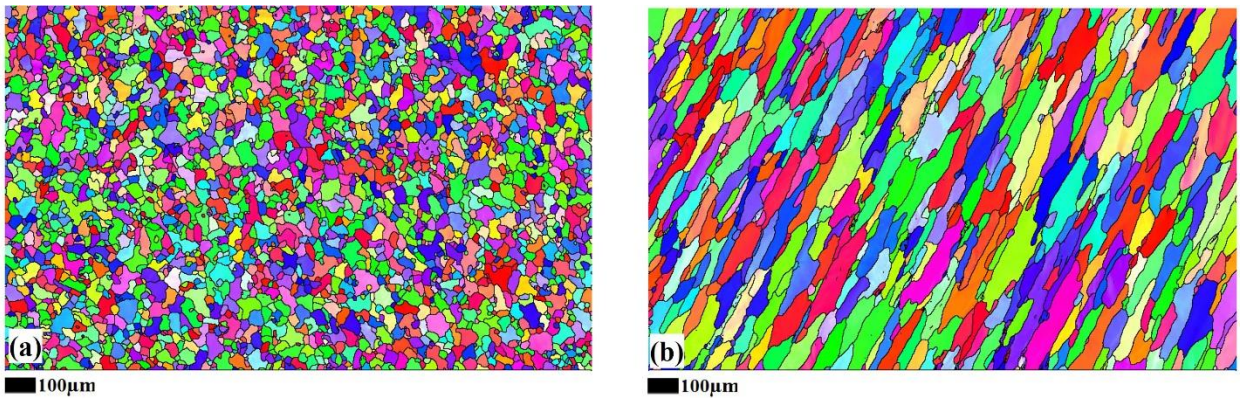

Fig. 4.62. EBSD IPF maps of the as-received (a) AA 2017-T451 and (b) AA 2624-T351 aluminum alloys.

The IPF map of the region close to the edge of the AA2017-T451 alloy shows shear band observed as dark region which could not be indexed. Inability to index the shear bands could be as a result of large strains or extremely fine grains inside the shear band region in this alloy, both of which have been reported in metallic alloys subjected to dynamic shock loading. For example, the strains inside adiabatic shear bands found in HY 100 and AISI 4340 steel were reported to range between

100 and 1000% [158] while TEM investigations have confirmed the presence of nanograins inside of transformed adiabatic shear bands observed in Monel [159]. In the current study, ultrafine grains were observed adjacent to the dark shear band region in the IPF map of AA 2017 alloy, suggesting ultrafine grain inside the transformed band. Ultrafine or nanograins observed inside shear bands are reported to form by dynamic recrystallization as reported in different metallic alloys, including aluminum alloy [142], titanium alloy [160], copper alloy [117], steel [91] and tantalum alloy [161], among others.

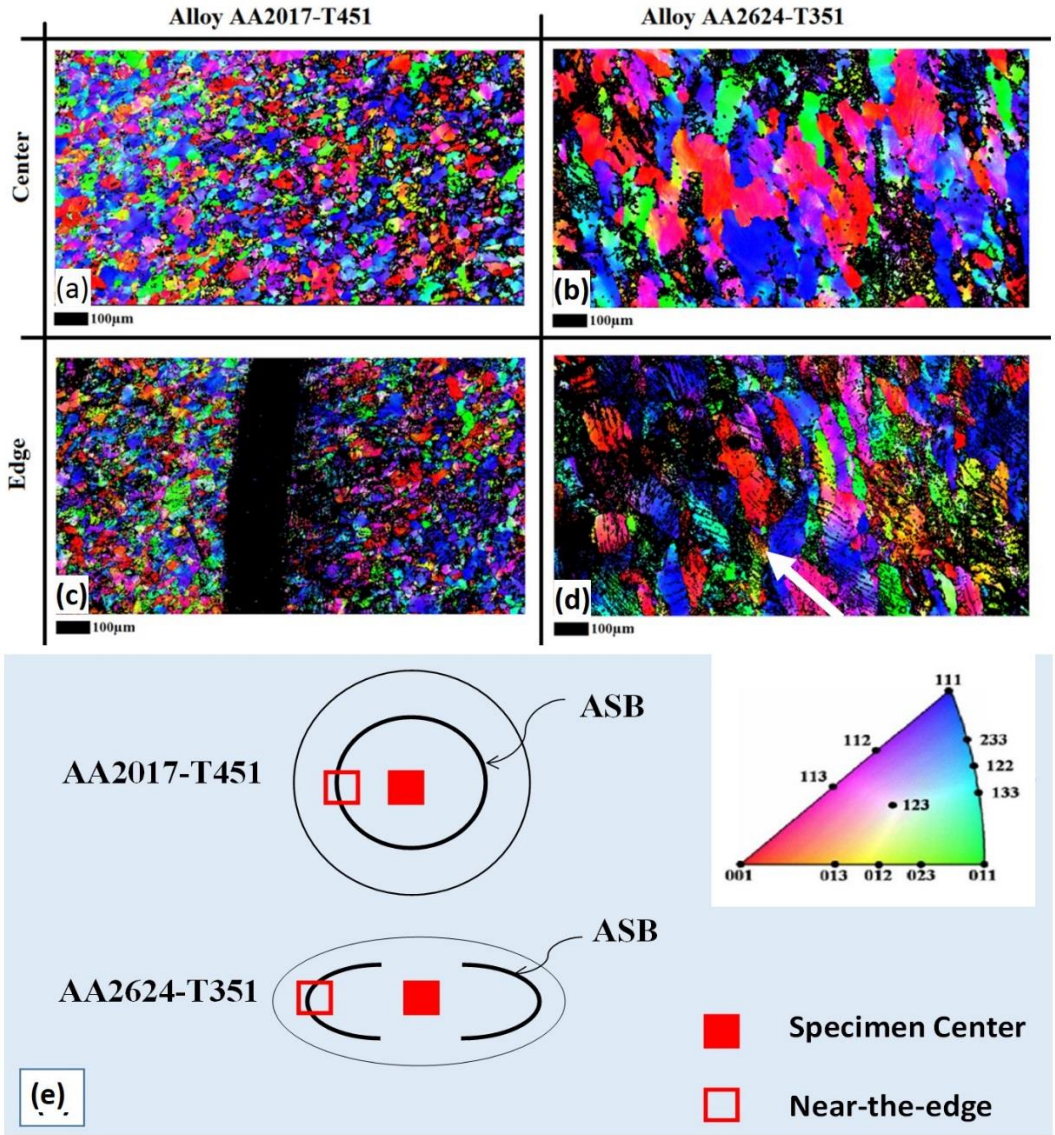

Fig. 4.63. IPF maps of deformed AA2017-T451 and AA2624-T351 at (a-b) center and (c-d) near-the-edge of the compression plane. The arrow indicates two of the grains with significant banded structure. Sketches of shear bands' morphologies on compression plane showing location of EBSD measurements, i.e. center and near-the-edge, are presented in (e).

Ultrafine grains were observed adjacent to the dark shear bands that could not be indexed by EBSD in the AA 2017 alloy (Fig. 4.63). Few grains adjacent to the shear band and far away from the AA 2017 alloy are highlighted in IPF color notation in Fig. 4.64. The DRX grains are distinguished from deformed grains by the spread of orientation in the IPF triangle. The orientation of the grains near the edge of the shear bands converges to a point, which suggests strain free (DRX) grains. On the other hand, the grains far away from the shear bands show a wide orientation spread which is an indication of plastic deformation. The AA 2624-T351 alloy exhibits relatively large grains with curved boundaries. A clear difference is noticeable in the microstructure at the near-the-edge and the center region of the impacted specimens. Significant amount of banded structures, indicated by arrows in Fig. 4.63, were observed within some grains in the near-the-edge region of the deformed AA 2624-T351 specimens, where shear bands were observed under an optical microscope. Previous EBSD measurements on an aluminum alloy [162], pure titanium [163] and two nickel-based [164,165] superalloys, which were also confirmed by TEM studies, show that these band structures are indication of dislocation tangles or networks forming cells. Regions within the bands were observed, from TEM investigation, to be relatively free of dislocations [165]. Based on these results of previous EBSD and TEM measurements, it is suggested that the banded structures indicated by arrows in Fig. 4.63 are dislocation tangle zones [163]. During EBSD measurement, Kikuchi patterns are usually difficult to index where large amount of dislocations are present [164].

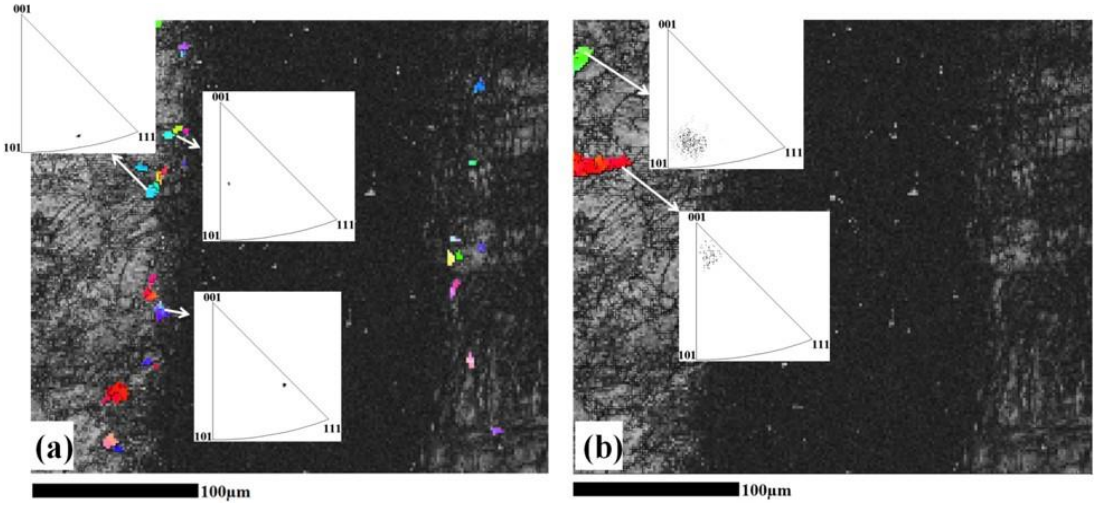

Fig. 4.64. (a) The orientations of the selected grains in AA 2017-T451 near the edge converge to a point; a signature of strain free (DRX) grain and (b) grains far away from the band carries the footprint of deformation indicated as a wide orientation spread.

Although the microstructures of the two alloys in the as-received condition on the plane perpendicular to the rolling direction are morphologically different (Fig. 4.63), they exhibited nearly the same high angle boundary fractions Fig. 4.65. High strain-rate deformation under the same impact momentum however led to higher in-grain misorientation (kernel misorientation) in AA 2624-T351 sample with overall shift in the distribution towards the higher local misorientations for both the center and the edge in comparison with the AA2017-T451 alloy (Fig. 4.66). Also a shift in misorientation distribution is observed from center to edge for both specimens. The average kernel misorientation or local angle misorientation (LAM) is a method used to correlate plastic deformation to misorientation within microstructure [142]. As explained earlier, the banded grain structure in the deformed AA2624-T351 shows evidence of significant dislocation tangle zones that are predominant at the sample edge of AA2624-T351 alloy. Such dislocation tangle zones are characterized by misorientation arrays with misorientation angle between 4 and 9 deg. [166]. A point-to-origin misorientation profile plot, illustrated in Fig. 4.67 for few different CD//<001> grains taken from both center and edge of the sample, shows that grains located at the edge of the samples (along ASB region) exhibit sharp spikes at a regular intervals, indicating large misorientation changes at the shear bands. These are indications of the presence of dislocation tangles or forest as confirmed in EBSD and TEM investigations in previous studies [162-165] and proposed in this paper. The average misorientation of these set of grains (both center and edge) were observed to be nearly same.

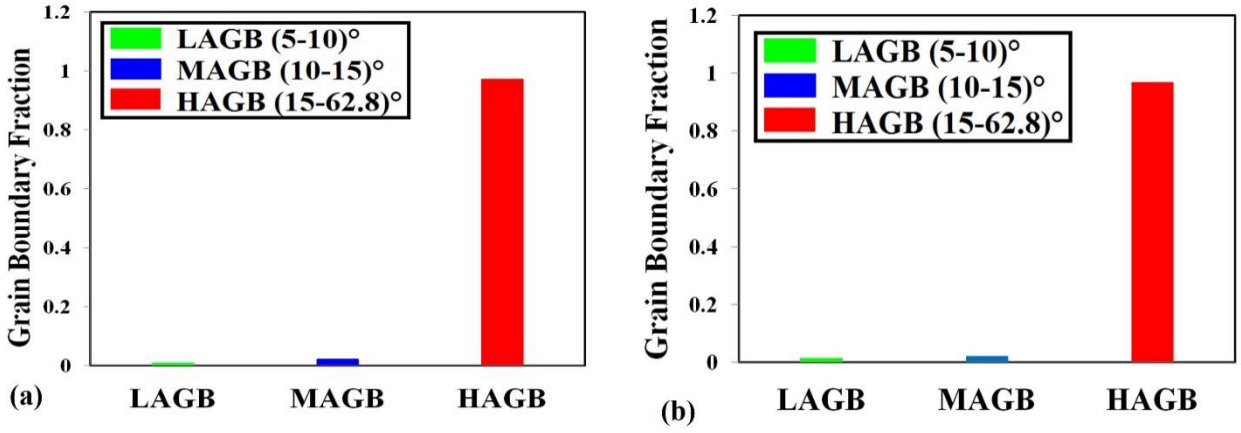

Fig. 4.65. Grain boundary fraction plot for the as-received (a) AA2017-T451 and (b) AA2624-T351 alloy.

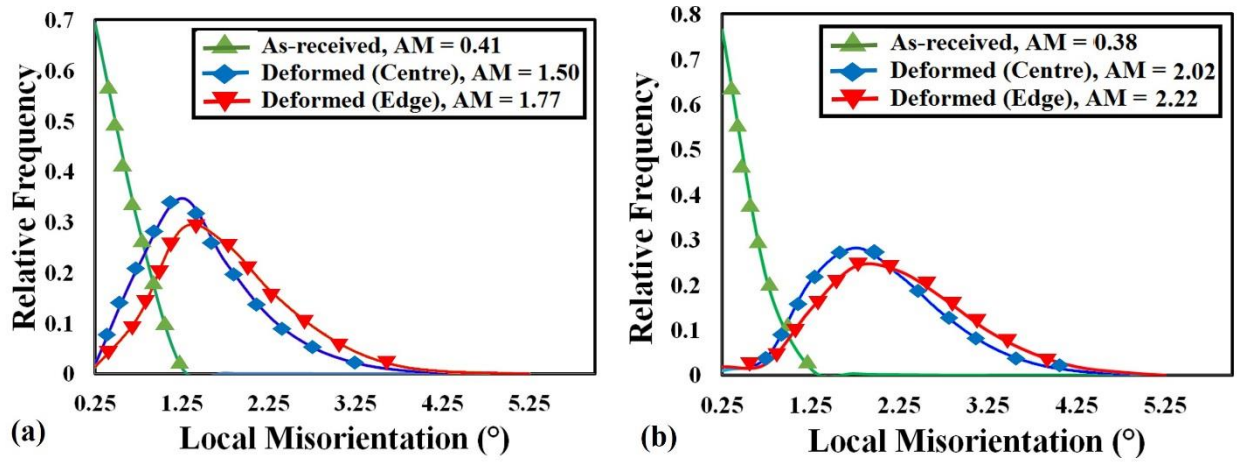

Fig. 4.66. Local average misorientation (Kernel) distribution in (a) AA2017-T451 and (b) AA2624-T351 alloy.

The results of the analysis of the deformation process in both alloys also indicate that LAGBs grow at the expense of HAGBs. The grain boundary fraction plot in Fig. 4.68 suggests that the deformation resulted in dislocation activities leading to increased sub-boundaries with low angle misorientation evolving into LAGBs. The effect is more pronounced in the AA2624-T351 specimen. On the other hand, the more pronounced presence of fine grains with HAGBs in the deformed AA2017-T451 specimen suggests induced partial recovery and dynamic recrystallization of the microstructure leading to more fine and uniform distribution of grains. Evidently, there are noticeable differences in the post compression microstructure for the two alloys in both grain sizes and character of boundaries. It can also be speculated that such differences in grain size and homogeneity of the microstructure was also influenced by the strain rate during compression loading. Though the two alloys were subjected to the same impact momentum, higher strain rates was attained in AA 2017-T451 than attained in AA 2624-T351. The energy stored in dislocations increases with increase in both strain and strain rate [167], and that possibly assisted in faster recovery and recrystallization in the AA2017-T451 alloy leading to lower average misorientation and grain refinement.

Significant texturing is observed to occur with shock loading of the alloys as can be depicted from Fig. 4.69. Development of CD//<111> (within 15 deg tolerance) in both alloys is clearly followed by a decrease in the area fraction of CD//<110> grains. Following the high strain-rate deformation of the as-received alloys, the CD//<110> grains underwent slip deformation accompanied by

rotation to the near CD//<111> orientations. To understand the increased strength of CD//<111> orientation after deformation, the Schmid factor (SF) for different orientations of grains in the as-received microstructures was calculated (Fig. 4.70). SF gives an indication of how easy it is for slip to occur for a particular slip system and load direction for a given orientation of a crystal with the assumption that strain is homogenous throughout the polycrystalline material [168]. In the present study, the active slip system chosen was $(111)[1\bar{1}0]$ along the z-compression direction of the test specimens. The Schmid factor of the as-received alloys were calculated for the orientation at each point and the obtained data are presented in Fig. 70. The white regions in the map represent high SF value corresponding to (111) grains. The SF estimated for (110) orientations (selected few designated "x" in both as-received alloys in Fig. 70a & c) is much lower than other orientations in the microstructures. This implies that the ease at which slip will occur on $(111)[1\bar{1}0]$ slip system for the CD//<110> orientations is low and as such, these set of grains are near hard orientation "forcing" them to rotate to CD//<111> orientation with higher SF [118]. Fig. 70 (b and d) also shows that no grain(s) are of extreme hard orientation since the minimum Schmid factor obtained for both alloys are 0.275 and 0.285 for the deformed AA2017-T451 and AA2624-T351 specimens respectively.

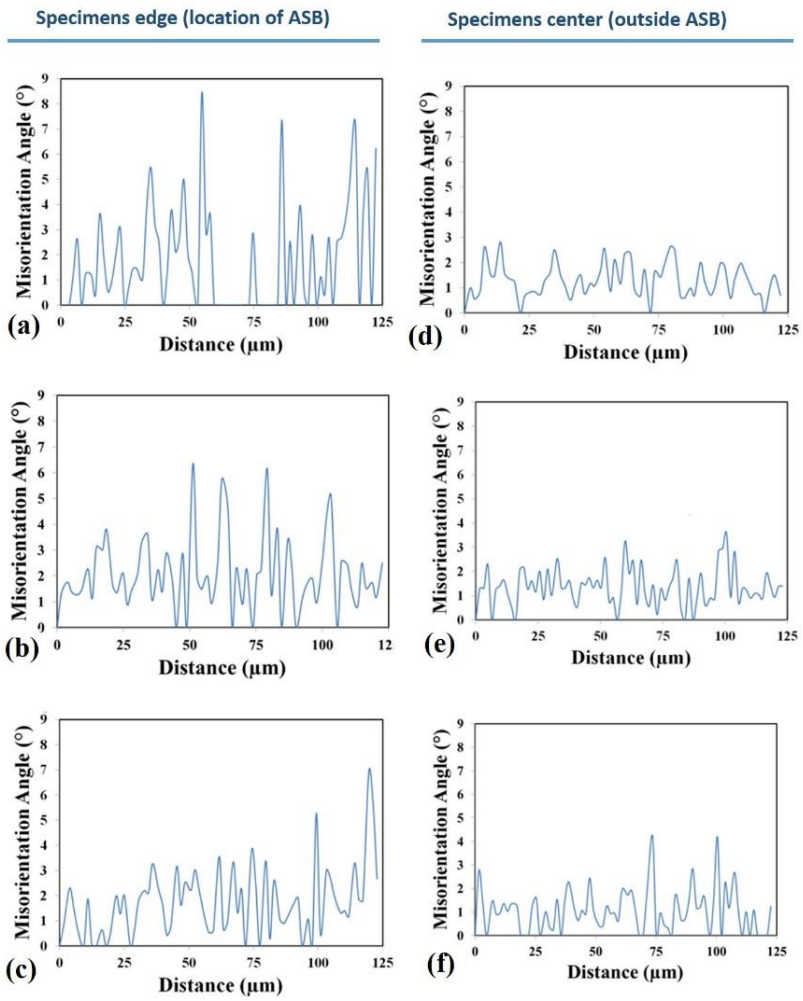

Fig. 4.67. A point-to-origin misorientation profile plots for few different CD//<001> grains taken from both edge (a-c) and center (d-f) of deformed AA2624-T351 sample.

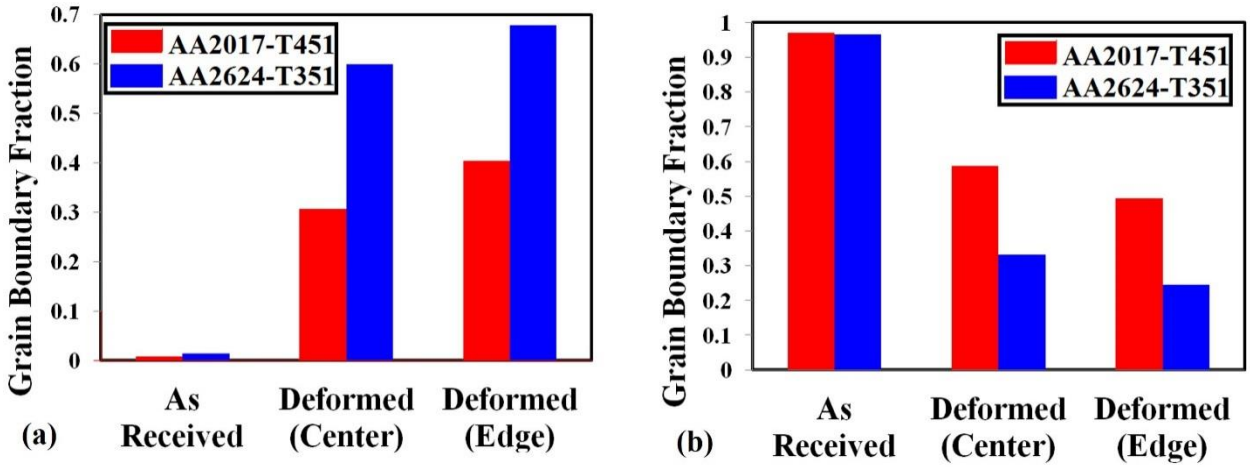

Fig. 4.68. (a) LAGB and (b) HAGB fraction plot for deformed AA2017-T451 and AA2624-T351 aluminum alloys.

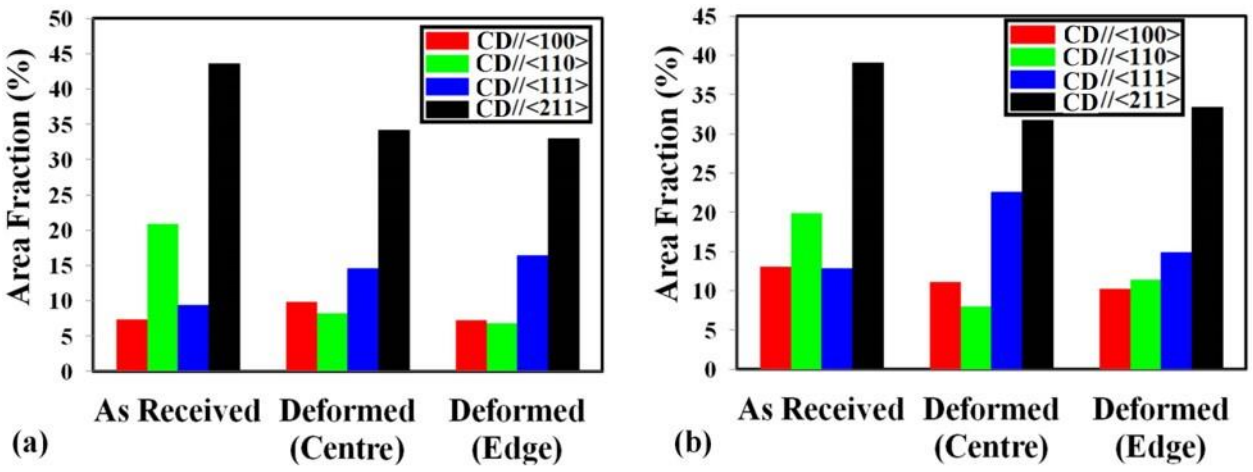

Fig. 4.69. Area fraction of selected fibre (CDs) in impacted (a) AA2017-T451 and (b) AA2624-T351 aluminum alloys.

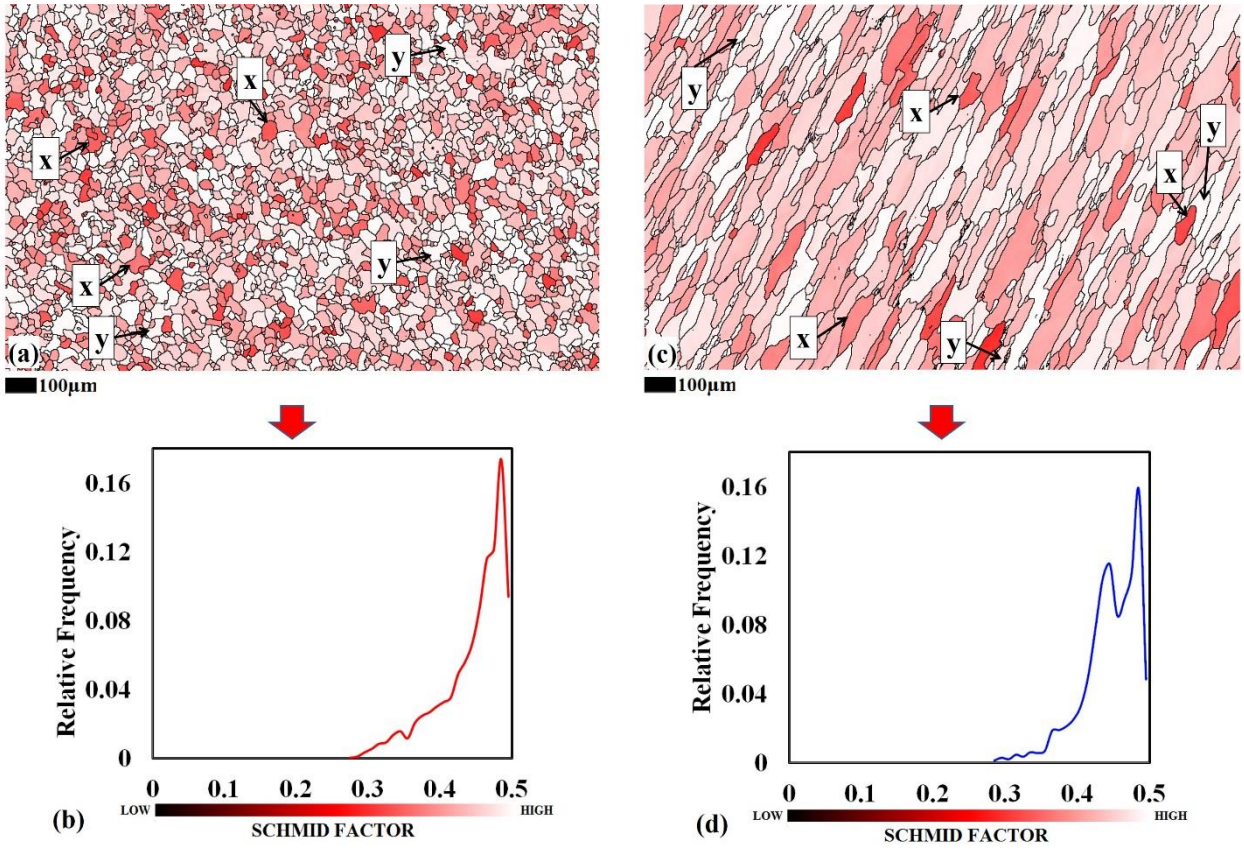

Fig. 4.70. Schmid factor (SF) map and corresponding SF distribution of as-received samples of (a) AA2017-T351 and (b) AA2624-T351: “x” and “y” denotes CD//<110> and CD//<111> orientations respectively.

CHAPTER FIVE

SUMMARY, CONCLUSIONS AND RECOMMENDATIONS

5.1 Summary

The dynamic impact responses of AA 2017, AA 2024 and AA 2624 aluminum alloys were investigated. The alloys received in natural aging condition were machined into cylindrical test specimens, 9.5 mm in diameter and 10.5 mm long. The test specimens for each alloy were divided into three groups. The first group was tested in the as received natural aging condition while the specimens in the second group were artificially aged to produce T651 temper. The last group was annealed to produce O temper before mechanical testing. The results of hardness test, quasi-static compression test, dynamic impact test, microstructure and texture analysis on the as received and heat treated alloys are presented and discussed in this thesis. It was found that the morphology and composition of particles in the investigated alloys are functions of the temper condition. Whereas annealing reduces the hardness of all three alloys, the artificial aging steps reduces the hardness of AA 2017-T451 specimen and increases the hardness of AA 2024-T351 and AA 2624-T351 specimens. Hump-free region on dynamic hardening curves at mid-strain range indicates slip as the deformation mechanism in all the three alloys under both dynamic impact and quasi-static compressive loading. In age-hardened conditions, alloys with low Cu:Mg ratio (AA 2024 and AA 2624) under both quasi-static and dynamic loading shows higher mechanical strength than alloys with high Cu:Mg ratio (AA 2017) which indicates high strengthening effect of Mg additions in the AA 2000 series aluminum. The mechanism of failure of the precipitation hardened specimen of the alloys is typical of ductile fracture occurring sequentially by nucleation, growth, and coalescence of micro-voids inside the transformed bands. Fracture analysis shows that fracture surface feature on ASB region are elongated coarse dimple, while fine dimples were the major characteristics of region outside ASB.

5.2 Conclusions

The following were the fundamental conclusions drawn from this project:

1. Flow softening leading to the formation of ASBs in specimens under quasi-static loading occur once a minimum critical strain value is reached. Meanwhile, ASBs were formed in

specimens under dynamic shock loading once a critical strain and strain rate values are reached.

2. Under both loading conditions, the tendency for strain localization and occurrence of adiabatic shear bands (deformed or transformed) is a function of temper condition, strain, strain rate, strain hardening rate and mechanical strength of the specimen.
3. In the naturally-aged condition, AA 2024 shows higher susceptibility to formation of deformed and transformed band than AA 2624 and AA 2017 in that order, though it (AA 2024) became the least susceptible in the artificially-aged condition.
4. The geometry of ASB on the compression plane is not just a function of sample shape, it also depends on the grain morphology. It was observed that elongated grains can arrest propagating shear band depending on the angle the band makes with elongated grains. The higher the angle of inclination, the lower the tendency for further shear band propagation, and vice-versa.
5. On the texture evolution in the dynamic impact of AA 2017-T451 and AA 2624-T351 alloys, AA 2017-T451 specimen showed a higher tendency for the evolution of ultra-fine DRX grains within the transformed shear band. The grains around the shear band region in AA 2017-T451 has lower in-grain-misorientation and higher fraction of high angle boundaries than those in AA 2624 specimen. High deformation rate leads to the development of CD//<111> orientations at the expense of CD//<110> orientations in both alloys.

5.3 Recommendations for future work

1. Since precipitates are major strength contributor, high resolution TEM should be used to study the structure and morphology of these precipitates and how they are affected by adiabatic heating and intense strain localization during dynamic impact loading of the alloys.
2. Study on the selected alloys, especially the newly-developed AA 2624 alloy under both torsional and tensile loading in quasi-static and dynamic conditions should be explored.
3. Texture analyses on the AA 2024 alloy before and after impact need to be done to determine texture evolution in the alloy during dynamic impact loading.

REFERENCES

[1] M. Zeren, “Effect of copper and silicon content on mechanical properties in Al–Cu–Si–Mg alloys,” *J. Mater. Process. Technol.*, vol. 169, no. 2, pp. 292–298, Nov. 2005.

[2] R. Kilaas and V. Radmilovic, “Structure determination and structure refinement of Al2CuMg precipitates by quantitative high-resolution electron microscopy.,” *Ultramicroscopy*, vol. 88, no. 1, pp. 63–72, Jun. 2001.

[3] S. Hirosawa, T. Sato, A. Kamio, and H. M. Flower, “Classification of the role of microalloying elements in phase decomposition of Al based alloys,” *Acta Mater.*, vol. 48, no. 8, pp. 1797–1806, May 2000.

[4] J. R. Davies, *Alloying: Understanding the basics*, First. Ohio, USA: ASM International, 2001, p. 353.

[5] C. Wolverton, “Crystal structure and stability of complex precipitate phases in Al–Cu–Mg–(Si) and Al–Zn–Mg alloys,” *Acta Mater.*, vol. 49, no. 16, pp. 3129–3142, Sep. 2001.

[6] J. Zhang, Y. N. Huang, C. Mao, and P. Peng, “Structural, elastic and electronic properties of θ (Al2Cu) and S (Al2CuMg) strengthening precipitates in Al–Cu–Mg series alloys: First-principles calculations,” *Solid State Commun.*, vol. 152, no. 23, pp. 2100–2104, Dec. 2012.

[7] G. Sha, R. K. W. Marceau, X. Gao, B. C. Muddle, and S. P. Ringer, “Nanostructure of aluminium alloy 2024: Segregation, clustering and precipitation processes,” *Acta Mater.*, vol. 59, no. 4, pp. 1659–1670, Feb. 2011.

[8] Y. Wang and Z. Jiang, “Dynamic compressive behavior of selected aluminum alloy at low temperature,” *Mater. Sci. Eng. A*, vol. 553, pp. 176–180, 2012.

[9] C. K. S. Moy, M. Weiss, J. Xia, G. Sha, S. P. Ringer, and G. Ranzi, “Influence of heat treatment on the microstructure, texture and formability of 2024 aluminium alloy,” *Mater. Sci. Eng. A*, vol. 552, pp. 48–60, 2012.

[10] D. Steglich, W. Brocks, J. Heerens, and T. Pardoen, “Anisotropic ductile fracture of Al 2024 alloys,” *Eng. Fract. Mech.*, vol. 75, pp. 3692–3706, 2008.

[11] M. Sayuti, A. A D. Sarhan, T. Tanaka, M. Hamdi, and Y. Saito, “Cutting force reduction and surface quality improvement in machining of aerospace duralumin AL-2017-T4 using carbon onion nanolubrication system,” *Int. J. Adv. Manuf. Technol.*, vol. 65, pp. 1493–1500, 2013.

[12] M. Bethencourt, F. J. Botana, M. J. Cano, M. Marcos, J. M. Sánchez-Amaya, and L. González-Rovira, “Behaviour of the alloy AA2017 in aqueous solutions of NaCl. Part I: Corrosion mechanisms,” *Corros. Sci.*, vol. 51, no. 3, pp. 518–524, 2009.

[13] C. Froustey and J. L. Lataillade, “Influence of large pre-straining of aluminium alloys on their residual fatigue resistance,” *Int. J. Fatigue*, vol. 30, pp. 908–916, 2008.

[14] Z. Huda, “Precipitation Strengtehening and Age-Hardening in 2017 Aluminum Alloy for Aerospace Application,” vol. 26, no. 4, pp. 558–564, 2009.

[15] M. Cailler, O. Debbouz, M. Dannawi, and T. Latouche, “Mechanical characterization by dynamical tensile loading of 2017 aluminium alloy joints welded by diffusion bonding,” *J. Mater. Sci.*, vol. 26, pp. 4997–5003, 1991.

[16] M. A Rekik, T. Makhlouf, and N. Njah, “Evolution of microstructural and mechanical properties of an industrial 2017 Aluminium alloy processed by equal channel angular extrusion,” *IOP Conf. Ser. Mater. Sci. Eng.*, vol. 28, p. 012039, 2012.

[17] I. Ozdemir, S. Muecklich, H. Podlesak, and B. Wielage, “Thixoforming of AA 2017 aluminum alloy composites,” *J. Mater. Process. Technol.*, vol. 211, no. 7, pp. 1260–1267, 2011.

[18] C. M. Cepeda-Jiménez, O. A. Ruano, M. Carsí, and F. Carreño, “Study of hot deformation of an Al-Cu-Mg alloy using processing maps and microstructural characterization,” *Mater. Sci. Eng. A*, vol. 552, pp. 530–539, 2012.

[19] J. C. Malas, S. Venugopal, and T. Seshacharyulu, “Effect of microstructural complexity on the hot deformation behavior of aluminum alloy 2024,” *Mater. Sci. Eng. A*, vol. 368, pp. 41–47, 2004.

[20] M. N. Ilman, “Chromate inhibition of environmentally assisted fatigue crack propagation of aluminium alloy AA 2024-T3 in 3.5% NaCl solution,” *Int. J. Fatigue*, vol. 62, pp. 228–235, 2014.

[21] S. Khan, O. Kintzel, and J. Mosler, “Experimental and numerical lifetime assessment of Al 2024 sheet,” *Int. J. Fatigue*, vol. 37, pp. 112–122, 2012.

[22] R. Dolbeer and S. Wright, “Wildlife strikes to civil aircraft in the United States 1990–2007,” *Other Bird Strike Aviat. Mater.*, vol. 24, pp. 1–57, 2008.

[23] G. Gottstein, I. Hurtado, and L. Lo, “Simulation of the evolution of GP zones in Al-Cu alloys : An extended Cahn - Hillard Approach,” *Acta mater.*, vol. 48, pp. 2969–2984, 2000.

[24] S. C. Wang and M. J. Starink, “Precipitates and intermetallic phases in precipitation hardening Al–Cu–Mg–(Li) based alloys,” *Int. Mater. Rev.*, vol. 50, no. 4, pp. 193–215, Aug. 2005.

[25] K. Raviprasad, C. . Hutchinson, T. Sakurai, and S. . Ringer, “Precipitation processes in an Al-2.5Cu-1.5Mg (wt. %) alloy microalloyed with Ag and Si,” *Acta Mater.*, vol. 51, no. 17, pp. 5037–5050, Oct. 2003.

[26] M. Wierzbinska and J. Sieniawski, “Microstructural Changes of Al-Cu Alloys After Prolonged Annealing at Elevated Temperature,” *Recent Trends Process. Degrad. Alum. Alloy.*, 2011.

[27] S. P. Ringer and K. Hono, “Microstructural Evolution and Age Hardening inmAluminium Alloys : Atom Probe Field-Ion Microscopy and Transmission Electron Microscopy Studies,” 2000.

[28] Y. Jing, C. Li, Z. Du, F. Wang, and Y. Song, “The thermodynamic analysis of Guinier-Preston zones in aged supersaturated Al-Cu alloys,” *Calphad Comput. Coupling Phase Diagrams Thermochem.*, vol. 32, pp. 164–170, 2008.

[29] M. Karlík and B. Jouffrey, “High resolution electron microscopy study of Guinier-Preston (GP1) zones in Al-Cu based alloys,” *Acta Mater.*, vol. 45, no. 8, pp. 3251–3263, 1997.

[30] M. Karlík, B. Jouffrey, and S. Belliot, “The copper content of Guinier–Preston (GP1) zones in Al–1.84 at.% Cu alloy,” *Acta Mater.*, vol. 46, no. 5, pp. 1817–1825, 1998.

[31] Richard W. Hertzberg, *Deformation and Fracture Mechanics of Engineering Materials*, Fourth. USA: John Wily & Sons, Inc, 1996, pp. 125–142.

[32] T. Nakajima, M. Takeda, and T. Endo, “Strain Enhanced Precipitate Coarsening during Creep of a Commercial Magnesium Alloy AZ80,” *Mater. Trans.*, vol. 47, no. 4, pp. 1098–1104, 2006.

[33] P. I. Gouma, D. Lloyd, and M. Mills, “Precipitation processes in Al–Mg–Cu alloys,” *Mater. Sci. Eng. A*, vol. 319–321, pp. 439–442, Dec. 2001.

[34] S. C. Wang and M. J. Starink, “Two types of S phase precipitates in Al–Cu–Mg alloys,” *Acta Mater.*, vol. 55, no. 3, pp. 933–941, Feb. 2007.

[35] Z. Zhang, B. L. Xiao, and Z. Y. Ma, “Hardness recovery mechanism in the heat-affected zone during long-term natural aging and its influence on the mechanical properties and fracture behavior of friction stir welded 2024Al–T351 joints,” *Acta Mater.*, vol. 73, pp. 227–239, Jul. 2014.

[36] M. J. Starink and S. C. Wang, “The thermodynamics of and strengthening due to co-clusters: General theory and application to the case of Al–Cu–Mg alloys,” *Acta Mater.*, vol. 57, no. 8, pp. 2376–2389, May 2009.

[37] A. Charai, T. Walther, C. Alfonso, A. Zahra, and C. Y. Zahra, “Coexistence of clusters , GPB zones , S"- , S ’ - and S-phases in an Al-0.9% Cu-1.4% Mg alloy,” vol. 48, pp. 2751–2764, 2000.

[38] P. Ratchev, B. Verlinden, P. De. Smet, and P. Van Houtte, “Precipitation hardening of an Al-4.2 wt% Mg-0.6 wt% Cu alloy,” vol. 46, no. 10, 1998.

[39] S. C. Wang and M. J. Starink, “Precipitates and intermetallic phases in precipitation hardening Al–Cu–Mg–(Li) based alloys,” *Int. Mater. Rev.*, vol. 50, no. 4, pp. 193–215, Aug. 2005.

[40] S. P. Ringer, S. K. Caraher, and I. J. Polmear, “Response to comments on cluster hardening in an aged Al-Cu-Mg alloy,” *Scr. Mater.*, vol. 39, no. 11, pp. 1559–1567, Nov. 1998.

[41] S. Ringer, T. Sakurai, and I. Polmear, “Origins of hardening in aged Al- Cu-Mg-(Ag) alloys,” *Acta Mater.*, vol. 45, no. 9, pp. 3731–3744, 1997.

[42] L. Kovarik, M. K. Miller, S. A. Court, and M. J. Mills, “Origin of the modified orientation relationship for S(S″)-phase in Al–Mg–Cu alloys,” *Acta Mater.*, vol. 54, no. 7, pp. 1731–1740, Apr. 2006.

[43] V. Radmilovic, R. Kilaas, U. Dahmen, and G. J. Shiflet, “Structure and morphology of S-phase precipitates in aluminum,” *Acta Mater.*, vol. 47, no. 15–16, pp. 3987–3997, Nov. 1999.

[44] Z. R. Liu, J. H. Chen, S. B. Wang, D. W. Yuan, M. J. Yin, and C. L. Wu, “The structure and the properties of S-phase in AlCuMg alloys,” *Acta Mater.*, vol. 59, no. 19, pp. 7396–7405, Nov. 2011.

[45] L. F. Mondolfo, *Aluminum Alloys - Structure and Properties*. Butterworths, London: Elsevier, 1976, pp. 497–505.

[46] J. R. Davis, “Tensile Testing,” J. R. Davis, Ed. Ohio, USA: ASM International, 2004, p. 13.

[47] G. Owolabi, D. Odoh, A. Peterson, A. Odeshi, and H. Whitworth, “Measurement of the Deformation of Aluminum Alloys under High Strain Rates Using High Speed Digital Cameras,” *World J. Mech.*, vol. 03, no. 02, pp. 112–121, 2013.

[48] Y. B. Xu, W. L. Zhong, Y. J. Chen, L. T. Shen, Q. Liu, Y. L. Bai, and M. A. Meyers, “Shear localization and recrystallization in dynamic deformation of 8090 Al–Li alloy,” *Mater. Sci. Eng. A*, vol. 299, no. 1–2, pp. 287–295, Feb. 2001.

[49] J. Luo and M. Q. Li, “Strain rate sensitivity and strain hardening exponent during the isothermal compression of Ti60 alloy,” *Mater. Sci. Eng. A*, vol. 538, pp. 156–163, 2012.

[50] S. Nemat-Naser, “Introduction to high strain-rate testing, high strain rate tension and compression tests,” in *ASM Handbook Vol 8*, 2000, pp. 942–55.

[51] S. E. Schoenfeld and T. W. Wright, “A failure criterion based on material instability,” *Int. J. Solids Struct.*, vol. 40, no. 12, pp. 3021–3037, Jun. 2003.

[52] F. Jiang, H. Zhang, L. Li, and J. Chen, “The kinetics of dynamic and static softening during multistage hot deformation of 7150 aluminum alloy,” *Mater. Sci. Eng. A*, vol. 552, pp. 269–275, Aug. 2012.

[53] B. Verlinden, A. Suhadi, and L. Delaey, “A generalized constitutive equation for an AA6060 aluminium alloy,” *Scr. Metall. Mater.*, vol. 28, no. 11, pp. 1441–1446, Jun. 1993.

[54] B. L. Zhang, M. S. Maclean, and T. N. Baker, “Hot deformation behaviour of aluminium alloy 6061 / SiC p MMCs made by powder metallurgy route,” vol. 16, no. August, pp. 897–902, 2000.

[55] B. Zhang and T. N. Baker, “Effect of the heat treatment on the hot deformation behaviour of AA6082 alloy,” *J. Mater. Process. Technol.*, vol. 153–154, pp. 881–885, Nov. 2004.

[56] J. Peirs, W. Tirry, B. Amin-Ahmadi, F. Coghe, P. Verleysen, L. Rabet, D. Schryvers, and J. Degrieck, “Microstructure of adiabatic shear bands in Ti6Al4V,” *Mater. Charact.*, vol. 75, pp. 79–92, Jan. 2013.

[57] D. H. Li, Y. Yang, T. Xu, H. G. Zheng, Q. S. Zhu, and Q. M. Zhang, “Observation of the microstructure in the adiabatic shear band of 7075 aluminum alloy,” *Mater. Sci. Eng. A*, vol. 527, no. 15, pp. 3529–3535, Jun. 2010.

[58] C. Z. Duan and L. C. Zhang, “Adiabatic shear banding in AISI 1045 steel during high speed machining: Mechanisms of microstructural evolution,” *Mater. Sci. Eng. A*, vol. 532, pp. 111–119, Jan. 2012.

[59] D. L. Zou, B. F. Luan, Q. Liu, L. J. Chai, and J. W. Chen, “Characterization of adiabatic shear bands in the zirconium alloy impacted by split Hopkinson pressure bar at a strain rate of 6000s−1,” *Mater. Sci. Eng. A*, vol. 558, pp. 517–524, Dec. 2012.

[60] D. Yang, Y. An, P. Cizek, and P. Hodgson, “Development of adiabatic shear band in cold-rolled titanium,” *Mater. Sci. Eng. A*, vol. 528, no. 12, pp. 3990–3997, May 2011.

[61] Y. Yang, F. Jiang, B. M. Zhou, X. M. Li, H. G. Zheng, and Q. M. Zhang, “Microstructural characterization and evolution mechanism of adiabatic shear band in a near beta-Ti alloy,” *Mater. Sci. Eng. A*, vol. 528, no. 6, pp. 2787–2794, Mar. 2011.

[62] V. F. Nesterenko, M. A. Meyers, and T. W. Wright, “Self-organization in the initiation of adiabatic shear bands,” *Acta Mater.*, vol. 46, no. 1, pp. 327–340, Dec. 1998.

[63] D. L. Zou, L. Zhen, C. Y. Xu, and W. Z. Shao, “Characterization of adiabatic shear bands in AM60B magnesium alloy under ballistic impact,” *Mater. Charact.*, vol. 62, no. 5, pp. 496–502, May 2011.

[64] L. Zhen, D. L. Zou, C. Y. Xu, and W. Z. Shao, “Microstructure evolution of adiabatic shear bands in AM60B magnesium alloy under ballistic impact,” *Mater. Sci. Eng. A*, vol. 527, pp. 5728–5733, 2010.

[65] M. Ping-li, Y. Jin-cheng, L. Zheng, and D. Yang, “Microstructure evolution of extruded Mg-Gd-Y magnesium alloy under dynamic compression,” *J. Magnes. Alloy.*, vol. 1, no. 1, pp. 64–75, 2013.

[66] B. Hwang, S. Lee, Y. C. Kim, N. J. Kim, and D. H. Shin, “Microstructural development of adiabatic shear bands in ultra-fine-grained low-carbon steels fabricated by equal channel angular pressing,” *Mater. Sci. Eng. A*, vol. 441, pp. 308–320, 2006.

[67] F. Yuan, P. Jiang, and X. Wu, “Annealing effect on the evolution of adiabatic shear band under dynamic shear loading in ultra-fine-grained iron,” *Int. J. Impact Eng.*, vol. 50, pp. 1–8, Dec. 2012.

[68] H. M. Ghomi and A. G. Odeshi, “The effects of microstructure, strain rates and geometry on dynamic impact response of a carbon–manganese steel,” *Mater. Sci. Eng. A*, vol. 532, pp. 308–315, Jan. 2012.

[69] Z. P. Wan, Y. E. Zhu, H. W. Liu, and Y. Tang, “Microstructure evolution of adiabatic shear bands and mechanisms of saw-tooth chip formation in machining Ti6Al4V,” *Mater. Sci. Eng. A*, vol. 531, pp. 155–163, Jan. 2012.

[70] X. Teng, T. Wierzbicki, and H. Couque, “On the transition from adiabatic shear banding to fracture,” *Mech. Mater.*, vol. 39, no. 2, pp. 107–125, Feb. 2007.

[71] S. Boakye-Yiadom and M. N. Bassim, “Effect of prior heat treatment on the dynamic impact behavior of 4340 steel and formation of adiabatic shear bands,” *Mater. Sci. Eng. A*, vol. 528, no. 29–30, pp. 8700–8708, Nov. 2011.

[72] Y. Xu, J. Zhang, Y. Bai, and M. A. Meyers, “Shear Localization in Dynamic Deformation: Microstructural Evolution,” *Metall. Mater. Trans. A*, vol. 39, no. 4, pp. 811–843, Feb. 2008.

[73] M. J. Hadianfard, R. Smerd, S. Winkler, and M. Worswick, “Effects of strain rate on mechanical properties and failure mechanism of structural Al–Mg alloys,” *Mater. Sci. Eng. A*, vol. 492, no. 1–2, pp. 283–292, Sep. 2008.

[74] M. A. Zikry, M. R. Pothier, and J. N. Baucom, “High strain-rate shear-strain localization in f . c . c . crystalline materials : a perturbation analysis,” vol. 37, 2000.

[75] Q. Xue, J. F. Bingert, B. L. Henrie, and G. T. Gray, “EBSD characterization of dynamic shear band regions in pre-shocked and as-received 304 stainless steels,” *Mater. Sci. Eng. A*, vol. 473, no. 1–2, pp. 279–289, Jan. 2008.

[76] H. Y. Wang, E. S. Xue, W. Xiao, Z. Liu, J. B. Li, and Q. C. Jiang, "Influence of grain size on deformation mechanisms in rolled Mg–3Al–3Sn alloy at room temperature," *Mater. Sci. Eng. A*, vol. 528, no. 29–30, pp. 8790–8794, Nov. 2011.

[77] H. Asgari, J. A. Szpunar, and A. G. Odeshi, "Texture evolution and dynamic mechanical behavior of cast AZ magnesium alloys under high strain rate compressive loading," *Mater. Des.*, vol. 61, pp. 26–34, Sep. 2014.

[78] L. Jiang, J. J. Jonas, A. A. Luo, A. K. Sachdev, and S. Godet, "Influence of {10-12} extension twinning on the flow behavior of AZ31 Mg alloy," *Mater. Sci. Eng. A*, vol. 445–446, pp. 302–309, 2007.

[79] E. El-Danaf, S. R. Kalidindi, and R. D. Doherty, "Influence of deformation path on the strain hardening behavior and microstructure evolution in low SFE FCC metals," *Int. J. Plast.*, vol. 17, pp. 1245–1265, 2001.

[80] A. A. Salem, S. R. Kalidindi, and R. D. Doherty, "Strain hardening of titanium: Role of deformation twinning," *Acta Mater.*, vol. 51, pp. 4225–4237, 2003.

[81] A. S. Khan, A. Pandey, T. Gnäupel-Herold, and R. K. Mishra, "Mechanical response and texture evolution of AZ31 alloy at large strains for different strain rates and temperatures," *Int. J. Plast.*, vol. 27, no. 5, pp. 688–706, 2011.

[82] R. Korla and A. H. Chokshi, "Strain-rate sensitivity and microstructural evolution in a Mg-Al-Zn alloy," *Scr. Mater.*, vol. 63, no. 9, pp. 913–916, 2010.

[83] Y. Yang, H. G. Zheng, Z. J. Shi, and Q. M. Zhang, "Effect of orientation on self-organization of shear bands in 7075 aluminum alloy," *Mater. Sci. Eng. A*, vol. 528, no. 6, pp. 2446–2453, Mar. 2011.

[84] Q. Xue, M. A. Meyers, and V. F. Nesterenko, "Self-organization of shear bands in titanium and Ti-6Al-4V alloy," *Acta Mater.*, vol. 50, pp. 575–596, 2002.

[85] Y. Yang, Y. Zeng, D. H. Li, and M. Li, "Damage and fracture mechanism of aluminium alloy thick-walled cylinder under external explosive loading," *Mater. Sci. Eng. A*, vol. 490, no. 1–2, pp. 378–384, Aug. 2008.

[86] Y. Yang, D. H. Li, H. G. Zheng, X. M. Li, and F. Jiang, "Self-organization behaviors of shear bands in 7075 T73 and annealed aluminum alloy," *Mater. Sci. Eng. A*, vol. 527, no. 1–2, pp. 344–354, Dec. 2009.

[87] A. G. Odeshi, A. O. Adesola, and A. Y. Badmos, "Failure of AA 6061 and 2099 aluminum alloys under dynamic shock loading," *Eng. Fail. Anal.*, vol. 35, pp. 302–314, Dec. 2013.

[88] A. O. Adesola, A. G. Odeshi, and U. D. Lanke, "The effects of aging treatment and strain rates on damage evolution in AA 6061 aluminum alloy in compression," *Mater. Des.*, vol. 45, pp. 212–221, Mar. 2013.

[89] G. M. Owolabi, A. G. Odeshi, M. N. K. Singh, and M. N. Bassim, "Dynamic shear band formation in Aluminum 6061-T6 and Aluminum 6061-T6/Al2O3 composites," *Mater. Sci. Eng. A*, vol. 457, no. 1–2, pp. 114–119, May 2007.

[90] M. A. Meyers, Y. B. Xu, Q. Xue, M. T. Pérez-Prado, and T. R. McNelley, "Microstructural evolution in adiabatic shear localization in stainless steel," *Acta Mater.*, vol. 51, no. 5, pp. 1307–1325, Mar. 2003.

[91] J. F. C. Lins, H. R. Z. Sandim, H.-J. Kestenbach, D. Raabe, and K. S. Vecchio, "A microstructural investigation of adiabatic shear bands in an interstitial free steel," *Mater. Sci. Eng. A*, vol. 457, no. 1–2, pp. 205–218, May 2007.

[92] M. N. Bassim, "Study of the formation of adiabatic shear bands in steels," *J. Mater. Process. Technol.*, vol. 119, no. 1–3, pp. 234–236, Dec. 2001.

[93] A. G. Odeshi and M. N. Bassim, "High strain-rate fracture and failure of a high strength low alloy steel in compression," *Mater. Sci. Eng. A*, vol. 525, no. 1–2, pp. 96–101, Nov. 2009.

[94] S. M. Fatemi-Varzaneh, A. Zarei-Hanzaki, and J. M. Cabrera, "Shear banding phenomenon during severe plastic deformation of an AZ31 magnesium alloy," *J. Alloys Compd.*, vol. 509, no. 9, pp. 3806–3810, 2011.

[95] D. L. Zou, L. Zhen, Y. Zhu, C. Y. Xu, W. Z. Shao, and B. J. Pang, "Deformed microstructure and mechanical properties of AM60B magnesium alloy under hypervelocity impact at a velocity of 4kms-1," *Mater. Sci. Eng. A*, vol. 527, no. 15, pp. 3323–3328, 2010.

[96] D. L. Zou, L. Zhen, Y. Zhu, C. Y. Xu, W. Z. Shao, and B. J. Pang, "Deformed microstructure evolution in AM60B Mg alloy under hypervelocity impact at a velocity of 5kms-1," *Mater. Des.*, vol. 31, no. 8, pp. 3708–3715, 2010.

[97] D. Rittel and Z. G. Wang, "Thermo-mechanical aspects of adiabatic shear failure of AM50 and Ti6Al4V alloys," *Mech. Mater.*, vol. 40, pp. 629–635, 2008.

[98] L. Jianchong, N. Hai, Z. Jiaqi, H. Dong, L. Shukui, F. Qunbo, and H. Dongmei, "Effects of Microstructural Factors on Adiabatic Shear Behaviors of Ti6441 Alloys," *Rare Met. Mater. Eng.*, vol. 42, no. 6, pp. 1105–1107, 2013.

[99] F. Zhu, H. N. Tian, X. Li, G. H. Cao, D. Gerthsen, C. G. Oertel, and W. Skrotzki, "Formation mechanism of shear bands in ultrafine lamellar Ti–Fe eutectics," *Appl. Phys. Lett.*, vol. 98, no. 8, p. 081906, 2011.

[100] Y. Yang, H. G. Zheng, Z. D. Zhao, Q. Zhang, Q. M. Zhang, F. Jiang, and X. M. Li, "Effect of phase composition on self-organization of shear bands in Ti-1300 titanium alloy," *Mater. Sci. Eng. A*, vol. 528, no. 25–26, pp. 7506–7513, Sep. 2011.

[101] Y. Guo and Y. Li, "A novel approach to testing the dynamic shear response of Ti-6Al-4V," *Acta Mech. Solida Sin.*, vol. 25, no. 3, pp. 299–311, Jun. 2012.

[102] J. Li, J. Yu, and Z. Wei, "Influence of specimen geometry on adiabatic shear instability of tungsten heavy alloys," *Int. J. Impact Eng.*, vol. 28, no. 3, pp. 303–314, Mar. 2003.

[103] T. D. Rostova and V. V. Zakharov, "Nonferrous metals and alloys," *Met. Sci. Heat Treat.*, vol. 39, no. 5–6, pp. 236–239, 1997.

[104] H. Inagaki and S. kohara, "Shear Bands IN Colled Rolled Al-Mg Alloy Polycrystals," *Z. Met.*, vol. 88, no. 7, pp. 570–575, 1997.

[105] W. B. LEE and K. C. CHAN, "A microplasticity analysis of shear band cracks in rolled 2024 aluminum alloy," *Int. J. Fract.*, vol. 52, pp. 207–221, 1991.

[106] K. Piela and A. Korbel, "The effect of shear banding on spacial arrangement of the second phase particles in the aluminum alloy," *Mater. Sci. Forum*, vol. 217–222, pp. 1037–1042, 1996.

[107] L. Wang, J. Wang, C. Guo, and J. Chen, "Observation of macroscopic shear band in aluminum based alloy during equal-channel angular pressing," *Trans. Nonferrous Met. Soc. China*, vol. 14, no. 5, pp. 957–960.

[108] D. Peirce, R. J. Asaro, and A. Needleman, "Material rate dependence and localized deformation in crystalline solids," *Acta Metall.*, vol. 31, no. 12, pp. 1951–1976, Dec. 1983.

[109] L. Anand and S. R. Kalidindi, "The process of shear band formation in plane strain compression of fcc metals: Effects of crystallographic texture," *Mech. Mater.*, vol. 17, no. 2–3, pp. 223–243, Mar. 1994.

[110] R. W. Armstrong and F. J. Zerilli, "Dislocation mechanics aspects of plastic instability and shear banding," *Mech. Mater.*, vol. 17, no. 2–3, pp. 319–327, Mar. 1994.

[111] S. Medyanik, W. Liu, and S. Li, "On criteria for dynamic adiabatic shear band propagation," *J. Mech. Phys. Solids*, vol. 55, no. 7, pp. 1439–1461, Jul. 2007.

[112] M. T. Pérez-Prado, J. A. Hines, and K. S. Vecchio, "Microstructural evolution in adiabatic shear bands in Ta and Ta-W alloys," *Acta Mater.*, vol. 49, pp. 2905–2917, 2001.

[113] A. O. Adesola and A. G. Odeshi, "A comparative study of the compressive behaviour of 2099-T6 and 6061-T6 aluminum alloys under quasi-static and dynamic shock loading .," pp. 2075–2084, 2010.

[114] B. Verlinden, J. Driver, I. Samajdar, and R. D. Doherty, *Thermo-Mechanical Processing of metallic materials*, First. Oxford, UK: Elsevier Ltd, 2007, pp. 85–108.

[115] J. Hines, K. Vecchio, and S. Ahzi, "A model for microstructure evolution in adiabatic shear bands," *Metall. Mater. Trans. A*, vol. 29, no. January 1998, 1998.

[116] J. A. Hines and K. S. Vecchio, "Recrystallization kinetics within adiabatic shear bands," *Acta Mater.*, vol. 45, no. 2, pp. 635–649, 1997.

[117] V. F. Nesterenko, M. A. Meyers, J. C. LaSalvia, M. P. Bondar, Y. J. Chen, and Y. L. Lukyanov, "Shear localization and recrystallization in high-strain, high-strain-rate deformation of tantalum," *Mater. Sci. Eng. A*, vol. 229, no. 1–2, pp. 23–41, Jun. 1997.

[118] H. J. McQueen and S. Bergerson, "Dynamic recrystallization of copper during hot torsion," *Met. Sci. J.*, vol. 6, no. 1, pp. 25–29, 1972.

[119] B. Derby, "The dependence of grain size on stress during dynamic recrystallisation," *Acta Metall. Mater.*, vol. 39, no. 5, pp. 955–962, May 1991.

[120] L. Tang, Z. Chen, C. Zhan, X. Yang, C. Liu, and H. Cai, "Microstructural evolution in adiabatic shear bands of copper at high strain rates: Electron backscatter diffraction characterization," *Mater. Charact.*, vol. 64, pp. 21–26, Feb. 2012.

[121] Q. Xue, M. A. Meyers, and V. F. Nesterenko, "Self organization of shear bands in stainless steel," *Mater. Sci. Eng. A*, vol. 384, no. 1–2, pp. 35–46, Oct. 2004.

[122] S. P. Timothy and I. M. Hutchings, "Initiation and growth of microfractures along adiabatic shear bands in Ti-6Al-4V," *Mater. Sci. Technol.*, vol. 1, pp. 526–530.

[123] M. E. Kassner and T. A. Hayes, "Creep cavitation in metals," *Int. J. Plast.*, vol. 19, pp. 1715–1748, 2003.

[124] Z. Y. Gao, F. S. Han, J. Wu, and Q. Z. Wang, "Mechanism of void formation in grain interior of ODS alloys," *J. Alloys Compd.*, vol. 419, pp. 126–132, 2006.

[125] A. G. Odeshi, M. N. Bassim, and S. Al-Ameeri, "Effect of heat treatment on adiabatic shear bands in a high-strength low alloy steel," *Mater. Sci. Eng. A*, vol. 419, no. 1–2, pp. 69–75, Mar. 2006.

[126] X. B. Wang, "Temperature-Dependent Shear Strain Localization of Aluminum-Lithium Alloy in Uniaxial Compression Using Zerilli-Armstrong and Gradient Plasticity Models," *Mater. Sci. Forum*, vol. 519–521, pp. 789–794, 2006.

[127] T. Kamijo, A. Fujiwara, and H. Inagaki, "Shear bands in high purity Al," *Scr. Met. Mater.*, vol. 25, pp. 949–954, 1991.

[128] E. El-Danaf, S. R. Kalidindi, R. D. Doherty, and C. Necker, "Deformation texture transition in brass: critical role of micro-scale shear bands," *Acta Mater.*, vol. 48, no. 10, pp. 2665–2673, Jun. 2000.

[129] K. Morii and Y. Nakayama, "The Effect of Θ' Precipitates on Shear Band Formation in Rolled Single Crystals of Al-2%Cu Alloy," *Scr. Metall.*, vol. 20, pp. 1237–1240, 1986.

[130] K. M. Roessig and J. J. Mason, "Adiabatic shear localization in the impact of edge-notched specimens," *Exp. Mech.*, vol. 38, no. 3, pp. 196–203, Sep. 1998.

[131] M. Zhou, A. J. Rosakis, and G. Ravichandran, "Dynamically Propagating Shear Bands in Impact-Loaded Prenotched Plates-I. Experimental Investigations of Temperature Signatures And Propagation Speed," *J. Mech. Phys. Solids*, vol. 44, no. 6, pp. 981–1006, 1996.

[132] A. Bhattacharyya, D. Rittel, and G. Ravichandran, "Strain Rate Effect on the Evolution of Deformation Texture for α-Fe," *Metall. Mater. Trans. A*, vol. 37, no. April, pp. 1137–1145, 2006.

[133] Y. B. Chun and C. H. J. Davies, "Texture effects on development of shear bands in rolled AZ31 alloy," *Mater. Sci. Eng. A*, vol. 556, pp. 253–259, Oct. 2012.

[134] W. C. Liu, T. Zhai, C.-S. Man, B. Radhakrishnan, and J. G. Morris, "Effect of initial texture on texture evolution in cold-rolled AA 5182 aluminium alloy," *Philos. Mag.*, vol. 84, no. 31, pp. 3305–3321, Nov. 2004.

[135] N. P. Gurao, R. Kapoor, and S. Suwas, "Effect of Strain Rate on Evolution of the Deformation Microstructure and Texture in Polycrystalline Copper and Nickel," *Metall. Mater. Trans. A*, vol. 41, no. 11, pp. 2794–2804, Jul. 2010.

[136] L. Guo and F. Fujita, "Effect of equivalent strain and redundant shear strain on microstructure and texture evolution during hot rolling in Mg–3Al–1Zn alloys," *J. Mater. Sci.*, vol. 47, no. 17, pp. 6213–6219, May 2012.

[137] N. P. Gurao, R. Kapoor, and S. Suwas, "Texture evolution in high strain rate deformed Cu – 10Zn alloy," *Mater. Sci. Eng. A*, vol. 558, pp. 761–765, 2012.

[138] A. Bhattacharyya, D. Rittel, and G. Ravichandran, "Effect of strain rate on deformation texture in OFHC copper," *Scr. Mater.*, vol. 52, no. 7, pp. 657–661, Apr. 2005.

[139] X. Li, F. Jiao, T. Al-Samman, and S. Ghosh Chowdhury, "Influence of second-phase precipitates on the texture evolution of Mg–Al–Zn alloys during hot deformation," *Scr. Mater.*, vol. 66, no. 3–4, pp. 159–162, Feb. 2012.

[140] H. Paul, P. Uliasz, M. Miszczyk, W. Skuza, and T. Knych, "An Sem/Ebsd Study of Shear Bands Formation in Al-0.23%wt.Zr Alloy Deformed in Plane Strain Compression /

Krystalograficzne Aspekty Formowania Sie Pasm Scinania W Stopie Al-0.23%Wag.Zr Odkształcanym W Próbie Nieswobodnego Sciskania," *Arch. Metall. Mater.*, vol. 58, no. 1, Jan. 2013.

[141] N. P. Gurao, A. O. Adesola, A. G. Odeshi, and J. A. Szpunar, "On the evolution of heterogeneous microstructure and microtexture in impacted aluminum–lithium alloy," *J. Alloys Compd.*, vol. 578, pp. 183–187, Nov. 2013.

[142] Joseph C. Benedyk, "International Temper Designation Systems for Wrought Aluminum Alloys: Part II - Thermally Treated (T Temper) Aluminum Alloys," *Light Met. Age Int. Mag. Light Met. Ind.*

[143] R. B. C. Cayless, "Alloy and Temper Designation Systems for Aluminum and Aluminum Alloys," in *ASM Handbook Vol 2: Properties and Selection: Nonferrous Alloys and Special-Purpose Materials*, USA, 1990, pp. 38–116.

[144] C. Weinong and S. Bo, *Split Hopkinson (Kolsky) Bar: Design, Testing and Applications (Mechanical Engineering Series)*, Illustrate. New York: Springer Science & Business Media, 2010, pp. 1–35.

[145] P. E. J. Rivera Diaz Del Castillo, P. Reischig, and S. Van Der Zwaag, "Tailoring of Ostwald ripening behaviour in multicomponent Al alloys," *Scr. Mater.*, vol. 52, pp. 705–708, 2005.

[146] A. Mirjalili, H. J. Aval, and S. Serajzadeh, "An investigation into the microstructure of friction-stir welded and artificially aged AA2017," *J. Mater. Eng. Perform.*, vol. 22, no. November, pp. 3566–3571, 2013.

[147] T. S. Parel, S. C. Wang, and M. J. Starink, "Hardening of an Al–Cu–Mg alloy containing Types I and II S phase precipitates," *Mater. Des.*, vol. 31, pp. S2–S5, Jun. 2010.

[148] A. K. Mukhopadhyay, V. Singh, K. S. Prasad, C. R. Chakravorty, and D. Metallurgical, "ON S (AlXuMg) PRECIPITATION IN AN Al-Cu-Mg ALLOY CONTAINING SMALL ADDITIONS OF BERYLLIUM," vol. 44, no. 8, 1996.

[149] S. K. Shaha, F. Czerwinski, W. Kasprzak, and D. L. Chen, "Work hardening and texture during compression deformation of the Al-Si-Cu-Mg alloy modified with V, Zr and Ti," *J. Alloys Compd.*, vol. 593, pp. 290–299, 2014.

[150] A. K. Mukhopadhyay and V. V. R. Rao, "Characterization of S (Al 2 CuMg) phase particles present in as-cast and annealed Al – Cu – Mg (– Li)– Ag alloys," vol. 268, pp. 8–14, 1999.

[151] L. Liu, J. H. Chen, S. B. Wang, C. H. Liu, S. S. Yang, and C. L. Wu, "The effect of Si on precipitation in Al-Cu-Mg alloy with a high Cu/Mg ratio," *Mater. Sci. Eng. A*, vol. 606, pp. 187–195, 2014.

[152] D. Steele, D. Evans, P. Nolan, and D. J. Lloyd, "Quantification of grain boundary precipitation and the influence of quench rate in 6XXX aluminum alloys," *Mater. Charact.*, vol. 58, no. 1, pp. 40–45, Jan. 2007.

[153] D. Raabe, M. Herbig, S. Sandlöbes, Y. Li, D. Tytko, M. Kuzmina, D. Ponge, and P.-P. Choi, "Grain boundary segregation engineering in metallic alloys: A pathway to the design of interfaces," *Curr. Opin. Solid State Mater. Sci.*, vol. 18, no. 4, pp. 253–261, Aug. 2014.

[154] S. J. Pérez-Bergquist, G. T. (Rusty) Gray, E. K. Cerreta, C. P. Trujillo, and A. Pérez-Bergquist, "The dynamic and quasi-static mechanical response of three aluminum armor alloys: 5059, 5083 and 7039," *Mater. Sci. Eng. A*, vol. 528, no. 29–30, pp. 8733–8741, Nov. 2011.

[155] N. Hansen, "Hall-petch relation and boundary strengthening," *Scr. Mater.*, vol. 51, pp. 801–806, 2004.

[156] H. Ma, L. Huang, Y. Tian, and J. Li, "Effects of strain rate on dynamic mechanical behavior and microstructure evolution of 5A02-O aluminum alloy," *Mater. Sci. Eng. A*, vol. 606, pp. 233–239, Jun. 2014.

[157] S. Ragu Nathan, V. Balasubramanian, S. Malarvizhi, and A. G. Rao, "Effect of welding processes on mechanical and microstructural characteristics of high strength low alloy naval grade steel joints," *Def. Technol.*, no. July, pp. 1–10, 2015.

[158] J. D. and Y. C. Chi, "On the measurement of local strain and temperature during the formation of adiabatic shear bands," *Mater. Sci. Eng. A*, vol. 157, pp. 195–210, 1992.

[159] Y. L. B. Q. Li, Y.B. Xu, Z.H. Lai, L.T. Shen, "Dynamic recrystallization induced by plastic deformation at high strain rate in a Monel alloy," *Mater. Sci. Eng. A276*, pp. 250–256, 2000.

[160] M. A. Meyers and Han-Ryong Pak "Observation of an adiabatic shear band in titanium by high-voltage transmission electron microscopy," *Acta Met.*, vol. 34, pp. 2493–2499, 1986.

[161] Z. L. Murr, L.E., Shih, H.K., Niou, C. S., "Dynamic recrystallization in the shaped charge regime," *Scr. Met. Mater.*, vol. 29, pp. 567–572, 1993.

[162] P. J. Hurley and F. J. Humphreys, "The application of EBSD to the study of substructural development in a cold rolled single-phase aluminium alloy," *Acta Mater.*, vol. 51, no. 4, pp. 1087–1102, Feb. 2003.

[163] Y. J. Chen, Y. J. Li, J. C. Walmsley, S. Dumoulin, and H. J. Roven, "Deformation Structures of Pure Titanium during Shear Deformation," *Metall. Mater. Trans. A*, vol. 41, no. April, pp. 787–794, 2010.

[164] A. O. Hayama, H. R. Sandim, J. F. Lins, M. Hupalo, and A. Padilha, “Annealing behavior of the ODS nickel-based superalloy PM 1000,” *Mater. Sci. Eng. A*, vol. 371, no. 1–2, pp. 198–209, Apr. 2004.

[165] H. Beladi, P. Cizek, and P. D. Hodgson, “On the characteristics of substructure development through dynamic recrystallization,” *Acta Mater.*, vol. 58, no. 9, pp. 3531–3541, May 2010.

[166] P. J. Hurley and F. J. Humphreys, “Characterizing the deformed state in Al-0.1 Mg alloy using high-resolution electron backscattered diffraction,” *J. Microsc.*, vol. 205, no. October 2001, pp. 218–225, 2002.

[167] L. W. Meyer, N. Herzig, T. Halle, F. Hahn, L. Krueger, and K. P. Staudhammer, “A basic approach for strain rate dependent energy conversion including heat transfer effects: An experimental and numerical study,” *J. Mater. Process. Technol.*, vol. 182, no. 1–3, pp. 319–326, Feb. 2007.

[168] K. S. Ng and A. H. W. Ngan, “Breakdown of Schmid’s law in micropillars,” *Scr. Mater.*, vol. 59, no. 7, pp. 796–799, Oct. 2008.

APPENDIX A

Standard Operating Procedure for SHPB located in room 2C24, Engineering Building, University of Saskatchewan, Canada.

1. Introduction

The split Hopkinson pressure bar (SHPB) is used to conduct high strain rate evaluation of structural materials in compression. This equipment was designed and constructed by University of Saskatchewan Engineering Shop. This procedure details the Standard Operating Procedure which I developed for safe operation of the equipment as part of my M.Sc. work.

2. Safety

1) Do not insert the sample into the sample chamber with your fingers, always use a tweezers
2) Always close the sample chamber before impact as impacted samples could shatter and scatter in different directions
3) Wear safety glasses and ear protections when samples before pressing the firing button. Note that all lab users at the time of SHPB operation should use the ear protection
4) Never hold a freshly impacted specimen with bare hand as it may be very hot. Allow it to cool before carrying with unprotected hands
5) When job is completed, detach the air in-let hose from the air in-let valve and release residual air in tank. Close the safety switch and switch off all appliances. Disconnect the amplifier from source and turn off the air source valve
6) Return the barrel cap in position as shown in Fig. A.1c

3. SHPB components

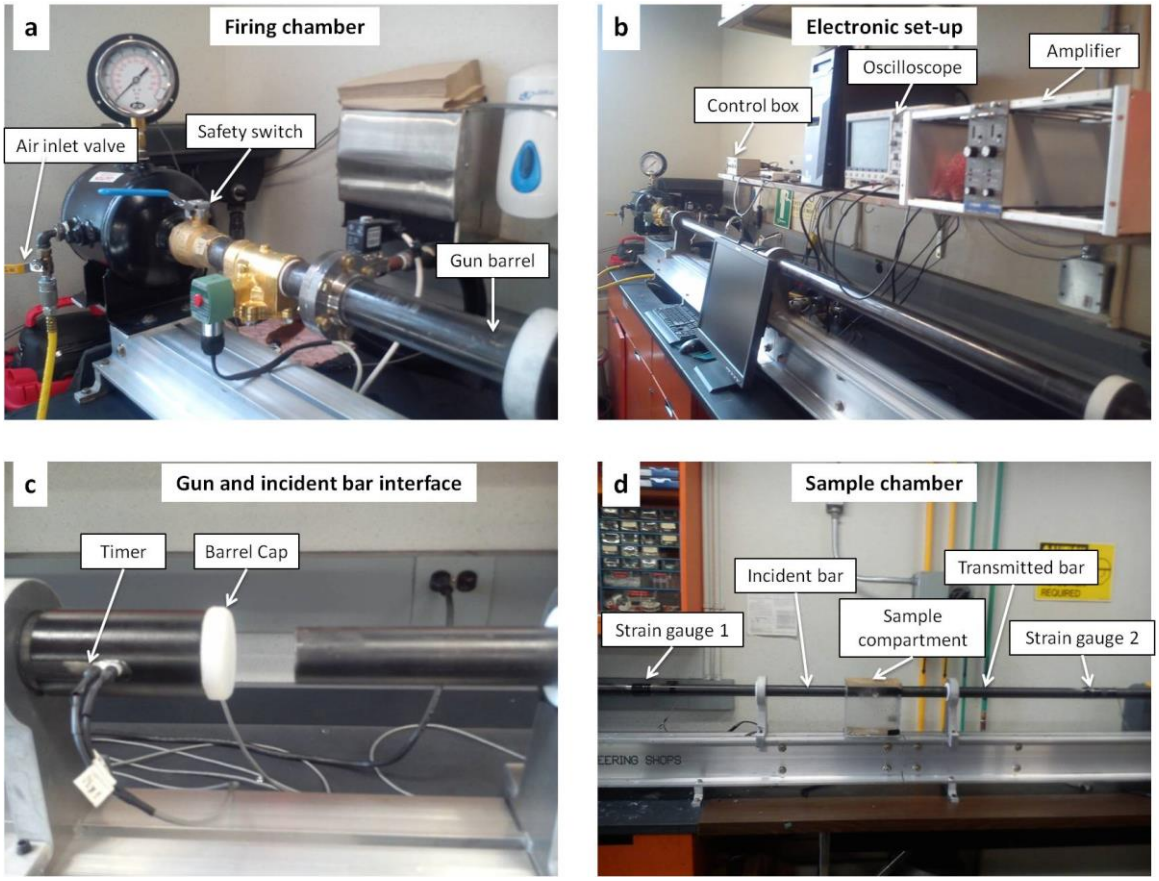

Fig. A.1 SHPB components

4. Procedure

4.1 Getting Started

4.1.1 SHPB

1. Remove the barrel cap (Fig. A.1c)
2. Plug in the oscilloscope and amplifier (Hint: amplifier comes on when plugged with no signal light to indicate if it is on or off)
3. Switch on the oscilloscope and the computer in that order
4. On the control box (Fig. A.1b), switch on the firing system with the key turned to manual
5. Turn the safety switch (Fig. A.1a) open
6. With the air in-let valve (Fig. A.1a) and the air source valve in off position, insert the air in-let hose
7. Turn on the air source valve and air in-let valve in that order

4.1.2 Digital Storage Oscilloscope (DSO)

1. Insert a flash drive to save generated data
2. On the DSO (Fig. A.1b), click "save/recall" button to select saved data destination
3. Set the vertical control for strain gage 1 (on input/incident bar) and strain gage 2 (on output/transmitted bar) as shown in Table A.1. Test parameters on Table A.1 only holds when conducting impact test on metallic materials.

Table A.1

Job Description	**Firing pressure (KPa)**	**Strain gage 1 (mV/division)**	**Strain gage 2 (mV/division)**
Calibration	60-100 @ 5KPa interval	200	200
Experiment	100-300	500	200
Experiment (higher Firing pressure)	Above 300	1000 (1V)	500

4. Set the horizontal control to 200µs per division
5. Set the first two "push to zero" button towards the center or to the center of the bottom half (for calibration) of the display screen
6. Set the "trigger position to a level slightly above the signal level for strain gage 1.

N: B Ensure that generated data are saved after each impact. "Single" button should be subsequently pressed to allow the oscilloscope to capture the next triggering event.

4.1.3 Operating Software (Labview)

1. On the desktop, click the lab view icon
2. Click "c:\...\VI's\monitor pressure.vi" under open
3. Click "file" on the popped-up "monitor pressure.vi" and on the recent files, click "c:\...\dmd173\Documents\VI's\vel test.vi"

NB: Firing pressure is monitored by the software when the "run" on the "monitor pressure.vi" is clicked.

4.2 Compression test

1. Lubricate compression planes of the sample
2. With the aid of a tweezers, place the sample between the incident and the transmitted bar in the sample chamber (see Fig A.2). **Ensure sample is located at the center of the bars**

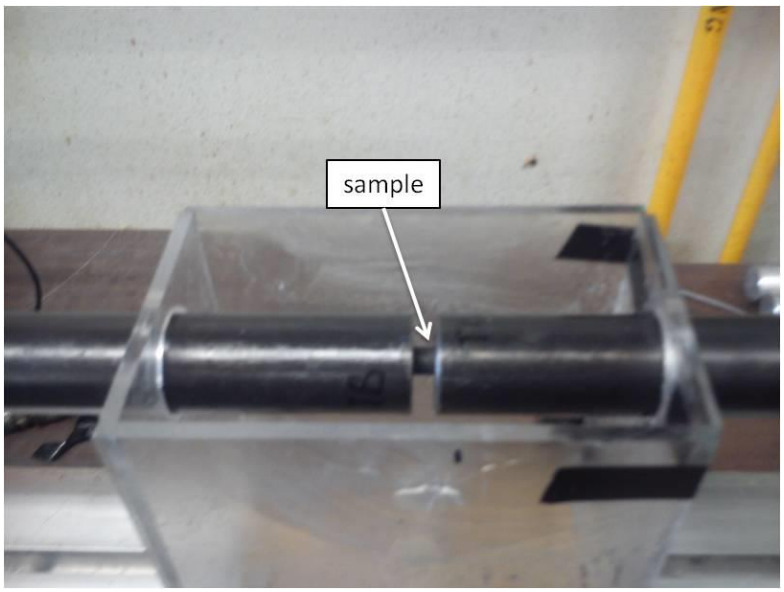

Fig. A.2 Sample sandwiched between bars before impact

3. Close the sample chamber
4. In order to avoid disturbing the timer sensors (Fig. A.1c), gradually push the striker bar (usually protrude out of the gun barrel) inward for ease of retraction, and then press the "ret." button on the control box.
5. Press "single" on the DSO
6. Gradually open the air in-let valve till the desired firing pressure is obtained
7. Once the desired firing pressure is obtained, click "stop" (on the "monitor pressure.vi"), "run" (on the "vel test.vi") and "fire" (on the control box) in quick succession. (Delay may lead to time-out and velocity of the striker will not be recorded)
8. Save data
9. Repeat 1-8

5 Highlights / Critical Control Points

Always keep the air in-let switch in "off" position when connecting to the air supply and keep in this position except when filling up the tank to the desired firing pressure. Once the air supply hose is disconnected after experiment, open the air inlet valve (vertical position) to eliminate residual pressure inside the pressure cylinder and keep this valve open when the equipment is not running. The safety valve must be closed whenever the equipment is not running.

APPENDIX B

Analyzing elastic wave data to generate stress, strain and strain rate data in SHPB operation

1 Overview

Recall the three equations (Eqs. 10-12) for generating the stress, strain and strain rate of an impacted specimen from an elastic wave data on page 38. From these equations, two sets of constants are required:

- One from the calibration of the SHPB- It should be stated that the raw data obtained from dynamic impact test in this equipment are the time, voltage 1 (for incident and reflected signals) and voltage 2 (for transmitted signal). The constant obtained from calibration of SHPB is a conversion factor that help convert voltage 1 into ε_I and ε_R and voltage 2 to ε_T in Eqs. 10-12. Calibration steps are highlighted in the next section.

- The other constants are coefficients of ε_T and ε_R in Eqs. 10-12- For ease of analysis, these constants are generated separately on an excel sheet. The constants are$(A_B/A_S)\ E_B$ and $-2\ \left(\frac{C_B}{L_S}\right)$. **N.B.-** Both $\varepsilon\ and\ \dot{\varepsilon}$ have the same coefficients (Eqn. 11 and 12).

Steps in generating these constants are highlighted in the next section.

2 Calibration of SHPB to generate conversion factor of voltage to strain amplitude

- Follow the SHPB procedure in section 4 of **APPENDIX A** but take note of the following:
  a. Rather than have a sample sandwiched between the incident and transmitter bar (Fig. A.2), calibrations are conducted without sample but ensure the ends of the bars are in contact as shown in Fig. B.1

  b. Follow the steps in section 4.1.2 of APPENDIX A but bear in mind to use DSO settings corresponding to calibration in Table A.1

- Data analysis to generate the conversion factor is highlighted below:
  a. Figure B.2 is a sample of an analyzed data for calibration. Follow these sequence on an excel sheet to analyze raw data generated from every calibrating impact pressures

b. While columns F and G are unchanged with respect to columns B and C, the essence of column E is to convert column A (seconds) to micro-seconds to ease analysis

Fig. B.1 Position of the incident and transmitted bars the sample chamber during calibration

c. The essence of column I, J and K is to ensure both raw data graph (volts 1 and 2) starts from the origin

d. Values in columns L and M are the peak (maximum) values of volts 1 and 2 (columns J and K) respectively

e. Once all peak values of volts 1 and 2 have been generated, create a new excel sheet as shown in Fig. B.3

f. As shown in Fig. B.3, strain amplitude (column G) is calculated using $\varepsilon = \frac{1}{2} . \frac{V_{st}}{C_B}$. Where V_{st} is the striking velocity (column C) and C_B elastic bar wave speed of the bar material (maraging steel) which was calculated on page 38 to be approximately 4750 m s^{-1}

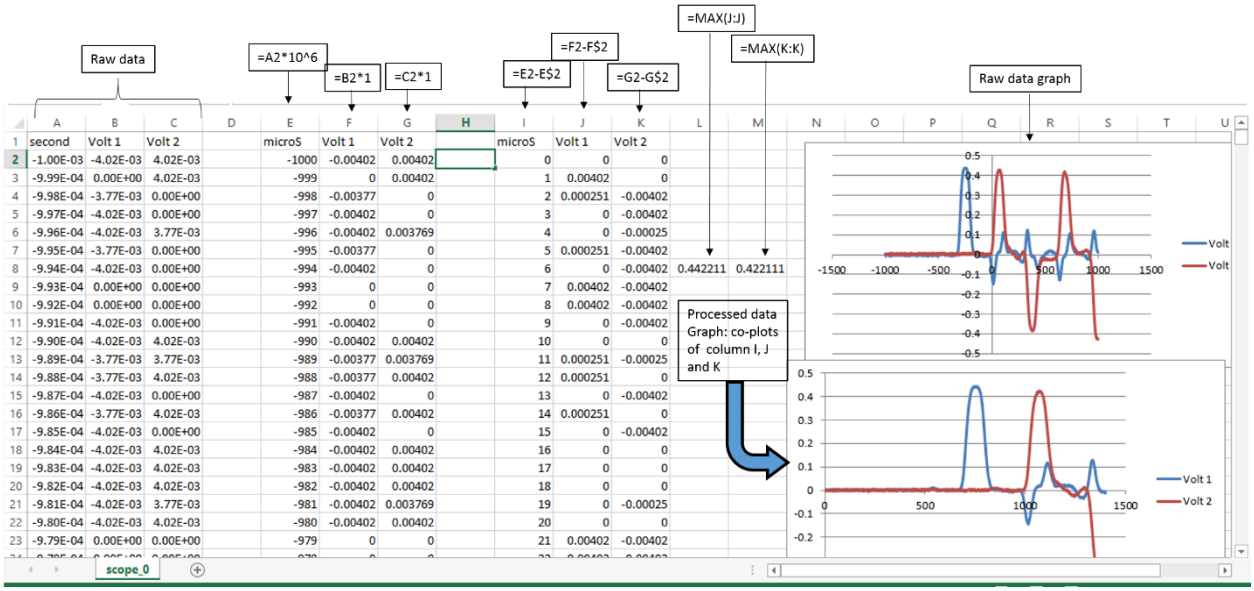

Fig. B.2

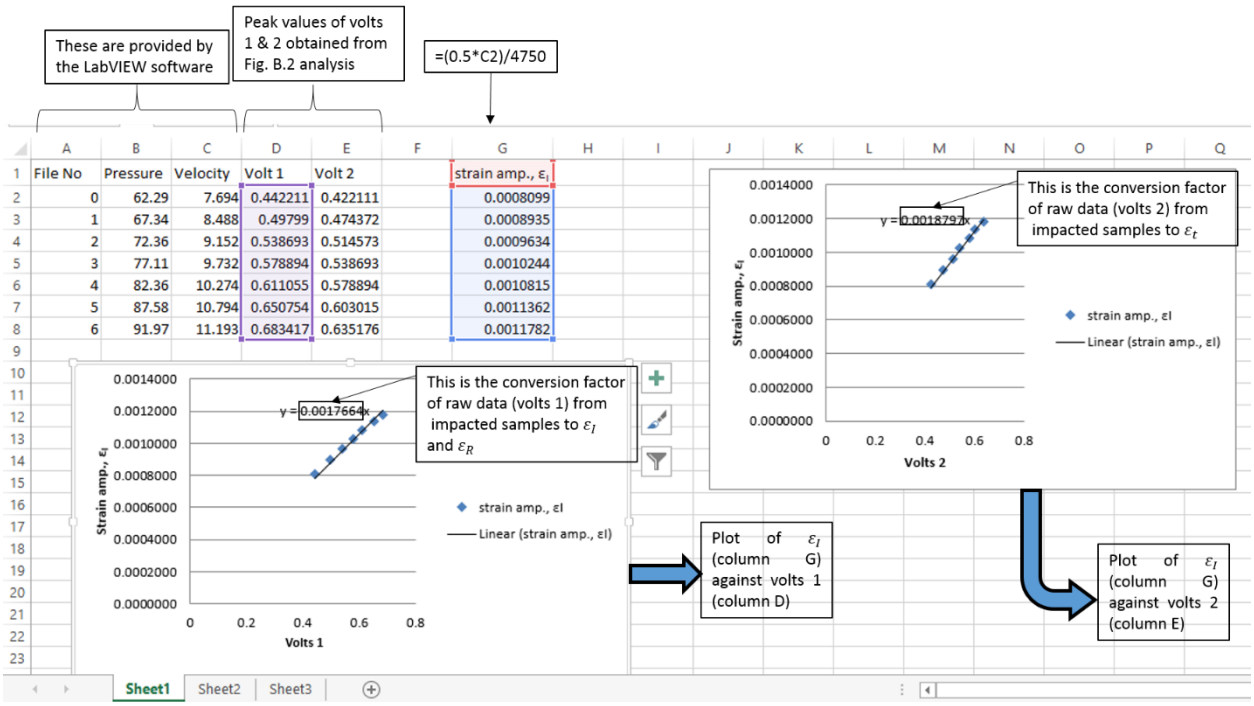

Fig. B.3

3 Generating another constants (coefficients of ε_T and ε_R in equations 10-12)

Having generated the conversion factor required to convert raw data (volts 1 & 2) to strain amplitudes ε_I, ε_R and ε_T in previous section, this section highlights how to obtain the coefficients of ε_T (for σ) and ε_R (for ε and έ) in Eqs. 10-12 for each impacted specimen. *See Fig. B.4.*

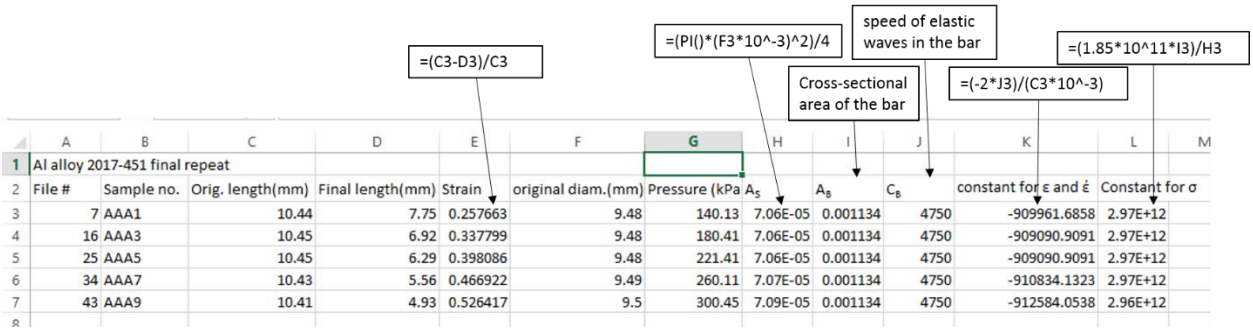

	A	B	C	D	E	F	G	H	I	J	K	L	M
1	Al alloy 2017-451 final repeat												
2	File #	Sample no.	Orig. length(mm)	Final length(mm)	Strain	original diam.(mm)	Pressure (kPa	A_5	A_B	C_B	constant for ε and ε̇	Constant for σ	
3	7	AAA1	10.44	7.75	0.257663	9.48	140.13	7.06E-05	0.001134	4750	-909961.6858	2.97E+12	
4	16	AAA3	10.45	6.92	0.337799	9.48	180.41	7.06E-05	0.001134	4750	-909090.9091	2.97E+12	
5	25	AAA5	10.45	6.29	0.398086	9.48	221.41	7.06E-05	0.001134	4750	-909090.9091	2.97E+12	
6	34	AAA7	10.43	5.56	0.466922	9.49	260.11	7.07E-05	0.001134	4750	-910834.1323	2.97E+12	
7	43	AAA9	10.41	4.93	0.526417	9.5	300.45	7.09E-05	0.001134	4750	-912584.0538	2.96E+12	
8													

Fig. B.4

N.B. – Fig. B.4 should be constructed for each set of specimens. For instance, conducting a shock loading test on AA 2017-T451 and AA 2017-T651 requires two excel spread sheets. One for the AA 2017-T451 impacted specimens and the other for AA 2017-T651 impacted specimens

4 Obtaining the stress, strain and strain rate data

All constants required to generate the stress, strain and strain rate data have been explained in the previous sections (**APPENDIX B**, section 2 & 3). Figure B.5 shows the steps to follow on an excel spread sheet constructed for every impacted sample.

- Constants used in columns X, Y and Z are the constants obtained by calibrating the SHPB (see **APPENDIX B**, section 2) while coefficients of ε_T and ε_R in Eqs. 10-12 obtained in APPENDIX B, section 3 are used in columns AE, AF and AG in Fig. B.5b
- The curves corresponding to certain columns in Fig. B.5 is shown in Fig. B.6
- While Fig. B.6a corresponds to columns A, B and C in Fig. B.5a, the essence of columns I, J and K is to set both volts 1 & 2 to the same reference level (Fig. B.6b)
- As indicated in Fig. B.6b, the incident and reflected pulses are generated from volt 1 while volt 2 gives the transmitted pulse. Other part of the pulses are treated as noise and therefore discarded in further analysis
- Figure B.6c (generated from columns M, N, and O) is the most critical aspect of this analysis and as such, care must duly be taken. The incident pulse is copied from column J (volt 1) starting from when the volts are permanently increasing (usually from zero or near zero value) to that point where it just drop below zero. While the reflected pulse is copied from column J (volt 1) starting from when the volts are permanently decreasing (usually from zero or near zero value) to that point where it is just above zero. The transmitted pulse

is copied from column K (volt 2) starting from when the volts are permanently increasing (usually from zero or near zero value) to that point where it just drop below zero

- The essence of columns R, S, T and U is to set all pulses to the origin (Fig. B.6d)
- Fig. B.6f is the smoothened stress-strain curve of Fig. B.6e

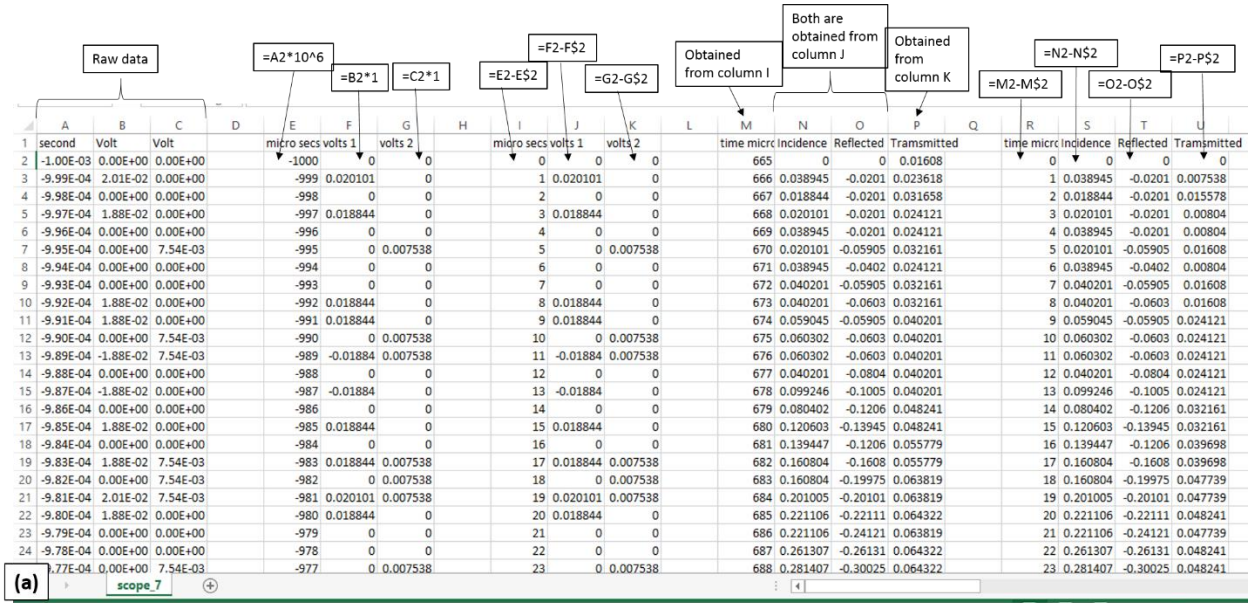

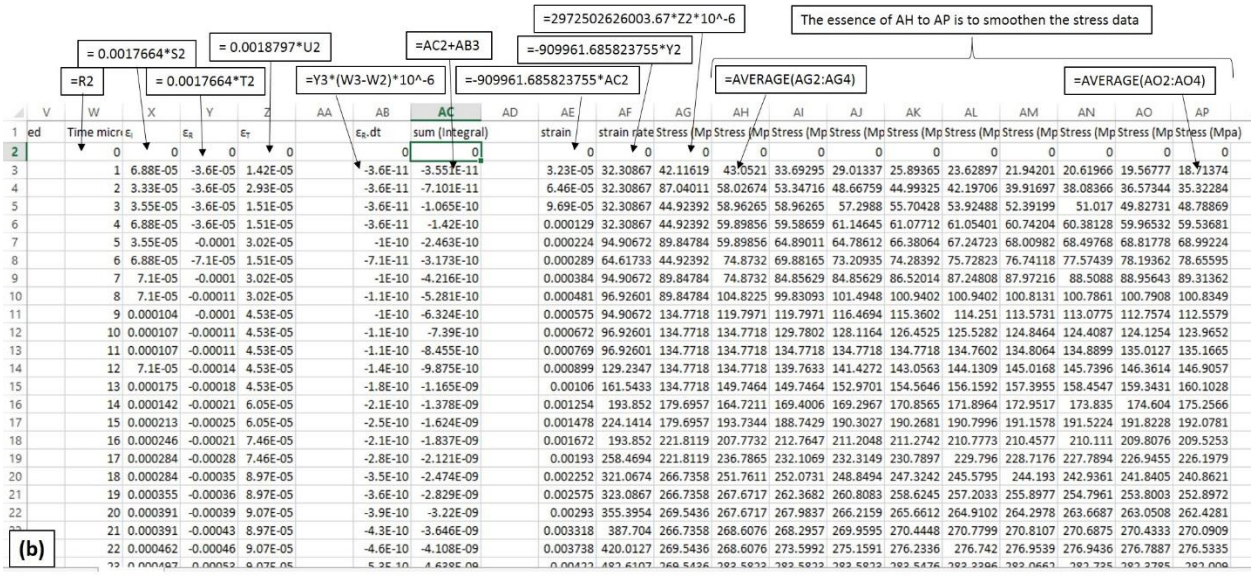

Fig. B.5

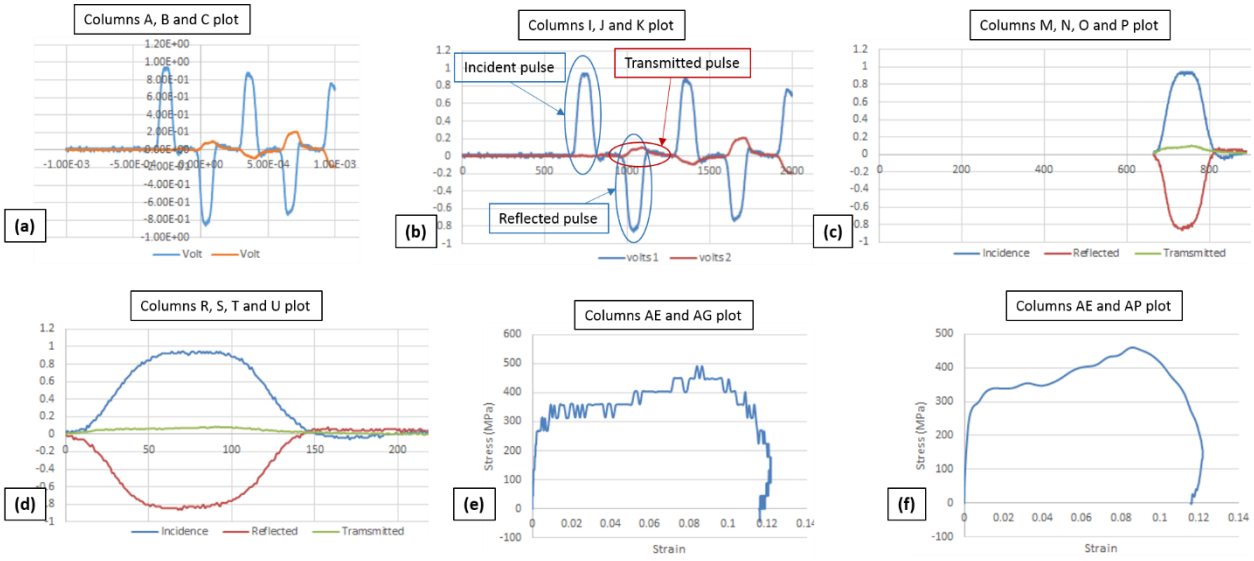
Columns A, B and C plot
(a)
Volt
Volt
Columns I, J and K plot
Incident pulse
Transmitted pulse
Reflected pulse
(b)
volts 1
volts 2
Columns M, N, O and P plot
(c)
Incidence
Reflected
Transmitted
Columns R, S, T and U plot
(d)
Incidence
Reflected
Transmitted
Columns AE and AG plot
(e)
Stress (MPa)
Strain
Columns AE and AP plot
(f)
Stress (MPa)
Strain

Fig. B.6

APPENDIX C

Copy Right Permissions

Chapter 2, Fig. 2.1

This is a License Agreement between Ahmed Tiamiyu ("You") and Elsevier ("Elsevier") provided by Copyright Clearance Center ("CCC"). The license consists of your order details, the terms and conditions provided by Elsevier, and the payment terms and conditions.

All payments must be made in full to CCC. For payment instructions, please see information listed at the bottom of this form.

Supplier	Elsevier Limited The Boulevard,Langford Lane Kidlington,Oxford,OX5 1GB,UK
Registered Company Number	1982084
Customer name	Ahmed Tiamiyu
Customer address	57, College drive Saskatoon, SK S7N 5A9
License number	3586921281315
License date	Mar 13, 2015
Licensed content publisher	Elsevier
Licensed content publication	Acta Materialia
Licensed content title	Precipitation processes in an Al-2.5Cu-1.5Mg (wt. %) alloy microalloyed with Ag and Si
Licensed content author	K. Raviprasad, C. R. Hutchinson, T. Sakurai and S. P. Ringer
Licensed content date	6 October 2003
Licensed content volume number	51
Licensed content issue number	17
Number of pages	14

Start Page	5037
End Page	5050
Type of Use	reuse in a thesis/dissertation
Intended publisher of new work	other
Portion	figures/tables/illustrations
Number of figures/tables/illustrations	1
Format	both print and electronic
Are you the author of this Elsevier article?	No
Will you be translating?	No
Original figure numbers	Fig. 1
Title of your thesis/dissertation	Mechanical Response and Microstructure Evolution in Selected 2000 Series Aluminum Alloys Under Quasi-static and Dynamic Shock Loading
Expected completion date	Aug 2015
Estimated size (number of pages)	200
Elsevier VAT number	GB 494 6272 12
Permissions price	0.00 USD
VAT/Local Sales Tax	0.00 USD / 0.00 GBP
Total	0.00 USD
Terms and Conditions	

Chapter 2, Fig. 2.2

This is a License Agreement between Ahmed Tiamiyu ("You") and Elsevier ("Elsevier") provided by Copyright Clearance Center ("CCC"). The license consists of your order details, the terms and conditions provided by Elsevier, and the payment terms and conditions.

All payments must be made in full to CCC. For payment instructions, please see information listed at the bottom of this form.

Supplier	Elsevier Limited The Boulevard,Langford Lane Kidlington,Oxford,OX5 1GB,UK
Registered Company Number	1982084
Customer name	Ahmed Tiamiyu
Customer address	57, College drive Saskatoon, SK S7N 5A9
License number	3590920251717
License date	Mar 16, 2015
Licensed content publisher	Elsevier
Licensed content publication	Materials Characterization
Licensed content title	Microstructural Evolution and Age Hardening in Aluminium Alloys Atom Probe Field-Ion Microscopy and Transmission Electron Microscopy Studies
Licensed content author	S.P. Ringer,K. Hono
Licensed content date	January–February 2000
Licensed content volume number	44
Licensed content issue number	1-2
Number of pages	31
Start Page	101
End Page	131
Type of Use	reuse in a thesis/dissertation
Portion	figures/tables/illustrations
Number of figures/tables/illustrations	1

Format	both print and electronic
Are you the author of this Elsevier article?	No
Will you be translating?	No
Original figure numbers	fig. 1
Title of your thesis/dissertation	Mechanical Response and Microstructure Evolution in Selected 2000 Series Aluminum Alloys Under Quasi-static and Dynamic Shock Loading
Expected completion date	Aug 2015
Estimated size (number of pages)	200
Elsevier VAT number	GB 494 6272 12
Permissions price	0.00 USD
VAT/Local Sales Tax	0.00 USD / 0.00 GBP
Total	0.00 USD

Chapter 2, Fig. 2.3

This is a License Agreement between Ahmed Tiamiyu ("You") and Elsevier ("Elsevier") provided by Copyright Clearance Center ("CCC"). The license consists of your order details, the terms and conditions provided by Elsevier, and the payment terms and conditions.

All payments must be made in full to CCC. For payment instructions, please see information listed at the bottom of this form.

Supplier	Elsevier Limited The Boulevard,Langford Lane Kidlington,Oxford,OX5 1GB,UK
Registered Company Number	1982084
Customer name	Ahmed Tiamiyu
Customer address	57, College drive Saskatoon, SK S7N 5A9
License number	3585311484596

License date	Mar 10, 2015
Licensed content publisher	Elsevier
Licensed content publication	Acta Materialia
Licensed content title	The structure and the properties of S-phase in AlCuMg alloys
Licensed content author	Z.R. Liu,J.H. Chen,S.B. Wang,D.W. Yuan,M.J. Yin,C.L. Wu
Licensed content date	November 2011
Licensed content volume number	59
Licensed content issue number	19
Number of pages	10
Start Page	7396
End Page	7405
Type of Use	reuse in a thesis/dissertation
Portion	figures/tables/illustrations
Number of figures/tables/illustrations	1
Format	both print and electronic
Are you the author of this Elsevier article?	No
Will you be translating?	No
Original figure numbers	Fig. 1.
Title of your thesis/dissertation	Mechanical Response and Microstructure Evolution in Selected 2000 Series Aluminum Alloys Under Quasi-static and Dynamic Shock Loading
Expected completion date	Aug 2015
Estimated size (number of pages)	200
Elsevier VAT number	GB 494 6272 12
Permissions price	0.00 USD
VAT/Local Sales Tax	0.00 USD / 0.00 GBP
Total	0.0 USD

Chapter 2, Fig. 2.4

This is a License Agreement between Ahmed Tiamiyu ("You") and Elsevier ("Elsevier") provided by Copyright Clearance Center ("CCC"). The license consists of your order details, the terms and conditions provided by Elsevier, and the payment terms and conditions.

All payments must be made in full to CCC. For payment instructions, please see information listed at the bottom of this form.

Supplier	Elsevier Limited The Boulevard,Langford Lane Kidlington,Oxford,OX5 1GB,UK
Registered Company Number	1982084
Customer name	Ahmed Tiamiyu
Customer address	57, College drive Saskatoon, SK S7N 5A9
License number	3644430020805
License date	Jun 08, 2015
Licensed content publisher	Elsevier
Licensed content publication	International Journal of Solids and Structures
Licensed content title	A failure criterion based on material instability
Licensed content author	S. E. Schoenfeld, T. W. Wright
Licensed content date	June 2003
Licensed content volume number	40
Licensed content issue number	12
Number of pages	17
Start Page	3021
End Page	3037

Type of Use	reuse in a thesis/dissertation
Portion	figures/tables/illustrations
Number of figures/tables/illustrations	1
Format	both print and electronic
Are you the author of this Elsevier article?	No
Will you be translating?	No
Original figure numbers	Fig. 1
Title of your thesis/dissertation	Mechanical Response and Microstructure Evolution in Selected 2000 Series Aluminum Alloys Under Quasi-static and Dynamic Shock Loading
Expected completion date	Aug 2015
Estimated size (number of pages)	200
Elsevier VAT number	GB 494 6272 12
Permissions price	0.00 USD
VAT/Local Sales Tax	0.00 USD / 0.00 GBP
Total	0.00 USD

Chapter 2, Fig. 2.5

This is a License Agreement between Ahmed Tiamiyu ("You") and Elsevier ("Elsevier") provided by Copyright Clearance Center ("CCC"). The license consists of your order details, the terms and conditions provided by Elsevier, and the payment terms and conditions.

All payments must be made in full to CCC. For payment instructions, please see information listed at the bottom of this form.

Supplier	Elsevier Limited The Boulevard,Langford Lane Kidlington,Oxford,OX5 1GB,UK

Registered Company Number	1982084
Customer name	Ahmed Tiamiyu
Customer address	57, College drive Saskatoon, SK S7N 5A9
License number	3600911214018
License date	Apr 02, 2015
Licensed content publisher	Elsevier
Licensed content publication	Acta Materialia
Licensed content title	Self-organization in the initiation of adiabatic shear bands
Licensed content author	None
Licensed content date	19 December 1998
Licensed content volume number	46
Licensed content issue number	1
Number of pages	14
Start Page	327
End Page	340
Type of Use	reuse in a thesis/dissertation
Portion	figures/tables/illustrations
Number of figures/tables/illustrations	1
Format	both print and electronic
Are you the author of this Elsevier article?	No
Will you be translating?	No
Original figure numbers	Fig. 13

Title of your thesis/dissertation	Mechanical Response and Microstructure Evolution in Selected 2000 Series Aluminum Alloys Under Quasi-static and Dynamic Shock Loading
Expected completion date	Aug 2015
Estimated size (number of pages)	200
Elsevier VAT number	GB 494 6272 12
Permissions price	0.00 USD
VAT/Local Sales Tax	0.00 USD / 0.00 GBP
Total	0.00 USD
Terms and Conditions	

Chapter 2, Fig. 2.8

This is a License Agreement between Ahmed Tiamiyu ("You") and Elsevier ("Elsevier") provided by Copyright Clearance Center ("CCC"). The license consists of your order details, the terms and conditions provided by Elsevier, and the payment terms and conditions.

All payments must be made in full to CCC. For payment instructions, please see information listed at the bottom of this form.

Supplier	Elsevier Limited The Boulevard,Langford Lane Kidlington,Oxford,OX5 1GB,UK
Registered Company Number	1982084
Customer name	Ahmed Tiamiyu
Customer address	57, College drive Saskatoon, SK S7N 5A9
License number	3600920219839
License date	Apr 02, 2015
Licensed content publisher	Elsevier

Licensed content publication	Materials Science and Engineering: A
Licensed content title	Shear localization and recrystallization in high-strain, high-strain-rate deformation of tantalum
Licensed content author	V.F. Nesterenko,M.A. Meyers,J.C. LaSalvia,M.P. Bondar,Y.J. Chen,Y.L. Lukyanov
Licensed content date	30 June 1997
Licensed content volume number	229
Licensed content issue number	1-2
Number of pages	19
Start Page	23
End Page	41
Type of Use	reuse in a thesis/dissertation
Intended publisher of new work	other
Portion	figures/tables/illustrations
Number of figures/tables/illustrations	1
Format	both print and electronic
Are you the author of this Elsevier article?	No
Will you be translating?	No
Original figure numbers	Fig. 19
Title of your thesis/dissertation	Mechanical Response and Microstructure Evolution in Selected 2000 Series Aluminum Alloys Under Quasi-static and Dynamic Shock Loading
Expected completion date	Aug 2015
Estimated size (number of pages)	200

Elsevier VAT number	GB 494 6272 12
Permissions price	0.00 USD
VAT/Local Sales Tax	0.00 USD / 0.00 GBP
Total	0.00 USD

Chapter 2, Fig. 2.9

This is a License Agreement between Ahmed Tiamiyu ("You") and Elsevier ("Elsevier") provided by Copyright Clearance Center ("CCC"). The license consists of your order details, the terms and conditions provided by Elsevier, and the payment terms and conditions.

All payments must be made in full to CCC. For payment instructions, please see information listed at the bottom of this form.

Supplier	Elsevier Limited The Boulevard,Langford Lane Kidlington,Oxford,OX5 1GB,UK
Registered Company Number	1982084
Customer name	Ahmed Tiamiyu
Customer address	57, College drive Saskatoon, SK S7N 5A9
License number	3600921117654
License date	Apr 02, 2015
Licensed content publisher	Elsevier
Licensed content publication	Materials Characterization
Licensed content title	Microstructural evolution in adiabatic shear bands of copper at high strain rates: Electron backscatter diffraction characterization
Licensed content author	None

Licensed content date	February 2012
Licensed content volume number	64
Licensed content issue number	n/a
Number of pages	6
Start Page	21
End Page	26
Type of Use	reuse in a thesis/dissertation
Intended publisher of new work	other
Portion	figures/tables/illustrations
Number of figures/tables/illustrations	1
Format	both print and electronic
Are you the author of this Elsevier article?	No
Will you be translating?	No
Original figure numbers	Fig. 5
Title of your thesis/dissertation	Mechanical Response and Microstructure Evolution in Selected 2000 Series Aluminum Alloys Under Quasi-static and Dynamic Shock Loading
Expected completion date	Aug 2015
Estimated size (number of pages)	200
Elsevier VAT number	GB 494 6272 12
Permissions price	0.00 USD
VAT/Local Sales Tax	0.00 USD / 0.00 GBP
Total	0.00 USD

Terms and Conditions

INTRODUCTION

1. The publisher for this copyrighted material is Elsevier. By clicking "accept" in connection with completing this licensing transaction, you agree that the following terms and conditions apply to this transaction (along with the Billing and Payment terms and conditions established by Copyright Clearance Center, Inc. ("CCC"), at the time that you opened your Rights link account and that are available at any time athttp://myaccount.copyright.com).

GENERAL TERMS

2. Elsevier hereby grants you permission to reproduce the aforementioned material subject to the terms and conditions indicated.

3. Acknowledgement: If any part of the material to be used (for example, figures) has appeared in our publication with credit or acknowledgement to another source, permission must also be sought from that source. If such permission is not obtained then that material may not be included in your publication/copies. Suitable acknowledgement to the source must be made, either as a footnote or in a reference list at the end of your publication, as follows:

"Reprinted from Publication title, Vol /edition number, Author(s), Title of article / title of chapter, Pages No., Copyright (Year), with permission from Elsevier [OR APPLICABLE SOCIETY COPYRIGHT OWNER]." Also Lancet special credit - "Reprinted from The Lancet, Vol. number, Author(s), Title of article, Pages No., Copyright (Year), with permission from Elsevier."

4. Reproduction of this material is confined to the purpose and/or media for which permission is hereby given.

5. Altering/Modifying Material: Not Permitted. However figures and illustrations may be altered/adapted minimally to serve your work. Any other abbreviations, additions, deletions and/or any other alterations shall be made only with prior written authorization of Elsevier Ltd. (Please contact Elsevier at permissions@elsevier.com)

6. If the permission fee for the requested use of our material is waived in this instance, please be advised that your future requests for Elsevier materials may attract a fee.

7. Reservation of Rights: Publisher reserves all rights not specifically granted in the combination of (i) the license details provided by you and accepted in the course of this licensing transaction, (ii) these terms and conditions and (iii) CCC's Billing and Payment terms and conditions.

8. License Contingent Upon Payment: While you may exercise the rights licensed immediately upon issuance of the license at the end of the licensing process for the transaction, provided that you have disclosed complete and accurate details of your proposed use, no license is finally effective unless and until full payment is received from you (either by publisher or by CCC) as provided in CCC's Billing and Payment terms and conditions. If full payment is not received on a timely basis, then any license preliminarily granted shall be deemed automatically revoked and shall be void as if never granted. Further, in the event that you breach any of these terms and conditions or any of CCC's Billing and Payment terms and conditions, the license is automatically revoked and shall be void as if never granted. Use of materials as described in a revoked license, as well as any use of the materials beyond the scope of an unrevoked license, may constitute copyright infringement and publisher reserves the right to take any and all action to protect its copyright in the materials.

9. Warranties: Publisher makes no representations or warranties with respect to the licensed material.

10. Indemnity: You hereby indemnify and agree to hold harmless publisher and CCC, and their respective officers, directors, employees and agents, from and against any and all claims arising out of your use of the licensed material other than as specifically authorized pursuant to this license.

11. No Transfer of License: This license is personal to you and may not be sublicensed, assigned, or transferred by you to any other person without publisher's written permission.

12. No Amendment Except in Writing: This license may not be amended except in a writing signed by both parties (or, in the case of publisher, by CCC on publisher's behalf).

13. Objection to Contrary Terms: Publisher hereby objects to any terms contained in any purchase order, acknowledgment, check endorsement or other writing prepared by you, which terms are inconsistent with these terms and conditions or CCC's Billing and Payment terms and conditions. These terms and conditions, together with CCC's Billing and Payment terms and conditions (which are incorporated herein), comprise the entire agreement between you and publisher (and CCC) concerning this licensing transaction. In the event of any conflict between your obligations established by these terms and conditions and those established by CCC's Billing and Payment terms and conditions, these terms and conditions shall control.

14. Revocation: Elsevier or Copyright Clearance Center may deny the permissions described in this License at their sole discretion, for any reason or no reason, with a full refund payable to you. Notice of such denial will be made using the contact information provided by you. Failure to receive such notice will not alter or invalidate the denial. In no event will Elsevier or Copyright Clearance Center be responsible or liable for any costs, expenses or damage incurred

by you as a result of a denial of your permission request, other than a refund of the amount(s) paid by you to Elsevier and/or Copyright Clearance Center for denied permissions.

LIMITED LICENSE

The following terms and conditions apply only to specific license types:

15. **Translation**: This permission is granted for non-exclusive world **English** rights only unless your license was granted for translation rights. If you licensed translation rights you may only translate this content into the languages you requested. A professional translator must perform all translations and reproduce the content word for word preserving the integrity of the article. If this license is to re-use 1 or 2 figures then permission is granted for non-exclusive world rights in all languages.

16. **Posting licensed content on any Website**: The following terms and conditions apply as follows: Licensing material from an Elsevier journal: All content posted to the web site must maintain the copyright information line on the bottom of each image; A hyper-text must be included to the Homepage of the journal from which you are licensing athttp://www.sciencedirect.com/science/journal/xxxxx or the Elsevier homepage for books athttp://www.elsevier.com; Central Storage: This license does not include permission for a scanned version of the material to be stored in a central repository such as that provided by Heron/XanEdu.

Licensing material from an Elsevier book: A hyper-text link must be included to the Elsevier homepage at http://www.elsevier.com . All content posted to the web site must maintain the copyright information line on the bottom of each image.

Posting licensed content on Electronic reserve: In addition to the above the following clauses are applicable: The web site must be password-protected and made available only to bona fide students registered on a relevant course. This permission is granted for 1 year only. You may obtain a new license for future website posting.

17. **For journal authors:** the following clauses are applicable in addition to the above:

Preprints:

A preprint is an author's own write-up of research results and analysis, it has not been peer-reviewed, nor has it had any other value added to it by a publisher (such as formatting, copyright, technical enhancement etc.).

Authors can share their preprints anywhere at any time. Preprints should not be added to or enhanced in any way in order to appear more like, or to substitute for, the final versions of articles however authors can update their preprints on arXiv or RePEc with their Accepted Author Manuscript (see below).

If accepted for publication, we encourage authors to link from the preprint to their formal publication via its DOI. Millions of researchers have access to the formal publications on Science Direct, and so links will help users to find, access, cite and use the best available version. Please note that Cell Press, The Lancet and some society-owned have different preprint policies. Information on these policies is available on the journal homepage.

Accepted Author Manuscripts: An accepted author manuscript is the manuscript of an article that has been accepted for publication and which typically includes author-incorporated changes suggested during submission, peer review and editor-author communications.

Authors can share their accepted author manuscript:

- immediately
    - via their non-commercial person homepage or blog
    - by updating a preprint in arXiv or RePEc with the accepted manuscript
    - via their research institute or institutional repository for internal institutional uses or as part of an invitation-only research collaboration work-group
    - directly by providing copies to their students or to research collaborators for their personal use
    - for private scholarly sharing as part of an invitation-only work group on commercial sites with which Elsevier has an agreement
- after the embargo period
    - via non-commercial hosting platforms such as their institutional repository
    - via commercial sites with which Elsevier has an agreement

In all cases accepted manuscripts should:

- link to the formal publication via its DOI
- bear a CC-BY-NC-ND license - this is easy to do
- if aggregated with other manuscripts, for example in a repository or other site, be shared in alignment with our hosting policy not be added to or enhanced in any way to appear more like, or to substitute for, the published journal article.

Published journal article (JPA): A published journal article (PJA) is the definitive final record of published research that appears or will appear in the journal and embodies all value-adding

publishing activities including peer review co-ordination, copy-editing, formatting, (if relevant) pagination and online enrichment.

Policies for sharing publishing journal articles differ for subscription and gold open access articles:

Subscription Articles: If you are an author, please share a link to your article rather than the full-text. Millions of researchers have access to the formal publications on Science Direct, and so links will help your users to find, access, cite, and use the best available version.

Theses and dissertations which contain embedded PJAs as part of the formal submission can be posted publicly by the awarding institution with DOI links back to the formal publications on Science Direct.

If you are affiliated with a library that subscribes to Science Direct you have additional private sharing rights for others' research accessed under that agreement. This includes use for classroom teaching and internal training at the institution (including use in course packs and courseware programs), and inclusion of the article for grant funding purposes.

Gold Open Access Articles: May be shared according to the author-selected end-user license and should contain a Cross Mark logo, the end user license, and a DOI link to the formal publication on Science Direct.

Please refer to Elsevier's posting policy for further information.

18. **For book authors** the following clauses are applicable in addition to the above: Authors are permitted to place a brief summary of their work online only. You are not allowed to download and post the published electronic version of your chapter, nor may you scan the printed edition to create an electronic version. **Posting to a repository:** Authors are permitted to post a summary of their chapter only in their institution's repository.

19. **Thesis/Dissertation**: If your license is for use in a thesis/dissertation your thesis may be submitted to your institution in either print or electronic form. Should your thesis be published commercially, please reapply for permission. These requirements include permission for the Library and Archives of Canada to supply single copies, on demand, of the complete thesis and include permission for Proquest/UMI to supply single copies, on demand, of the complete thesis. Should your thesis be published commercially, please reapply for permission. Theses and dissertations which contain embedded PJAs as part of the formal submission can be posted publicly by the awarding institution with DOI links back to the formal publications on Science Direct.

and that the licensor is not represented as endorsing the use made of the work. The full details of the license are available at http://creativecommons.org/licenses/by-nc-nd/4.0. Any commercial reuse of Open Access articles published with a CC BY NC SA or CC BY NC ND license requires permission from Elsevier and will be subject to a fee.

Commercial reuse includes:

- Associating advertising with the full text of the Article
- Charging fees for document delivery or access
- Article aggregation
- Systematic distribution via e-mail lists or share buttons

Posting or linking by commercial companies for use by customers of those companies.
20. **Other Conditions**:

Chapter 2, Fig. 2.10

All payments must be made in full to CCC. For payment instructions, please see information listed at the bottom of this form.

License Number	3646601097326
Order Date	Jun 12, 2015
Publisher	AIP Publishing LLC
Publication	Applied Physics Letters
Article Title	Formation mechanism of shear bands in ultrafine lamellar Ti–Fe eutectics
Author	F. Zhu,H. N. Tian,X. Li, et al.
Online Publication Date	Feb 23, 2011
Volume number	98
Issue number	8
Type of Use	Thesis/Dissertation
Requestor type	Student
Format	Print and electronic
Portion	Figure/Table
Number of figures/tables	1

Title of your thesis / dissertation	Mechanical Response and Microstructure Evolution in Selected 2000 Series Aluminum Alloys Under Quasi-static and Dynamic Shock Loading
Expected completion date	Aug 2015
Estimated size (number of pages)	200
Total	0.00 USD

Terms and Conditions

AIP Publishing LLC -- Terms and Conditions: Permissions Uses

AIP Publishing LLC ("AIPP"") hereby grants to you the non-exclusive right and license to use and/or distribute the Material according to the use specified in your order, on a one-time basis, for the specified term, with a maximum distribution equal to the number that you have ordered. Any links or other content accompanying the Material are not the subject of this license.

1. You agree to include the following copyright and permission notice with the reproduction of the Material:"Reprinted with permission from [FULL CITATION]. Copyright [PUBLICATION YEAR], AIP Publishing LLC." For an article, the copyright and permission notice must be printed on the first page of the article or book chapter. For photographs, covers, or tables, the copyright and permission notice may appear with the Material, in a footnote, or in the reference list.
2. If you have licensed reuse of a figure, photograph, cover, or table, it is your responsibility to ensure that the material is original to AIPP and does not contain the copyright of another entity, and that the copyright notice of the figure, photograph, cover, or table does not indicate that it was reprinted by AIPP, with permission, from another source. Under no circumstances does AIPP, purport or intend to grant permission to reuse material to which it does not hold copyright.
3. You may not alter or modify the Material in any manner. You may translate the Material into another language only if you have licensed translation rights. You may not use the Material for promotional purposes. AIPP reserves all rights not specifically granted herein.
4. The foregoing license shall not take effect unless and until AIPP or its agent, Copyright Clearance Center, receives the Payment in accordance with Copyright Clearance Center Billing and Payment Terms and Conditions, which are incorporated herein by reference.

5. AIPP or the Copyright Clearance Center may, within two business days of granting this license, revoke the license for any reason whatsoever, with a full refund payable to you. Should you violate the terms of this license at any time, AIPP, AIP Publishing LLC, or Copyright Clearance Center may revoke the license with no refund to you. Notice of such revocation will be made using the contact information provided by you. Failure to receive such notice will not nullify the revocation.
6. AIPP makes no representations or warranties with respect to the Material. You agree to indemnify and hold harmless AIPP, AIP Publishing LLC, and their officers, directors, employees or agents from and against any and all claims arising out of your use of the Material other than as specifically authorized herein.
7. The permission granted herein is personal to you and is not transferable or assignable without the prior written permission of AIPP. This license may not be amended except in a writing signed by the party to be charged.
8. If purchase orders, acknowledgments or check endorsements are issued on any forms containing terms and conditions which are inconsistent with these provisions, such inconsistent terms and conditions shall be of no force and effect. This document, including the CCC Billing and Payment Terms and Conditions, shall be the entire agreement between the parties relating to the subject matter hereof.

This Agreement shall be governed by and construed in accordance with the laws of the State of New York. Both parties hereby submit to the jurisdiction of the courts of New York County for purposes of resolving any disputes that may arise hereunder.

Chapter 2, Fig. 2.11

This is a License Agreement between Ahmed Tiamiyu ("You") and Springer ("Springer") provided by Copyright Clearance Center ("CCC"). The license consists of your order details, the terms and conditions provided by Springer, and the payment terms and conditions.

All payments must be made in full to CCC. For payment instructions, please see information listed at the bottom of this form.

License Number	3646600484212
License date	Jun 12, 2015
Licensed content publisher	Springer
Licensed content publication	Metallurgical and Materials Transactions A

Licensed content title	A model for microstructure evolution in adiabatic shear bands
Licensed content author	Joy A. Hines
Licensed content date	Jan 1, 1998
Volume number	29
Issue number	1
Type of Use	Thesis/Dissertation
Portion	Figures
Author of this Springer article	No
Order reference number	None
Original figure numbers	Fig. 15
Title of your thesis / dissertation	Mechanical Response and Microstructure Evolution in Selected 2000 Series Aluminum Alloys Under Quasi-static and Dynamic Shock Loading
Expected completion date	Aug 2015
Estimated size(pages)	200
Total	0.00 USD

Terms and Conditions

Introduction

The publisher for this copyrighted material is Springer Science + Business Media. By clicking "accept" in connection with completing this licensing transaction, you agree that the following terms and conditions apply to this transaction (along with the Billing and Payment terms and conditions established by Copyright Clearance Center, Inc. ("CCC"), at the time that you opened your Rights link account and that are available at any time at http://myaccount.copyright.com).

Limited License

With reference to your request to reprint in your thesis material on which Springer Science and Business Media control the copyright, permission is granted, free of charge, for the use indicated in your enquiry.

Licenses are for one-time use only with a maximum distribution equal to the number that you identified in the licensing process.

Example 1: Springer Science + Business Media makes no representations or warranties with respect to the licensed material.

Example 2: Springer Science + Business Media makes no representations or warranties with respect to the licensed material and adopts on its own behalf the limitations and disclaimers established by CCC on its behalf in its Billing and Payment terms and conditions for this licensing transaction.

Indemnity
You hereby indemnify and agree to hold harmless Springer Science + Business Media and CCC, and their respective officers, directors, employees and agents, from and against any and all claims arising out of your use of the licensed material other than as specifically authorized pursuant to this license.

NoTransferofLicense
This license is personal to you and may not be sublicensed, assigned, or transferred by you to any other person without Springer Science + Business Media's written permission.

NoAmendmentExceptinWriting
This license may not be amended except in a writing signed by both parties (or, in the case of Springer Science + Business Media, by CCC on Springer Science + Business Media's behalf).

ObjectiontoContraryTerms
Springer Science + Business Media hereby objects to any terms contained in any purchase order, acknowledgment, check endorsement or other writing prepared by you, which terms are inconsistent with these terms and conditions or CCC's Billing and Payment terms and conditions. These terms and conditions, together with CCC's Billing and Payment terms and conditions (which are incorporated herein), comprise the entire agreement between you and Springer Science + Business Media (and CCC) concerning this licensing transaction. In the event of any conflict between your obligations established by these terms and conditions and those established by CCC's Billing and Payment terms and conditions, these terms and conditions shall control.

Jurisdiction
All disputes that may arise in connection with this present License, or the breach thereof, shall be settled exclusively by arbitration, to be held in The Netherlands, in accordance with Dutch law, and to be conducted under the Rules of the 'Netherlands Arbitrage Instituut' (Netherlands Institute of Arbitration).***OR:***

All disputes that may arise in connection with this present License, or the breach thereof, shall be settled exclusively by arbitration, to be held in the Federal Republic of Germany, in accordance with German law.

Other terms and conditions:

Questions? customercare@copyright.com or +1-855-239-3415 (toll free in the US) or +1-978-646-2777.